Technische Universität München
TUM School of Engineering and Design

Rerating of Electronic Components for Improved Lunar Mission Night Survival

János Daniel Biswas

Vollständiger Abdruck der von der TUM School of Engineering and Design der Technischen Universität München zur Erlangung des akademischen Grades eines

Doktors der Ingenieurwissenschaften (Dr.-Ing.)

genehmigten Dissertation.

Vorsitz: Prof. Dr.-Ing. Agnes Jocher

Prüfer der Dissertation:

1) Prof. Dr. rer. nat. Dr. h.c. Ulrich Walter
2) Prof. Dr.-Ing. Philipp Reiß

Die Dissertation wurde am 28.09.2022 bei der Technischen Universität München eingereicht und durch die TUM School of Engineering and Design am 30.01.2023 angenommen.

Acknowledgements

Thank you to everyone who enabled me to pursue my research for the past years and helped me to make this dissertation possible.

The past six years have been a challenging time, made enjoyable by all of my colleagues at the Chair of Astronautics. A particular thanks to my colleagues from the exploration group, Daniel Kaschubek, Laura Grill, Matthias Killian and Christian Gscheidle who shared my passion for space exploration and on whom I could always count for fruitful discussions. To Martin Dziura and Sebastian Rückerl, the two wizards that kept this institute running even during the recent pandemic and to Florian Schummer with whom I shared a hobby of tinkering with broken down vacuum chambers. Thank you also to Martin Rott, who helped to steer me through the darkness of TUM bureaucracy and always assisted me with the latest vacuum experiments. Thank you also to Uta Fellermair for all her assistance in organizational matters.

Thank you to my many external colleagues for the many years of excellent cooperation. A special thanks to Simon Sheridan and Thibaud Chupin, with whom work was not only productive, but always also a lot of fun. To Jeremi Gancet, for keeping our H2020 consortium together. To Lutz Richter and Tim Tattusch, for the fruitful years working together.

Thank you to my supervisor, Prof. Ulrich Walter, who gave me the opportunity to start this work, who always encouraged independent thinking and whose door always stood open if advice or other forms of support were necessary.

A special thanks to Philipp Reiß, who introduced me to the world of lunar exploration when I was still a working student, mentored me throughout my time at the institute and now served as my co-advisor for this dissertation.

Finally, thank you to my family, friends and my girlfriend, who supported me throughout this journey.

Abstract

One of the most challenging problems in lunar exploration is the extreme environment encountered during the lunar night: the slow rotation of the Moon requires surface systems to endure 14.75 days in complete darkness, with surface temperatures below -200°C. A similar environment is encountered in the proposed exploration of the lunar poles, especially in or around permanently shadowed regions. The problem is exacerbated by the ongoing trend towards privatization and miniaturization of exploration systems, as radioisotope power sources are unavailable for the majority of these mission and with current plans including miniature rovers or CubeSat-like surface deployed stand-alone payloads. Previous studies have explored the development of dedicated low temperature electronics that are able to operate without any additional thermal control. However, so far these developments have not been widely adopted, because of the high necessary development effort and the inability of this approach to keep pace with the rapid pace of development in space electronics. The present thesis investigates the use of the inherent low temperature capability of existing space electronics through rerating to reduce thermal control efforts.

First, the low temperature rerating potential of an electronic system is explored on the basis of the LUVMI-X Deployable Payload Platform (DPP) electronics. To this end, the three core systems, the command & data handling system, the power distribution system and the communication system are examined. For the command and data handling system, a set of six single board computers is evaluated at low temperatures, yielding a -109°C limit for the preferred board. A system level test is performed for the power system, yielding full functionality to -85°C and partial functionality to -123°C. Detailed low temperature testing of each component shows that an exchange of four components results in a workable design that allows operation to -120°C. Due to funding limitations, only a low fidelity version of the communication system could be tested but the results show successful receipt and transmission of S-band signals down to -91°C and microcontroller responses down to -130°C. The results serve as an example on how electronics can be operated at temperatures significantly below their manufacturer ratings.

In a second step, a study on energy storage options for lunar night survival is presented. While previous studies have examined potential low temperature energy storage devices, it is unclear which storage technology will provide the most benefit for lunar night survival application. Therefore, an overview of existing energy storage technologies is presented and a pre-selection of promising technologies is made. The selected devices are tested to determine the temperature dependent capacity. Based on this data, the theoretical night survival time is calculated for a simplified system for each device and temperature. The results show that each device has an optimal operating temperature and that dedicated low temperature batteries do not provide any benefit compared to conventional high energy density batteries.

In a third step, the impact of low temperature rerated components on the night survivability is examined in thermal simulations of three example systems: The DPP, a lunar polar rover and a lunar lander. A simplified thermal model of each system is created and exposed to simulated lunar night conditions, while the necessary heating power is monitored. The results show, that an insular thermal architecture is necessary, as low temperature components need to be effectively insulated against high temperature components like the battery to prevent heat loss. It is shown that low temperature rerating can significantly outperform possible improvements by conventional thermal design, especially for small systems, but only diminishing returns are achieved for rerating temperatures below -80°C.

Finally, an experimental prototype of the DPP is built in its baseline configuration and in an advanced configuration that utilizes a rerated power system. The prototypes are tested in thermal-vacuum. The results confirm the feasibility and benefit of low temperature rerating for improved lunar night survival.

Zusammenfassung

Eines der größten Probleme bei der Erforschung des Mondes sind die extremen Bedingungen während der Mondnacht: Aufgrund der langsamen Rotation des Mondes müssen Oberflächensysteme 14,75 Tage in völliger Dunkelheit bei Oberflächentemperaturen von unter -200°C aushalten. Ähnliche Bedingungen werden auch bei der geplanten Erkundung der Mondpole, angetroffen, insbesondere in oder in der Nähe der dauerhaft beschatteten Regionen. Frühere Studien haben sich mit der Entwicklung spezieller Tieftemperatur-Elektronik befasst, die ohne zusätzliche thermische Kontrolle auskommt. Bislang haben sich diese Entwicklungen jedoch nicht durchgesetzt, da sie einen hohen Entwicklungsaufwand erfordern und mit der rasanten Entwicklung der Raumfahrtelektronik nicht Schritt halten können. Die vorliegende Arbeit untersucht die Nutzung der inhärenten Tieftemperaturfähigkeit bestehender Raumfahrtelektronik durch Rerating, um den Aufwand für die thermische Kontrolle zu reduzieren.

Zunächst wird das Tieftemperatur-Rerating-Potenzial eines elektronischen Systems anhand der Elektronik der LUVMI-X Deployable Payload Platform (DPP) erforscht. Drei Kernsysteme, das Command- und Datenverarbeitungssystem, das Energieverteilungssystem und das Kommunikationssystem werden untersucht. Für das Command- und Datenverarbeitungssystem wird ein Satz von sechs Einplatinencomputern bei niedrigen Temperaturen getestet, wobei sich ein Grenzwert von -109°C für die bevorzugte Platine ergibt. Für das Stromversorgungssystem wird ein Test auf Systemebene durchgeführt, bei dem die volle Funktionalität bis -85°C und eine Teilfunktionalität bis -123°C festgestellt wird. Detaillierte Tieftemperaturtests der einzelnen Komponenten zeigen, dass ein Austausch von vier Komponenten zu einem funktionierenden Design führt, das einen Betrieb bis -120°C ermöglicht. Eine Low-Fidelity-Version des Kommunikationssystems wird getestet und die Ergebnisse zeigen den erfolgreichen Empfang und die Übertragung von S-Band-Signalen bei bis zu -91°C und die Funktionalität des Mikrocontrollers bei bis zu -130°C.

In einem zweiten Schritt wird eine Studie über Energiespeicheroptionen für das Überleben in der Mondnacht vorgestellt. Es wird ein Überblick über bestehende Energiespeichertechnologien gegeben und eine Vorauswahl an vielversprechenden Technologien getroffen. Die ausgewählten Geräte werden getestet, um die temperaturabhängige Kapazität zu bestimmen. Auf der Grundlage dieser Daten wird die theoretische Nachtüberlebenszeit für ein vereinfachtes System für jede Technologie und jede Temperatur berechnet. Die Ergebnisse zeigen, dass jede Technologie eine optimale Betriebstemperatur hat und dass spezielle Niedrigtemperaturbatterien im Vergleich zu herkömmlichen Batterien mit hoher Energiedichte keine Vorteile bieten.

In einem dritten Schritt wird die Auswirkung von Komponenten mit niedriger Temperatur auf die Überlebensfähigkeit bei Nacht in thermischen Simulationen von drei Beispielsystemen untersucht: Der DPP, einem polaren Mondrover und einer Mondlandefähre. Für jedes System wird ein vereinfachtes thermisches Modell erstellt und den simulierten Mondnachtbedingungen ausgesetzt, während die erforderliche Heizleistung überwacht wird. Die Ergebnisse zeigen, dass eine insulare thermische Architektur notwendig ist, da Tieftemperaturkomponenten wirksam gegen Hochtemperaturkomponenten wie die Batterie isoliert werden müssen, um Wärmeverluste zu verhindern. Es wird gezeigt, dass die Verbesserung bei niedrigen Temperaturen die möglichen Verbesserungen durch konventionelles thermisches Design deutlich übertreffen kann, insbesondere bei kleinen Systemen. Für Temperaturen unter -80°C können jedoch nur abnehmende Erträge erzielt werden.

Schließlich wird ein experimenteller Prototyp der DPP in seiner Basiskonfiguration und in einer fortgeschrittenen Konfiguration gebaut, die ein rerated power system verwendet. Die Prototypen werden im Thermal-Vakuum getestet. Die Ergebnisse bestätigen die Durchführbarkeit und den Nutzen der Umschaltung auf niedrige Temperaturen, um das Überleben in der Mondnacht zu verbessern.

Contents

Abbreviations

ADC *Analogue to digital converter*
ALSEP *Apollo Lunar Surface Experiment Package*
CDH Command & Data Handling Module
CLPS *Commercial Lunar Payload Services*
CMOS *Complementary Metal-Oxide-Semiconductor*
COTS *Commercial-of-the-shelf*
CTE Coefficient of Thermal Expansion, *Coefficient of thermal expansion*
DPP Deployable Payload Platform
DRAM *Dynamic Random-Access Memory*
EASEP *Early Apollo Scientific Experiments Package*
EEE *Electrical, Electronic and Electro-mechanical*
EMPS *Extendable Modular Power Supply*
EPS Electrical Power System
FPGA Field Programmable Gate Arrays
IC *Integrated Circuit*
LUVMI *Lunar Volatiles Mobile Instrumentation*
LUVMI-X *LUVMI-extended*
LVS Lunar Volatiles Scout
MER *Mars Exploration Rover*
MLI *Multi-Layer-Insulation*
MOSFET *Metal oxide field effect transistor*, *Metal oxide field effect transistor*
MSL *Mars Science Laboratory*
MSM *Mission Survival Module*
PWM *Pulse-Width-Modulation*
RHU Radio-isotopic Heater Unit
RTG Radioisotope Thermo-Electric Generator
SOI *Silicon on Insulator*
SRAM *Static Random-Access Memory*
VDA *Vapor Deposited Aluminum*
VIPER Volatiles Exploration Polar Exploration Rover
WEB *Warm-Electronics-Box*, *Warm-Electronic-Box*

1 Introduction

1.1 Motivation

This section is a modified excerpt from (Biswas et al. 2021b), written by the author of this thesis

After decades of very limited activity, a renaissance of lunar exploration has started in recent years. Perhaps kick-started by the Lunar X-Prize and by the desire of space agencies to explore the resource potential of the Moon, a large number of surface missions have recently been announced by agencies and private enterprises. This new wave of lunar surface exploration, spearheaded by the landing of Chang'e 3 in 2013, and possibly culminating in the announced crewed NASA Artemis landings in the mid-2020s, targets more ambitious science objectives and will be more sustainable than Apollo era exploration. An overview of current missions in planning is shown in Figure 1-1: Until 2029, a total of 30 lunar missions are in planning by institutional and commercial entities from all over the world. Out of these 30 missions, 21 include a surface segment that will attempt a soft landing on the Moon, ten of these will include a rover for mobility and at least one manned surface mission (Artemis 3) is planned.

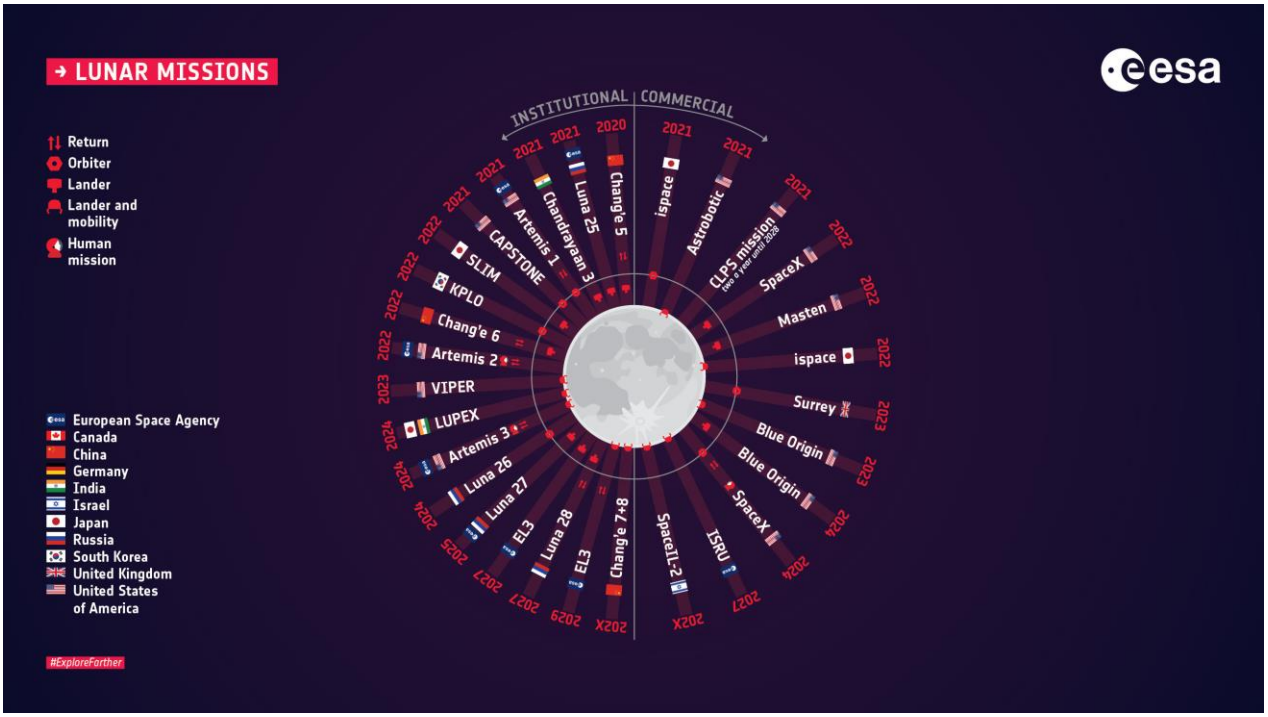

Figure 1-1: Graphical overview of currently planned lunar missions (ESA 2020)

For any lunar surface mission, one of the most demanding challenges is the extreme environment of dust, radiation, vacuum and especially its thermal environment. In the absence of a tempering atmosphere, surface temperatures range from about 50 K to 390 K, depending on daytime, latitude and surrounding topography (Williams et al. 2017). Maximum daytime temperatures are more moderate near the poles, but low solar elevation causes significant shadowing by local topography that severely impact surface temperatures. In addition, the relatively long duration of a lunar month (average synodic lunar day) of 29.531 days (Vaniman et al. 1991) lead to an average nighttime duration of 354.4 h. In the absence of solar

illumination and faced with the extremely low temperatures of the surface and space, there will be no external energy source available.

Keeping systems operational during the lunar night requires thermal control to keep internal temperatures within component envelopes. Insulation, such as multi-layer insulation (MLI), low emissivity coatings or aerogel reduce heat loss at night, but excessive insulation causes overheating during the day. Ensuring reliable operation during, or survival of this period is "*probably the most demanding energy storage challenge that will be faced in the exploration of the solar system*" (Petro 2020). This is especially true for some of the currently planned missions. Building on the advances in spacecraft miniaturization demonstrated by CubeSat technology in recent years, many of the proposed or planned missions involve surface systems with a mass of less than 25 kg. Examples include the Sorato (4 kg) and Polar Ice Explorer (12kg) rovers of ispace inc. (Walker 2018), Cuberover (4 kg) from Astrobotic (Astrobotic 2020a), Mission One (5 kg) of Pulispace (Khan et al. 2018) or the stationary Robex Remote Unit concept (3 kg and 10 kg) (Tsakyridis et al. 2019). Together with further similar examples, these standalone units make a new class of lunar surface systems that are considerably smaller than what has flown previously. Considering the significant time, effort and cost involved in the preparation and execution of any lunar mission, it should be a priority to maximize the operational lifetime of deployed systems. Despite this, it is expected that the majority of early commercial lunar systems are not planned to survive the first lunar day (Petro 2020).

Even missions that do not aim for full nighttime survival can already face similar challenges. One of the major objectives among the current lunar missions is the desire to explore the lunar polar areas, either to investigate cold trapped volatiles deposits, to benefit from the unique illumination environment or simply because it has not been visited by any mission before (Carpenter 2019; Lawrence 2016). In these regions, the lunar day and night cycle does not follow its normal trajectory, as the low solar elevation and harsh lunar topography cause long shadows and thus irregular illumination patterns. This causes many large permanently shadowed regions (PSRs) and a few small areas with higher illumination and shorter nights. Accessing PSRs, which are the prime locations for the exploration of lunar volatiles, requires rovers to temporarily operate in shadow on with surface temperatures as low as 50 K (Williams et al. 2017).

Previous studies have proposed various approaches to address extreme environments encountered in space exploration, such as the development of low temperature tolerant systems, new insulation strategies or the provision of external energy supplies through remote energy transfer. However, so far the majority of these approaches could not be successfully implemented because of insufficient technical maturity or excessive development effort. The present thesis investigates low temperature rerating of existing electronic components as a fast and cost effective method to improve lunar nighttime operational capability, without sacrificing daytime performance.

1.2 Background

1.2.1 Previous Robotic Lunar Missions

The very first spacecraft to perform a soft landing on the Moon was the soviet Luna-9 lander in 1966, a small sphere shaped probe that carried a single camera and a radiation detector. Equipped with primary batteries, the probe lasted for four earth days on the surface (Huntress and Marov 2011). Further 22 missions have succeeded it since, as Table 1-1 shows. The US Surveyor program managed to safely land a total of five landers. These landers were the first that were designed for lunar night survival. Temperature sensitive electronics were housed in two warm electronics boxes that were insulated by MLI and kept at +4.4°C and -17.8°C by electric heaters from a 3500 Wh battery. Radiators were decoupled by a set of bimetallic switches (NASA JPL 1966). Surveyor 3 died during its first lunar night, the other four managed to survive up to six nights with varying degrees of damage. Surveyor 6 and 7 even achieved a combined 120 hours of night-time operation (NASA JPL 1969; Creel 2018).

In addition to the short-term manned excursions, a set of long-term experiment packages was deployed during the manned Apollo missions: The Early Apollo Scientific Experiments Package (EASEP) of Apollo 11 and the Apollo Lunar Surface Experiment Packages (ALSEP) of Apollo 12 to 17. EASEP was solar powered

but with Radio-isotopic Heater Units (RHUs) and survived its first lunar night but died during noon on the second day. The following ALSEP packages operated flawlessly for up to 98 lunar day/night cycles (Creel 2018) and were shut down only due to programmatic reasons. Each package consisted of a central control station, a Radioisotope Thermo-Electric Generator (RTG) as power supply and of multiple payload units. The central station was heavily insulated to keep its electronics between -17.8°C and +51.7°C. The electronics were enveloped by MLI and separated from the main structure by thermal insulators. The wires between that connected the different units were thermally decoupled from the electronics by manganin inserts (Harris 1972).

In 1970 and 1973, the Soviet Union deployed the two remote operated Lunokhod rovers on the lunar surface, which were also major successes in terms of lunar night survivability. With masses of 756 kg and 836 kg, the two solar powered rovers managed to survive ten and four months. The rovers used a pressurized chassis that allowed internal heat transfer through forced convection, an intricate mechanism that allowed a lid to close over the main radiator to reduce heat loss at night and a massive RHU with 11 kg of polonium-210 to provide warmth during the night. Lunokhod I eventually failed when the pressure in its chassis suddenly dropped, which likely caused internal overheating and Lunokhod II was lost when it scraped a crater wall, causing dust to settle on the radiators and solar panels, which caused critical thermal and power issues (Huntress and Marov 2011).

After the end of the Apollo era, the landing of Chang'e 3 with the Yutu rover in 2013 marked the end of nearly four decades without human activity on the lunar surface. The Chang'e 3 lander was designed to operate for 12 months and the rover for three months. Its thermal control system used a "subcabin" approach, in which systems that were obsolete after landing were housed apart from systems that were needed after the landing. This way, heating power was concentrated only on those elements that were still needed. Internal heat transfer was facilitated by loop heat pipes and two phase thermosyphons. An external RHU provided heat for the lunar night, which was connected to switchable heat pipes, allowing the heat flow to be shut-off during the day (SI et al. 2014). The lander furthermore features a small RTG to provide electrical base power supply during the lunar night, when solar power is not available (Ye et al. 2017). Yutu featured a similar design, though no it had no RTG and entered a hibernation mode during the lunar night. In 2019, Chang'e 4 followed to perform the first far side landing, relying on a mostly identical design. So far, both landers and the second Yutu rover are still fully operational while the first Yutu rover survived at least 31 months but lost mobility in the first lunar night (Krebs 2019). A more detailed examination of the thermal design of these missions is given by Bauer (2021).

In conclusion, previous missions have displayed successful lunar night survival capability by relying on RHUs/RTGs to supply heat/power. The non-nuclear Surveyor landers achieved some night survival by relying on passive survival.

Table 1-1: Previous examples of long-term payload supporting equipment on the lunar surface

Mission	Nation	Mass (dry) [kg]	Year	Power Supply	Night-Survival Performance	Source
Luna-9 Lander	UDSSR	105	1966	-	First Soft Landing	(Huntress and Marov 2011)
Luna-13 Lander	UDSSR	113	1966	-	-	(Huntress and Marov 2011)
Luna-16 Lander	UDSSR		1970	-	Sample Return	-
Luna-17 Lander	UDSSR		1970	-	-	-
Luna-17 Lunokhod-1	UDSSR	756 kg	1970	Solar /Battery + RHU	Operated for 10 months (11 lunar days),	(Howell 2016; Huntress and Marov 2011)
Luna-20 Lander	UDSSR		1972		-	-

Mission	Nation	Mass (dry) [kg]	Year	Power Supply	Night-Survival Performance	Source
Luna-21 Lander	UDSSR		1973		-	-
Luna-24 Lander	UDSSR		1976		-	-
Luna-24 Lunokhod-2	UDSSR	~800 kg	1976	Solar /Battery + RHU	Operated for 4 months, died thermal problem due to dust on radiator	(Zak 2018)
Surveyor 1 Lander	USA	~300 kg	1966	Solar /Battery	Survived first lunar night, some data until 6th day	(NASA JPL 1966)
Surveyor 3 Lander	USA	~300 kg	1967	Solar /Battery	Died during first night	(NASA JPL 1967)
Surveyor 5 Lander	USA	~300 kg	1967	Solar /Battery	Survival until 4th night	(NASA JPL 1969)
Surveyor 6 Lander	USA	~300 kg	1967	Solar /Battery	40h operation during 1st night, but damaged	(Creel 2018)
Surveyor 7 Lander	USA	~300 kg	1968	Solar /Battery	80h operation into first night, survived until second	(Creel 2018)
Apollo 11/ EASEP 11	USA	~50 kg	1969	Solar /Battery + RHU	Survived first night, died at noon second night	(O'Brien 2019)
Apollo 12/ ALSEP 12	USA	25 kg	1969	RTG	Survived 98 lunar day/night cycles	(Creel 2018)
Apollo 14/ ALSEP 14	USA	25 kg	1971	RTG	Survived 83 lunar day/night cycles	(Creel 2018)
Apollo 15/ ALSEP 15	USA	25 kg	1971	RTG	Survived 77 lunar day/night cycles	(Creel 2018)
Apollo 16/ ALSEP 16	USA	25 kg	1972	RTG	Survived 68 lunar day/night cycles	(Creel 2018)
Apollo 17/ ALSEP 17	USA	25 kg	1972	RTG	Survived 60 lunar day/night cycles	(Creel 2018)
Chang'e 3 Lander	China	1200 kg	2013	Solar /Battery + RTG	8 years +	(Li et al. 2015)
Chang'e 3 Rover	China	120 kg	2013	Solar /Battery + RHU	Total of 31 months, but problems from 1st night on	(Li et al. 2015)
Chang'e 4 Lander	China	1200 kg	2019	Solar /Battery + RTG	24 months +	(Krebs 2019)
Chang'e 4 Rover	China	120 kg	2019	Solar /Battery + RHU	24 months +	(Krebs 2019)
Chandrayaan-2 Vikram Lander	India	1250 kg	2019	Solar /Battery	Planned for 14 days (failed)	(Sundararajan 2018)
Chandrayaan-2 Pragyan Rover	India	27 kg	2019	Solar /Battery	Planned for 14 days (failed)	(Sundararajan 2018)
Beresheet	Israel	600 kg	2019	Solar /Battery	Planned for 3 days (failed)	(eoPortal Directory 2019)

1.2.2 Currently Planned Missions or Mission Concepts

An overview of the currently planned missions or mission concepts is given in Table 8-1. Launch dates were taken from publications or press releases and are usually optimistic estimates. Some of the mission concepts do not yet have sufficient funding for a flight mission and may never actually fly. Few publications include data on expected surface lifetime, but all of the listed systems are solar / battery powered and do not include RHUs. The only mission that fully plans for night-time survival is the VIPER rover, which will use the relatively short nights of a solar oasis near the South Pole (see section 1.2.3). So far, no details have been published on the thermal control system of VIPER, except that it may contain loop heat pipes with actuated valves to regulate heat flow and reduce heat loss at night (Patton 2021). It is likely that all mission operators will attempt to revive their systems on the surface after the first night, but no specific provisions in that regard have been found in the published literature.

While any mission will benefit from the ability to survive the lunar night, some missions also require to operate in shadow. This is especially relevant for missions designed to investigate permanently shadowed regions, for example to detect cold trapped volatiles. In these cases, the mission success depends on the system's ability to operate in complete shadow with environmental temperatures similar to, or colder than those found during the lunar night and the thermal control systems of these systems are specifically designed to operate both during the day and in shadow. For reference, the following paragraphs show a few thermal design examples of some of the planned systems.

The first example is the Peregrine lander. It is developed by Astrobotic and will first fly in 2022 as part of the NASA CLPS program and will operate at a mid-latitude of approximately 45°. It has a wet mass of 1283 kg and a design lifetime of 8 earth days. As a large system, one of the challenges of this design are the large differences in heat flux experienced by the different parts of the lander. The sun facing side and top mounted solar panels will get hot, while the parts in shadow will get rather cold. The design was therefore simplified by restricting the orientation of the lander on the surface, which enabled specific design solutions for the hot and cold sides, but the lander may take damage if its orientation on the surface is off by more than 45°. Components are placed on the lander depending on their temperature limits and heat dissipation. The thermal design also includes a heat switch between transponder and radiator and a diode heat pipe, which is switched off by the influence of lunar gravity. Critical components for the thermal design were the battery (+10…35°C) and the transponder (-10…55°C) (Mauro 2019). An image of the Peregrine thermal model is shown in Figure 1-2.

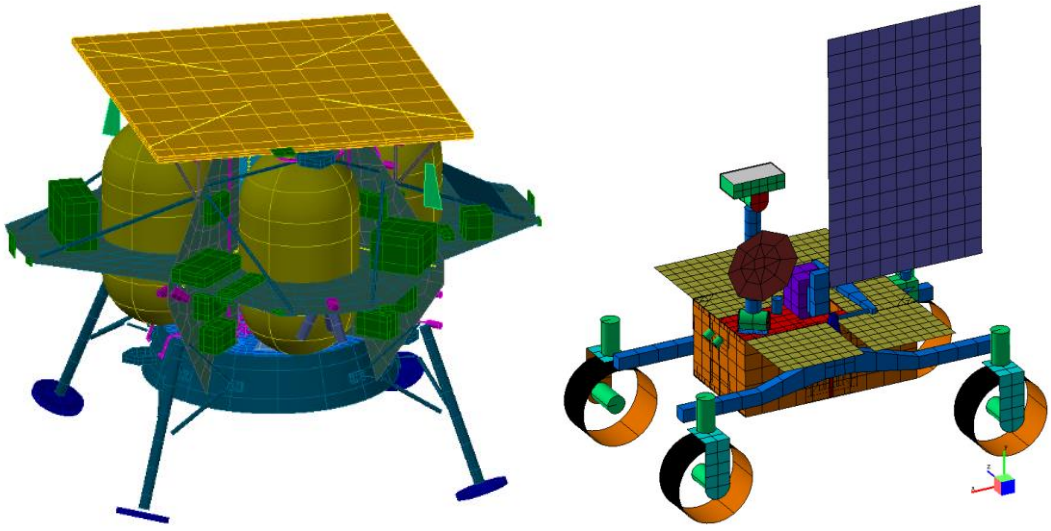

Figure 1-2: Thermal models of the Peregrine lander (Mauro 2019) [left] and LUVMI (Fau et al. 2019) [right].

Figure 1-2 also shows an ESATAN model of LUVMI. LUVMI and its successor LUVMI-X are concept rovers with a mass of about 50 kg that carry a suite of instruments for the exploration of volatiles in and around cold traps near the lunar poles. As such, it is adapted to the low solar elevation angles near the poles, with the

vertically mounted solar panel. In this configuration, the top surface is white painted to act as radiator, while the rest of the rover chassis is insulated by either VDA coating or MLI. It is worth noting, that in this case, the thermal hot case is experienced when the solar elevation is highest, which occurs when the rover is positioned on a sun facing slope. The rover also needs to be capable to operate in shadow for up to 48 h, which is achieved by thermally decoupling the rover avionics from the radiator with a heat switch. The most critical components for LUVMI are the battery (-10…60°C) and the navigation camera (-10…55°C) (Fau et al. 2019; Losekamm et al. 2021). A similar design is used for the 18 kg MoonRanger rover, which is scheduled to fly on the Masten-XL lander in 2022. Like LUVMI, it is designed to operate in the Polar Regions and in shadow. Its avionics are mounted to the top surface of the chassis that acts as radiator, though no heat switch is used in this design. The in-shadow operational time is not disclosed, but it needs to activate its survival heater after approximately one hour to keep its critical components within operational temperatures (-10…35°C) (Fisch et al. 2020). An image of the MoonRanger thermal model is shown in Figure 1-3.

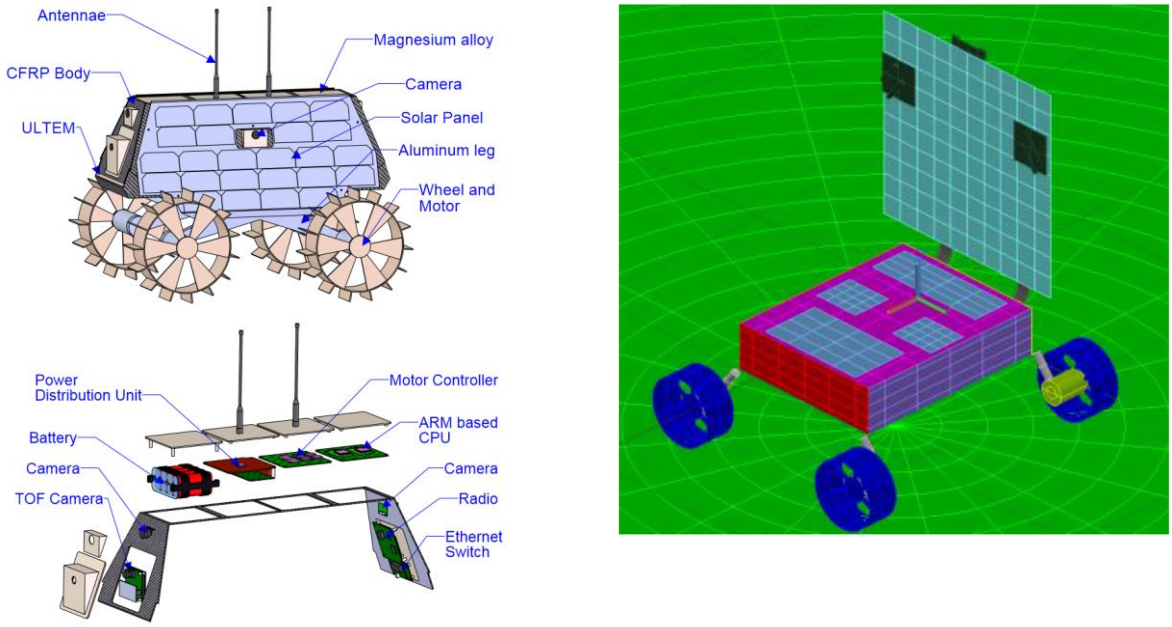

Figure 1-3: Render images of the Sorato rover design (left), thermal model of the MoonRanger micro-rover (right) (Fisch et al. 2020)

An even more challenging design is implemented for the Sorato rover, which has a mass of just 4 kg. No mass was available for an external solar panel, so the solar cells are directly mounted to the chassis. To thermally decouple the high absorptivity cells from the chassis, the cells are attached directly onto the MLI covering the rover. As with the other rover examples, the avionics are mounted to the top surface of the rover, which is covered with a silver-teflon coating for high emissivity to act as radiator. Its most critical component is the battery (-5…45°C) (Oikawa et al. 2018; Tanaka 2018).

In conclusion, currently planned small lunar surface systems rely on classical thermal design strategies, with insulated and heated compartments, typically coupled with some device to regulate the heat loss towards the radiator like heat switches or variable conductance heat pipes. This limits these systems to very short periods of in-shadow operation. Passive survival has not been investigated in depth. Radioisotope heaters are not available for a majority of these missions.

1.2.3 Related Research at the Chair of Astronautics (TUM)

Lunar Volatiles Scout (LVS)

The Lunar Volatiles Scout is a small, integrated instrument for soil sampling and analysis designed for the search of volatiles bound in lunar regolith, developed by the Chair of Astronautics (TUM), OHB System and the Open University. During operation, the instrument inserts a heating element surrounded by an enclosing shell into the regolith. The heating element releases volatiles that are then analyzed by a miniature ion-trap mass spectrometer (Biswas et al. 2020). Due to its small size and moderate mass, the instrument is particularly suited for operation on small rovers that allow the instrument to determine the lateral distribution of volatiles within the range of the rover. However, the most interesting targets for investigation of lunar volatiles are the polar areas, where volatiles are suspected to exist in large quantities in cold traps, especially in permanently shadowed regions. Thus, optimal application of the LVS instrument requires a rover that is able to enter and operate in permanently shadowed regions. Mission studies have been performed (Losekamm et al. 2022; Gscheidle et al. 2022), showing that this is feasible, but operational lifetime of the rovers in shadow is constrained by the necessity to compensate heat loss by battery powered heaters. Methods to reduce heat loss would extend operational lifetime and thus increase mission success and scientific return. Two images of the LVS are shown in Figure 1-4.

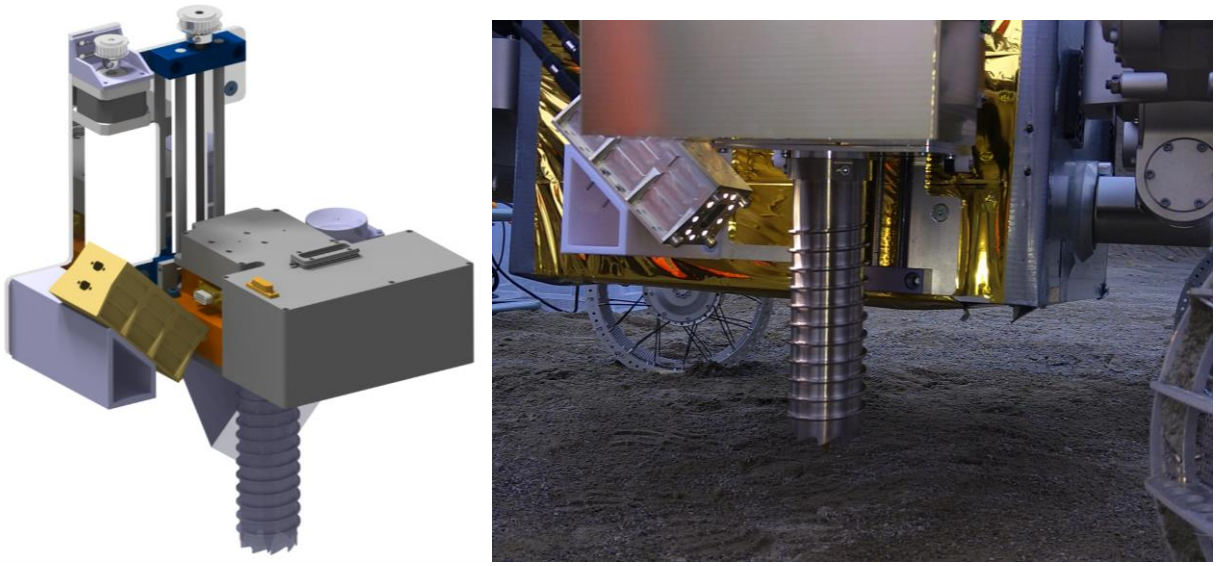

Figure 1-4: Rendered image of the LVS with linear actuator and SurfCam++ imager (left) and image of the LVS prototype attached to the LUVMI-X platform during a demonstration campaign.

Deployable Payload Platform (DPP)

The Deployable Payload Platform standalone payload platform was designed to carry the Volatiles & Context Analysis Suite Sensor to perform stationary long-term measurements of the lunar exosphere, especially changes of the exosphere caused by outgassing events of lunar volatiles bound in polar cold traps. Such events could occur during (micro-) meteorite impacts or changes in illumination, especially during sunrise. The DPP adheres to a 2-Unit CubeSat form factor and is designed to be carried by the LUVMI-X rover platform (Losekamm et al. 2021). It consist of the payload and a support module, featuring an independent power system with solar cells and battery, a communication system with an S-Band transceiver and patch antenna for direct-to-earth communication and a Command & Data Handling module (CDH). A detailed description of its elements can be found in 0.

As sunrise is the most important event to observe for the payload, night-time survival would be highly beneficial for the DPP. The original design achieved a 48 h survival period in shadow with a 96 Wh battery module, which would be sufficient to withstand shorter temporary shadowing periods that occur frequently

in certain areas at the lunar poles. However, the ability to survive longer in-shadow periods will allow the DPP to be used in wider areas and allow for longer accumulation times for the volatiles in its environment. For this reason, methods were investigated to improve the night-time survivability of the payload.

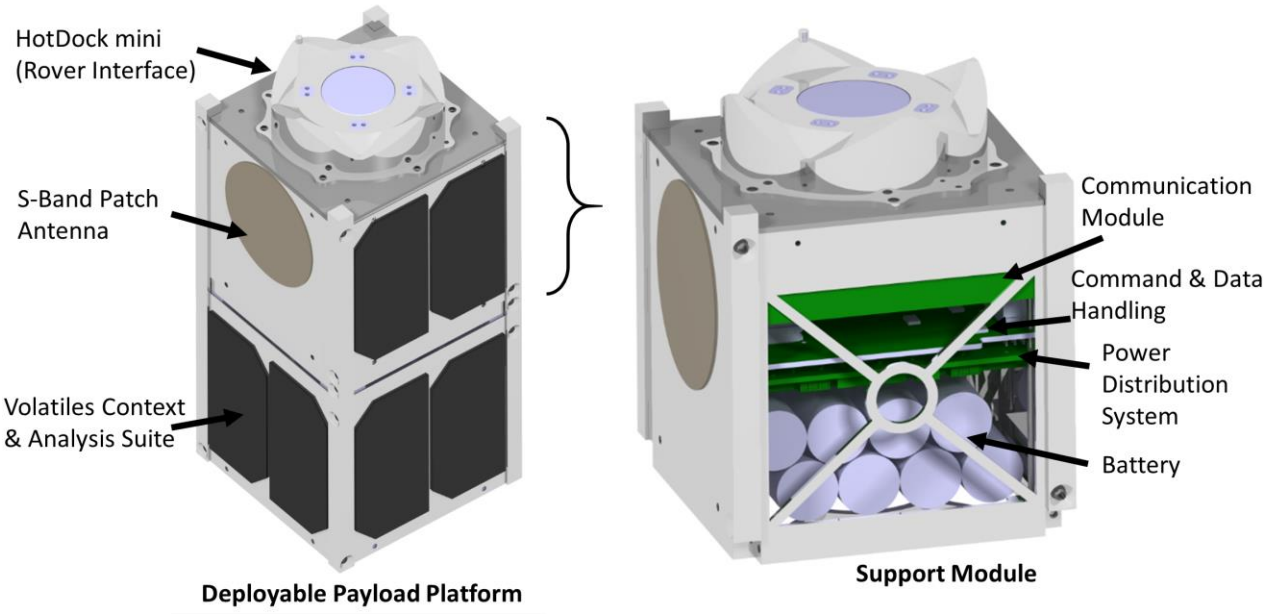

Figure 1-5: Render image of the LUVMI-X Deployable Payload Platform (left) and the Support module in detail (right)

1.2.4 Classification and Elements of Robotic Lunar Surface Systems

Robotic lunar surface systems can be classified by type, size, launch date and power source. Figure 1-6 shows the landed masses of historic lunar missions and near future planned lunar missions from Table 1-1 and Table 8-1. It is shown that while the planned manned return to the Moon will included surface systems as large as or even larger than the Apollo landers, a significant amount of new systems will be much smaller than even the ALSEP systems of the Apollo era. Surface systems can further be distinguished by their power source, which is either solar / battery powered, solar / battery powered with RHU assistance, nuclear powered or externally powered. The focus of the present thesis are solar / battery powered systems of smaller size, since it is a highly relevant group with many exciting missions of this type in planning and it is the group for which lunar night survival is the most challenging.

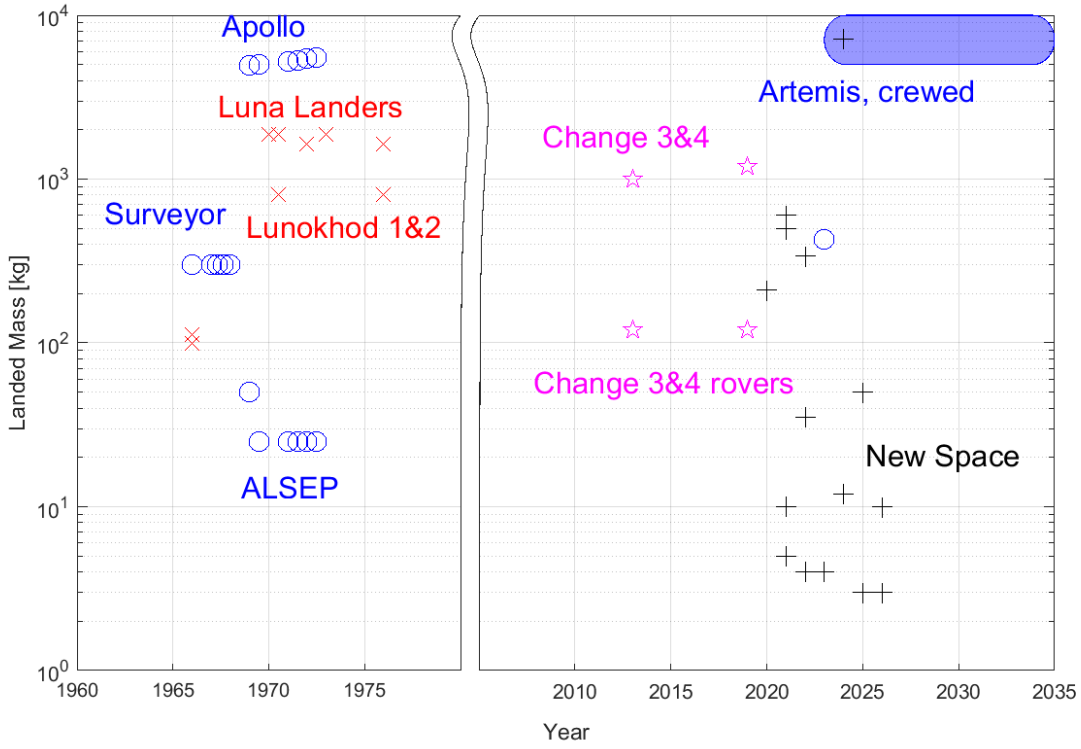

Figure 1-6: Past and planned lunar surface missions by landed mass.

Finally, robotic surface systems can be classified by their degree of autonomy into: landers, rovers, standalone payloads and payloads. Depending on this class, each system contains different electronic subsystems, as shown in Figure 1-7. Payloads are the simplest class and are usually subsystems of one of the other classes. There is a wide variety of existing payloads and payload concepts, all of which can require different elements. However, usually a payload contains a sensor element specific to its application and a more generic payload computer or On-Board computer. An overview of existing payloads for the NASA CLPS program is presented in Table 8-2. Standalone payloads complement the payload elements by a power system that typically includes solar cells and a battery or an RTG and a communication module and antenna. Landers include all of the elements of a Standalone payload, but additionally have a propulsion system and flight avionics like an ADCS and navigation sensors like cameras. However, if the lander does not plan to relaunch, these elements are not required to operate after landing. Rovers also contain all of the elements of a standalone payload in addition to navigation sensors / cameras, motion controllers and actuators, which also need to survive during the lunar night.

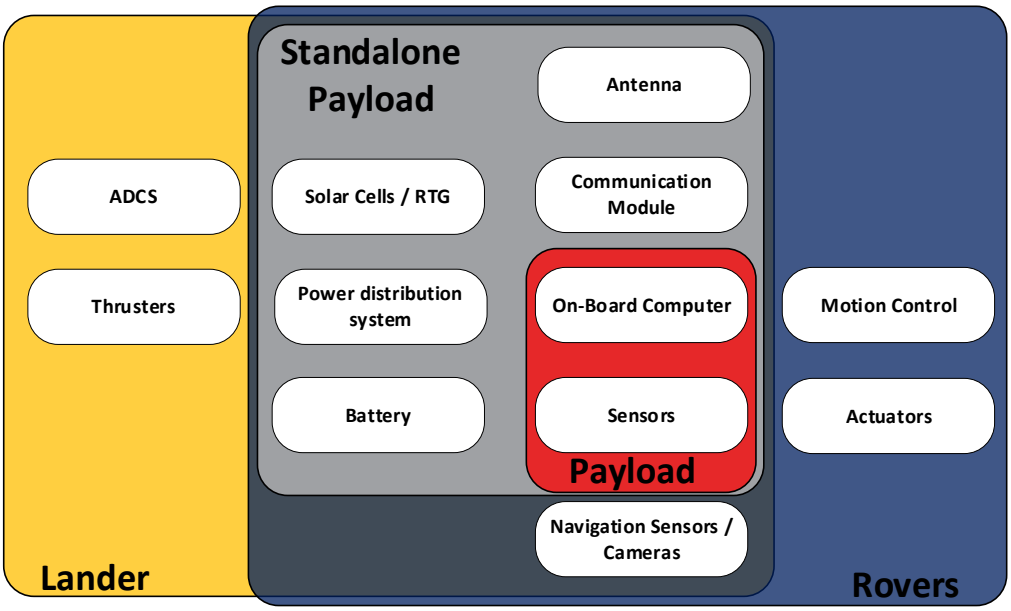

Figure 1-7: Venn diagram showing elements of different types of robotic lunar surface systems

1.2.5 Definitions

Lunar Night Survival

For robotic systems, survival of the lunar night means the retention throughout or reestablishment of operational capability after the lunar night, including responsiveness towards the control center. Night survival may be achieved passively or actively. Passive survival means a system is switched off during the night, active means it remains operational. Passive survival of an entire system likely also means reduced thermal control capability, which likely results in subsystems exposed to temperatures close to environmental temperatures. Active survival usually includes active thermal control that maintains subsystem temperatures within acceptable limits. While some of the results of this thesis are relevant to passive survival, its main focus is active survival, as this also includes active operation in shadow.

Also, due to the peculiar illumination conditions at the lunar poles and the lack of an atmosphere, the conditions in local shadow on the lunar day side are very similar to the lunar surface in the depth of the night. For this reason, for the context of this thesis, night survival and survival in local shadow are considered equivalent.

Electrical, Electronic and Electro-Mechanical (EEE) Components

While the low temperatures associated with lunar night survival can be challenging to all components of a lunar surface system, this study is restricted to its impact on Electrical, Electronic and Electro-mechanical (EEE) components, as these elements are responsible for the core functionalities of surface systems and they are also the most susceptible to low temperatures. EEE components include but are not restricted to batteries, power management elements, radio transceivers, microcontrollers, actuators and sensors. A list of EEE components relevant to space systems is provided by ECSS Executive Secretariat (2021).

1.3 State of the Art

1.3.1 Recent Studies on Lunar Night Survival

With the recent resurgence in interest in lunar exploration, a number of recent studies have also investigated lunar night survival strategies. The proposed solutions follow three basic themes: reduce the heat loss through improved insulation, ensure external power supply, or increase low temperature tolerance.

All lunar surface systems use insulation to reduce the heat loss of surfaces in shadow, but the extent of insulation that can be practically implemented is limited, mainly because excessive insulation can cause overheating during the lunar day. Practical designs include heat switches, louvers or other methods to actively or passively regulate heat flow, but maximum turn-down ratios remain limited. In addition, even full coverage of a rover body with MLI will not be sufficient to achieve full night survival, therefore more elaborate insulation methods are necessary.

In a study for the (cancelled) Lunar Mission Survival Module (MSM) for the Selene-2 mission concept, Ogawa et al. (2014) have proposed the deployment of a two-layered tent like structure that encloses the MSM, with each tent layer consisting of MLI (see Figure 1-8). The system furthermore relies on the extremely low thermal conductivity of the regolith below the tent to prevent heat loss. As a result, the system achieved simulated lunar night survival in a thermal vacuum experiment. A similar design was proposed by Kim (2020) with the Thermal Shelter concept. This concept consists of a deployable two layer tent created from MLI and inflatable pillars. The structure is deployed by a rover during the lunar day. It can therefore utilize the thermal energy of the enclosed hot regolith, though reportedly only a 22% reduction in heat loss is achieved for the rover. A more advanced version of this concept was proposed by Sacksteder et al. (2010) in the form of the Thermal Wadi. The design increases the available thermal mass by creating a solid rock from regolith through melting. This thermal mass, also enclosed by a tent like structure can be used to heat a rover during the night. Finally, Ulamec et al. (2010) proposed to submerge a payload container in regolith, such that only the solar cell covered upper lid remains visible. This enables the design to fully leverage the insulating properties of the regolith and can enable night survival for the investigated system. These concepts manage to significantly increase the thermal insulation for the investigated systems. However, the proposed solutions also strongly affect the overall system architecture, are difficult to deploy and in most cases also lack technological readiness. This makes them difficult to implement with existing designs for landers / rovers.

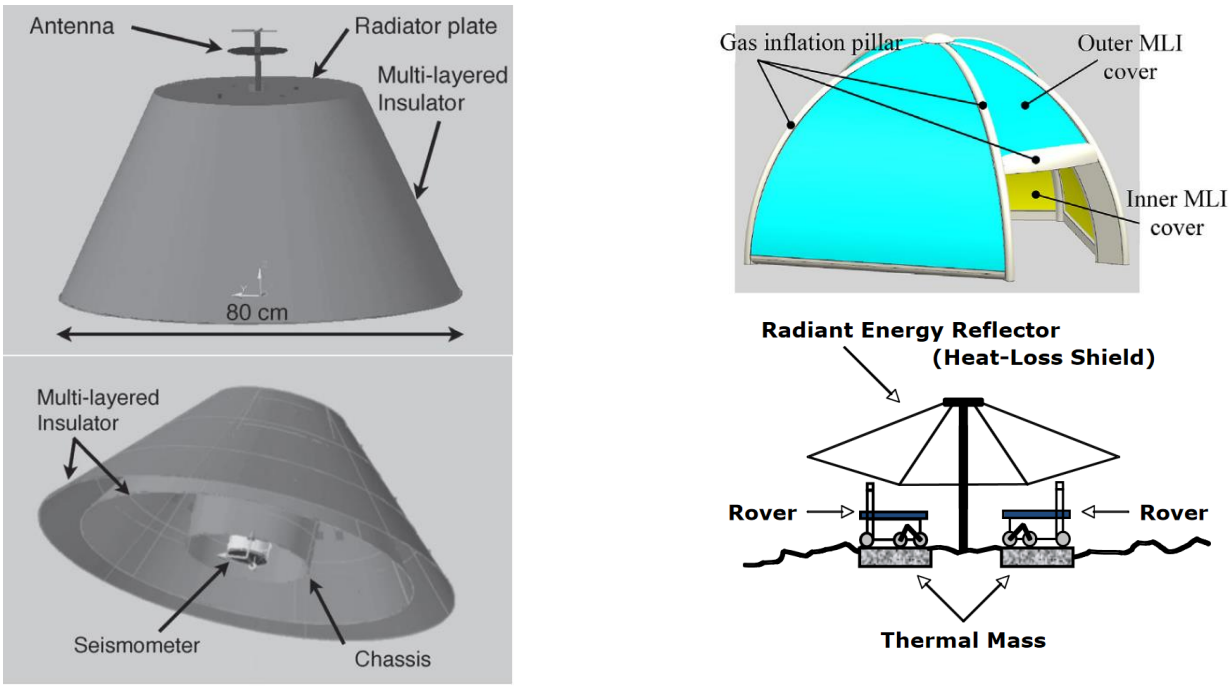

Figure 1-8: Left: Selene 2 MSM (Ogawa et al. 2014); Top Right: Thermal Shelter concept (Kim 2020); Bottom Right: Thermal wadi concept (Sacksteder et al. 2010)

A possible way to supply power to surface systems at night is by remote transmission from lunar orbit. In theory, an orbiting platform of sufficient size could supply power to a surface element through either solar reflectors (Bewick et al. 2011) or active radiofrequency or laser transmission (Torres Soto and Summerer 2008). However, such systems suffer from multiple drawbacks. Remote power transmission is inefficient even over short distances but will be extremely inefficient over very large distances. Orbit selection is crucial,

as lower orbits will reduce transmission distances, but increase relative velocities and shorten visibility times. In any case, these concepts lack technical maturity and will add substantial cost to any mission scenario. Therefore they will not be relevant in the near future.

Another approach is to use the specific illumination conditions at the lunar poles, where the local night for highly elevated sites can be significantly shorter. For example, several locations on the rim of Shackleton crater receive illumination for 94% of the lunar year (Solar Oases), reducing the maximum duration of the local night to just 43 h (Emerson J. Speyerer and Mark S. Robinson 2013). The approach can also be viable for certain rover missions if missions are designed to chase the sun. For example, Colaprete et al. (2018) proposed a mission scenario for the solar powered Resource Prospector rover near the North Pole that extended the baseline mission duration from 12 to 46 days by using this approach. The mission concept has since evolved into the Volatiles Exploration Polar Exploration Rover (VIPER) and the traverse has been refined to sustain a 90 day mission duration (Colaprete et al. 2020a). While this method can be very effective, it is restricted to a few very specific regions and may not be suitable for all missions. It also requires a minimum in-shadow survival capability to bridge the remaining nighttime periods.

1.3.2 Low Temperature Tolerant Systems

There are three basic approaches for the operation of space systems in extreme environments, such as low temperatures. The first approach is to protect the systems from the environment by the means of insulation, heaters and other thermal control means. In the context of lunar night survival, this approach requires excessive insulation, which is impractical for many, especially smaller missions. The second approach is to design systems that are tolerant to the environmental conditions. This would be the best option, but it is considered prohibitively expensive as it requires all components to be specifically designed for a given environment and may not be physically possible in all cases. Finally, hybrid architectures (see Figure 1-9) are possible, in which some tolerant systems are exposed to the environment and non-tolerant systems are protected by insulation. At this point, the majority of lunar systems follow the first approach, with most electronics housed in a central Warm-Electronics-Box (WEB) and peripheral components such as motors protected by heaters and further insulation. Hybrid systems have been used to some extent for Mars systems, for example the Mars Exploration Rovers MER and Mars Science Laboratory (MSL) rover used low temperature tolerant motors and motor controllers that were located directly at the joints instead inside the WEB (Kolawa 2007) and required no further heating in addition to conventional electronics housed inside a heated compartment.

A hybrid architecture was recently investigated on a theoretical level for the LUVMI-X rover (Urbina et al. 2019). Low temperature tolerant components were used to reduce the necessary heating power during the lunar night. An inventory of existing low temperature components was presented and a hypothetical low temperature architecture of a rover was compared to a conventional baseline architecture. It was shown that the low temperature architecture could enable a 30% increase in operational time in shadow.

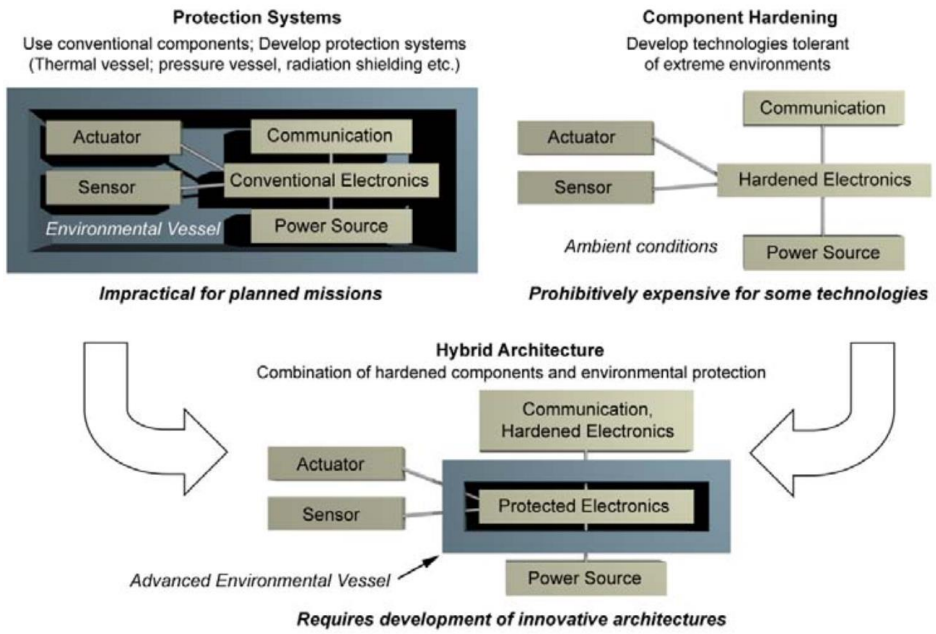

Figure 1-9: Hybrid system architectures for extreme environments (Kolawa 2007)

Electronic Systems

Most semiconductors remain operational at temperatures well below common ratings. Empirically determined low temperature limits lie at -150°C for bipolar silicon, -180°C for CMOS, -230°C for SOI and -269°C for SiGe bipolar CMOS, while theoretical limits are at -269°C for all of the above (Kolawa 2007). Specialized cryogenic electronics exist and are widely in use in various physics disciplines, such as super-conduction, various detector technologies, quantum computing, lasers and others (Gutiérrez-D et al. 2001). Specialized cryogenic electronics are also used extensively in space telescopes, as lower temperatures reduce noise, especially for infrared measurements. For example, the cryogenic side of the James Webb space telescope features actuators, multiple detectors and data acquisition electronics, the coolest of which need to operate at a temperature below 7 K (Wright et al. 2015). However, the main spacecraft electronics and more sophisticated data handling units are kept at the illuminated side of the spacecraft and maintained at 298 K (Greenhouse et al. 2004). A review of past space missions utilizing cryogenics is provided by Lindner et al. (2001).

However, such systems are often not directly applicable to the challenges posed by space exploration. For a lunar mission, electronics systems need to operate throughout a wide dynamic temperature range over multiple cycles. In addition they must withstand the harsh radiation environment and must withstand the journey to the Moon, including vacuum exposure, launch loads and varying thermal environments. This poses a much greater challenge than continuous operation at a stationary cryogenic temperature. Multiple research efforts have been undertaken in the past to close this gap and to develop low temperature electronics for space exploration purposes.

In the late 90s, NASA JPL investigated low temperature avionics for the Nanorover study, a proposed miniature rover that was planned to land on an asteroid as part of the MUSES-C mission. The rover was envisioned with a mass of 1.3 kg, a volume of 1.666 cm^3, an average power consumption of 2.5 W and an infrared and X-ray spectrometer as payload. Due to the small dimensions, classical thermal design architectures were deemed as unfeasible, therefore the electronics were designed to work in a temperature range of -170 to +125°C. The study investigated the operation of a set of standard electronic components at these temperatures and presented the plans for the development of a complete avionics system with on-board computer, motor controllers for ten brushless DC motors, payload electronics, temperature monitoring, solar cells and 9600 baud rate radio transceiver (Newell et al. 2001). However, the mission was cancelled and the project was not pursued further.

A similar research effort in this direction was made at NASA Glenn Research Center in the early 2000s, with the goal of developing cryogenic electronics for unspecified space exploration missions. For the research, the group evaluated both commercial-of-the-shelf (COTS) and custom-made components. A range of standard components that were either procured as COTS or manufactured specifically for the purpose was evaluated over a wide temperature range, down to liquid nitrogen temperature of -196°C. The program yielded good solutions for MOSFETs, DC/DC converters, ADCs, bipolar transistors, oscillators, operational amplifiers, diodes, temperature sensors and PWM controllers (Patterson 2001; Patterson et al. 2002a; Patterson 2003; Patterson et al. 2006; Patterson et al. 2008; Ray et al. 1995).

Building on these successes a research project at the University of Arkansas has investigated the design of a DC motor driver capable of operating from -230°C to 130°C. The project included the evaluation of COTS resistors, capacitors, diodes and the custom design of an 8051 compliant microcontroller and has shown promising results (Bourne et al. 2008; Garrett et al. 2007 - 2007). However, it is unclear if the project could be concluded successfully, as no follow on studies seem to have been published.

More dedicated research on the use of COTS components was performed by Buchanan et al. (2012) on various ICs for an address driver board, by Valiente-Blanco et al. (2013) on resistors, diodes and capacitors for general purposes and by Ihmig et al. (2015) on flash memory for terrestrial cryogenic storage applications for biomaterials. Other studies investigated cryogenic application of power electronics to improve efficiencies in terrestrial power conversion elements (Rajashekara and Akin 2013 - 2013; Gui et al. 2020). More recently, research in the context of supercomputing and quantum computing has investigated cryogenic operation of memory elements as a way of improving computation speeds (Shamiul Alam et al. 2021). In all cases, suitable solutions could be identified, though the approach has multiple problems. When components are operated outside of their specifications, the manufacturer does not ensure reliability. This means that failure temperatures can vary for different production lots and there are even significant deviations within component batches, especially for temperatures close to the overall failure temperature. This means that either each used component needs to be tested individually, or a significant safety margin should be used to account for this uncertainty. In any case, component batches need to be verified, as the same component, type may come from different manufacturing lines that may use slightly different materials. Aside from reliability concerns, low temperatures can also change the behavior of components. This may affect any component, examples include changes of bandwidth for filters, changes in gain for amplifiers, changes in frequency for oscillators, changes in power supply stability and many more. A more detailed list is provided by (Carrasco et al. 2018). The software CoolSPICE offers a simulation environment that is able to account for some of these effects (Akturk et al. 2012).

In light of the amount of successful research on low temperature operation of components, some manufactures have begun to include lower temperatures in their qualification procedures. An overview of such commercially available low temperature rated components is provided by Urbina et al. (2019), though at this point, availability is limited to a few specialized components. For the sake of completeness, Hassan et al. (2018) provides a review on the current state of the art for the design of specialized low temperature chips, but this is considered outside the scope of this thesis.

1.3.3 Low Temperature Tolerant Components

Based on an abundance of previous studies, a large body of data is available on the low temperature compatibility of specific components.

Resistors:

A study from the Universidad Carlos III de Madrid (Valiente-Blanco et al. 2013) investigated multiple types of resistors between room temperature and -180°C. Of the investigated types, Ceramic body wire wound resistors and Ceramic composition resistors performed the worst with deviations of >100% and >25% over the investigated temperature range. Copper clad steel wire and vitreous enamel coating resistors, Carbon film resistor with alumina core, Metal film Cu-leaded resistors and Metal glaze leaded resistors performed satisfactorily with less than 10% deviation. Metal film Holco series and Metal film tinned copper leaded wire resistors showed the best low temperature performance with less than 1% deviation over the temperature

range. After thermal cycling, all of the investigated resistors recovered their original resistances, except the ceramic body wire wound resistors, which showed significant deterioration. In a similar investigation, Bourne et al. (2008) reached the same conclusions, with satisfactory results for Thin film, Thick film, Power film, Wirewound and Metal foil resistors and significant deviations for ceramic based resistors. However, in their study, carbon based resistors showed the greatest deviations due to thermal cycling (1%).

Capacitors:

Valiente-Blanco et al. (2013) have also investigated various capacitor types between room temperature and -180°C. It was shown that aluminum electrolytic and ceramic capacitors were unsuitable for low temperature application, as aluminum electrolytic capacitors lost all of their capacitance at -40°C and ceramic capacitors only retained around 50% at this temperature. Impregnated metallized paper, metallized PET film and solid tantalum capacitors retained more than 80% of their original capacitance and Mica capacitors remained almost unchanged. Thermal cycling showed significant degradation for ceramic capacitors and minor effects on solid tantalum capacitors, but no effect on Impregnated metallized paper, metallized PET film and solid tantalum capacitors. In a similar study, Bourne et al. (2008) another set of capacitors, confirming the high suitability of Mica capacitors. They further showed that NPO ceramic is also highly suitable with negligible deviation at -180°C and that Polyester capacitors may also be used but only retain 90% capacitance at -180°C. In their study, thermal cycling had very little effect on NPO ceramic, while Mica and polyester showed up to 0.5% change in capacitance due to cycling.

Inductors:

Gerber et al. (2004) investigated four different types of inductor core materials at low temperature from 10 Hz to 100 kHz: Molypermalloy powder cores, high flux powder cores, Kool Mu cores and ferrite cores. The results show that high flux powder cores and molypermalloy powder cores show very little deviation between 25°C and -180°C. Kool Mu cores retain about 60% of their inductance at -180°C. Ferrite cores already lose about 30% of their inductance at -50°C and only retain about 20% at -180°C. In general temperature effects were not dependent on frequency. A similar study was conducted by Chen et al. (2018), in which N87 ferrite and Vitroperm war investigated. At -180°C the N87 retained about 20% of its permeability at 20 kHz, while the Vitroperm retained about 60%.

Diodes:

Bourne et al. (2008) tested a range of 11 Schottky, Switching and Zener diodes that were chosen to represent a selection of different semiconductor materials based on Si, GaAs and Ge semiconductors. Supplier ratings indicated lower operational temperature limits between -65°C and -50°C. The purpose of the study was qualification down to -230°C, therefore the authors were concerned about carrier freeze out in Si diodes. However testing was only performed down to -184°C, as only a liquid nitrogen testing facility was available. The results showed satisfactory results for the GaAs Schottky, Si Schottky, Si Switching and Si switching diodes. Forward voltages increased by about 20% for most devices at -184°C, while incremental resistances remained mostly stable or decreased. Reverse breakdown voltages also decreased with temperatures, especially the GaAs type but all retained at least the ability to block low voltages. The investigated Germanium based diodes exhibited a very high forward voltage drop the authors therefore discourage the use of this type and encourage the use of SiGe type diodes. The study further investigated a set of three types of silicon based Zener diodes. All Zener diodes worked at -184°C, however in all cases the reverse diode voltages decreased by about 10%.

MOSFETs and Derived Semiconductor Devices:

In general, low temperatures do not necessarily degrade MOSFET operation, however some performance parameters can change. MOSFET gain usually even increases with lower temperatures and the threshold voltage becomes more positive for n-channel MOSFETs and more negative for p-channel MOSFETs (Newell et al. 2001). MOSFET operation at low temperatures has been investigated in multiple studies with good results and at different temperatures (Newell et al. (2001): -170°C, Bourne et al. (2008): -184°C, Maddox (1976): -269°C). Literature reviews of MOSFET operation at very low temperatures are provided by

Rajashekara and Akin (2013 - 2013) and Gui et al. (2020) with regard to power electronics, indicating good functionality of various types below -170°C.

Newell et al. (2001) also successfully tested the following derived components at -170°C and with a 50krad radiation exposure: Power MOSFETs, Analog Multiplexers, Operational Amplifiers, Analog Switch, Analog to digital converters (ADC). A problem occurred with the investigated operational amplifiers: two types were tested, one rad hard that did not work well at low temperatures, one that worked well at low temperatures but that was not rad hard. Therefore the non-rad hard component was selected and additional tantalum shielding was used. The same additional shielding was needed for the ADCs. Unfortunately, the study did not provide actual part numbers or suppliers. One long-term issue was mentioned however, that is hot carrier injection. This is caused by mobility of carriers from the channel to the gate oxide and in turn cause build-up of charge that can lead to eventual failure. Carrier mobility is increased at low temperature, therefore the life time of MOSFET components will likely also decrease in cold temperatures. The authors provide a conservative minimal estimate of eight months for the investigated parts in such conditions. In conclusion, MOSFETs and derived components seem to generally work well down to temperatures of -170°C and even below.

Microcontrollers:

Specialized low temperature microcontrollers have been developed previously. Newell et al. (2001) described the full implementation of a rover avionics system, including a Mongoose V microprocessor that was successfully tested at -170°C. They further outlined the fundamental operation of semiconductors at these temperatures and discussed some failure modes. For example, Microcontrollers can fail due to increased propagation delays. This can theoretically be alleviated by reducing input system voltage, though this may not be practical in some systems. Hollosi et al. (2008) developed an 8051-pin compatible Null Convention Logic microcontroller based on the IBM SiGe5AM 0.5 µm process. The device was successfully tested down to -271°C.

Memory Units:

Ihmig et al. (2015) have investigated multiple batches of flash memory units at temperatures down to -196°C for monitoring of cryogenic bio-storage applications. Six batches of commercially available, low voltage serial flash memory units of undisclosed types, manufactured at different times and from two different countries of origin were investigated. At -185°C, approximately 80% of the investigated devices remained functional, at -196°C, this rate dropped to about 50%. No detailed information was given on the overall pass rates at temperatures between room temperature and -185°C. However, an investigation of the mean program time showed largely unchanged behavior of the devices down to -80°C, program times start to significantly increase at -130°C and continue to rise more steeply until -185°C.

Hanamura et al. (1986) have investigated Static Random-Access Memory (SRAM) devices at -196°C and -269°C and have shown that the devices not only remained operational, but that propagation delays and chip select-access times have been reduced. Wyns and Anderson (1989) have investigated multiple Dynamic Random-Access Memory (DRAM) units from five different manufacturers at temperatures down to -184°C. No failures were observed above -98°C and some tested devices remained operational down to -184°C. Improved access times and memory retention were observed.

Clocks:

Patterson et al. (2006) have investigated two solid-state resistor-tunable oscillators and a silicon-germanium voltage-controlled oscillator at very low temperatures. All three devices were able to operate down to -195°C, however the solid-state resistor-tunable devices showed a continuous, but nonlinear decrease in output frequency, resulting in a 5-7% decrease at -195°C, while the silicon-germanium device showed a 5% increase at -195°C at all investigated voltages.

In a later study, Patterson and Hammoud (2010a) have investigated the following COTS silicon oscillators at low temperatures: A LTC6906H from Linear Tech (rated -40 to +125°C), an ASFLM1 from Abracon (rated

0 to +70°C), an EMK21 from Ecliptek (rated -40 to + 85°C), a STCL1100 from STMicroeletronics (rated -20 to +85°C) and a SiT1100AI from SiTime (rated -40 to + 85°C). Of these devices, the ASFLM1 exhibited the best low temperature performance (despite the poorest low temperature rating) and operated with very little deviation down to -190°C. The EMK21 and SiT1100AI operated with even less deviation but only down to -110°C, below which their output became unstable and showed fluctuations in frequency. The STCL1100 was able to operate down to -190°C, but showed a 50% change of frequency at this temperature and the LTC6906 was only able to operate in a stable manner down to a temperature of -55°C. The five devices were also subjected to twelve thermal hot / cold cycles, but no significant changes in the operational characteristics were observed.

Digital Interfaces:

Shepherd et al. (2013 - 2013) have designed a High Temperature Silicon-on-Insulator Null-Convention-Logic data interface module for digital interfacing of peripheral instruments on extreme environment spacecraft. The device was RS-485 compliant, operated from -175°C to 225°C, demonstrated a data rate of over 35 Mbps and was moderately radiation tolerant. In a similar study, a RS-485 and ISO 11898 compatible SiGe BiCMOS transceiver was designed and built for an extreme temperature range by England et al. (2014). The devices was successfully tested and has proven to be operational from -183°C to 117°C. The transceiver was shown to also be radiation tolerant up to a TID of 2 Mrad and enabled a maximum data rate of 20 Mbps. No information was found on the viability of COTS parts in this category.

Voltage Converters and Regulators

Patterson et al. (2006) have investigated the low temperature behavior of multiple custom built and some COTS DC-DC converters. The custom built devices were built from COTS parts of CMOS and MOSFET type and were able to operate down to -196°C. Of the investigated COTS converters, some operated down to -80°C and others down to -120°C. Similar results were obtained in a follow on study (Patterson and Hammoud 2010b), in which nine types of COTS DC/DC converters were investigated. Most devices were rated down to -40°C, one was rated at -20°C and one was rated at -55°C. Of the investigated devices, one ceased to work at -40°C (Calex 24S3.15HE, rated -40 to +100°C), one at -80°C, three at -120°C, two at -160°C, one at -180°C and a single one continued to work below -195°C (Power Tend PT4110A).

Optocouplers:

Patterson et al. (2010) tested a Fairchild gate drive Optocoupler of type FOD3150 at temperatures between -190 to +110°C. The device was able to operate without change from -100 to +110°C and continued to operate down to -190°C, but with a significant change in propagation delay. In the test, this lead to a discrepancy between input and output signal duty cycle and will be relevant in cases where fast switching is necessary. Thermal cycling was also performed for 12 cycles and the results showed little effect on the device was observed.

Communication Systems:

The only known instance of a low temperature implementation of a space communication system was developed for the Nanorover by Newell et al. (2001). For this rover, a 9600 baud rate radio was developed and tested for operation at -170°C. However, very little information on this design is provided. No information on the use of COTS parts in this context has been found.

Motor Controllers:

The Nanorover design also included ten custom designed three phase brushless DC motor drivers with Hall Effect sensor interfaces. The devices were tested successfully for operation at -170°C, but no further information was provided (Newell et al. 2001). Bourne et al. (2008) presented a custom designed motor driver for brushed DC motors for a temperature range from -230°C to +130°C. However, only components have been tested, testing of the completed device was not reported. Patterson et al. (2002b) have investigated the design of a stepper motor controller for extreme environments down to -243°C. For this

purpose a set of switching devices, logic devices and drive circuit components were tested down to -263°C. A majority of parts functioned well during performance and cycle testing, though some devices failed at - 193°C. The development found utilization in the Mid-Infrared instrument of the James Webb Space Telescope (Wright et al. 2015).

Field Programmable Gate Arrays (FPGA):

Keymeulen et al. (2007 - 2007) have reported the use of a FPGA on a Xilinx protoboard with a 100 MHz PowerPC and 2 MHz clock to implement a reconfigurable analog array for extreme temperatures. They report successful operation of the FPGA at -180°C, but no detailed analysis is presented.

Solders

In addition to component functionality, die attachment is a concern. Potential problems for soft solders are differences in thermal expansion coefficients (CTE) leading to temperature induced mechanical stresses and brittleness at low temperature. Cold temperatures generally increase the strength and decrease the ductility of soft solders. Thermal cycling generally aggravates these problems. Multiple soft solders have been extensively used for low temperature applications. Recommended types include indium / indium alloy solder and PbSn alloys with high Pb and low Sn content or with an addition of Sb. Discouraged are high Sn content alloys. Hard solders (i.e. brazing) will likely be more reliable, but increased strength of the die attachment may transmit more CTE induced stress to the components and generally require significantly higher temperatures during assembly. A detailed overview on the topic is given by Kirschmann et al. (1999).

Summary

Table 8-3 provides a summary of the data on low temperature data for electronic components presented above. It should be noted that pperformance parameters change for all components with temperature. Successful application in literature does not necessary transfer to other applications, it does however give an indication which components are the most likely to cause problems. Exact manufacturing details (e.g. dotation of a semiconductor) influence performance and are not usually known to the end user. The same component, sold by the same supplier can vary, as individual production lots may differ in relevant details like substrate composition, process resolution etc, resulting in changing low temperature performance. This problem is exacerbated by the fact that such changes are not usually transparent to the user and can only be determined by in-depth research, if at all. Operational temperature rating is not a good indicator for low temperature performance. Devices with an extremely poor low temperature rating may prove to work well at cryogenic temperatures, while others with a good rating may turn out to not work beyond their specified range.

Newell et al. (2001) recommend to use digital functions as much as possible. In case analog circuits are necessary, close loop feedback systems (such as in an operational amplifier) are recommended. Classical analog circuits that are based on characterized values of capacitance, inductance or similar are likely affected by large temperature changes and will therefore need to be carefully recharacterized (Newell et al. 2001).

1.3.4 Batteries

For lunar night survival, energy storage is the most critical function. Unfortunately, batteries are typically also the most critical part in terms of operational temperature and either become unstable at high temperatures or lose their capacity at low temperatures. The current state of the art for rechargeable batteries both for terrestrial and for space applications are lithium ion batteries, due to their high energy density and cycle life (De-Leon 2017). Practical energy densities of common state of the art cells are as high as 260 Wh/kg and typical operational temperatures range between -20°C and +60°C.

No battery technology exists that can deliver meaningful amounts of energy at temperatures below -150°C, for this reason batteries will need to be heated to remain operational during the lunar night. Dedicated low temperature batteries exist and have been investigated in the context of space exploration, but minimum achievable operational temperatures are only as low as -60°C (Smart et al. 1999b; Smart et al. 1999a; Smart

et al. 2004; Smart et al. 2008; Smart et al. 2010; Smart et al. 2017; Saft 2014). In addition, due to the high additional effort of ensuring low temperature capability, these cells tend to have lower energy densities than common state of the art cells. It is therefore unclear if the use of low temperature batteries will increase operational lifetime during the lunar night or if the lower energy density also translates into shorter lifetimes. Some lithium ion batteries have already been proven to withstand passive cryogenic freezing batteries (Grandjean et al. 2019; Nandini et al. 2018), though it is not yet clear if that is also valid for other cell types.

In the near future, multiple emerging technologies like lithium metal anodes and sulfur based cathodes promise to significantly increase practical energy densities and early prototypes are already available (Liu et al. 2019; Ould Ely et al. 2018; Oxisenergy 2019; SolidEnergy Systems 2019), some of which have been specifically developed for low temperature environments (Cai et al. 2020). However, current prototypes still suffer from limited temperature stability, cycle life and safety concerns, which make them unsuitable for use in space applications.

In terms of primary batteries, the current state of the art for space exploration are lithium thionyl chloride cells. Cells of this type achieve energy densities of up to 700 Wh/kg and are rated to temperatures as low as -60°C. However, extractable energy densities decrease with temperature and the highest energy densities can only be achieved if the cells are discharged at very low currents, requiring discharge times in excess of the two weeks of lunar night. Higher current cells are limited to about 450 Wh/kg. Cells of this type have been used on various space exploration missions, for example on the Rosetta / Philae comet lander mission (Cénac-Morthé et al. 2016). Other promising types include Lithium carbonmonoflouride cells with current energy densities also reaching 700 Wh/kg and lithium iron disulfide cells with energy densities of only up to 350 Wh/kg but good low temperature performance (Krause et al. 2018).

1.3.5 Mechanisms & Structures

Cryogenic mechanisms exist and have been in use in various disciplines, including space applications. Examples include cryocoolers (e.g. Stirling coolers) and fluid control devices for cryogenics fuels (e.g. fuel pumps, valves). For this reason, a wide range of solutions exists and many can be bought of the shelf.

Cryogenic mechanisms require dry lubricants, such as lamellar solids (e.g. molybdenum / tungsten disulfide, graphite, and boron nitride), polymer coatings (e.g. PTFE, PEEK, and Polyimide), soft metal coatings (e.g. gold, lead) or low shear strength solids (e.g. sulfides, fluorides). Drawbacks include higher friction, shorter lifetimes and higher susceptibility to contamination than wet lubricants. Cryogenic bearings are available, based on CTE-matched materials. Actuators, such as motors or piezoelectric actuators also exist. (Urbina et al. 2019).

1.3.6 Research Gaps

While past successes of lunar surface systems in terms of night-time survival and operation must not be understated, the underlying solutions are not applicable to some of the problems faced by current designers. Reliable nighttime survival and operation was only achieved by the use of RHUs and RTGs, which are unavailable to most of the current landers and rovers. The solar and battery powered Surveyor landers achieved some success in this regard, but were plagued by failures and could only operate for limited times (see section 1.2.1). The majority of currently planned missions will rely on solar / battery power and therefore providing nighttime survival or operation capability remains challenging. Some systems plan for in-shadow operation to achieve specific science goals, but significant provisions need to be made in terms of insulation and energy storage. Therefore, there is a lack of strategies to enable lunar nighttime survival and operation. This is especially true since improved miniaturization has enabled the design of some fairly small systems (see section 1.2.2) with less margins for thermal control and a more challenging surface area to volume ratio.

Some dedicated night survival strategies have been developed and published, based on improved insulation, external power supply concepts or improved low temperature tolerance. However, the improved insulation or external power supply concepts rely on bulky or impractical solutions that are incompatible with proposed mission architectures or are not practical for the foreseeable future (see section 1.2.3).

The use of low temperature tolerant or hybrid systems has been previously investigated by numerous studies for many applications. Low temperature compatibility can either improve the nighttime survivability or reduce the thermal control burden for lunar surface systems. Due to the $\sim T^4$ dependence of heat loss in vacuum, even moderate differences in temperature can significantly change required heating power. This approach is particularly promising, because it can be implemented with existing designs and requires only limited modification of the thermal control system. However, while there have been many successful applications of such technology in terrestrial applications and in space telescopes, no actual successful planetary exploration missions have materialized despite a number of promising research projects.

These previous research efforts aimed to develop electronics for an extremely wide temperature range, which would allow their application on many planetary mission without additional thermal control. A visualization of the targeted temperature ranges of previous studies is shown in Figure 1-10. However, the problem with this approach is that a wide temperature range also requires a higher development effort.

Almost all parts, even consumer electronics can be used between 0°C and 60°C. The lower or higher the targeted operational temperature limit, the less existing parts can be utilized, meaning a higher selection and qualification effort or the necessity to develop custom parts. For example, Newell et al. (2001) developed a complete rover avionics system from scratch, including the custom design of a microcontroller. In addition to the high development effort, these highly specialized parts are also less likely to be reused by other missions. Furthermore, such custom developments will not be able to keep the pace of development of the more and more privatized space community. Modern missions increasingly rely on standardized of-the-shelf components developed in the context of the nanosatellite boom of recent years, but the majority of these parts receive standard temperature ratings (see section 2.4).

The majority of studies that developed low temperature applications largely relied on the selection and requalification of existing components with common temperature ratings. It is likely to assume that most electronics systems can be used beyond their rated temperature range, because, “rather than in the wafer fabrication process, the key differences between specialized products and their consumer grade counterparts lie in character and extent of the quality assurance measures they are subjected to” (Bauer 2020). However, while previous studies have used this method to design systems with fairly ambitious low temperature limits and a growing number of studies have presented results on low temperature suitability of individual components, there is no discussion on the achievable benefits of this approach vs. the required effort. A targeted lower temperature limit will result in fewer useable parts and thus in a higher selection and requalification effort. At the same time, there will likely be diminishing returns for increasingly low temperature limits for components. Thus, instead of complete redevelopment of surface exploration systems for low temperature compatibility, it may be more beneficial to attempt to modify and requalify existing state-of-the-art systems to a moderate target temperature limit determined by a careful trade-off between effort and potential benefit. This is the key premise of this study.

While there has been extensive research of the low temperature compatibility of individual components and dedicated development of new systems, so far little research has been published on the suitability of larger assemblies or subsystems. A particular knowledge gap is the low temperature usability of microcontrollers and related elements. Microcontrollers represent the core element of a majority of electronic systems and are therefore indispensable.

Particular attention must also be paid to the energy storage system. A wide range of technologies exist, some specifically developed for low temperature utilization (see 1.3.4), but it is currently unclear, which technology is ideal for lunar night survival and how the technology needs to be operated to achieve optimal results. In addition, it is unclear how batteries and low temperature re-rated components can be integrated into a system’s thermal design such that operational lifetime during the lunar night can actually be improved. If the lower temperature limit of the utilized components exceeds the minimum environment temperatures, some measure of thermal control is still necessary. It is also likely that the re-rating potential of different subsystems will diverge. Especially the energy storage system will require a much higher operational temperature as the rest of the electronics. A classical hybrid architecture (see Figure 1-9), in which hardened electronics can be exposed to the environment and non-hardened components are insulated and thermally

controlled may not be possible. Instead, a layered hybrid architecture could be needed, in which each system is kept within its required limits and the system as a whole is arranged in such a way that only minimal heating power is necessary. While this is not fundamentally new, it is unclear if such a design can be implemented into a relatively small system like the DPP and still provide sufficient operational benefit to justify the additional design effort.

Passive survival could also be an important strategy to extent operation of systems beyond the first lunar day. This involves the controlled shutdown of a system before the lunar night, in which it would cool down without any heating to almost ambient temperatures and a controlled wake-up procedure once solar illumination returns. While this method would not allow operation during the night, even the survival of a single night would already double the duration of an average planned mission. However, very little research is currently available on the challenges involved with this approach and it is unclear what system designers can do to improve chances of survival.

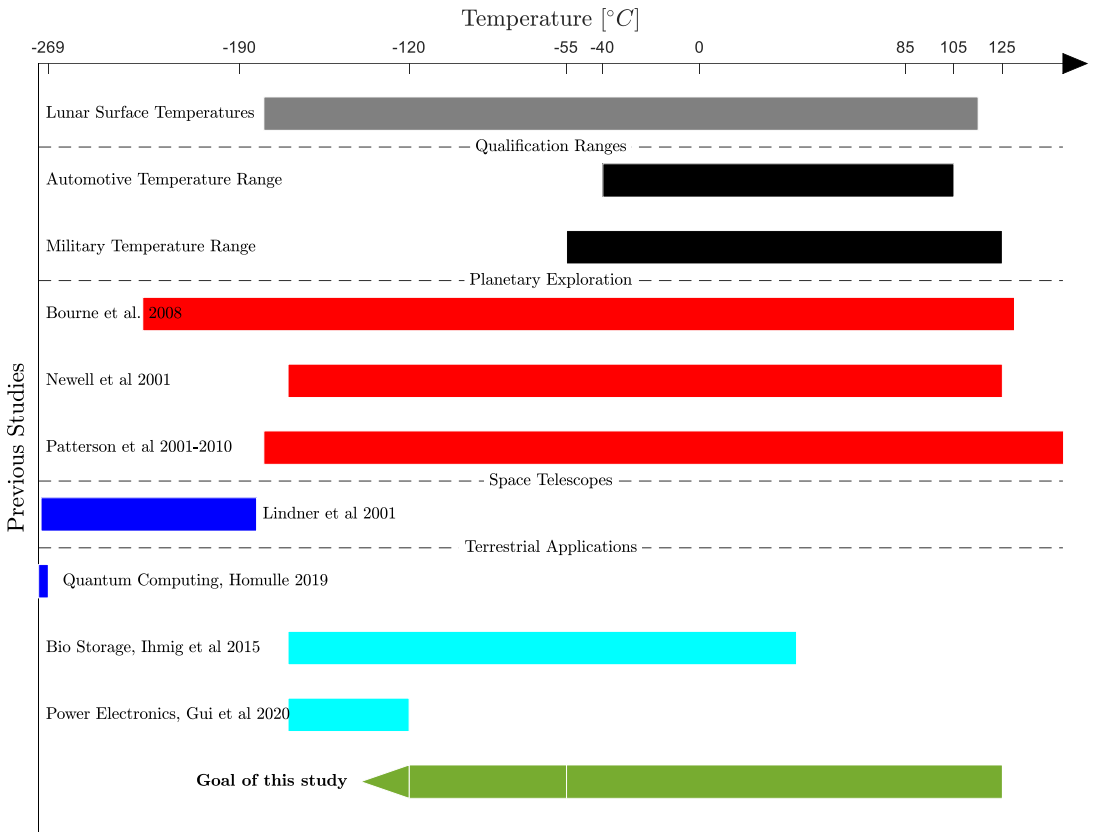

Figure 1-10: Visualisation of targeted operational temperature ranges of previous low temperature studies.

1.4 Scope of thesis

1.4.1 Research Hypothesis and Objectives

The core research hypothesis for this thesis is split into two parts and is defined in the following:

1. With little or no modifications, a majority of electronic components can be utilized at significantly lower temperatures than their manufacturer ratings indicate.
2. Utilization of this extended temperature range allows to significantly improve night survival and operation for lunar surface systems.

The validity of this hypothesis will be determined by addressing the research objectives below. Objective one is to investigate how far components can be rerated for low temperature application, what risks are involved and what changes are necessary to systems to achieve this. The second objective will address energy storage solutions. A major shortcoming of previous developments on low temperature electronics was to neglect the energy storage solution. Finally, objective three is to assess how much operational lifetime in lunar nights can be increased by translating low temperature rerating into actual thermal architectures.

Objective 1:	**Determine if and how electronic components relevant to lunar surface exploration can be utilized at temperatures below their ratings.**
Objective 2:	**Identify ideal energy storage and its optimal operating point for lunar night survival.**
Objective 3:	**Investigate how extended temperature ranges of subsystems can be translated into valid thermal systems and determine their benefit compared to standard temperature ranges.**

1.4.2 Approach

Chapter 2 will present the theoretical foundations necessary for the discussion of the topics in this thesis.

The first objective will be investigated in chapter 3 in two steps: The most critical component for the low temperature use of electronic systems is the microcontroller. It is usually the most complex part and thus also the most challenging to replace and there is also very little available research on the viability of low temperature utilization of microcontrollers. Therefore, the first step will be to investigate the low temperature performance of a selection of microcontrollers that are commonly used in space applications. In a second step, the individual subsystems of the DPP will be investigated and suitable solutions for low temperature operation will be identified. The target temperature is be -120…-100°C, but in the end a trade-off between design effort, cost and benefit will determine the ideal rerating temperature.

The second objective will be addressed in chapter 4: First a literature review of existing energy storage solutions will identify the most promising technologies. Then, a selection of technologies will be tested for their low temperature performance. Based on this data, the night survival performance will be calculated as a function of temperature and system insulation, which will also determine the optimal operational temperature for each technology. This will then allow the comparison of each technology based on their actual optimal performance during night survival.

The third objective will be addressed in chapter 5. Simulation models for three case studies of representative lunar surface systems will be presented: The LUVMI-X DPP, a polar rover and a lunar lander. For each of these systems, thermal designs will be presented that utilize different grades of low temperature rerating and their performance will be evaluated against their reference designs.

Finally, in chapter 6 the results of the previous chapters will be validated experimentally. A thermal prototype of the DPP, including a functional battery and power management system will assembled and tested at its respective low temperature limit. Additionally, an advanced prototype that utilizes low temperature rerating will be tested and its performance compared to the baseline version. The test results are then used to confirm the validity of the thermal simulations in chapter 5.

2 Fundamentals

2.1 Lunar Surface Environment

The Moon orbits the earth with a semi-major axis of 384 748 km, with a sidereal orbital period of 27.322 days, which is also equivalent to the sidereal rotation time due to tidal lock. Its orbit is inclined by 5.145° against the ecliptic and its rotational axis is further inclined by 6.683°, resulting in an angle between the Moons rotational axis and the normal of the ecliptic of only 1.54°. It has a mass of $7.353{\cdot}10^{22}$ kg and a radius of 1738 km, the gravitational acceleration on its surface (at the equator) is only $1.62\,m/s^2$. With 10^4 molecules/cm^3 during daytime and $2{\cdot}10^5$ molecules/cm^3, its atmosphere is virtually non-existent. (G. H. Heiken et al. 1991).

The solar radiation on the lunar surface varies between $1316\,W/m^2$ and $1421\,W/m^2$, depending on the distance of the Moon to the Sun (Ulamec et al. 2010). Average surface temperatures depend strongly on latitude and can reach 390 K at local noon at the equator, but only 250 K in the polar areas (latitude > 80°). During the night, temperatures sink to values between 100 K (equator) and 50 K (polar areas) (Williams et al. 2017). Though in general, local temperatures can deviate significantly from averaged values. Local temperatures depend mainly on local illumination because of the low thermal conductivity of thermal regolith. Sun-facing surfaces or slopes will get significantly hotter than slopes facing in other directions and shadowing due to the surface topography can significantly cool certain areas. This is especially true for polar areas, where the low angle of solar incidence and the rough terrain result in abundant permanently shadowed regions (PSRs). Temperatures in these regions can remain perpetually below 50 K (Paige et al. 2010). On the other hand, other areas near the poles can be exposed to above average illumination, with certain highly elevated areas being almost perpetually sunlit (Mazarico et al. 2011).

The lunar surface is almost completely covered by lunar regolith. This is a layer of fragmental and unconsolidated rocky material that covers almost the entire surface of the Moon. Two regolith types are distinguished: Mare and Highland regoliths. The most important properties with regard to thermal control are density, specific heat, thermal conductivity and optical surface properties. Schreiner et al. (2016) have compiled a comprehensive overview over available thermophysical property models for regolith, the following references were taken from their publication.

The bulk density of lunar regolith depends mainly on its local compaction and thus varies greatly and increases with depth and age of the landscape. The average bulk density for the topmost 15 cm is 1500 kg/m^3, but 1740 kg/m^3 at a depth of 30-60 cm (G. H. Heiken et al. 1991).

For the specific heat, a model by Hemingway et al. (1973) is recommended for applications at temperatures from 100 K to 350 K:

$$C_p = c_a + c_b T + c_c T^2 + c_d T^3 + c_e T^4$$

With the coefficients $c_a = -2.32 \cdot 10^{-2}\,J/kgK$, $c_b = 2.13 \cdot 10^{-3} J/kgK^2$, $c_c = 1.50 \cdot 10^{-5} J/kgK^3$, $c_d = -7.37 \cdot 10^{-8} J/kgK^4$ and $c_e = 9.66 \cdot 10^{-11} J/kgK^5$.

For thermal conductivity of lunar regolith, a model by Cremers (1975) is recommended:

$$k = c_{cond} + c_{rad} T^3$$

The following coefficients are average values across different types of Apollo samples: $c_{cond} = 1.09 \cdot 10^{-3} W/mK$, $c_{rad} = 2.22 \cdot 10^{-11} W/mK^4$.

Albedo of lunar regolith is extremely low, with a values between 0.05 and 0.1 for thermal infrared and 0.06-0.07 for shortwave infrared and visible light (Conel and Nash 1970). If transmittance is neglected, absorptivity of solar light is then 0.93-0.94. Emissivity in the thermal infrared ranges between 0.88 and 1 (Salisbury et al. 1973b).

2.2 Thermal Control Elements

This section presents common thermal control elements and their properties relevant for this study. The elements presented in this section are used as input for case studies in chapter 5.

2.2.1 Structural Materials

Table 2-1 shows an overview of the thermal conductivities of various materials commonly used for aerospace structures.

Table 2-1: Thermal conductivity of various materials, adapted from Bauer (2021)

Material	Thermal conductivity λ at 20 °C (W m^{-1} K^{-1})	Source
Alumina (α-Al_2-O_3 ceramic)	35.6 - 39	(Cardarelli 2018)
Aluminium (Al)	235	(Vinaricky 2016)
Aluminium alloy AA-6061 (Al-1Mg-0.6Si-0.3Cu)	180	(Cardarelli 2018)
Aluminium alloy AA-7075 (Al-5.7Zn-2.6Mg-1.6Cu)	125	(Cardarelli 2018)
Beryllium (Be)	210	(Cardarelli 2018)
Carbon fiber (Amoco P100)	550	(Gluck and Baturkin 2002)
CHO-THERM (thermal gasket material)	1.2 – 3.8[1)]	(Gluck and Baturkin 2002)
Copper (Cu)	394	(Vinaricky 2016)
Fiberglass-epoxy (CCO-BL)	1 – 2	(Gluck and Baturkin 2002)
Gold (Au)	297	(Vinaricky 2016)
Graphite (C, bulk)	95	(Graphite24.com)
Iron (Fe)	80	(Vinaricky 2016)
Lambda Gel® (thermal gasket material)	1.0 – 6.5[1)]	(Taica Corporation)
Lead (Pb)	35.6	(Cardarelli 2018)
Macor® (machinable glass)	1.46	(Cardarelli 2018)
Manganin® alloy (Cu-Mn12-Ni)	22.0	(Isabellenhütte Heusler GmbH & Co. KG 2014)
Manganese (Mn)	7.82	(Cardarelli 2018)
Nickel (Ni)	92	(Vinaricky 2016)
Polyetheretherketon (PEEK)	0.25	(König GmbH Kunststoffprodukte 2016)
Pyrex® 7740 (labware glass)	1.13	(Cardarelli 2018)
S-glass epoxy	0.42	(Gluck and Baturkin 2002)
Silica (α-SiO_2 quartz)	1.38	(Cardarelli 2018)
Silica Aerogel (pure, 1 mbar)	0.008	(Donabedian et al. 2002)
Silica Aerogel (with carbon black, 1 mbar)	0.004	(Donabedian et al. 2002)
Silver (Ag)	419	(Vinaricky 2016)
Soft solder (70Sn-30Pb)	50.0	(Cardarelli 2018)
Titanium (Ti)	21.9	(Cardarelli 2018)
Titanium alloy Ti-6A1-4V	6 - 8	(Gluck and Baturkin 2002)
X10-Cr-Ni18-8 high-alloy steel	15	(Vinaricky 2016)

[1)] Effective interface conductivity rises if material is compressed (Gluck and Baturkin 2002).

2.2.2 Thermal Surface Finishes

Table 2-2 shows an overview of the thermos-optical surface properties of a selection of commonly used aerospace surface finishes.

Table 2-2: Thermo-optical Properties of common aerospace surface finishes, adapted from Bauer (2021)

Surface Finish	Solar Absorptance α	IR Emissivity ε	Source

Reflective Surfaces			
FSS-99 overcoated silver	0.03	0.02	(Gilmore et al. 2002)
Sheldal Au-Polyamide tape	0.30	0.03	(Sheldal Corporation)
Sheldal Al-Polyamide tape	0.14	0.035	(Sheldal Corporation)
Second Surface Tapes			
Sheldal 12.5 µm Al-FEP SSM tape	0.14	0.40	(Sheldal Corporation)
Sheldal 25 µm Al-FEP SSM tape	0.14	0.48	(Sheldal Corporation)
Sheldal 51 µm Al-FEP SSM tape	0.14	0.60	(Sheldal Corporation)
Sheldal 127 µm Al-FEP SSM tape	0.14	0.75	(Sheldal Corporation)
Sheldal 254 µm Al-FEP SSM tape	0.15	0.85	(Sheldal Corporation)
Coatings and Paints			
80-U leafing aluminium paint	0.29	0.31	(Gilmore 2002a)
Barium sulphate with polyvinyl alcohol white coating	0.06	0.88	(Gilmore 2002a)
Dow Coming Thermatrol DC-92-007 white coating	0.19	0.82	(Gilmore 2002a)
Magnesium-Oxide white paint	0.09	0.90	(Gilmore 2002a)
NASA/GSFC NS74 white paint	0.17	0.92	(Gilmore 2002a)
Miscellaneous			
Aluminium louver vane	0.14[1)]	0.10	(Hardt et al. 2002)
Lunar Surface	-	1.00	(Salisbury et al. 1973a)
Multilayer insulation (very small surfaces)	-	0.03…0.05[2)]	(Donabedian et al. 2002)
PCB (typical)	-	0.80	(Plotog et al. 2010 - 2010)
Solar Cell	0.65	0.90	Estimate
Ultem (Polyimide), dusty	0.5	0.5	Estimate

2.2.3 Variable Resistance Devices

A common method to deal with extreme differences in heat flow between hot and cold condition is the introduction of variable resistance devices, i.e. devices that can change their thermal resistance based on temperature or through external control to regulate the heat flow. Due to the extreme nature of the lunar day/night cycle, variable resistance devices are crucial elements for most lunar surface systems.

Louvers

In principle, a louver is a device that occludes a radiator surface, when no heat rejection is required and that opens when heat rejection is necessary. This is usually implemented by a set of rectangular blades (“vanes”) mounted on rotary joints that are placed above the radiator surface. In the open configuration, the vanes are rotated perpendicular to the radiator, to provide visibility from the radiator to deep space. In the closed configuration, the vanes are parallel to the radiator surfaces and slightly overlap, thus effectively shutting off all visibility from the radiator. Heat flow ratios, i.e. the ratio of heat loss from the open to the closed configuration can effectively be determined by the optical surface properties of the radiator and vanes. However, due to physical limitations of the surface finishes and because even open louvers still cause some occlusion of the radiator, achievable heat flow ratios for louver are less than 6:1 (Gilmore 2002b). Practical examples of louver systems can be found in Evans (2019) or Sierra Nevada Cooperation (2018).

Heat Switches

Heat switches are devices that can change their thermal conductance based on temperature or on a control signal, typically by opening/closing a physical gap between two surfaces. This effectively changes the

primary mode of heat flow from conduction to radiation, which enables very high heat flow ratios up to 100:1. The most common type of heat switch use temperature dependent volume changes of paraffin compounds to provide passive switching functionality. This way, the switching temperature can be set by the phase change temperature of the paraffin, which is determined by its composition. Practical examples of heat switches can be found in Sierra Nevada Cooperation (2018).

Variable Conductance Heat Pipes

In their basic form, heat pipes are high thermal conduction devices that allow high heat flows over relatively large distances by transporting latent heat of a fluid that evaporates at the hot end and condenses at the cold end. Variable conductance heat pipes extent this principle by the addition of a non-condensable gas. At lower temperatures, the non-condensable gas inhibits the gas flow of the evaporated fluid to the condenser, thus restricting the heat flow. As temperatures rise, the partial pressure of the evaporated fluid increases, thus the influence of the inhibiting non-condensable gas decreases and heat flow increases. Heat flow ratios can reach up to 5:1 (Anderson et al. 2009).

2.3 Thermal Control Architectures

Table 2-3 shows an overview over the most important aspects of a thermal architecture for a lunar surface system: The first aspect is the positioning of the radiator. The radiator must be placed such that it is the least exposed to external heat fluxes. Ideal placement is determined by the landing location and time of operation. At equatorial latitudes, solar elevation during the day can reach up to 90°, thus upward facing surfaces can be exposed to a high amount of solar illumination. It is therefore more beneficial to place the radiator sideways and away from the sun, even though it may then see some albedo or infrared heat from the surface. Another method can be to restrict mission operations during local noon, thus avoiding operation during high solar elevations. For missions in polar latitudes, upward facing radiators are optimal, as solar elevations are low and therefore the top is usually the least exposed surface.

The next consideration is solar cell mounting. External surfaces are usually covered with thermal surface finishes with low absorbance and emissivity. However, solar cell surfaces have high absorbance/emissivity and will therefore usually see high heat fluxes. Solar cell mounting therefore severely impacts thermal design. Three approaches are common: Solar cells on external structures / solar sails than can be easily decoupled from the core systems, solar cells mounted on insulation, e.g. adhesively mounted onto MLI and direct solar cell mounting, leading to a hot structure that requires internal thermal decoupling.

Heat flow regulation is necessary to account for changing heat dissipation or external heat fluxes. This relies on variable resistance devices. Common methods were discussed in section 2.2.3.

Another important factor is spacecraft orientation. This is especially relevant to landers and stationary payloads, since in these cases orientations are fixed after landing / placement. If the orientation is determined prior to launch, the thermal control systems can be tailored towards this orientation. This provides additional options, for example for the radiator placement.

Table 2-3: Thermal architecture aspects for lunar surface missions

Category	Typical Options	
Radiator positioning	Side (Equatorial)	Top (for polar missions)

Solar cell mounting	External Structure / Sail	Mounted on MLI	Hot structure / internal decoupling
Heat flow regulation	Heat Switch, Louver, Variable flow heat pipes		
Orientation	Fixed	Free, but preferred	Free
Temperature levels	Single WEB	Insular	Layered

The final consideration are temperature levels inside the spacecraft. A common thermal design includes a warm electronic box (WEB), in which all temperature sensitive components are placed. The advantages are that this is relatively simple and heat dissipation from all components contributes to maintain operational temperatures in the cold case. The problem with this approach is, that all components are maintained at the same temperatures, therefore not all components can be operated at their limits. This is of particular importance to this study, since some components may be more compatible with low temperatures than others. Alternative approaches are insular or layered architectures. An insular architecture separates components with different temperature limits and provides them with independent temperature control, thus allowing operation at different temperatures. A layered approach also separates component based on temperature limits, but places the components in series, such that heat loss from hotter parts warms the adjacent colder parts. However, this approach is highly complex, especially since it needs to work for both cold and hot case. A visualisation of these approaches is shown in Figure 2-1.

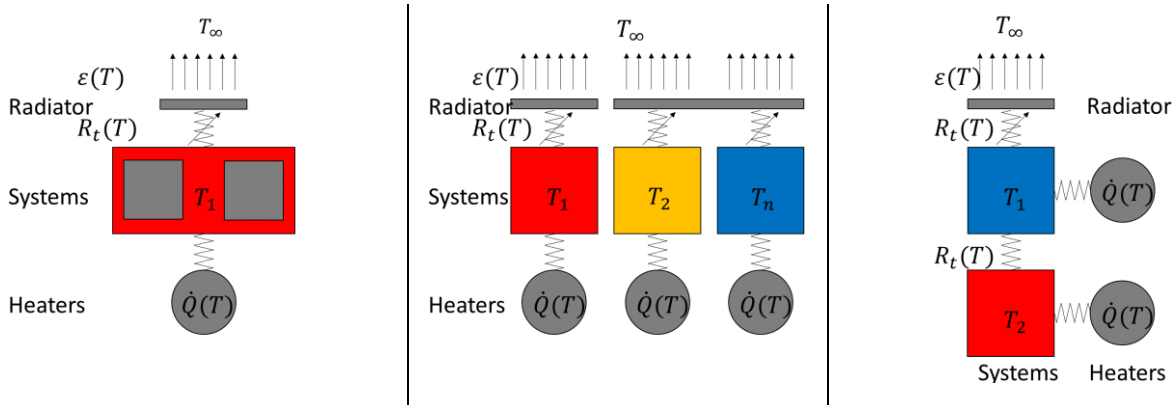

Figure 2-1: Schematics of thermal architectures: Single WEB (left), insular architecture (middle) and layered architecture (right).

2.4 Component Qualification Procedures

Selection of hardware for institutional space missions is usually based on a reliability preference order, that favour the selection of more strictly rated components and imposes additional qualification procedures on less strictly rated components (NASA Goddard 1996). Therefore, many military grade components can be used without additional testing, whereas commercial consumer grade components need to be qualified in-house. However, while military and space applications require various tests that are not relevant for industrial / automotive applications, thermal and temperature related testing is not necessarily stricter. Table 2-5 shows a comparison of temperature related testing conditions, Table 2-4 shows typical temperature ratings for different component grades. Note that test conditions for hot temperatures are not comparable for space applications, as the absence of atmospheric pressure significantly inhibits heat transport and can therefore lead to hot spots for parts with high heat dissipation.

Table 2-4: Common temperatures ratings for electronic components (adapted from (Bauer 2020), based on (Liang and Meng 2017 - 2017))

Grade	Typical operating temperature range
Commercial / Consumer	0 °C to +70 °C
Industrial	– 40 °C to +85 °C
Automotive	– 40 °C to +125 °C
Military	– 55 °C to +125 °C

Table 2-5: Qualification test procedures related to thermal performance for automotive, military and space applications (adapted from McDermott et al. 2002).

Test Condition	Automotive	Military (MIL-STD-883 / MIL-PRF-38535)	Space (NASA GSFC 311-INST)
Thermal shock	-65°C to 150°C, 500 cycles, 10 minutes/cycles	-55°C to 125°C, 15 cycles, 10 second transfer time, 2 minute dwell	Not required
Span of life	150°C, 2000 hours, 30% overvoltage, performing operational tests	125°C, 1000 hours, all Vcc's at max voltage	Max junction temperature, 1000 hours, all Vcc's at max voltage, performing operational tests
Thermal cycling	-65°C to 150°C, 1000 cycles, 1 hour per cycle	-65°C to 150°C, 100 cycles, 10 minute dwell	-65°C to 150°C, 10 cycles, 10 minute dwell

With regard to low temperature rerating, the most relevant test condition is thermal cycling. Thermal shock can be of relevance, but only if sudden temperature changes are expected. If functional testing reveals that a component can be utilized below its rated temperature envelope, additional qualification testing is necessary to ensure a minimum level of reliance. The testing procedure should conform to industry standards (e.g. NASA GSFC 311-INST). Therefore, it is important to understand that a components functional temperature limits, its cycle test temperature envelope and the actual temperature rating are not equal. Figure 2-2 shows the temperature curve for a thermal cycling test in accordance with MIL-STD-883. For a component rating of -55 °C to 125 °C, the component is tested at temperatures of at least -65 °C to 150 °C. The actual test temperatures may exceed this envelope up to -75 °C to 165 °C to ensure that the test article will in fact reach its qualification temperature. Thus, for a rating of -55 °C, a component must be functional to at least -75 °C, or safety margins need to be decreased.

Apart from test temperature, another important factor is the required lot size used for testing. Qualification standards propose appropriate lot sizes dependent on the device type and the desired reliance class. Alternatively, Liang and Meng (2017 - 2017) proposed a statistical approach that determines lot size based on a required confidence interval.

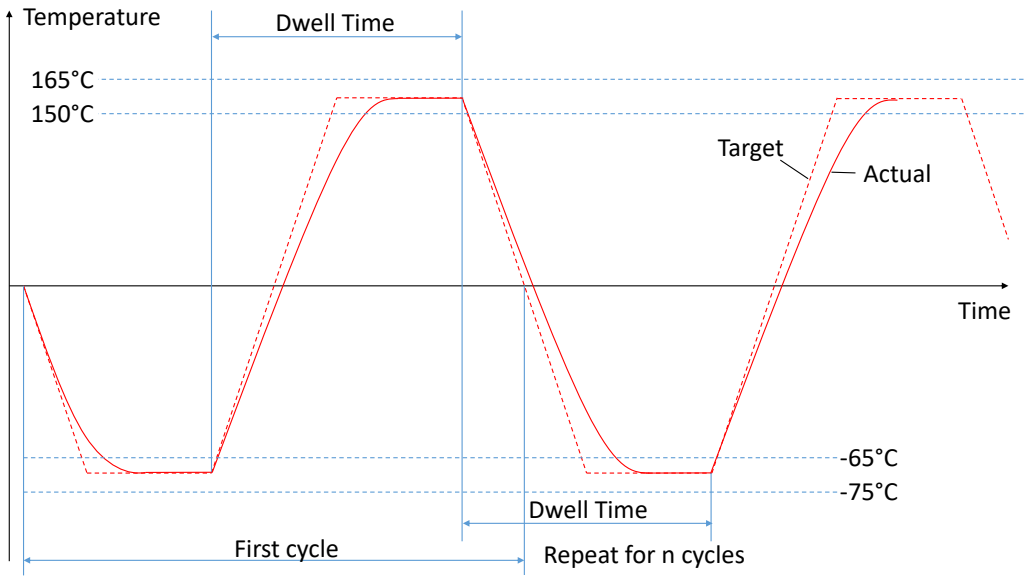

Figure 2-2: Temperature profile for thermal cycling testing in accordance with MIL-STD-833 (adapted from Department of Defence 2016).

Low temperature rerating has also previously been implemented for space exploration missions. Kolawa et al. (2013) have investigated low temperature rerating for a motor drive electronics assembly for the Mars Science Laboratory (Curiosity). The environmental temperature range for the mission was given as -128 °C to 20 °C, but qualification test limits were -143 °C to 125 °C for electronic components. Minimum mission life was 670 thermal cycles and the test procedure utilized 2000 cycles.

Similarly, Torres et al. (2017) have investigated components for the use on the Actuator Drive Electronics (ADE) for the Exomars rover. 95 different components were investigated, with component types including capacitors, connectors, diodes, fuses, inductors, integrated circuits, relays, resistors, transistors, transformers, optocouplers and hybrids. Test lot sizes ranged from two to ten and were chosen individually for each component, based on its criticality. The expected minimum temperature for the components was not reported, but a minimum environmental temperature of -113 °C was given. Thermal cycling was performed to -130°C for 200 cycles, providing a minimum safety margin of 17 K.

2.5 Thermal Margins

The functional temperature range of a component is not equal to its allowable temperature range on a space mission. Quality assurance and thermal design practices require numerous safety margins that significantly offset the actual useable temperature range. This is visualized in Figure 2-3. As discussed in the previous chapter, there is a qualification margin between allowable flight temperatures and qualification temperatures and there needs to be an additional functionality margin between the actual functional temperature range of a component to the qualification temperatures, otherwise significant numbers of failures will occur during qualification. Furthermore, a thermal design margin ensures that accounts for uncertainties in the thermal design process.

The extent of these margins is subject of discussion and has been defined differently by different agencies (Siebes et al. 2012). For the purposes of this study, the following margins are proposed: 10 K functionality margin, 10 K qualification margin and 15 K thermal design margin. This Thermal design margin was chosen, because the thermal analysis performed in this study remains rudimentary and this margin is recommended for early (Phase A) analyses (ECSS Executive Secretariat 2016). This means that the survival heater for a part that is able to function at -120°C needs to be designed for a -85°C set temperature.

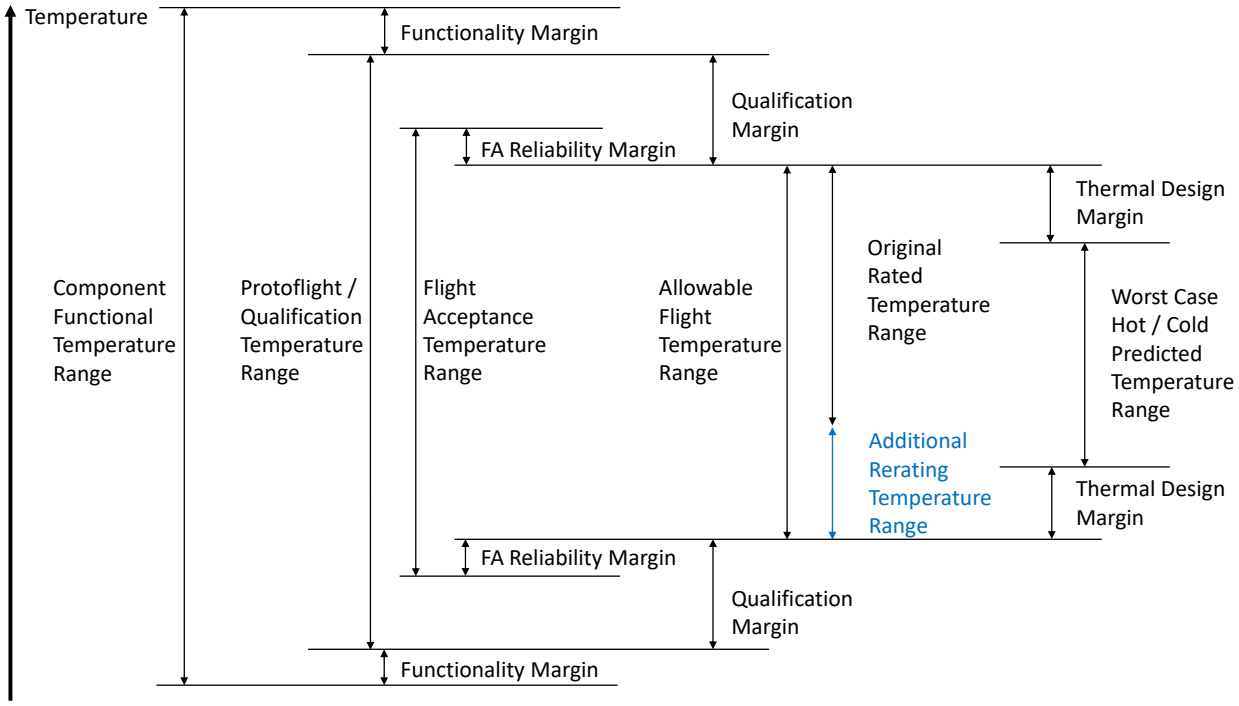

Figure 2-3: Visualisation of thermal temperature limits and margins (Based on Siebes et al. 2012).

3 Low Temperature Rerating

In this chapter, the rerating potential for an example system, the LUVMI-X DPP support module is examined. The system was chosen, because it is developed by the TUM Chair of Astronautics and therefore accessible for this study. The support module consists of the communication (COMM) module, the command & data handling (CDH) module, the electrical power system (EPS) and the battery. A detailed description of its elements can be found in 0. The first three systems will be investigated in this chapter, the battery will be investigated in chapter 4. For the investigated systems, the required components are tested for their functionality at temperatures below their ratings, to provide an overview of how many changes are necessary to achieve a desired rating. In the discussion, a suitable rerating temperature is then chosen and a replacement is proposed for non-operational components. Note that due to budgetary constraints, only a simplified COTS version of the communication module was investigated.

The chapter starts with a detailed description of the investigated subsystems. The test methodology is explained, then the test results for the different components are presented. First, the results of generic components (resistors and capacitors) are presented, because they are needed for all subsystems and for the experimental setup of the more complex components. Then the results for the microcontroller, the command & data handling system, the power distribution system and communication module are shown. Finally, the chapter concludes in the discussion.

3.1 Low Temperature Test Setup

Component testing requires a method to produce stable and predictable temperatures from room temperature down to cryogenic temperatures. Two different test setups have been used in the tests presented in this chapter. The first method is shown in Figure 3-1. The test specimens are suspended above a liquid nitrogen surface inside of a Dewar vessel. At atmospheric pressure, liquid nitrogen has a stable temperature of -196°C. Inside of an open vessel, the temperature increases above its surface. A measurement of the temperature as a function of distance is also shown in Figure 3-1 and shows an almost linear relationship. This allows convenient setting of the temperature of the test specimen, simply by adjusting the height at which the specimen is suspended inside the vessel. The specimen is connect by cables to the auxiliary electronics outside the Dewar vessel. Variations of this method are also used by similar studies (Buchanan et al. 2012; Valiente-Blanco et al. 2013). It is cheap and simple to use, but testing at atmospheric pressures can cause condensation and ice formation on test specimens. It was established at the Chair of Astronautics by Malzone (2020). The method was used for all tests, except the microcontroller testing in section 3.3. These microcontrollers were tested in a thermal vacuum chamber, as shown in Figure 3-2. The specimens were affixed on a heat exchanger and covered by Mylar foil for insulation. Liquid nitrogen was fed through a tube of the heat exchanger to cool it to required temperatures. This method is very representative of real lunar conditions, but complicated and expensive to use.

In either case, thermocouples were mounted on the specimens to determine the exact case temperature. It should be noted that junction temperatures can be 10-15°C higher than baseplate temperatures for normal components and even 25°C higher for high power electronics (Fairchild et al. 2002). For this reason, the test procedures included cold restarts, i.e. a shutdown of the test specimens at low temperature to ensure that internal temperatures reach case temperatures.

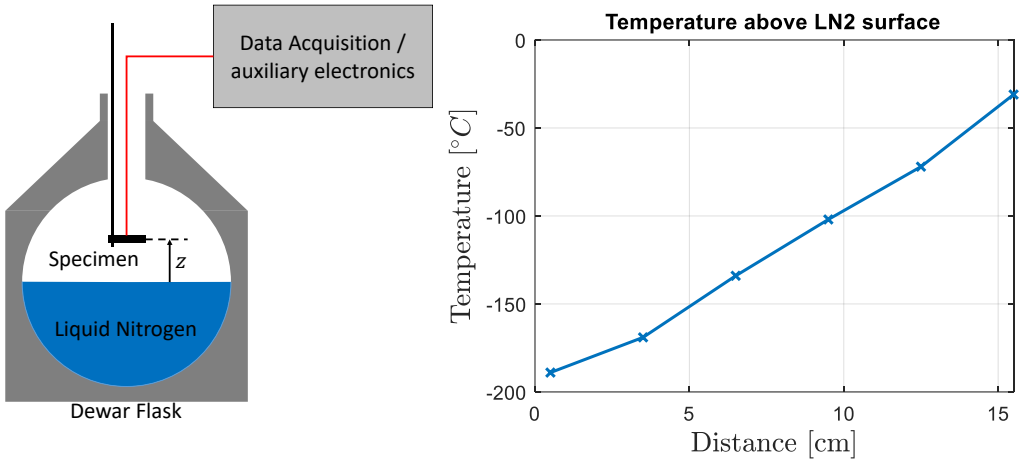

Figure 3-1: Left: Schematic of the dewar test setup; Right: Steady-state temperature in the Dewar above the LN2 surface.

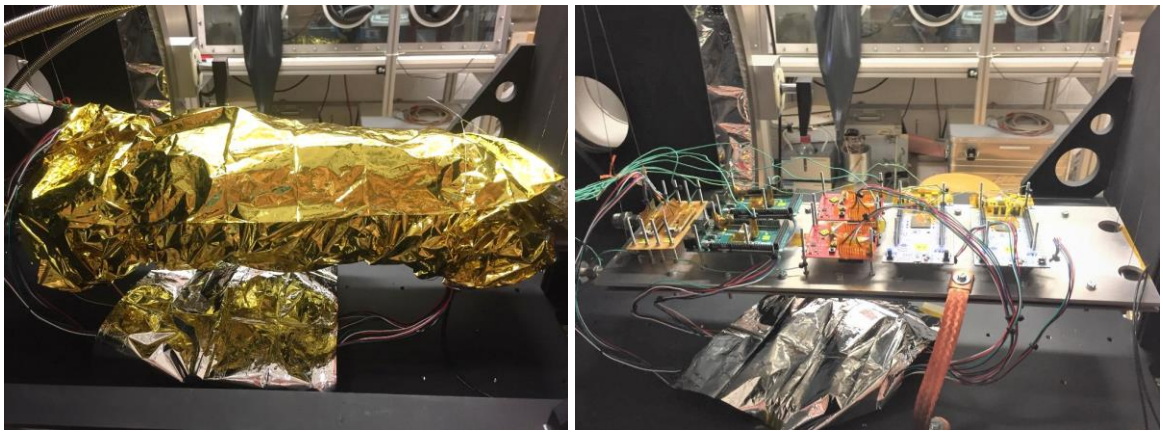

Figure 3-2: Images of the tested microcontroller mounted onto the liquid nitrogen heat exchanger in the thermal-vacuum chamber (Bauer 2020).

3.2 Basic Components

Resistors

Various studies have already examined different resistors under low temperatures and promising solutions have been identified (see Table 8-3). However, as resistors are crucial to any electronic circuit and thus necessary for many of other tests, it is necessary to further verify the behavior of the used resistors to ensure the validity of the other experiments. Two types were identified as suitable for the further experiments: Metal film and thin film resistors and four sizes of each (10Ω, 100Ω, 1kΩ and 100kΩ) were procured in SMD format and soldered onto a small custom PCB. The PCB was connected to a Multimeter and then cooled. Unfortunately due to a soldering problem, only the 100Ω and 100kΩ sizes of the Metal film resistors could be tested. The results are shown in Figure 3-3. All investigated resistors maintained their resistance within reasonable margins throughout the test, down to -180°C. The 10Ω thin film resistor showed a 7% deviation throughout the test, though internal resistance of the cabling due to a defective connection likely caused this.

Table 3-1: Overview of the investigated resistors

Type	Series	Resistance	Manufacturer	Footprint	Rating	Note
Metal Film	RN73H	10 Ω	KOA Speer	0603	-55…+155°C	No data
	RN73H	100 Ω	KOA Speer	0603	-55…+155°C	
	RN73H	1 kΩ	KOA Speer	0603	-55…+155°C	No data
	RN73H	100 kΩ	KOA Speer	0603	-55…+155°C	
Thin Film	RNCF	10 Ω	Stackpole	0603	-55…+155°C	
	RG	100 Ω	Susumu	0603	-55…+155°C	
	RG	1 kΩ	Susumu	0603	-55…+155°C	
	RG	100 kΩ	Susumu	0603	-55…+155°C	

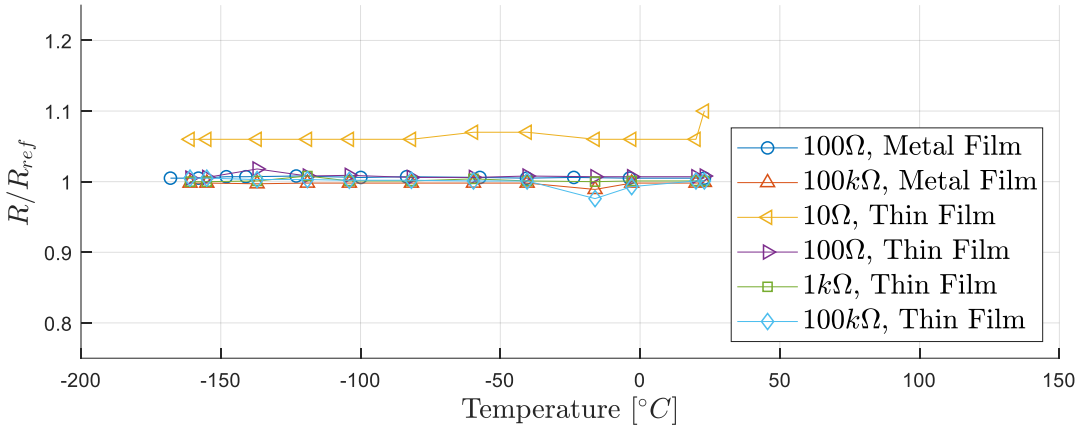

Figure 3-3: Resistance over temperature for the investigated resistor types

Capacitors

Similarly, to resistors, capacitors are basic electronic items that are necessary for any circuit and are thus needed for the other tests. Therefore, despite extensive literature on the low temperature behavior of these components, additional tests were performed to ensure their functionality. In addition, not all types are available in all sizes and with the required form factor. NP0/C0G and PPS capacitors are reported to have good low temperature stability (see section 0) but are only available for capacitances $< 1\mu F$. Therefore, PET, Tantal and ceramic capacitors are investigated as alternative options for larger sizes. The capacitors were built into a small RC-circuit, which was periodically charged / discharged by an Arduino microcontroller and the time constant was measured and used to determine the capacitance. The capacitors were arranged on two PCBs in 12 individual RC-circuits as described in Table 3-2. The results are shown in Figure 3-4.

Unfortunately a loss of data occurred for the 10 µF Tantal and the 1 µF PET tests between -63°C and +11°C. Apart from this, the measurements functioned well. As expected, the results show good performance of the NP0/C0G and PPS capacitors. For both of these types, two different capacitors of two different manufacturers were tested and all remained within 2% of their room temperature capacitance. The ceramic capacitors performed well until -110°C, at which point the capacitance started to change. There is a notable difference between the 100 nF and 10 nF capacitors, though either part came from a different manufacturer. The Tantal capacitors showed 22% and 24% deviations and the PET between 8% and 42%.

Table 3-2: Overview of the investigated capacitors

Type	Series	Capacitance	Resistor	Board	Manufacturer	Footprint	Rating	Deviation at -180°C
Tantal	TAC	100 nF	2 MΩ	1	AVX Corp.	0603	-55…+125°C	-24%
	TAC	10 µF	1 kΩ	2	AVX Corp.	0603	-55…+125°C	-22%
Ceramic	X7R	10 nF	2 MΩ	1	AVX Corp.	0603	-55…+125°C	-35%
	X7R	100 nF	2 MΩ	1	Samsung	0603	-55…+125°C	-9%
PPS	ECHU	100 nF	2 MΩ	1	Panasonic	3225	-55…+125°C	+2%
	SMR	1 µF	100 kΩ	2	Kemet	n/a	-55…+150°C	+1%
PET	CB	10 nF	2 MΩ	1	AVX Corp.	2220	-55…+125°C	-8%
	R82	100 nF	2 MΩ	1	Kemet	n/a	-55…+105°C	-42%
	R82	1 µF	100 kΩ	2	Kemet	n/a	-55…+105°C	-11%
	R60	10 µF	1 kΩ	2	Kemet	n/a	-55…+105°C	-10%
NP0/C0G	GRM	10 nF	2MΩ	1	Murata	1206	-55…+125°C	+2%
	C	100 nF	2MΩ	1	TDK Corp.	0603	-55…+125°C	+2%

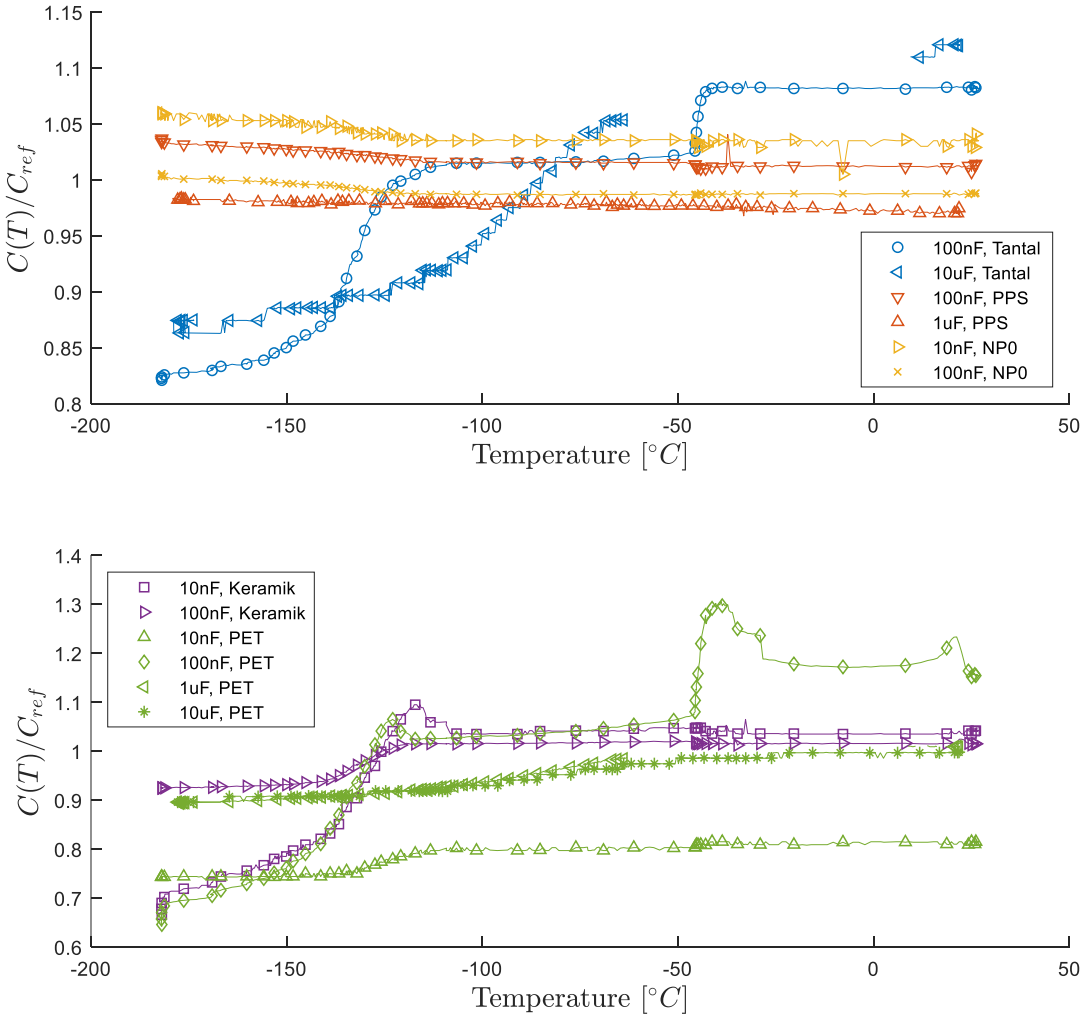

Figure 3-4: Capacitance over temperature for the investigated capacitators.

3.3 Common Microcontrollers

As identified in section 1.3.6, there is very little literature available on the low temperature usability of common modern microcontrollers. Therefore, in this set of experiments, a selection of microcontrollers was tested for their low temperature performance. The goal was to gain a general understanding of the low temperature behaviour of these components. For this purpose, four different types of microcontrollers were selected and tested. These experiments was conducted as part of a semester thesis (Bauer 2020), supervised by the author of the present thesis.

3.3.1 Test Specimens

Four microcontrollers were chosen for this investigation. The target of the selection was to choose devices that are commonly used in space missions but were at the same time inexpensive and easy to use. For this reason, the chosen devices represent COTS variants of devices that are used in space missions (Bauer 2020) and have been procured in the form of development boards that are compatible with Arduino software to keep programming effort manageable. Using a development board instead of only the IC is restricting, as the IC will only work while its peripheral components work as well. Therefore, the lower temperature limits determined in this test only represent an upper boundary, as it is possible that the microcontroller could have worked beyond this temperature without its peripherals. On the other hand, this significantly simplifies the experimental setup, as the development boards are ready to use and do not require the design and construction of test PCBs and come equipped with an easy to use programming interface. In addition, the

test results will provide additional information on the performance on the peripherals and on the feasibility of low temperature re-rating of the development board as a system. The four chosen devices are: The STMicroelectronics Nucleo 32L412KB, the Texas Instruments MSP-EXP430F5529LP, the STM Nucleo-144 L496ZG and the Arduino Mega 2560 Rev 3.

The Nucleo 32L412KB is a development board for the STM32 L412KB U6U microcontroller, a ultra-low power microcontroller of the popular STM32 family, which has space heritage (NanoAvionics 2020; German Orbital Systems GmbH 2016) . It was chosen for its low power features and as one of two representatives of the ARM-Cortex M4 architecture. The MSP-EXP430F5529LP carries the MSP430F5529 16-bit RISC microcontroller from the Texas Instruments MSP430 RISC ultra-low-power microcontroller family. It was chosen, because multiple members of the MSP430 family have been used in different CubeSat and deep space missions (George and Wilson 2018; Schoolcraft et al. 2017) and because of its low power consumption. The Nucleo-144 L496ZG with the STM32L496ZG microcontroller, which is another representative of the STM32 family. It was chosen as a more powerful alternative ARM-Cortex-M4 variant that also features low power consumption. Finally, the Arduino Mega 2560 Rev 3 is from Atmel and is a representative of the popular high performance, low power ATmega family which also has space heritage (Geeroms et al. 2019; ISIS - Innovative Solutions In Space B.V. 2019). Each of the microcontrollers was accompanied by a set of peripherals on their development boards and featured various types of memory as shown in Table 3-3 and Figure 3-5. As per datasheet, each of these parts had a lower temperature limit of -40°C.

Table 3-3: Overview of the selected development boards (Bauer 2020)

IDs	Manufacturer	MCU	Board	RAM	Flash	EEP ROM	Logic Level	Temperature Range	Source(s)	Comment
#3, #4	STMicro-electronics	STM32L412KB U6U 32-bit ARM Cortex M4 MCU	Nucleo-32L412KB	40 kB (SRAM)	128 kB	emulated in flash memory	3.3 V	-40 °C to +125 °C (MCU operation)	(STMicroelectronics 2015), (STMicroelectronics 2018)	Using on-board voltage regulators with external 9.5 V power supply
#5, #6	Texas Instruments	MSP430F5529 16-bit RISC MCU	MSP-EXP430 F5529LP	8 kB (SRAM)	128 kB	-	3.3 V	-40 °C to +85 °C (MCU operation)	(Texas Instruments Inc. 2013), (Texas Instruments Inc. 2009)	Using external 5 V supply
#7, #8	STMicro-electronics	STM32L496ZG 32-bit ARM Cortex M4 MCU	Nucleo-144L496ZG	320 kB (SRAM)	1 MB	emulated in flash memory	3.3 V	-40 °C to +85 °C (MCU operation)	(STMicroelectronics 2017),	using internal LDO regulator from external 5 V Supply
#20, #21	Arduino	Atmel ATMEGA2560-15AU 8-bit AVR MCU	Mega 2560 Rev. 3	8 kB (SRAM)	256 kB	4 kB	5.0 V	-40 °C to +85 °C (MCU operation)	(Guadalupi 2019), (Atmel Corporation 2005)	Using on-board voltage regulator and external 9.5 V Supply

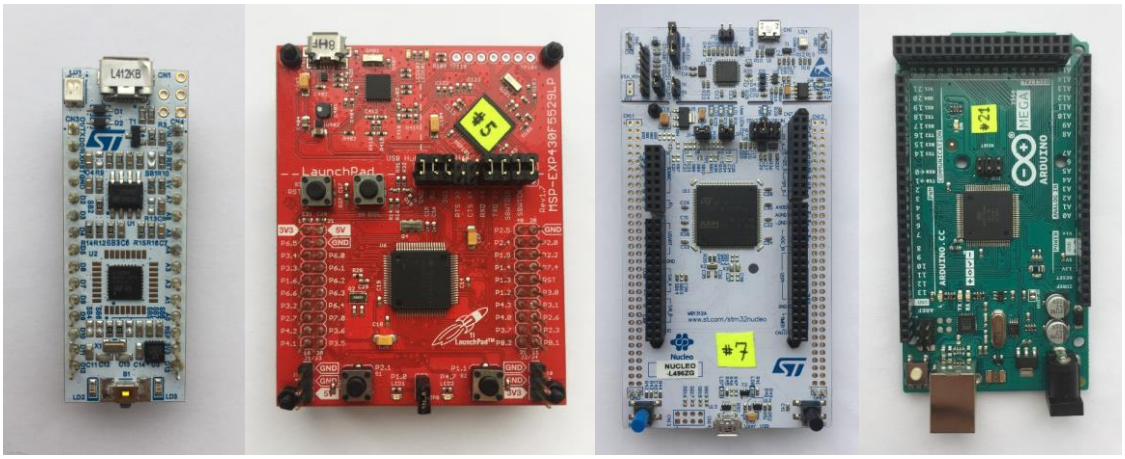

Figure 3-5: Images of the four types of investigated development boards. From left to right: STM Nucleo-32 L412KB, MSP-EXP430F5529LP, Nucleo-144L496ZG and Mega 2560 Rev. 3

3.3.2 Test Setup and Procedure

For this initial test, the eight test boards were mounted onto a cooling plate inside a vacuum chamber. The cooling plate was attached to a liquid nitrogen tube for cooling down to -196°C. The plate and microcontrollers were then encased by mylar foil to reduce heat loss and ensure even temperature distributions. Thermocouples were mounted onto each of the microcontrollers. Each of the microcontrollers was connected to an outside data acquisition controller by I2C bus and provided an additional analogue feedback voltage signal in case bus communication failed but the controller was still operational. Each of the tested microcontrollers was programmed to provide the following feedback through the I2C bus in regular intervals: Internal clock count, RAM state, flash memory state and EEPROM state (if applicable). The states of RAM, flash memory and EEPROM were determined by a program that read and rewrote 4byte increments into predefined memory fields of 4kByte in regular intervals, meaning the entire memory is tested once every 1000 iterations, similar to the method used by Avery et al. (2011). A more detailed description of the test setup and test procedure is provided in (Bauer 2020).

3.3.3 Results

A summary of the test results is presented in Table 3-4. The third column indicates the minimum usable case temperature. Note that in this test, this indicates the temperature of the microcontroller case while the device was running. The actual junction temperatures may have been up to 10 K higher (Fairchild et al. 2002) Nonetheless, all devices were usable at significantly lower temperature than their datasheet ratings indicated. In all cases, full functionality of the device remained until the device failed as a whole. No issues were detected during memory testing and the analogue feedback failed at the same point as the I2C communication. The most notable change in behaviour of the devices was observed in form of the clock signal, as shown in Figure 3-6. The internal clock count signals were compared to the clock count of the external DAQ controller and a relative drift factor $f_{drift}(T)$ was determined such that:

$$\Delta t_{external} = f_{drift}(T) \cdot \Delta t_{internal}$$

Note that the external clock was not calibrated, thus this data should only be used to compare the relative drift and not as absolute number. All devices showed a significant change in clock drift over the measured temperature range, though this change already started within the rated temperature limits and was mostly continuous and predictable. A simple countermeasure against this problem would be a thermal calibration, so that the drift is characterized and can be accounted for. For Dev #7 however, a jump in drift rate occurred at -99°C, which seemed to persist for the remainder of the test, but recovered after the test was concluded and the device was reheated to ambient temperatures. One unexpected problem that occurred during the test however was that failing devices started to interfere with the I2C bus communication. In their inoperable

state, their output to the I2C bus was undefined, which blocked other signals. Therefore, devices that are cooled beyond their operational capability should be deliberately switched off, e.g. by a bimetallic switch to avoid this problem.

Table 3-4: Overview of the results of the microcontroller test

Device ID	Device Type	Lowest Operational Case Temperature	Functionality at lowest operational temperature					Reboot after reheating
			Memory			Analogue Feedback	I2C Communication	
			RAM	Flash	EEPROM			
#3	STM Nucleo-32 L412KB	-108.8 °C	✓	✓	✓	✓	✓	✓
#4	STM Nucleo-32 L412KB	-112.1°C	✓	✓	✓	✓	✓	✓
#5	TI MSP-EXP430 F5529LP	-136.7 °C	✓	✓	n.a.	✓	✓	✓
#6	TI MSP-EXP430 F5529LP	-138.7 °C	✓	✓	n.a.	✓	✓	✓
#7	STM Nucleo-144 L496ZG	-127.3 °C	✓	✓	✓	✓	✓	✓
#8	STM Nucleo-144 L496ZG	-134.7 °C	✓	✓	✓	✓	✓	✓
#20	Arduino Mega 2560 Rev. 3	-75.2 °C	✓	✓	✓	✓	✓	✓
#21	Arduino Mega 2560 Rev. 3	-79.5 °C	✓	✓	✓	✓	✓	✓

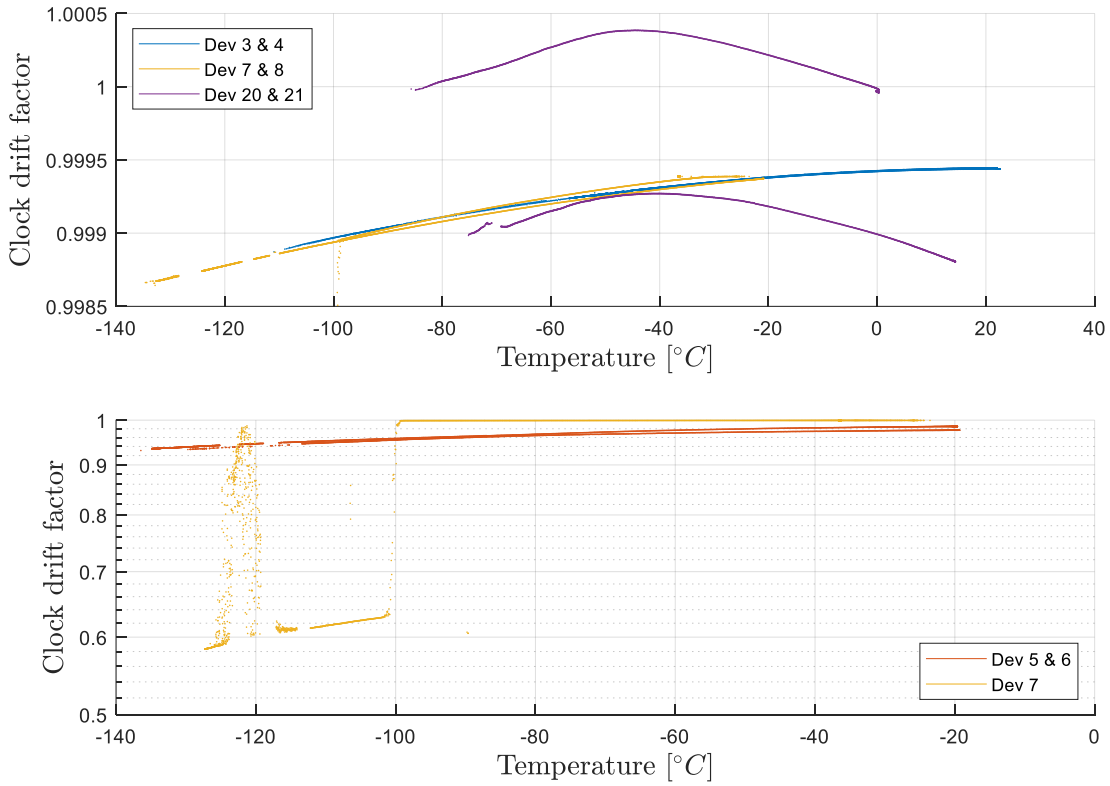

Figure 3-6: Results for the clock drift factor of the microcontroller test

3.4 Command & Data Handling Module Prototype

Tests for the command & data-handling module were conducted with the PEB1-VA41620 development board, as described in section 8.3.2. The test procedure was similar to the previous tests with the microcontroller development boards (see section 3.3). As the device was cooled, a memory test routine was running to verify any occurring memory errors. The internal clock count was compared against an external reference to determine the temperature dependent clock drift. Feedback was provided through UART communication, analogue feedback was implemented. During cooldown, the device was turned off in intervals to ensure internal temperatures to equalise with case temperature. The test was repeated three times with slightly differing procedures, as outlined in Table 3-5, the temperature curve, clock drift and memory results of the first test are shown in Figure 3-7. In each test, the device operated without issues to at least -109°C. In the second test, the device remained operational at -169°C. This discrepancy was likely caused by the shortened periods that the device was turned off. While it is unlikely that the internal temperature remained sufficiently high, the active state possibly prevented carrier freeze-out, allowing the device to remain operational even though a restart after an extended shutdown is not possible anymore. In test 1 and test 3, the device was not able to reboot after it failed at low temperature and had to be flashed to regain functionality. This was not the case in the second test, after which the device booted normally. This behaviour indicates, that the device overwrites part of its memory if it is attempted to turn it on at temperatures below -109°C. The device should therefore be cut from power, if temperatures cannot be maintained within the extended operational limits to prevent memory loss. On the other hand, while the device remained operational, no memory errors were detected. In conclusion, the device can be operated to at least -109°C.

Table 3-5: Test results for the test with the Vorago PEB1-VA41620 development board

	Test 1	Test 2	Test 3
Procedure:	Restart device at 10 K intervals, at least 30 s turned off	Restart device at 10 K intervals, at least 15 s turned off	Restart in 1 min intervals, at least 1 min turned off
Lower Limit Temperature (Loss of Signal):	-110.5 °C	-169.7°C	-109.5°C
Detected Memory Errors	0	0	0
Behaviour during Warm-up	No response	Successful reboot at -131.5°C	No response

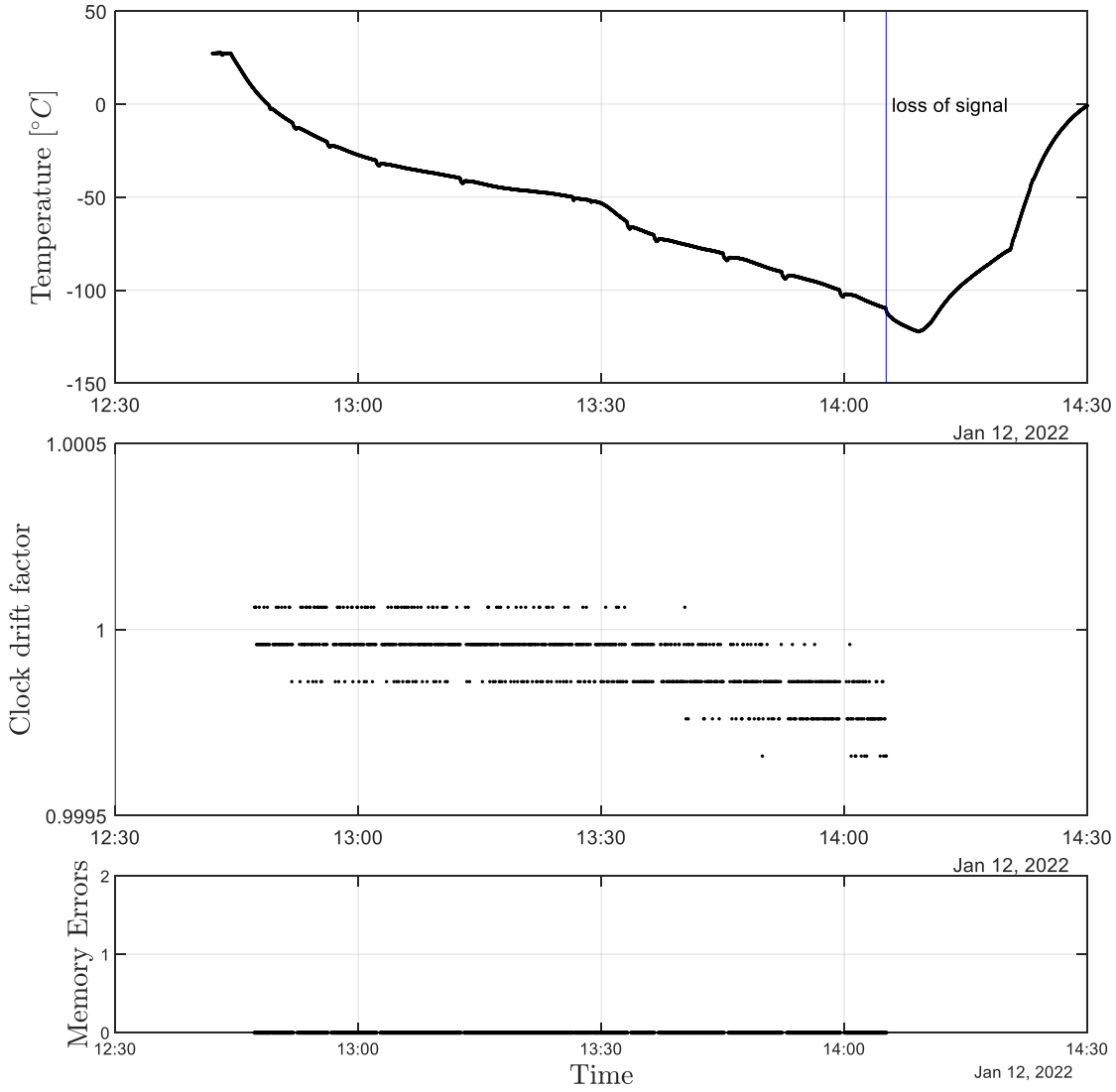

Figure 3-7: Results of test 1 for the PEB1-VA41620 development board. Top: Temperature over time; Middle: Clock drift factor over time; Bottom: Detected memory errors over time.

3.5 EMPS

The EMPS is used as reference system for the DPPs power system. The design of the DPPs power system for an actual flight model will likely look differently, however the EMPS provides a good reference, as it features all the required functionality that the DPP will require: A low power MCU for control, a lithium-ion battery interface with charge regulators, a solar cell interface that allows maximum power point tracking for battery charging, three voltage levels for different applications, five output channels for these voltage levels, current monitoring on all channels, various protection features and CAN and UART interfaces for communication. In terms of low temperature performance, the power system is the most crucial: It provides power to all other subsystems and it is always the first to be turned on. In this chapter, the performance of the EMPS as a complete system is evaluated first, then a closer look is taken on the individual components to determine if the overall performance can be improved.

3.5.1 System Level Test

Test Setup and Procedure

For the test, the battery is removed and the EMPS is connected to an input power supply at its charging input. The output channels are connected to an auxiliary readout circuit that uses voltage dividers and a Teensy 3.6 microcontroller to record the voltages at the output channels. The EMPS is controlled via UART commands from a laptop and the channels are regularly switched on and off in a pattern. The UART connection is also used to gather telemetry from the EMPS, including internal voltage measurements, temperatures, etc. The EMPS is then cooled according to the procedure described in section 3.1.

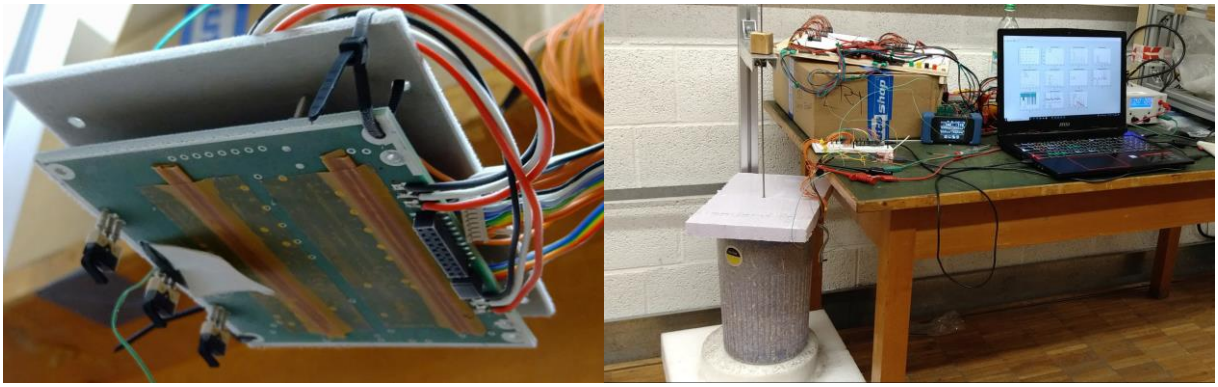

Figure 3-8: Images of the test setup for the EMPS system level test. Left: The EMPS suspended above the LN2 vessel; Right: Complete test setup with LN2 vessel, auxiliary electronics and laptop for data acquisition.

Results

Figure 3-9 shows the test results for the EMPS system level test. The module remained responsive to a temperature of -123°C (at the microcontroller). However, at -84°C (at the switches) the output of the 5 V channels was no longer available. The temperatures at the various temperature sensors are shown in Table 8-4. The results indicate that the MSP430 ceased operation at -123°C, stopping further communication with the board and turning off all other functionalities. This is about 10°C lower than the results obtained with the MSP430 development boards (see 3.3), however the model used on the EMPS is slightly different and the position of the temperature sensor also differs, therefore this discrepancy is within expectations. The results further suggest that the voltage regulators for the 5 V bus cease operation at -84°C, as the voltage of the 5 V bus drops independently of the switch state. In conclusion, the device seems fully operational until -84°C and partially operational to -123°C. However, due to the importance of the power system within any lunar surface system and due to its complexity, further investigation into the components of the EMPS are necessary.

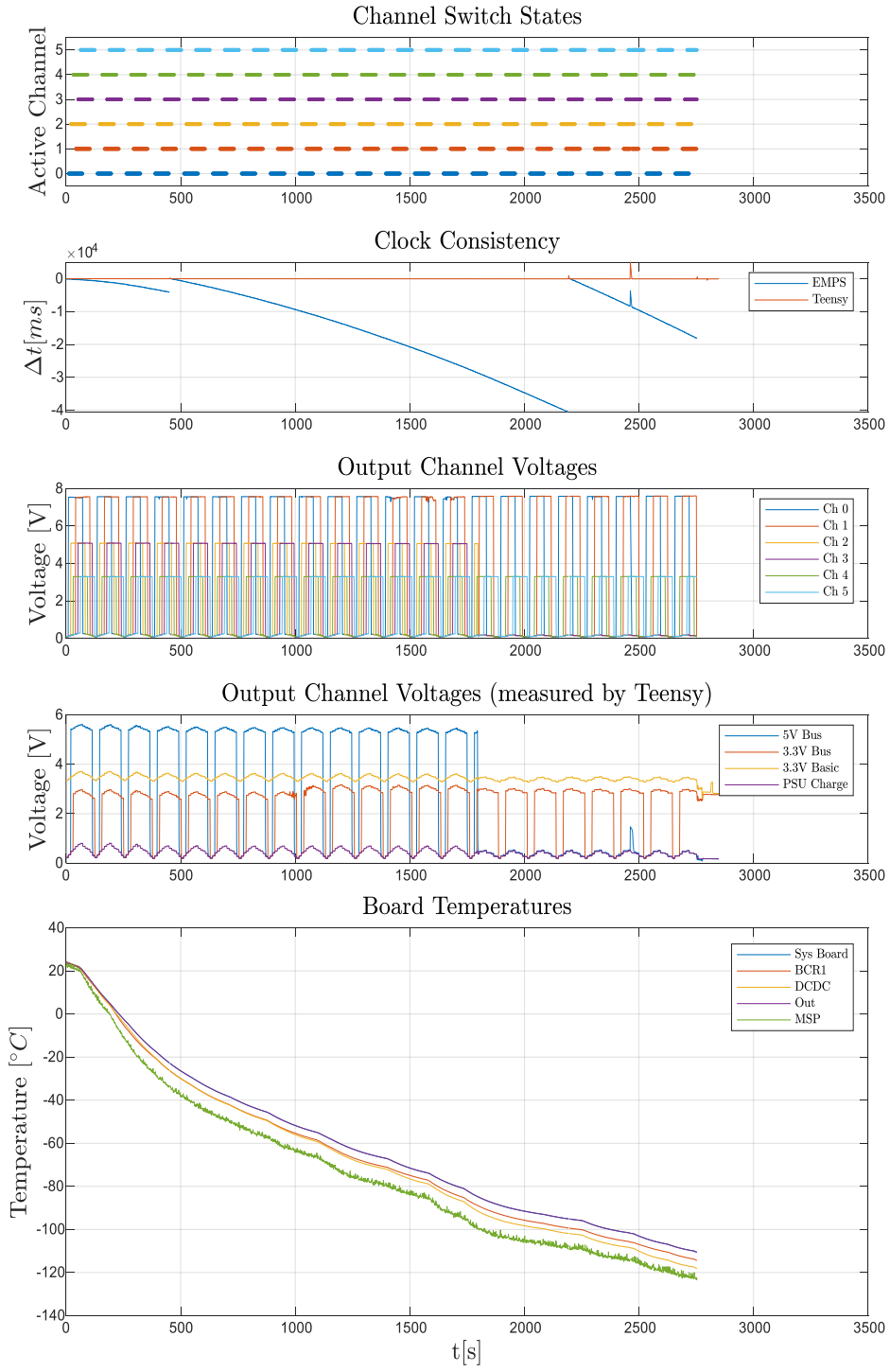

Figure 3-9: EMPS behaviour during cooldown. From top to bottop: Channel switch states, clock consistency, output channel voltages by the EMPS itself and by the teensy and board temperatures.

3.5.2 Component Level Testing

Table 3-6 shows a list of components from the EMPS. It includes the exact part numbers, package sizes/footprints and temperature ratings of the individual parts. In this chapter, each part is tested individually to provide further insight into the low temperature performance of the EMPS and to assess if the operational limit can be extended further by exchanging certain parts and to assess the required effort.

Table 3-6: List of Components used on the EMPS.

Type	Description	Additional Information	Temperature Rating [°C]	Note	Reference
Resistors	Precision Thick Film Chip Resistors	0.005 Ohm to 1 MOhm	-55 to +125 or -55 to +155		(Panasonic 2021)
Capacitors	Multilayer Ceramic Capacitor	30 pF to 22 uF	-55 to +125		(TDK Coorperation 2021)
Inductors	WE-MAPI SMD	1.5 uH and 2.2 uH	-40 to +125		(Würth 2020)
Zener Diode	CZRU52CX	3.6 V; 5.6 V; 9.1 V; 20 V;	-55 to +125		(COMCHIP 2002)
MOSFET	FDS8870	30V 18A 8SOIC	-55 to +150	not used after deployment	(Fairchild Semiconductor 2007)
eFuse	TPS25940AQRVCRQ1	2.7-V-18-V, 42mΩ, 0.6-5.2A	-40 to +125		(Texas Instruments 2021)
Optocoupler	SFH6156-4T	4-Pin SMD	-55 to +100		(Vishay 2021)
Battery Charge Regulator	BQ29209DRBT		-40 to +105		(Texas Instruments 2015)
Standalone Can Controller	MCP2515-E/ML	20-QFN (4x4)	-40 to +125		(Microchip Technology Inc. 2019)
CAN Transceiver	SN65HVD233D	8-pin SOIC (D)	-40 to +125		(Texas Instruments 2002b)
Power Switch	TPS2553DBVR	6-pin SOT-23 (DBV)	-40 to +125		(Texas Instruments 2020c)
	FPF2701MX	8-Pin SOP	-40 to +125		(Fairchild Semiconductor 2013)
Step-Down Voltage Converter	LM73606QRNPTQ1	6A 30WQFN	-40 to +125		(Texas Instruments 2018b)
Buck Step-Down Regulator	TPS62130AQRGTRQ1	16-Pin QFN	-40 to +125		(Texas Instruments 2020b)
	TPS62150AQRGTRQ1	16-Pin QFN			
Buck-Boost Converter	TPS63070RNMR	3.6A 15VQFN	-40 to +150		(Texas Instruments 2019)
Analogue Switch	TS5A3166-Q1	SC70-5	-40 to +125		(Texas Instruments 2014)
Digital-to-Analogue Converter	DAC7512E/2K5	8-pin SOP (DGK8)	-40 to +105		(Texas Instruments 2002a)
Buffer Gate	SN74LVC126A	14VQFN	-40 to +125		(Texas Instruments 2017)

Type	Description	Additional Information	Temperature Rating [°C]	Note	Reference
Comparator	LTC1540IDD#PBF-ND	8-DFN	-40 to +85		(Linear Technology Corporation 1997)
Current Monitor	INA226AIDGST	10-pin SOP (DGS10)	-40 to +125		(Texas Instruments 2020a)
Microcontroller	MSP430FR5989IRGC	64VQFN	-40 to +85		(Texas Instruments 2018a)

eFuse TPS25940

This device is used to limit the maximum power drawn from the EMPS and to ensure that the primary voltage remains within defined limits. It provides current monitoring and will automatically switch off if a set current limit is reached or voltage is out of limits. It further provides reverse current protection and feedback on the current and status. To test these features, a test circuit was designed, see Figure 8-6. The procedure varied the input voltage to stimulate a change in output current and to trigger the device. The current and feedback pin output were recorded and the devices was cooled down. Four devices were tested, the results are shown in Figure 3-10. The devices worked well down to -180°C. The output current limit changed between -1.5% to +3.5% compared to its room temperature value. The current feedback voltage increased by 3.5-5%, though this actually reduced the offset from its expected value. The undervoltage protection threshold decreased slightly, but at -180%, it was only 1% below its expected range as specified in the datasheet. The overvoltage protection threshold remained within its expected range throughout the whole test. It can be concluded that the device remains fully operational down to -180°C.

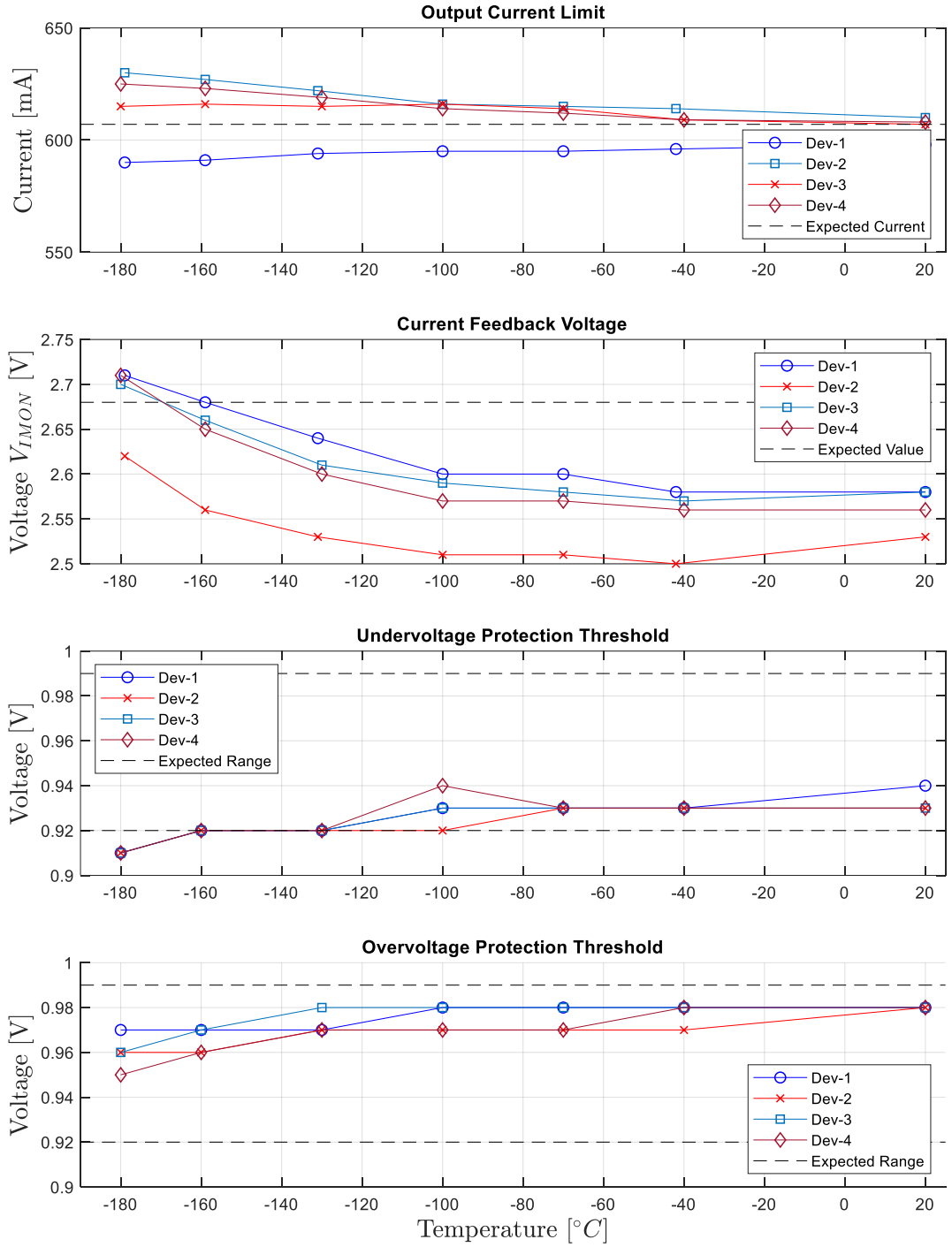

Figure 3-10: Test results for the eFuse from top to bottom: Output current limit, current feedback voltage, undervoltage protection threshold and overvoltage protection threshold.

Optocoupler SFH6156

Optocouplers are used to couple isolated circuits and is used in the EMPS to insulate its circuits from external systems. While not strictly necessary, for the operation of the DPP, optocouplers are frequently used components in power system architectures and were thus included in this investigation. A total of ten devices were tested. An image of one of the test articles is shown in Figure 8-5, the test circuit is shown in Figure

8-7. Each devices was subjected to a square wave as input signal, while the output was connected to a resistive load and the voltage drop over this load was monitored. An oscilloscope further compared the shape of the input and output signals. No change in the shape of the signal was observable. The predominant change over temperature was the ratio of input current to output current, as displayed in Figure 3-11. While the input current remained constant, the output current actually increased until -40°C, but then started to decrease. The devices remains fully operational at least down to -80°C. It can also be used at lower temperatures down to -180°C, but then provisions need to be made to account for the decreasing output current, or rather the increasing internal resistance. For example, the input current could be increased, by reducing the current limiting resistor. This could however become problematic at higher temperatures.

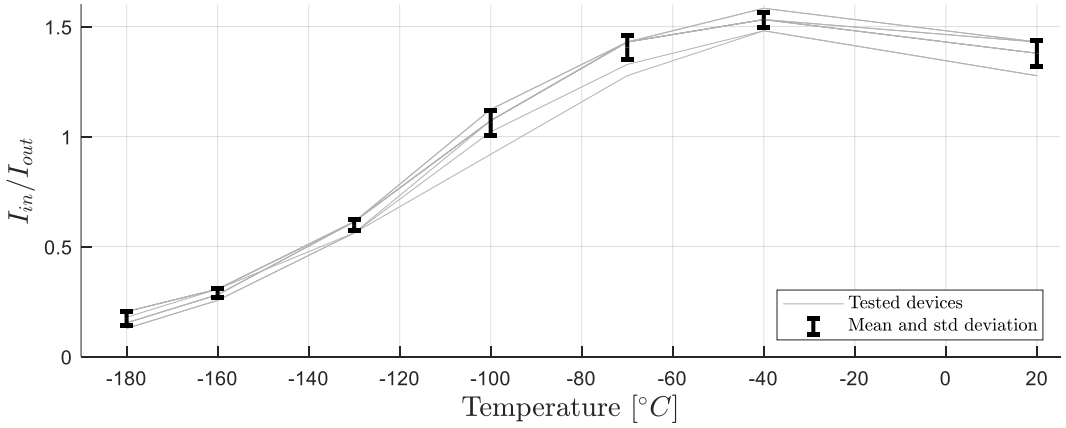

Figure 3-11: Output current vs. Input current over temperature for the Optocoupler SFH6156

Battery Charge Regulator BQ29209

This device balances the two in-series batteries of the EMPS and protects the batteries from overvoltage. It is therefore crucial to its operation. For the test circuits, two power supplies were used to emulate the batteries, the devices was connected as presented in Figure 8-8. During the test, one power supply was kept at a constant voltage of 3.9V, while the other was increased to determine at which voltage threshold the devices would start to balance the emulated battery. The threshold voltage was determined over temperature as well as the resulting balancing current. Eight devices were tested. The results are shown in Figure 3-12.

The devices performed well until -160°C. At this temperature, the threshold temperature had remained within 1% of its room temperature value. However, at -180°C, the device had stopped working properly and the balancing current remained continuously activated, regardless of the input voltages, rendering the devices useless at this temperature. The balancing current increased by 11% on average from 20°C to -160°C. In conclusion, the devices is fully useable to -160°C and not useable at all at lower temperatures.

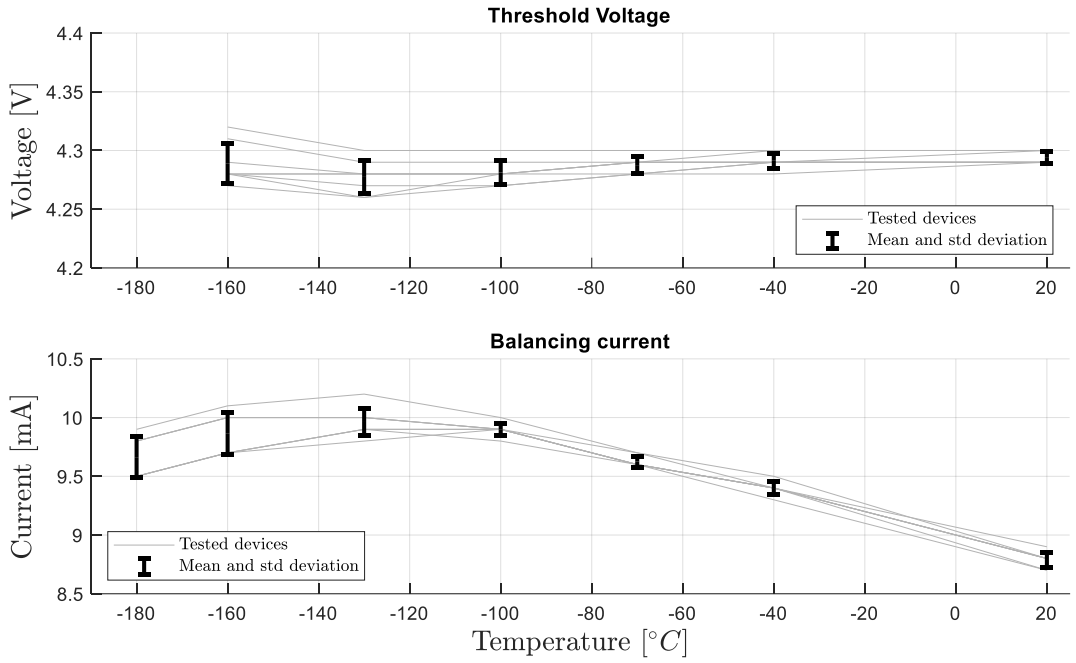

Figure 3-12: Test results for the battery charge regulator. Top: Threshold voltage at which balancing commenced (the other cell was kept at 3.9V); Bottom: Resulting balancing current.

Standalone CAN Controller MCP2515

The MCP2515 is a standalone CAN controller, allowing microcontrollers that do not have a native CAN implementation to communicate through the CAN bus. To operate, it requires a clock signal, from either a microcontroller or a dedicated oscillators and a can transceiver to generate the appropriate voltage levels. Two MCP2515 are used, each mounted on a MCP2515_CAN Bus module from AZ-Delivery. The module includes a crystal oscillator and a CAN transceiver and connects to a microcontroller through SPI. Both modules continuously send and receive commands. One module is cooled and the other is kept at room temperature. This way, both send and receive capability are tested. A single module was tested at cold temperature. Figure 3-13 shows the percentage of successfully transmitted messages in both directions. Outgoing messages start to show errors at about -60°C and the success rate drops to about 60% until -130°C. The success rate then drops to almost zero at -150°C. Notably, it increases again at lower temperatures, with a peak at -160°C. The success rate for received messages is constant until -138°C below which it drops drastically. The most likely explanation for this behavior is the temperature dependence of the oscillator. The MCP2515 remains responsive (through SPI) at all temperatures. This makes a synchronization issue due to a malfunctioning clock a likely explanation. During the test, both devices sent messages in regular intervals. When two devices send at the same time, the device with the lower identifier (in this case the reference module at room temperature) is allowed to continue, while other transmissions are interrupted. Therefore, the success rate for received messages remains good for the majority of the test. At -140°C, the discrepancy in synchronization becomes too severe, making further communication unreliable. In conclusion, the device is fully useable down to -130°C and can likely be used at lower temperatures, if a reliable clock source is used. Note that on the EMPS, the MSP430 provides the clock signal for the CAN controller, not an external oscillator.

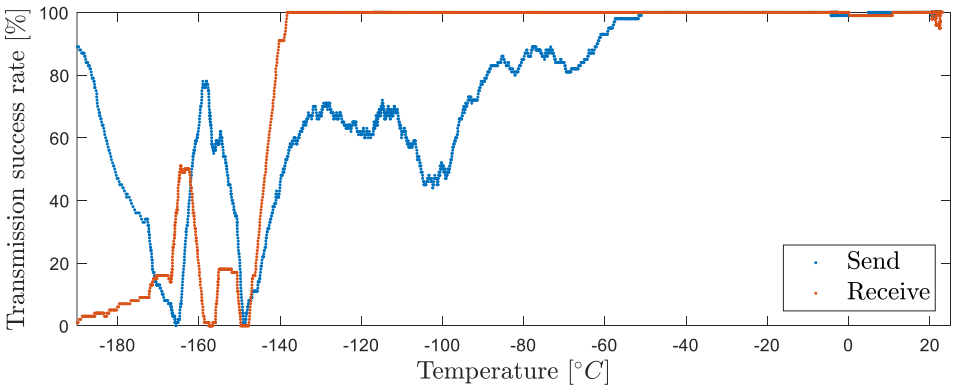

Figure 3-13: Test results for the MCP2515 Can Controller. The lines indicate the percentage of successfully sent or received messages as a function of temperature.

CAN Transceiver SN65HVD233

This devices serves as interface between a CAN controller and its CAN Network, translating the input signal into the required CAN low and CAN high signals. The device is crucial for the communication of the various subsystems. The designed test circuit for this component uses two Arduino Mega microcontrollers, each connected to one CAN transceiver. A signal (the word “A” in ASCII) is sent from the first microcontroller through the CAN network to the other. This enables to simultaneously test the send and receive functionality of the the transceivers. Additionally, an oscilloscope was used to monitor the signal shapes of both devices. Two pairs of transceivers were tested. The results are presented in Table 3-7: All tested devices worked without issues for the full tested temperature range. No errors were encountered, all signals were successfully translated. The devices is fully useable down to -180°C.

Table 3-7: Test results for the SN65 CAN Transceiver

Temperature [°C]:	18	-42	-62	-82	-102	-119	-141	-159	-182	16
Group one send:	“A”	“A”	“A”	“A”	“A”	“A”	“A”	“A”	“A”	“A”
Group one receive:	“A”	“A”	“A”	“A”	“A”	“A”	“A”	“A”	“A”	“A”
Group two send:	“A”	“A”	“A”	“A”	“A”	“A”	“A”	“A”	“A”	“A”
Group two receive:	“A”	“A”	“A”	“A”	“A”	“A”	“A”	“A”	“A”	“A”

Load Switch TPS2553DBVR

This device is a current limiting switch used to prevent inrush currents and is used in the EMPS to switch large loads on its battery voltage output channel. The maximum current can be set by a resistor and it provides a feedback bin that indicates possible failure modes. A single device was tested. During the test, the input voltage was varied from 2 V to 7 V. Additionally, at 4 V, the enable pin was briefly set to ground, to test the switching capability of the device. The results are shown in Figure 3-14. The device performed as intended at room temperature and was able to limit the current at about 120 mA. However, at -23°C, the current limitation failed and the current reached 220 mA, which was only limited by the input voltage. The figure also shows that at lower temperatures, the output voltage follows the input voltage and no more regulation takes place. It is unclear if this is caused by a temperature dependent increase in limit current, or if the current limiting functionality simply ceases to work. On the other hand, the switching functionality of the device worked throughout the investigated temperature range. In conclusion, the device is only fully useable to -20°C and useable as only a switch down to -180°C.

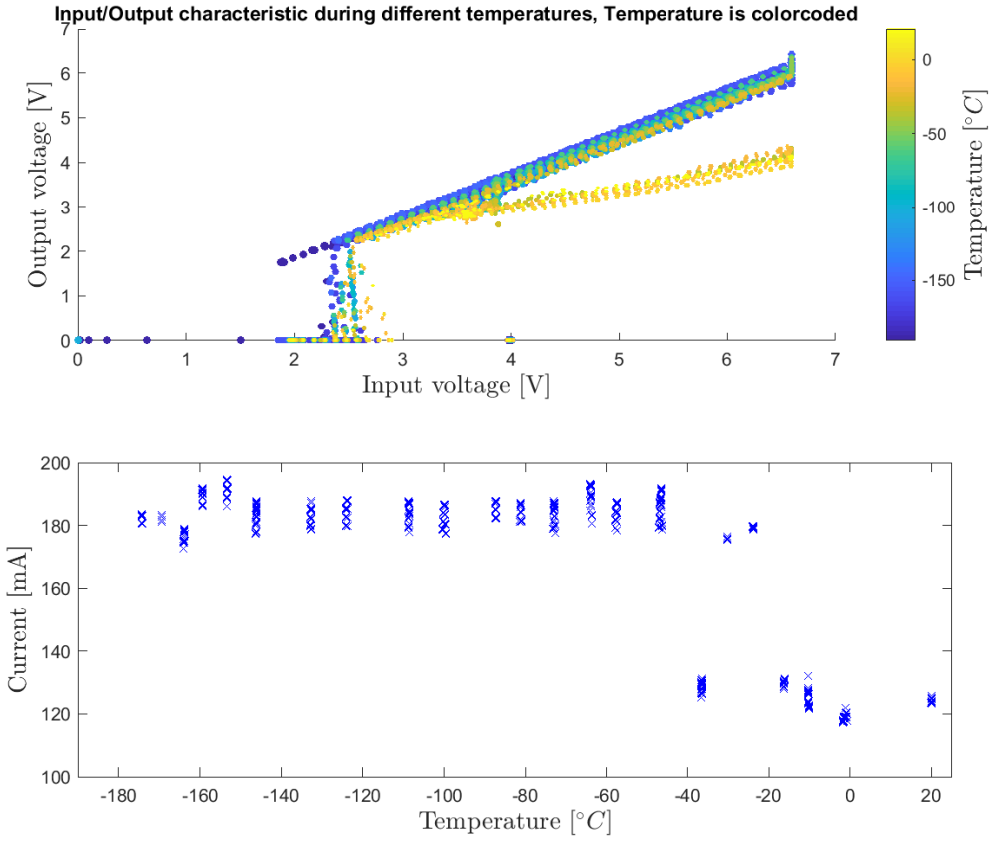

Figure 3-14: Test results for the TPS2553DBVR. Top: Output voltage over input voltage; Bottom: Maximum current over temperature.

Load Switch FPF2701MX

The FPF2701MX is another current limiting switch that can be used to safely turn loads on and off and is used in in the EMPS to limit the input charging current and the current for one of its output channels. A resistor can set the current limit and it provides two feedback pins for the switch status and failure modes. A simple test circuit was designed, that connect the switch to a resistive load and the current can be set by variation of the input voltage. The output current is monitored, allowing to determine the current limit. This is repeated as the devices is cooled down. A schematic of the test circuit is shown in Figure 8-10. Ten devices were tested, Figure 3-15 shows the change of the current limit in regards to its room temperature value. The devices work well until -100°C. At -130°C, only eight out of ten devices worked and at -145°C only six worked. A single device was tested further to observe the functionality of the feedback pins. The results are shown in Table 3-8. The feedback performed as intended down to -99.9°C. At -123°C, PGOOD remained off independent of the output voltage and at -159°C, FLAGB remained continuously on. In conclusion, the device works well to at least -100°C. It may be possible to extend the operation of some of the devices to -120°C, but at the expense of a significant deviation in the current limit and of the functionality of the digital feedback pins.

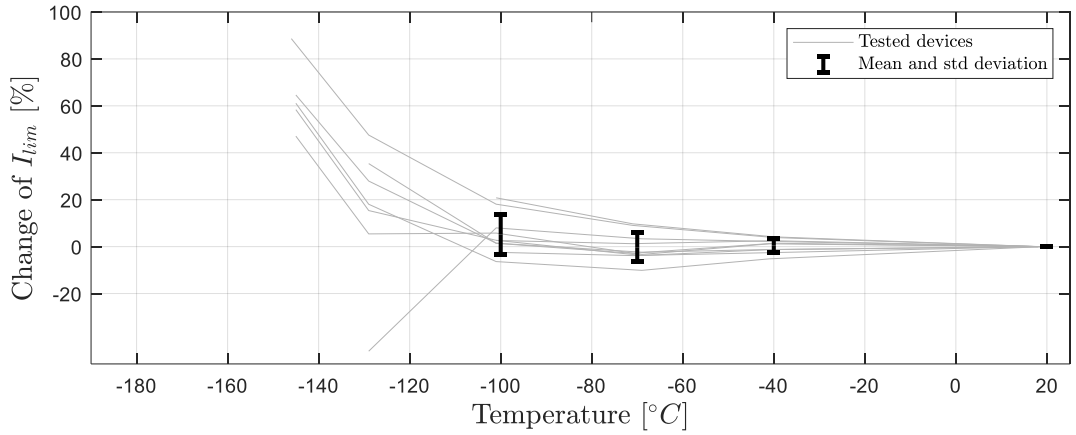

Figure 3-15: Change of limit current in relation to the room temperature value for the FPF2701MX.

Table 3-8: Digital output responses for the Load Switch

Temperature [°C]:	16.5	-41.2	-60.3	-81	-99.9	-123	-140	-159	-178
V_{in}	8.2	8.3	8.4	8.8	9	9.3	7	-	-
V_{out}	8,13	8,23	8,33	8,73	8,93	8,92	5,75	-	-
PGOOD	Ok	Ok	Ok	Ok	Ok	Always off	Always off	Good	Always on
FLAGB	Ok	Ok	Ok	Ok	Ok	Ok	Ok	Always on	Always on

Step-Down Converter LM73606

The LM73606 step-down voltage converter is used to generate a stable 5 V bus voltage for some of the output channels of the EMPS. With a maximum output current of 6 A, it can deliver up to 30 W of continuous power and is therefore intended to supply high power applications. Since the system level tests indicated problems with the 5 V output channels, the device is a suspected weak link in the EMPS. A test circuit was designed with the necessary peripherals that set the output voltage, as shown in Figure 8-11. A single device was tested, the results are shown in Figure 3-16. The device worked as intended down to -70°C, below which the voltage output voltage dropped significantly. It was attempted to raise the output voltage again by raising the input voltage, but this was not successful. The measurement was continued for the warm-up period with consistent results. However, after reheating, the output voltage was 15% higher than the original value, but returned to its original value after resetting the device. In conclusion, the device can only be used to -70°C.

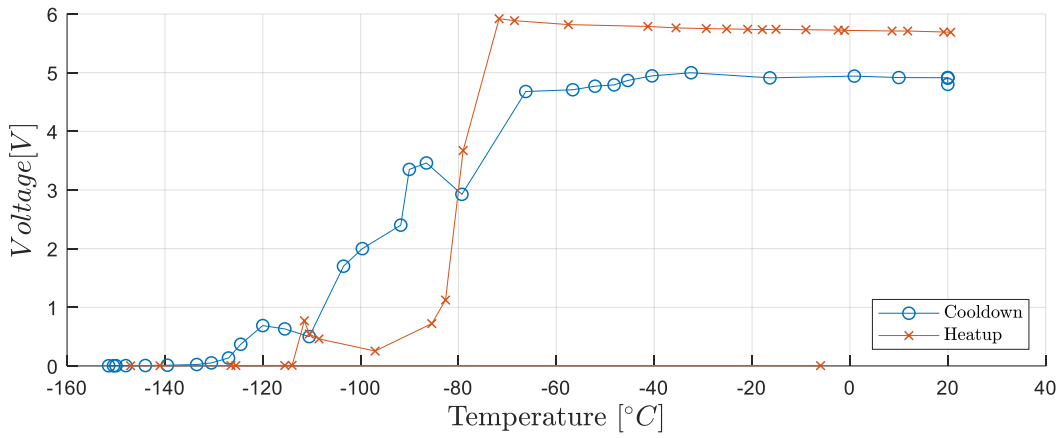

Figure 3-16: Output voltage of the LM73606 step-down converter over temperature

Buck Step-Down Converter TPS62130AQRGTRQ1

The TPS621130 is a buck step-down converter that is used to generate the 3.3 V bus for some of the output channels of the EMPS. It can convert input voltages from 3 to 17 V to an adjustable output range of 0.9 to 6 V and is rated for 3 A. A test setup was designed, as shown in Figure 8-12. In this case the resistors were adjusted to set the device to a 5 V voltage. A single device was tested. While the device was cooled, the input voltage was varied from 0 to 14 V in regular intervals. Figure 3-17 shows the output voltage as a function of input voltage and as a function of temperature. Note that the signal is not stable, as the input voltage was changed quite rapidly, thus the device had to constantly adjust. Nonetheless, the results show that across the investigated temperature range, the device was capable of producing a 5 V output with input voltages >5 V. Therefore the device is considered fully operational down to -180°C.

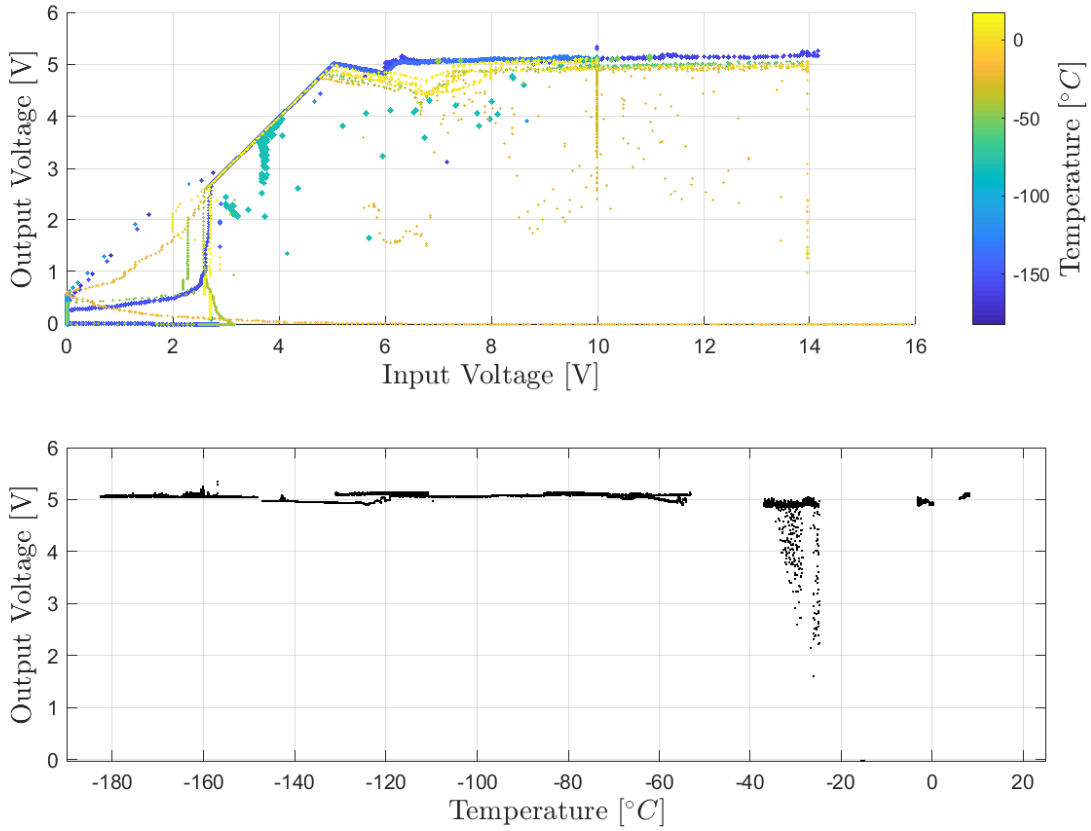

Figure 3-17: Test results for the TPS62130 voltage converter. Top: Output voltage over input voltage; Bottom: Output voltage over temperature for input voltages > 9.5 V.

Buck-Boost Converter TPS63070

The TPS63070 buck-boost converter is used as maximum power point tracker for the solar cells connected to the EMPS. As such it increases the voltage from the cells to the voltage required for battery charging while drawing the optimum amount of power from the cells (see Amann 2019 for more details). It is debatable whether functionality of this devices is necessary at low temperatures, as the solar cells are only available during periods of illumination, but functionality over the full range would be less restrictive in operational terms. For this reason, a test circuit was designed as presented in Figure 8-13. A single device was tested. While the device was cooled, the input voltage was varied from 1 V to 8 V in regular intervals. Figure 3-18 shows the results: The device remained operational down to -180°C. However, the required minimum voltage increased for cold starts. When the voltage was switched off and then the input voltage was increased, the device would start to operate at about 3 V. Once operational, the input voltage could be decreased to about 2.5 V. At cold temperatures, this minimum voltage for the startup increased to about 4 V, even though the minimum required voltage during operation remained constant. Additionally, the average output voltage started to decrease slightly at about -120°C, while it also became less stable, with oscillations (occurring during voltage changes) increasing from 0.25 V to 1.5 V. Note that there are also some high temperature outliers, where the output voltage did not reach the target value. These were likely caused by a loose contact and are of no importance, as they happened within the rated temperature of the device. In conclusion, the device is fully useable to -120°C and useable down to -180°C if the decreased voltage stability and increased minimum startup voltage are acceptable.

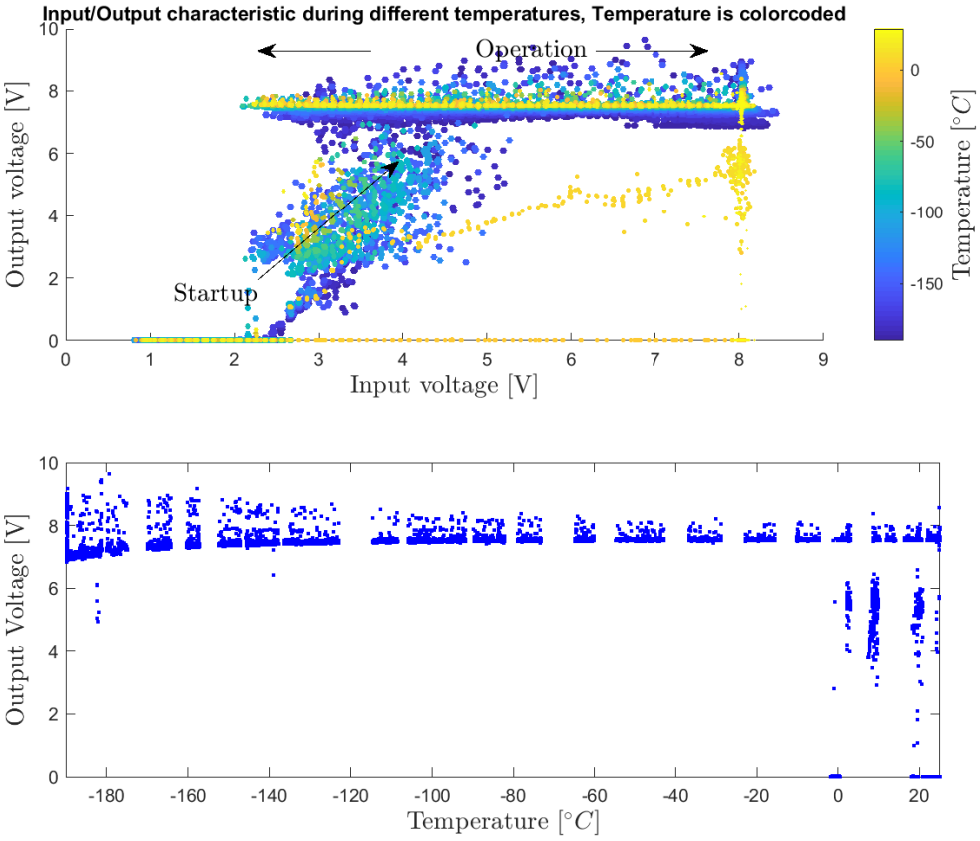

Figure 3-18: Test results for the TPS63070 buck-boost converter. Top: Output voltage over input voltage; Bottom: Output voltage over temperature for input voltages > 5 V.

Analogue Switch TS5A3166-Q1

The TS5A3166 is a simple switch without digital feedback, capable of turning a circuit on or off. A test circuit was designed as shown in Figure 8-14. Ten devices were tested for on-off functionality. A square wave was applied to the trigger pin of the switch and an oscilloscope observed the output signal. At each temperature, the devices were tested at the following frequencies of the square wave: 100 Hz, 1 kHz and 10 kHz. The results are presented in Figure 3-19. Devices were either fully functional at all investigated frequencies or not at all. No significant changes were observable on the oscilloscope. Of the investigated ten devices, one was not functional even at room temperature, indicating that it was damaged prior to testing. Another devices stopped working between -40°C and 20°C. It is not clear what the issue was, but the device could not be recovered. As this happened already within the rated temperature range, it is likely that this failure was not temperature related, but possibly due to a short circuit, e.g. compensating moisture / accumulating frost. A third device stopped working between -40°C and -60°C. After reheating the devices could be recovered and was fully functional. The likeliest explanation for this behavior was a loose contact that got unhinged during the test, rather than an actual failure. Therefore it is concluded that the device is likely fully functional to -180°C.

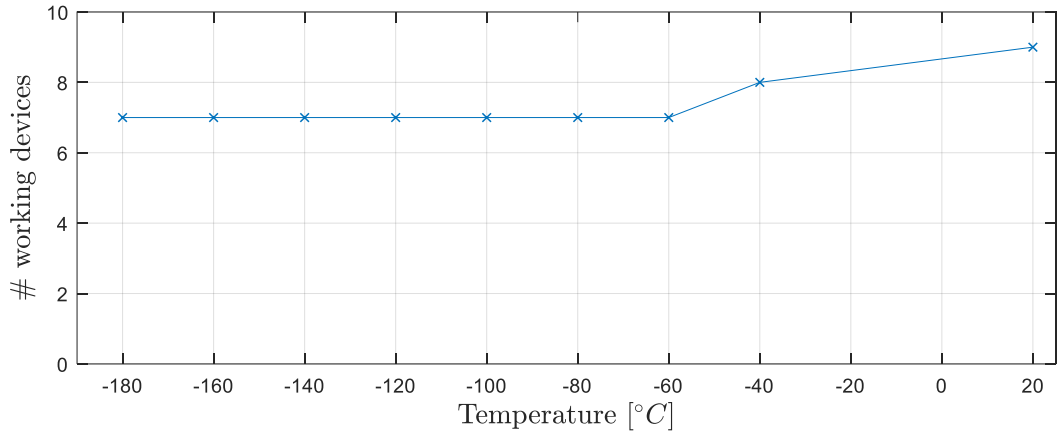

Figure 3-19: Test results for the Analogue Switch TS5A3166-Q1: The line indicates the number of devices that still worked at a given temperature out of a total of 10 devices.

Digital-to-Analogue Converter DAC7512E/2K5

This device is used to generate an analogue voltage signal as control input for the battery charge regulator. It receives a 12 bit digital instruction through its SPI interface and is able generate outputs between 0 and 5.5 V. A test circuit was designed, as shown in Figure 8-15. For the test, the device receives instructions to generate a saw-tooth voltage profile, while the device is cooled down. The output voltage is recorded by oscilloscope. Additionally, the maximum output current is measured for one device. Ten devices were investigated. The results are summarized in Figure 3-20. All devices functioned nominally down to -180°C. The maximum output current increases at lower temperature. It is concluded that the device is fully useable down to -180°C.

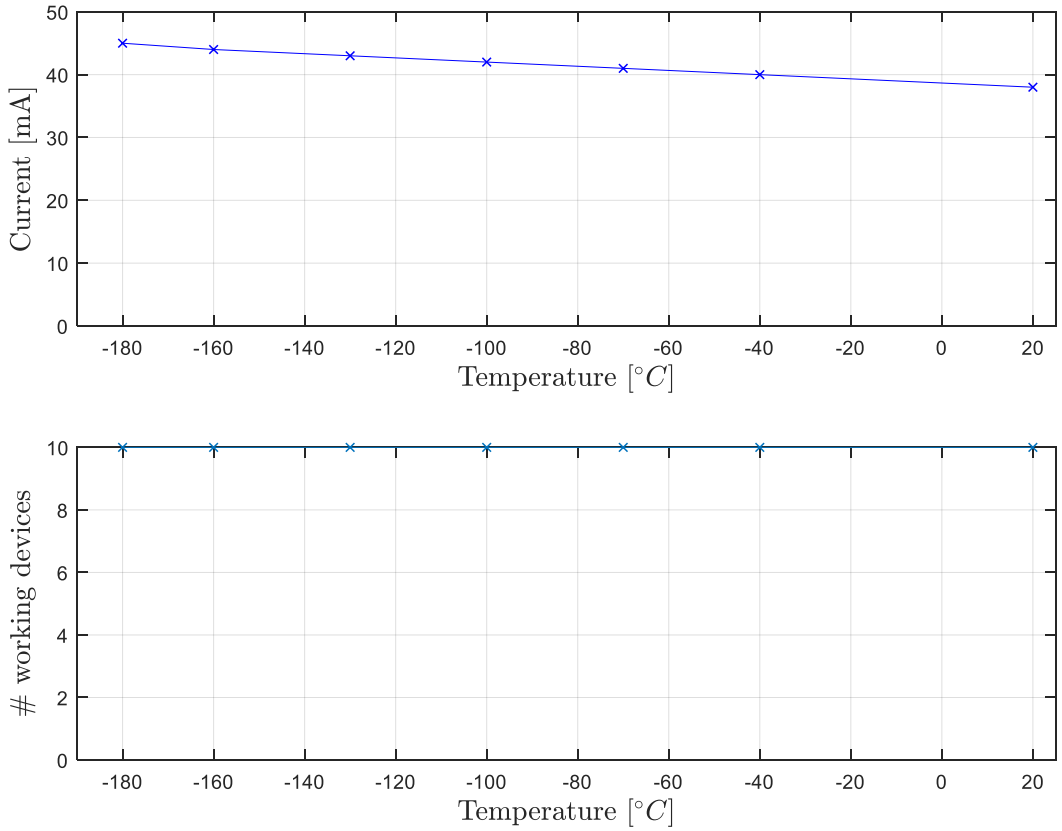

Figure 3-20: Test results for the DAC7512E/2K. Top: Maximum output current over temperature; Bottom: Number of devices operational over temperature.

Buffer Gates SN74LVC126A

This device provides a high impedance decoupling for the UART interface of the EMPS. It provides four simultaneous channels, allowing a single devices to buffer RX, TX, GND and an additional debug channel. For each channel, it provides functionality similar to that of an operational amplifier, accepting inputs up to 5.5 V and providing outputs from 1.65 to 3.6 V. As the four channels are identical, one channel was tested for a single device. During the test, the enable pin was constantly kept on high and a 5 V square wave was applied to the input pin. The voltage on the output pin was measured by an oscilloscope. The devices was able to maintain a stable output voltage over the whole temperature range, as shown in Figure 3-21. It is thus concluded that the devices is operational down to -180°C.

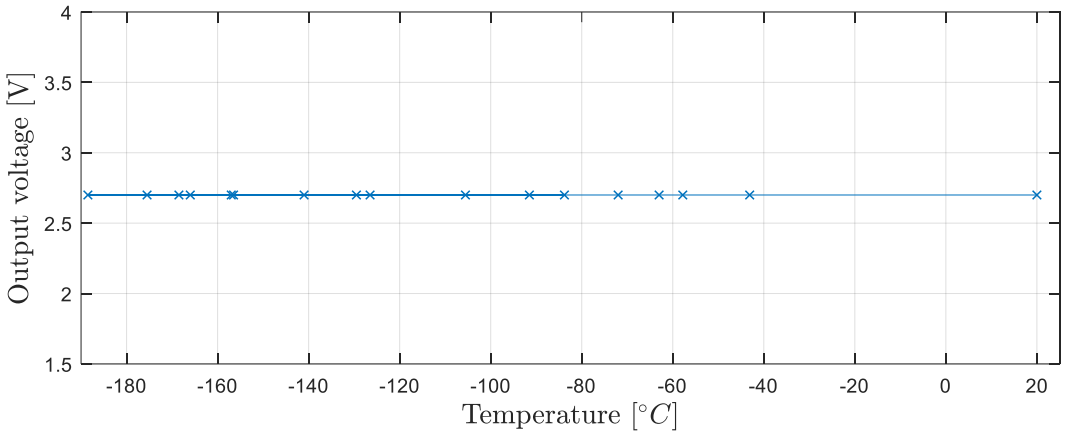

Figure 3-21: Output voltage over temperature for the SN74LVC126A Buffer Gates

Nano-comparator LTC1540

The LTC1540 is a comparator intended to be used in a hardware implementation of the under voltage protection for the EMPS. If the battery voltage falls under a predefined trigger voltage, the comparator disconnects the battery and thus prevents draining of the battery beyond safe levels. The hardware under voltage protection was never implemented and the current system relies only on a software implementation. For the DPP however, a hardware implementation could be beneficial, especially if it would also account for battery temperature, thus the device was included in this investigation. A test circuit was designed, as shown in Figure 8-16. The trigger voltage was set to 2.1 V at room temperature and a saw-tooth signal was applied to the input while the output voltage was observed. A single device was tested for two cycles. The device remained functional throughout the test. However, the trigger voltage changed significantly as Figure 3-22 shows. It remained nearly constant from room temperature to -35°C, where it increases and then drops to a lower level. A further, similar step occurs at -90°C. In conclusion, the device is fully useable only to -35°C, below which the trigger voltage changes noticeably even though the rated lower temperature limit is -40°C. Usage down to -180°C is possible, if the change in trigger voltage is taken into account.

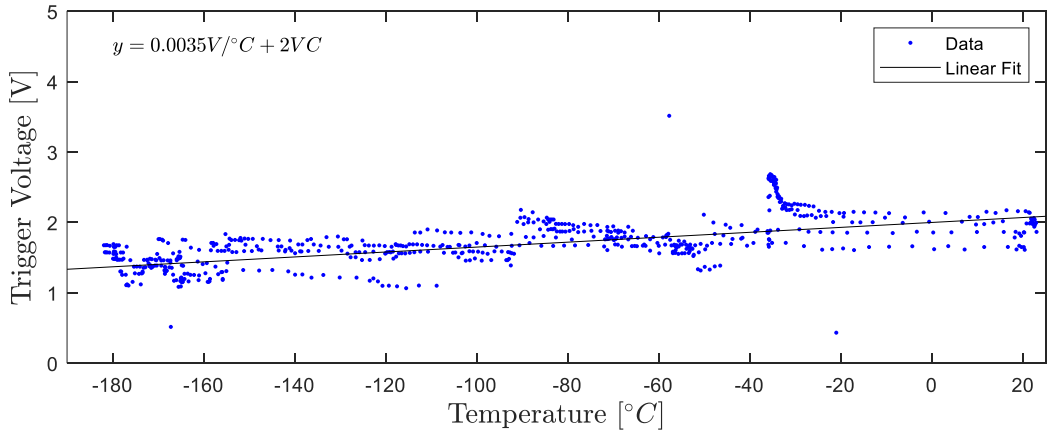

Figure 3-22: Trigger voltage of the LTC1540 over temperature

Current Monitor INA226

The INA226 is a small but precise current monitoring device. It measures the voltage drop over a shunt resistor and can operate on voltages up to 36 V. It is used to monitor the various currents of the EMPS through the battery and output channels. A test circuit was designed, as shown in Figure 8-17. A set of nine devices were tested. A constant current was generated for each device, with a 5 V voltage and two different resistors (1 kΩ and 470 Ω). Nine devices were tested, Figure 3-23 shows the results. The devices remained operational throughout the test. The measured current decreased at lower temperatures and underestimated the actual current on average by 12% at -180%. However this offset was reproducible and consistent for all nine devices and can therefore simply be accounted for by temperature calibration. In conclusion, the device is fully useable down to -180°C.

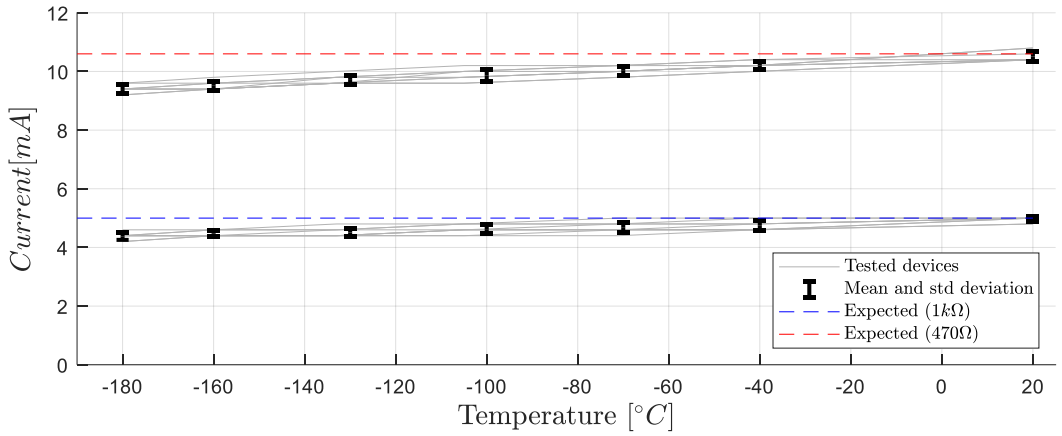

Figure 3-23: Measured current vs. expected current over temperature for the INA226

3.6 S-Band Transceiver

Due to resource constraints, it was not possible to test a real, space ready S-Band transceiver within this study. Such a module would contain a number of high frequency components that are not used in other systems and are likely sensitive to temperature variations. This does however not necessarily mean, that such systems cannot be operated beyond their lower temperature ratings. To demonstrate this, an ESP32-CAM microcontroller with integrated wifi module was subjected to a low temperature test. The MCU has a 32 Mbit flash memory and 520 Kbyte SRAM memory and provides UART communication. It is integrated with an 802.11 b/g/n wifi transceiver that operates at 2412 – 2484 MHz (S-Band) and provides two-way data rates at up to 54 Mbps. It has a maximum transmit power of 17 dBm. The device is rated at -20°C to 85°C (AI-Tinker 2017). It thus provides comparable functionality to the ISISpace S-Band transceiver that is baselined for the DPP, though at significantly lower transmission power. During testing, the device established a wireless connection to an outside reference transceiver (in the form of a common laptop) and was continuously queried through the connection. It was turned off in intervals for 30 s periods to allow the device to cool internally and then restarted. The response times were measured. Figure 3-24 shows the resulting response times over temperature. Overall, meaningful change in response time can be observed until the wireless signal is lost at -94°C. Some high response time outliers are present, but these occurred after restarts of the device. The microcontroller remained responsive through its UART connection down to a temperature of -130°C.

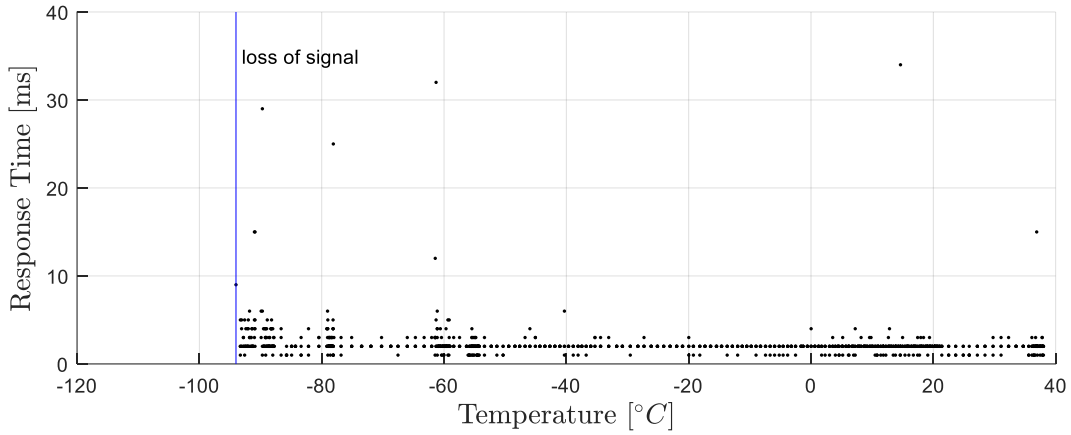

Figure 3-24: Response times for the wifi connection to the ESP32-Cam over temperature.

3.7 Discussion

This chapter addressed the first research objective of this thesis:

Objective 1:	**Determine if and how electronic components relevant to lunar surface exploration can be utilized at temperatures below their ratings.**

To this end, this chapter presented an analysis of the low temperature rerating potential of the electronics of the LUVMI-X DPP electronics. First, the low temperature suitability of some basic components was investigated, as these parts were needed for testing of more complex components. Two types of resistors were selected, based on their promising performance in previous studies: Metal film resistors and thin film resistors (Valiente-Blanco et al. 2013). In accordance with literature, the results from this investigation confirmed the high suitability of this type of resistor. More importantly, the resistor type is available in most common SMD footprints and can therefore be used in most applications without restrictions. In fact, the original EMPS design included the use of metal film resistors. Further test setups that required resistors used either type. Multiple types of capacitors were tested and suitable solutions could be identified: NP0/C0G and PPS capacitors showed excellent stability down to -180°C. Other types may also be used, if deviations in capacitance are acceptable.

A set of four microcontrollers, chosen for their space heritage and low power consumption, were investigated at low temperatures. In addition, the radiation hardened Vorago VA41620 MCU and the common ESP32 MCU were tested. The results are summarized in Figure 3-25. The tests were conducted with the MCUs mounted on development boards that included various peripherals; therefore, the tests may not reflect the actual low temperature limits of the MCUs themselves, but of the development boards as a whole. However, the results present an upper threshold for the minimum operational temperature. The least low temperature capable microcontroller, the ATMega2560 remained operational to -65°C, the best performing one to -126°C. This range essentially presents the rerating potential for the majority of existing electronic subsystems. It proves that most microcontrollers (including peripherals) can be used with very little adaptation at significantly lower temperatures than their ratings suggest. It also shows that the adaptation of electronics for operation beyond -120…-130°C is likely going to be challenging, as the majority of available microcontrollers will not work beyond this temperature. Extension of the operational capability beyond this point will require the use of specialized low temperature microcontrollers. Changes in low level operational parameters, such as logic level voltages may also allow existing microcontrollers to be extended further (e.g. Newell et al. (2001) indicated that lower voltages may counteract increased propagation delays, a common failure mode of logic devices at low temperature), but this equally requires in-depth knowledge of the device and high development effort. No issues were observed with regards to memory, but clock drift is an issue that needs to be accounted for. Either, a more stable external clock is used (e.g. Patterson and Hammoud 2010a) or a calibration and temperature measurement is used to digitally compensate against long-term

clock errors. Various digital interfaces were investigated and proven to work at low temperatures: UART to -120°C; CAN to -180°C, I2C to -125°C and SPI to -180°C. However, problems were identified with synchronisation or bus failure due to a defective device on the bus. In any case, the baseline command & data-handling system for the DPP, based on the PEB1-VA41620 development board remains operational to -109°C.

The components of the EMPS module were investigated in detail. Figure 3-26 shows a summary of the results. Six out of 15 devices operated throughout the entire tested range without restrictions. On the other hand, two devices, the LTC1540 and the TPS2553 already showed noticeable deviations inside of their rated operational limits. And five out of 15 components were not able to operate without issues below -120°C, though only one (the LM73606) failed completely. These results provide a good overview over the effort needed to extend the operational limits of the EMPS. Given that the MSP430 microcontroller remains operational to about -120°C, this seems to be a realistic target. Thus the following five components need to be revisited: LTC1540, TPS2553, LM73606, SFH6156 and FPF2701. The LTC1540 retains functionality down to -180°C, however its trigger voltage changes over temperature, as was shown in Figure 3-22. Therefore, the resistors used to generate the reference voltage need to be chosen such that this shift is accounted for. The TPS2553 loses its ability to accurately limit currents. Either it needs to be replaced (e.g. by the functionally similar FPF2701, the TPS25940 or by adding an inductivity) or the systems must be known well enough to accept a lack of current limiting. The LM73606 does not work at all below -70°C. It can be replaced by the TPS62130 that provides similar functionality, but provides a lesser maximum current. The SFH6256 optocoupler provides a lesser output current at lower temperatures. In the current EMPS design, it only triggers a MOSFET, which requires only minimal current and should therefore work as intended. In other use cases, an additional transistor may be needed to amplify its output. Finally, the FPF2701 loses its accuracy for the limit current at -120°C, but should otherwise remain functional at this temperature. A possible replacement could also be the TPS25940. The implementation of these changes and acceptance of the ensuing limitations enables the EMPS to be operated to a temperature of -120°C.

The presented results confirm the first part of the research hypothesis: **A majority of the investigated electronic components can in fact be utilized at significantly lower temperatures than their manufacturer ratings indicate**. No correlation is apparent between the rated lower temperature limit and the actual lower temperature limit. **This highlights, that manufacturer ratings only are a question of qualification and do not necessarily reflect actual design choices**. However, this study suffers from certain limitations. The most severe is the low sample size, first in the amount of different devices that were investigated, second in the amount of specimen per device type that have been investigated. Only six types of microcontrollers and 15 types of integrated circuits were investigated and of certain devices only a single specimen could be tested.

Another problem is that the test setups and procedures used in this study are incomplete and do not really test the components in all possible configurations and do not monitor all possible behaviours. For example, a switch may have a different, temperature dependent behaviour when it is actuated at high frequencies than at low frequencies. The definition of operational / non-operational is then often difficult and only determined by arbitrary thresholds on the deviation of certain output parameters. These are problems faced by all qualification efforts and not in itself strong arguments against low temperature re-rating. It was attempted to mitigate this problem by the “test as you fly” approach, meaning that the test setups were chosen to reflect the operational state that the components experience in the completed system. In any case, before any future design sees flight application, it will have to undergo a strict qualification campaign and needs to reflect appropriate margins that prevent components to actually reach their operational limits (as discussed in section 2.4).

It should be noted, that side from the employed methodology, low temperature rerating involves certain inherent risks. As mentioned in section 1.3.3, manufacturers do not ensure component quality beyond their ratings and low temperature performance can therefore vary between different production lots due to changes in materials or processes (Ihmig et al. 2015; Buchanan et al. 2012). This can be a significant problem in terms of quality assurance, as parts that have been requalified in the past may become unusable at low temperatures, possibly even without notice from the supplier. For smaller projects, the problem can

be solved by procuring a sufficiently large supply of components from single production lots, to avoid becoming affected by changes in production. However, this may not be feasible for larger projects or series production. Another problem is reduced cycle life due to mismatches in coefficients of thermal expansion (CTE). The majority of electronic components are manufactured from materials with matching CTE, but CTE can change with temperature and thus CTEs of different materials will diverge over large temperature ranges. Thus repeated thermal cycling will induce mechanical stress and possible eventual failure. This issues has been a particular concern for Mars missions (Kirschmann et al. 1999) and proposed solutions include the use of specialized solders and adhesives for sensitive connections. However, this problem is much less pronounced for the currently proposed lunar missions. Mars rovers are built to survive for years, resulting in hundreds or thousands of thermal cycles. The Moon has a much slower day/night cycle and current lunar missions would benefit greatly from the survival of just a handful or even just a single lunar night. Standard aerospace practices will likely suffice to ensure functionality for such a small number of cycles. Furthermore, the general methodology and lot sizes employed in this study are comparable to the previous rerating flight qualification program by Torres et al. (2017) for peripheral components of the Exomars program. Thus, while this study should be understood as an exploratory proof of concept and not as a dedicated qualification campaign, the approach can be extended to full flight qualification if necessary.

In any case, a workable design for a future DPP was identified that allows functionality of its power system at -120°C (manufacturer ratings at -40°C) and its command & data handling system at -110°C (manufacturer ratings at -55°C). No detailed investigation was possible on an actual space grade communications module, but results from testing with the EPS32 module have highlighted that high frequency components are no exception and also provide unused low temperature potential.

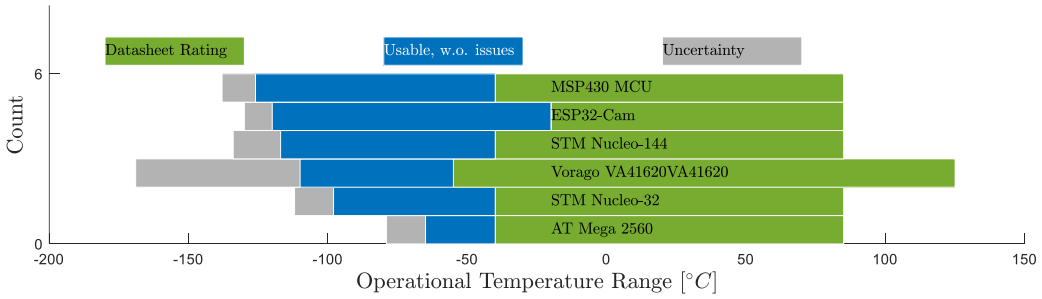

Figure 3-25: Results summary for the investigated microcontrollers.

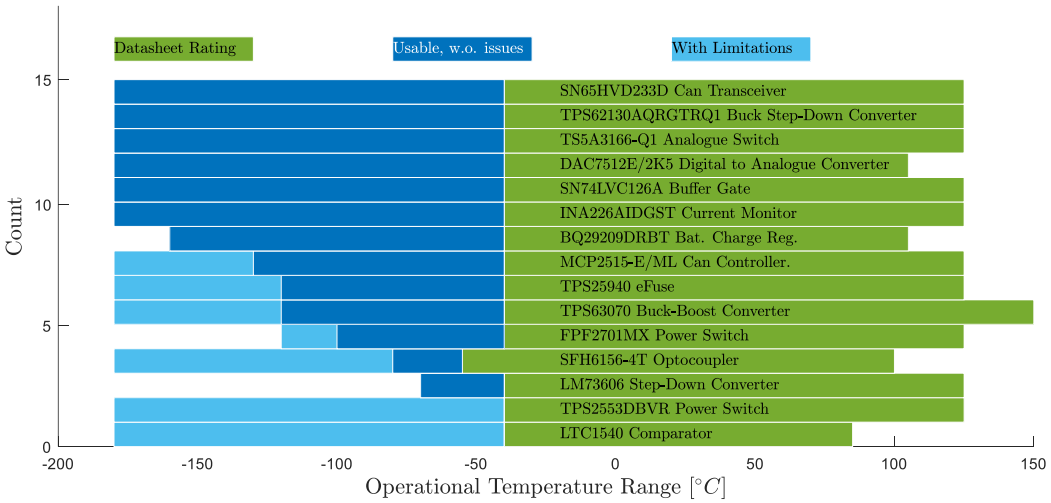

Figure 3-26: Results summary for the investigated EMPS components.

4 Energy Storage

This chapter is a modified excerpt from (Biswas et al. 2021b), written by the author of this thesis

Keeping systems operational during the lunar night requires thermal control to keep internal temperatures within component envelopes. Insulation, such as multi-layer insulation (MLI), low emissivity coatings or aerogel reduce heat loss at night, but heating is required to keep temperatures constant. For this reason, efficient energy storage is crucial to enable nighttime operation. Devices are usually selected based on energy density and temperature range. However, nominal capacity and temperature ranges are only of limited use for the comparison and selection of energy storage devices (Andrea 2020), as battery capacity generally significantly decreases towards lower temperatures, but increases for lower discharge currents (Senyshyn et al. 2015). The extent of these effects is not always reported in datasheets and presented values may not always be comparable. For example, self-heating of batteries is seldom documented, which can lead to higher apparent capacities at higher discharge currents (eg.Saft 2019a). In addition, the presented problem requires very low discharge currents, which are also not usually covered for rechargeable batteries.

Passive hibernation could be another strategy to extend mission operations beyond the first lunar day. In this case, the surface system would be switched off during the night and reawaken once the sun rises again. This would require non-operational survival of cryogenic temperatures. This has already been demonstrated by some lithium batteries (Grandjean et al. 2019; Nandini et al. 2018), but it is unclear if this also applies to other cells.

For these reasons, the present study investigates the suitability of a broad selection of batteries and other energy storage devices. First, a detailed overview of existing technologies is presented. A selection of devices are subjected to low current discharge testing over a wide temperature range. Temperature dependent capacity data is then used to calculate theoretical self-heated survival times to compare their performance. In addition, the selected batteries are tested for their ability to survive passive exposure to cryogenic temperatures.

4.1 Overview of Existing Technologies

4.1.1 Rechargeable Batteries

The majority of space systems rely on rechargeable batteries to buffer variations in power demand and gaps in supply, with lithium ion batteries as the most popular choice nowadays, due to their high energy density and high cycle life (De-Leon 2017). A wide range of subtypes exist, with different chemistries for anode, cathode and electrolyte. The most important properties relevant to lunar application are energy density, low temperature performance, high temperature tolerance and non-operational tolerance of cryogenic temperatures.

Current state of the art high energy density cells use lithium nickel cobalt aluminum oxide (NCA) as cathode and graphite or hard carbon as anode and practical energy densities reach 260 Wh/kg with typical operational temperature ranges between -20°C and +60°C. Various cell types have been developed that achieve lower operational temperatures by use of specialized electrolytes. Of particular note in this context are a series of batteries that have been developed by NASA and Yardney/EaglePicher for planetary exploration (Smart et al. 1999b; Smart et al. 1999a; Smart et al. 2004; Smart et al. 2008). Their latest generation cells employ an ester-based electrolyte and are reported to allow low rate discharge down to -65°C (Smart et al. 2017). Similar specialty cells are also exist from other manufacturers (e.g. (Saft 2014)), but these cells are not sold on the open market. Common low temperature cells available on the open market typically only operate down to -40°C (Saft 2019a; BostonPower 2011). In addition, while the use of low temperature electrolytes does not adversely affect specific energy, most low temperature cells feature lesser

energy density than common high energy density cells, due to bulky packaging or less frequent technology updates. Another interesting technology for low temperature applications is the use of lithium titanate oxide (LTO) as anode material. Among high power, service life and safety (Korthauer 2013), LTO batteries also exhibit good low temperature performance (Buchmann 2016). However, due to their lower voltage, LTO batteries usually have significantly lower energy densities than comparable cells with carbon-based anodes.

In the near future, further evolutions of lithium batteries promise even higher energy densities. Future anodes will likely use lithium metal, which could increase practical energy densities up to 500 Wh/kg (Liu et al. 2019). Further promising research goes in the direction of using sulfur as cathode material, potentially enabling energy densities up to 600 Wh/kg in the long run (Ould Ely et al. 2018). Early commercial cells for these technologies exist already (Oxisenergy 2019; SolidEnergy Systems 2019) and specialty lithium sulfur cells have already been developed for low temperature (Cai et al. 2020). However, problems remains in terms of cycle life, temperature stability and safety, making them currently unsuitable for space applications.

4.1.2 Primary Batteries

As with rechargeable batteries, the most promising primary batteries in terms of energy density are lithium based. In general, the energy densities of primary batteries are significantly higher and applicable temperature ranges are significantly wider than those of rechargeable batteries.

With respect to space exploration, the current state of the art technology are lithium thionyl chloride cells. This type can feature energy densities of up to 700 Wh/kg and are certified down to -60°C, though the highest energy densities are only available for bobbin type cells which provide only low discharge rates. Energy densities of higher current cells reach only about 450 Wh/kg. Due to its favorable properties, this cell type has already been used on some of the most challenging space exploration projects, such as the Rosetta/Philae comet lander (Cénac-Morthé et al. 2016). Lithium carbonmonoflouride cells can theoretically achieve even higher energy densities and they are seen as an attractive option for future space exploration missions, but practical designs are currently also limited to 700 Wh/kg. Finally, lithium iron disulfide cells feature a slightly lower energy density of only up to 350 Wh/kg, but feature good low temperature performance (Krause et al. 2018).

The obvious drawback of primary batteries is that they cannot be recharged and will therefore become useless once discharged. However, they could nonetheless be an attractive option to ensure operation for at least one lunar night.

4.1.3 Phase Change Materials (PCMs)

PCMs offer a passive alternative to active electrical heating. Storing energy in form of latent heat, PCMs can release energy upon temperature drop or retain heat in rising temperatures at a specific phase change temperature or temperature interval. A wide variety of compounds and mixtures for PCMs exist, but the most common types include inorganic salt hydrates, organic compounds such as paraffins, alcohols or organic acids and eutectics of organic materials, with paraffins most commonly used in space systems to date (Rochus et al. 2011). Although PCM application is inexpensive, relatively simple and can be built in a compact fashion, latent heat densities are significantly lower than energy densities for common batteries.

4.1.4 Capacitors

While capacitors generally have much lower energy densities than batteries, they can be used in hybrid systems as a buffer for battery driven systems, especially as they are usually less sensitive to low temperatures than batteries. The potential of using such hybrid battery/capacitor power systems has already been investigated in detail to improve either high power output (Shimizu and Underwood 2013) or low temperature performance (Chin et al. 2014b). High energy density capacitors (supercapacitors) can be distinguished into double-layer capacitors and hybrid capacitors. While the former are purely electrostatic and restricted to energy densities below 30 Wh/kg (Kurzweil and Dietlmeier 2015), the latter additionally use an electrochemical pseudocapacitance that provides them with some battery like characteristics and energy densities that can approach those of conventional lithium ion batteries (Altreonic NV 2019). In addition to

comparable energy densities, hybrid capacitors have a more favorable low temperature behavior, making them an interesting alternative to conventional batteries for the presented application.

4.1.5 Fuel Cells

Fuel cells provide an exciting alternative to battery storage. In its most basic form, a fuel cell will convert hydrogen and oxygen into water, electrical and thermal energy, yielding a total energy of $\Delta G^0 = 237.19 \frac{kJ}{mol_{H_2}}$.

Multiple fuel cell designs exist, but the only viable type option for miniature systems are polymer electrolyte membrane fuel cells (PEMFC) as they can be used at moderate temperatures and the low thickness of membrane electrode assemblies allow PEMFCs to be made relatively compact. For this reason, PEMFCs have been proposed and investigated as possible power sources for small devices, such as portable consumer electronics (Kundu and Dutta 2016) or unmanned aerial vehicles (Swider-Lyons et al. 01072013). Typical electrical efficiencies are 40-50%, though the additional dissipated heat would also be helpful for lunar night application (O'Hayre et al. 2016).

The achievable effective energy densities of fuel cell systems depend largely on the form of propellant storage. In general, a kilogram of hydrogen and oxygen in stoichiometric relation contain 13.17 MJ, which is equal to 3660 Wh of energy. Note that this is significantly lower than the theoretical energy density of 32.4 kWh/kg that hydrogen yields on the earth's surface, where oxygen is available from the environment. Hydrogen and oxygen may be stored as pressurized gases, as cryogenic liquids or chemically released from other compounds. Other potential fuels, such as methanol can be stored as liquids at room temperature.

Both hydrogen and oxygen can be stored as cryogenic liquids, which increases storage density and reduces pressures and therefore necessary wall strengths of the tanks. In the Space Shuttle, hydrogen was stored in the 614 l PRSA H_2 tank at a pressure of 15 bar at a temperature of 24 K and oxygen was stored at an overcritical state in the 320 l PRSA O2 tank at a pressure of 58 bar at a temperature of a 111 K. The tank dry masses were 103.2 kg for the PRSA H_2 and 97.7 kg for the PRSA O2, storing a maximum of 42 kg H_2 and 335 kg O2 (Marquardt et al. 2015). Taking the tank masses into account, this yields a theoretical energy density of 2387 Wh/kg and assuming 40 - 50% efficiency for a PEMFC, an electric energy density of 955-1194 Wh/kg. A few smaller scale LH_2 tanks have been developed for UAV applications (Swider-Lyons et al. 01072013)(Garceau et al. 2015), but no small, light-weight LO2 tanks are known to the authors. However, it is safe to say, that effective energy densities at very small scales are likely to be significantly worse. In addition, it will be virtually impossible to sufficiently insulate a small tank to prevent significant outgassing from integration before launch until deployment on the surface.

Hydrogen may also be stored in pressurized gas cylinders. This has been demonstrated on small scales for Unmanned Aerial Vehicles (UAVs) (Dutczak 2013). An excellent overview of available small sized gas cylinders for hydrogen storage from nine different manufacturers is given by (IntelligentEnergy 2019). Available models use either aluminum or polymer liner, encased in a carbon fiber wrap for additional strength and can withstand pressures up to 379 bar.

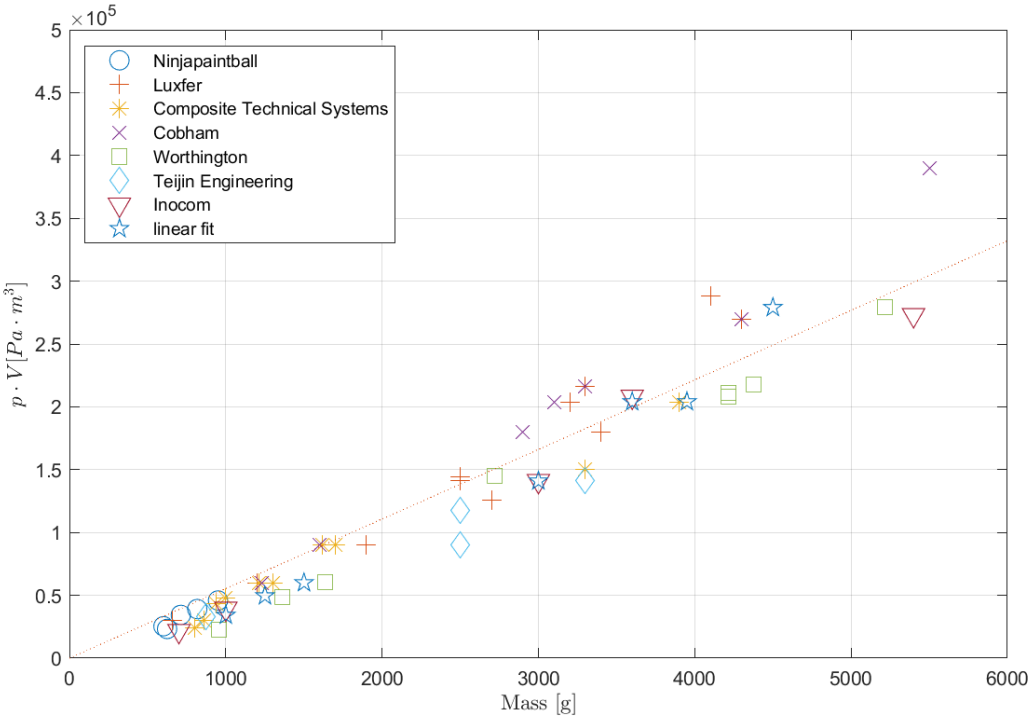

Figure 4-1: Gas content over mass of selected hydrogen cylinders from various manufacturers; Data from (IntelligentEnergy 2019)

Figure 4-1 shows the maximum gas content ($p \cdot V$, with the pressure p and volume V) of these cylinders over their respective wet masses. The data shows a mostly linear relationship of gas content over mass. A linear fit yields the following relationship for the gas constant as a function of cylinder dry mass m_0:

$$p\,V = \; c \cdot m_0$$

With the constant $c = \; 55.356 \frac{Pa \cdot m^3}{kg}$. The fit slightly overestimates the gas content at lower masses and can therefore be considered as optimistic. Using the ideal gas law, the number of gas molecules stored per mass of the gas container can be determined. In addition to the dry mass of the cylinder, the mass of the stored gas is added, providing the molar density:

$$\rho_{molar} = \frac{n}{m_0 + m_{gas}} = \frac{pV}{\frac{R_0 T}{M}\,(m_0 + m_{gas})} = \frac{1}{R_0 T\,\left(\frac{1}{c} + \frac{M}{R_0 T}\right)} \approx const$$

With the mass of the gas m_{gas}, the universal gas constant R_0 and the molecular mass M. For a temperature of $T = 300\,K$, this relationship yields a molar density (including tank mass) of $\rho_{molar,H2} = 21{,}2 \frac{mol}{kg}$ for hydrogen and $\rho_{molar,O2} = 13.0 \frac{mol}{kg}$ for oxygen. A combined oxygen and hydrogen storage system will therefore yield a theoretical energy density: $1825\,Wh/kg$ (excluding fuel cell and gas handling systems), which yields an electrical energy density of $730 - 912{,}5\,Wh/kg$, assuming 40-50% efficiency of a PEMFC. This energy density is lower than the values for cryogenic storage, but will not be as problematic for long-term storage.

Both hydrogen and oxygen may also be stored chemically bound in other compounds and then released on demand. This circumvents the problems of cryogenic or pressurized gas storage and allows compact designs, but naturally adds additional dead mass in the form of the carrier compounds. Consumer products exist that generate hydrogen by a chemical reaction of sodium borohydride and water (myFC 2013; Horizon 2013), with terrestrial (without oxygen storage) energy densities of 108-133 Wh/kg. Similar systems have

been proposed for UAVs with reported terrestrial energy densities up to 739.1 Wh/kg (Kwon et al. 2019; Kim 2014). On the oxygen side, numerous systems exist to provide emergency oxygen for airplanes, submarines, mining or medical applications, based on various chemicals. Depending on the used chemical, theoretical oxygen yield is between 39 wt% and 60 wt%. An overview of utilized chemicals and their performance is given by (Graf 2017). Actual systems have a significantly lower yield, since they include casing, ignition system and additional additives that ensure reaction stability. For example, UK based company Molecular Products offer a chemical oxygen generator that can produce 3000 l (at 1 atm) of oxygen with a mass of 15 kg (Molecular Products 2018) or OC Lugo Co. offers their model 3300 oxygen candle that can produce 3341 l (1 atm) of oxygen with a mass of 12.7 kg (Spruell 2019). This corresponds to a gas density of about $2 \cdot 10^4 Pa \cdot m^3/kg$ or about $0.11 kg/mol_{O2}$, which is actually less than most pressurized gas containers achieve. In addition, it may be problematic to reduce the oxygen production rate to a suitable level for continuous operation for 2 weeks and oxygen release temperatures range between 270°C to 520°C, depending on the mixture of the compound (Jin et al. 2015). In summary, a chemical hydrogen/oxygen storage system for vacuum operation, based on sodium chlorate and sodium borohydride will likely require a storage mass of at least $0.3\ kg/mol_{H2O}$, which corresponds to $110\ Wh/kg$ of useable electric energy. The potential thermal energy is $241\ Wh/kg$, if the exothermic reaction of the sodium chlorate is taken into account.

Finally, there are a range of fuel cells that accept other fuels, such as methanol in the direct methanol fuel cell (DMFC), which results in lower efficiencies, but can be stored in liquid form at terrestrial conditions (O'Hayre et al. 2016). However, in space these systems lose their advantage, as oxygen needs to be provided separately, which will require one of the previously discussed storage systems.

In conclusion, pressurized gas storage offers the most viable option for a potential small lunar fuel cell system. Achievable electrical energy densities for gas storage alone are not significantly higher than those of primary lithium batteries, but additional thermal energy from heat dissipation can be helpful during the lunar night. Additional mass for the fuel cell itself and periphery such as piping, valves and control systems need to be taken into account. Terrestrial fuel cell energy systems for UAVs (600 – 3000 W) have a mass of at least 0.5 W/g per power for the fuel cell stack, fluid system, buffer battery and other peripherals (e.g. (IntelligentEnergy 2020; DOOSAN 2021)), though mass per power ratios of space grade systems will likely be larger, especially for smaller systems.

No suitable fuel cell solution for lunar surface application exists today, therefore fuel cells were excluded from the remainder of this study. However, some interesting systems are in development, especially in terms of regenerative fuel cells which could become available in the near future (Guzik et al. 2018; Wærnhus et al. 2017).

4.1.6 Radioisotope Heater Units (RHUs) / Radioisotope Thermal Generators (RTGs)

Radioisotopes as an energy source for space exploration have been investigated since the 1959 and were first used in a successful mission in 1961 with the launch of the Transit 4a spacecraft. Since then, a wide range of RHU/RTG powered missions have followed, including all of the notable deep space missions like Pioneer, Voyager, Cassini and New Horizons. Radioisotope decay is reliable, independent of external circumstances, and therefore ideally suited for space exploration missions. The majority of existing systems utilize the plutonium isotope Pu-238. It predominantly emits alpha radiation, has a half-life period of 87.7 years and a specific power of 0.57 W/g. Over its full lifetime, this equates to an astonishing energy density of 0.63 MWh/g (Summerer and Stephenson 2011). However, actual RHUs contain radioisotopes bound in carrier compounds and require significant shielding, which reduce actual power densities. Furthermore, due to the large half-life period compared to mission duration, power density and not energy density presents the main design driver. The biggest restriction of RHU usage however is availability, as only a few nations so far have developed flight ready systems and application is highly restrictive and therefore costly (Petro 2020). Currently, only the United States, Russia and China have access to this technology. ESA has been pushing its “Radioisotope Power System Program” (RPS) in recent years with the aim of establishing a domestic RHU / RTG capability. The program is based on the Am-241 isotope, which was selected for its superior availability and cost-effectiveness in the European context. A 3 W (thermal power) RHU pellet and derived

10 W electrical power RTG is in development by the University of Leicester and a 100 W RTG based on a Stirling engine is in development by Thales Alenia Space UK (Barco et al. 2019).

An overview of existing or future RHU and RTG systems is provided in Table 4-1 and Table 4-2. Accessibility aside, RHUs are generally available in sizes relevant to small lunar surface systems, with the American Light-Weight Radioisotope Heater Unit presenting the most suitable option at a mass of 40 g. A meaningful comparison to battery technology can be made based on its energy output over the course of a lunar night. Over the course of the lunar night (354.4 h), the 1 W heat output releases 354.4 W/h of thermal energy. This therefore corresponds to a (thermal) energy density of 8860 Wh/kg. On the RTG side, only the Russian "Angel RTG" concept is suitable for small lunar surface systems with a planned mass of 0.5 kg. Though with a 0.2 W power output, its electrical energy output over the course of one lunar night is only 142 Wh/kg, thus comparable to lithium ion batteries. Larger RTGs have higher power densities, but are only suited for larger surface systems.

Table 4-1: Overview of current and future RHU systems

Name	Origin	Status	Mass	Heat Output	Specific Heat	Specific Energy release over lunar night	Source
General Purpose Heat Source	USA	Flight heritage	1.5 kg	250 W	166 W/kg	590667 Wh/kg	(NASA 2022a)
Light-Weight Radioisotope Heater Unit	USA	Flight heritage	40 g	1 W	25 W/kg	8860 Wh/kg	(NASA 2022b)
European RHU (in development)	ESA / UK	In development	200 g	3 W	14.7 W/kg	5316 Wh/kg	(Barco et al. 2019)
Moon-night survival device	China	Flight Heritage	390 g	4 W	10.2 W/kg	3635 Wh/kg	(Chen Deng-yi et al. 2016)
Angel	Russia	In development	85 g	8.5 W	100 W/kg	35440 Wh/kg	(Summerer 2006)

Table 4-2: Overview of current and future RTG systems

Name	Origin	Status	Mass	Power	Specific Power	Specific Energy release over lunar night	Source
Joint European Russian RTG	ESA / Russia	Cancelled	20.9 kg	110.4 W	5.2 W/kg	1872 Wh/kg	(Summerer and Stephenson 2011)
European RPS	ESA / UK	In development	10 kg	11 W	1.1 W/kg	389 Wh/kg	(Barco et al. 2019)
MMRTG	USA	Flight heritage	39 kg	110 W	2.8 W/kg	999 Wh/kg	(NASA 2020)
Next-Gen RTG	USA	Concept	44 – 62 kg	150 – 500 W	3.4 – 8 W/kg	-	(Matthes et al. 2018)
Angel RTG	Russia	Concept	0.5 kg	0.2 W	0.4 W/kg	142 Wh/kg	(Pustovalov 2007)
Chang'e ¾ RTG	China	Flight Heritage	Unkown	Unknown	Unknown	-	-

4.1.7 Summary

Figure 4-2 shows an overview of the effective energy densities of the discussed technologies. In terms of energy density, radioisotope heaters and derived thermal generators provide the best option, although the power density and thus the energy that is actually delivered over the night period and not the true energy content mainly limit the effective energy density for lunar night survival. Nonetheless, radioisotope heaters (including cladding) still provide effective energy densities one or two orders of magnitude higher than competing technologies. However, this does not change the fact that this technology is unavailable for most currently planned missions. Pressurized Hydrogen / Oxygen and high pressure regenerative fuel cells could provide an attractive option in the near future, especially if waste heat can be utilized to facilitate lunar night survival. However, achievable energy densities of complete systems (including valves, fuel cells, etc) will likely be only slightly better than high end rechargeable batteries and will only be viable for large systems. This leaves lithium based battery technology as the most viable option for current missions. For short term missions that only aim to operate through a single lunar night, primary lithium batteries appear to be the most viable option, as nominal gravimetric energy densities are significantly higher than for rechargeable lithium ion cells. Next generation rechargeable lithium metal cells will also significantly advance achievable energy densities, but at this time, cells remain at a prototype level and will likely face stability issues with high temperatures during the lunar daytime. Hybrid capacitors present an interesting alternative to common lithium ion batteries, as they promise comparable energy densities but possibly improved low temperature performance. The graphic clearly shows that phase change materials are a poor choice when it comes to lunar night survival, as the provided energy density is significantly lower than for lithium ion batteries. Finally, supercapacitors are outperformed by all other presented options, but may present superior low temperature performance.

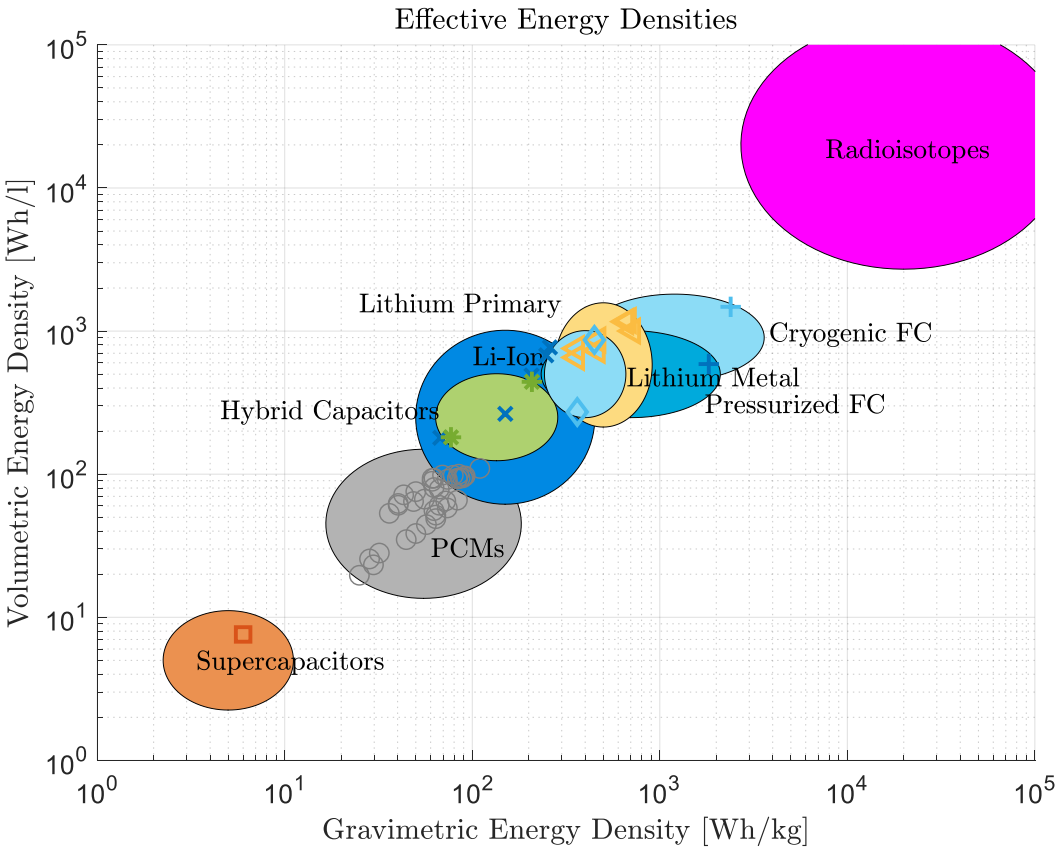

Figure 4-2: Effective energy densities in terms of lunar night survival for various energy storage technologies

4.2 Experimental Investigation

4.2.1 Experimental Setup

Table 4-3 shows a list of the energy storage systems that have been selected for further investigation. Two common high energy density lithium ion batteries, the Panasonic NCR18650BF and the LG Chem INR18650 have been chosen. The BP Swing 5300, the SAFT MP174565 xtd and the LTO TK 18650 NT35 represent common low temperature lithium ion batteries. A Maxwell BCAP3000 double layer capacitor and two HybridC Shenzen Toomen hybrid electrochemical capacitors are included, also for their low temperature performance.

Each cell type was tested for their temperature dependent discharge capacity and for their ability to survive exposure to cryogenic temperatures. Discharge capacity testing was conducted in a thermal-vacuum chamber, allowing for temperature cycling between -70°C and +100°C and at moderate vacuum ($<10^{-3}$ mbar). An Arbin MSTAT 4.3 was used for recharging, discharge capacity measurements and internal resistance measurements. Each cell was first subjected to a pre-conditioning test at ambient conditions (Mulder et al.), which consists of constant current constant voltage (CCCV) charging according to datasheet values, followed by a 30 min idling period and a constant current (CC) discharge with nominal discharge currents. This was repeated for at least 3 cycles and until cell capacity changed less than 2% between cycles, which ensures the cell is stable. For the temperature dependent discharge capacity test, the cells were mounted onto an aluminum experiment holder, which acted as a heat sink during the experiment to reduce self-heating (see Figure 4-3). The experiment holder was then mounted inside the thermal-vacuum chamber, which was evacuated. The cells were charged at 25°C, with a CCCV charge according to datasheet values, then the thermal shroud brought the cells to the target temperature. Once the temperature was constant, a CC discharge at a rate of 1/10C (nominal capacity over 10h) was conducted until the lower voltage limit was reached. Lower discharge currents would be more representative, but this was not possible due to time constraints. Test temperatures for each cell were T = [25°C, 10°C, 0°C, -10°C, -20°C, -30°C, -40°C, -50°C, -60°C, 40°C]. After reheating to 25°C and prior to recharging, another CC discharge was performed, since the cells did not fully discharge at the lowest temperatures.

For the cryogenic survival test, the cells were charged and discharged at ambient conditions with the same procedure as for the preconditioning test, but between each cycle, the cells were indirectly exposed to liquid nitrogen at a discharged state, until cell temperatures below -180°C were reached and subsequently reheated to ambient temperature. Each cell was tested for five cycles, discharge capacity was monitored and each cell was visually inspected after each cooling.

Finally, seven types of primary lithium batteries were also included in the study. Four lithium thionyl chloride were selected: The Tadiran TLH-5930 and Saft LS33600 because of their very high energy densities and the Tadiran SL-560 and Saft LSH20 since they offer a good compromise of energy density and power density. Detailed current and temperature dependent capacity data is available from datasheets, therefore no experiments were performed on these cells as part of the study. Capacity data for discharge rates of 1/300 C were taken from these datasheets at 4 different temperatures. Furthermore, two lithium carbon monoflouride cell types (Rayovac LiCFx Developmental D and EaglePicher LCF-133) and one lithium iron sulfide (Energizer L91) cell type were included. Capacity data for these cells were taken from (Krause et al. 2018) for three temperatures and at discharge currents of 0.013 C and 0.016 C, as these were the most comparable available data points.

Table 4-3: Investigated energy storage options

Energy Storage Device	Designator	Type	Gravimetric Energy Density (nominal) [Wh/kg]	Volumetric Energy Density (nominal) [Wh/l]	Temperature range (discharge, nominal)	Space heritage
Rechargeable Batteries / Capacitors						
Boston Power Swing 5300 (BostonPower 2011)	BP S5300	Li-Ion	207	490	-40…+70°C	Yes (Yayathi et al. 2016)
Panasonic NCR18650BF (Panasonic)	Pan 18650	Li-Ion	248	677	-20…+60°C	Yes (Darcy 2012)
LG Chem INR18650MJ1 (LG Chem 2014)	LG 18650	Li-ion	259.6	769	-20…+60°C	Yes (Darcy 2012)
Saft MP 174565 xtd (Saft 2019a)	Saft xtd	Li-ion	150	264	-40…+85°C	Yes
LTO TK 18650 NT35 (LTO)	LTO 18650	Li-ion (Lithium Titanate)	67.5	180	-30…+55°C	-
Shenzen Toomen NE HybricC TMDD1.3/18650 (Altreonic NV 2019)	HyC 18650	Electrochemical Double Layer Capacitor	77	181	-40…+80°C	-
Shenzen Toomen NE HybricC TMDD4.0/23680 (Altreonic NV 2019)	HyC 23680	Electrochemical Double Layer Capacitor	208	442	-40…+80°C	-
Maxwell BCAP3000 (Maxwell 2013)	Max 3000	Double Layer Capacitor	6	8	-40…+65°C	Yes (Chin et al. 2014a)
Primary Batteries						
Saft LS 33600 (Saft 2019b)	Saft 33600	Lithium Primary (Li-$SOCl_2$)	680	1185	-60…+85°C	-
Saft LSH 20 (Saft 2006)	Saft LSH	Lithium Primary (Li-$SOCl_2$)	468	867	-60…+85°C	Yes (Cénac-Morthé et al. 2016)
Tadiran SL-560 (Tadiran 2019)	Tad SL560	Lithium Primary (Li-$SOCl_2$)	360	756	-55…+130°C	-
Tadiran TLH-5930 (Tadiran 2006)	Tad TLH	Lithium Primary (Li-$SOCl_2$)	658	1163	-55…+130°C	-
Energizer L91 (Energizer)	Energizer FeS2	Lithium Primary (Li-FeS_2)	350	654	-40…+60°C	-
Rayovac LiCFx Developmental D (Rayovac 2016)	Rayovac CFx	Lithium Primary (Li-CFx)	716	1001	-20…+90°C	-
EaglePicher LCF-133	EP CFx	Lithium Primary (Li-CFx)	464	734	-40…+60°C	-

Energy Storage Device	Designator	Type	Gravimetric Energy Density (nominal) [Wh/kg]	Volumetric Energy Density (nominal) [Wh/l]	Temperature range (discharge, nominal)	Space heritage
Phase Change Materials						
PCM PlusIce Hydrated Salts (S) Range (PCM Products 2019b)	PCM HS	Phase Change Material	36-61	53-94	+8…+89°C	-
PCM PlusIce Organic Salts (A) Range (PCM Products 2019c)	PCM OS	Phase Change Material	44-83	35-66	+2…+95°C	-
PCM PlusIce Eutectic (E) Range (PCM Products 2019a)	PCM ES	Phase Change Material	25-109	70-395	-114…0°C	-

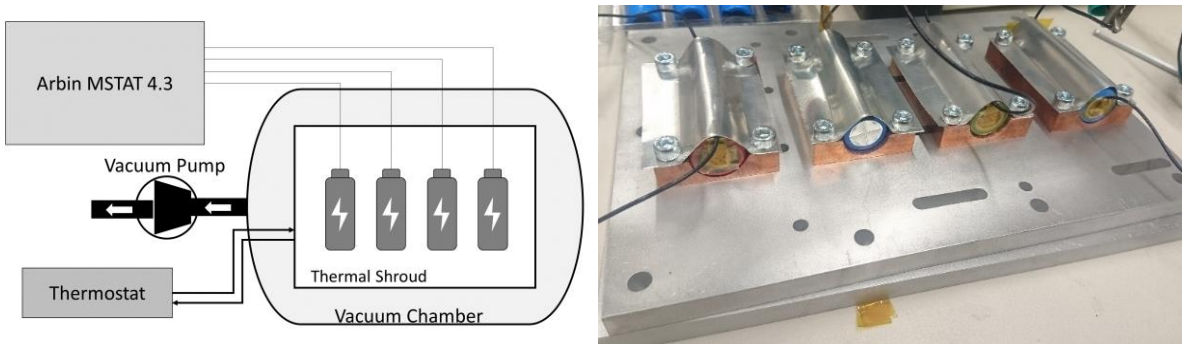

Figure 4-3: Left: Schematic of the experimental test setup; Right: Mounting of the batteries

4.2.2 Lifetime Calculation:

The most important parameter for comparison of the energy storage devices is the time that it is able to keep a system at a certain temperature by heat dissipation. This time depends on the available energy and the heat loss, which depends on the operational temperature and insulation. In the end, each thermal system is unique, but for the purpose of comparison a very simple model consisting of a radiator surface and an internal thermal resistance is used (see Figure 4-4). A surface area of 0.06 m² (corresponding to 1U CubeSat size) was arbitrarily chosen, with a surface emissivity of $\varepsilon = 0.1$. No incoming heat fluxes are taken into account. The model is implemented in SIMULINK and used to calculate the heat loss exhibited by the electronics at certain stationary temperatures. The heat losses are computed for various temperatures and internal resistances, the results are shown in Figure 4-4. Note that for low internal thermal resistances, the curve of heat loss over temperature is dominated by the behavior of the radiative heat loss on the outer surface, with the curve proportional to the fourth power of the temperature. With higher thermal resistance R_T, the heat loss is dominated by the behavior of the internal insulation, with the curves becoming linear.

Using this pre-calculated heat loss $\dot{Q}(T)$ and the temperature dependent discharge energy densities $\rho_E(T)$, it is possible to calculate the normalized time $t_N \left[\frac{s}{kg}\right]$, which shall be defined as the period that the electronics can be kept at a constant temperature per mass (or volume) of energy storage:

$$t_N = \frac{\rho_E(T)}{\dot{Q}(T, R_T)}$$

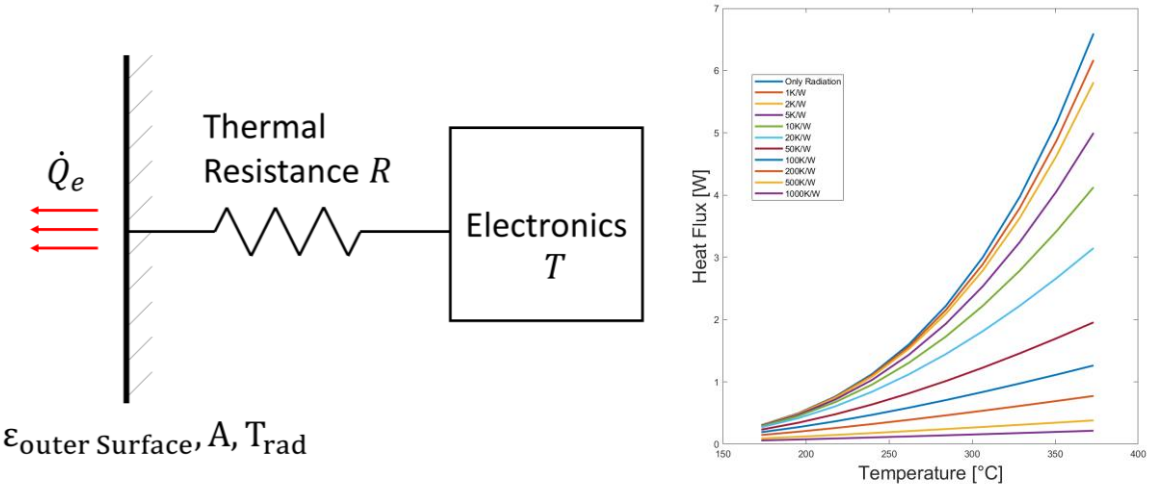

Figure 4-4: Left: Sketch of the used thermal model; Right: Heat loss as a function of temperature for various thermal resistances

4.3 Results

4.3.1 Energy Density vs. Temperature

All discharge tests were concluded successfully, no visible damage was observable on any of the tested cells. Initial cell temperatures were within +/- 2K of the target temperature for all cells except for the Max3000 supercapacitor, for which a tolerance of +/- 5K was used (due to its large thermal inertia). During testing, the cells remained within +/- 5K of the target temperature, therefore self-heating was moderate but generally higher for lower temperatures.

Figure 4-5 shows the gravimetric and volumetric energy densities of the investigated energy storage devices as a function of temperature. Actual data points are marked, the curves have been fitted with shape preserving interpolant splines in MATLAB. In general, the highest energy densities are achieved by primary batteries, followed by high energy density lithium-ion batteries. Among the presented primary cells, the highest overall energy densities are achieved by the bobbin type lithium thionyl chloride Saft 33600 cells or the lithium carbon monoflouride cells Rayovac CFx and EP CFx cells, however these types are outperformed by the high power lithium thionyl chloride Saft LSH20 and Tad TLH at temperatures below -30°C. Of particular interest is the Energizer FeS2 cell, which has the lowest energy density at room temperature of the presented primary cells, but also the highest remaining energy density at -40°C.

The high energy density Pan 18650 and LG 18650 have a relatively stable performance over their nominal operational temperature, but drop steeply at around -20°C, with almost no energy left at -30°C. In terms of gravimetric energy density, the electrochemical hybrid capacitor HyC 23680 almost matches the Pan18650 and LG18650, but with better low temperature performance. The best relative low temperature performance of the rechargeable devices is exhibited by the Max 3000 supercapacitor, with 50% of its nominal energy left at -50°C, but at 6 Wh/kg, its energy density is too low to remain practical. In addition, the Max 3000 suffered permanent damage after cooling to -50°C and -60°C, losing about 60% of its capacity in ambient conditions. The best low temperature energy density of the tested rechargeable devices is exhibited by the BP S5300, with 23% of its nominal capacity at -50°C, equivalent to a remaining energy density of 48.6 Wh/kg.

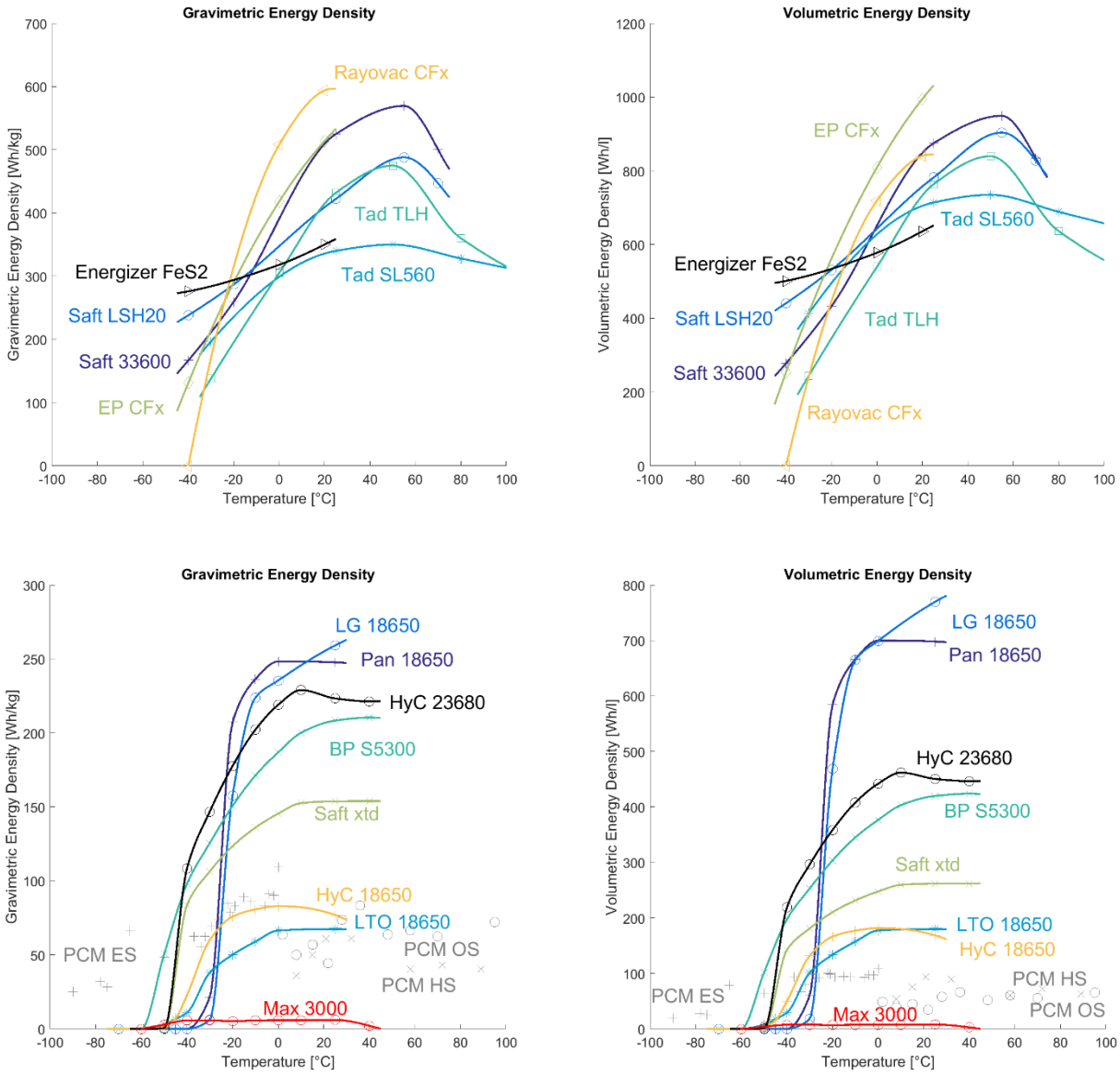

Figure 4-5: Gravimetric (left) and volumetric (right) energy densities of investigated primary batteries (top) and rechargeable energy storage devices (bottom).

4.3.2 Operational Lifetime

Figure 4-6 shows the gravimetric and volumetric normalized times for the investigated devices, for a system with no internal insulation. It can be seen that for each device, an optimum operational temperature exists, which allows the longest operational time. For the majority of devices, this maximum lies towards the lower end of the respective temperature limits, though this is not always the case. The optimum temperatures for the two high energy density primary batteries SAFT 33600 and Tad TLH are at about 8°C and 15°C, even though the rated low temperature limits are -60°C and -55°C. In addition, normalized times can vary significantly over temperatures. For example the HyC 23680 cells have a normalized time of $2.99 \cdot 10^4$ s/kg at 25°C, $3.89 \cdot 10^4$ s/kg at their rated low temperature limit of -40°C and a maximum of $4.58 \cdot 10^4$ s/kg at -20°C, which is 53% higher than at room temperature and 18% higher than at -40°C. This highlights the importance of determining the optimum operational temperature to achieve maximum operational times.

Figure 4-7 also shows the normalized operational times, but for a system in which the electronics are insulated with a thermal resistance of 200 K/W against the radiator. This reduces the heat loss and therefore generally increases normalized times, but it also makes higher temperature operation more viable as heat

loss in this case scales almost linearly as opposed to proportionally to the fourth power of the temperature. In this scenario, the highest normalized times are possible with the high energy density primary batteries. However, in volumetric terms, there is very little difference between these and rechargeable Pan 18650 and LG 18650 batteries, which effectively makes primary batteries unviable in volume restricted use cases. The high current primary battery Saft LSH20 presents a special case, as its normalized time with an internal insulation of $R = 200\ K/W$ is almost constant between -40°C and +60°C, meaning that increased heat loss at higher temperatures is almost equally made up by higher capacity.

The increased insulation has significantly shifted the optimum operational temperatures of most batteries. This is further highlighted in Figure 4-8, which shows the optimum operational temperatures for various internal thermal resistances for two batteries. In the case of the Saft 33600, the optimum operational temperature shifts from 11°C to 24°C if the thermal resistance is increased from 1K/W to 1000K/W and for the HyC 23680 the optimum shifts from -20°C to 4°C. Therefore, the optimum operational point needs to be determined for a given thermal design, taking the temperature dependent heat loss into account.

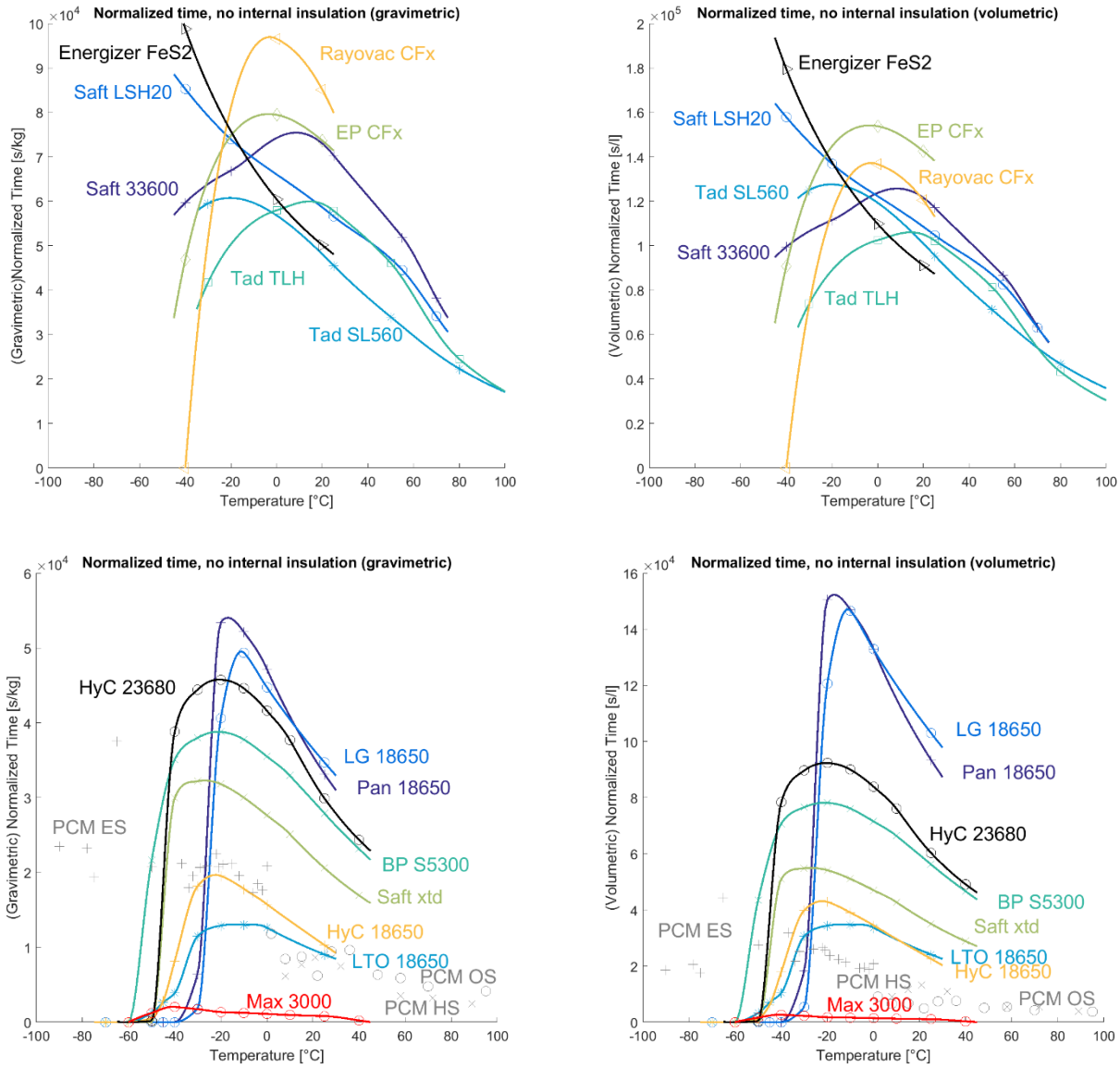

Figure 4-6: Gravimetric (left) and volumetric (right) normalized times of investigated primary batteries (top) and rechargeable energy storage devices (bottom) for a system with no internal insulation.

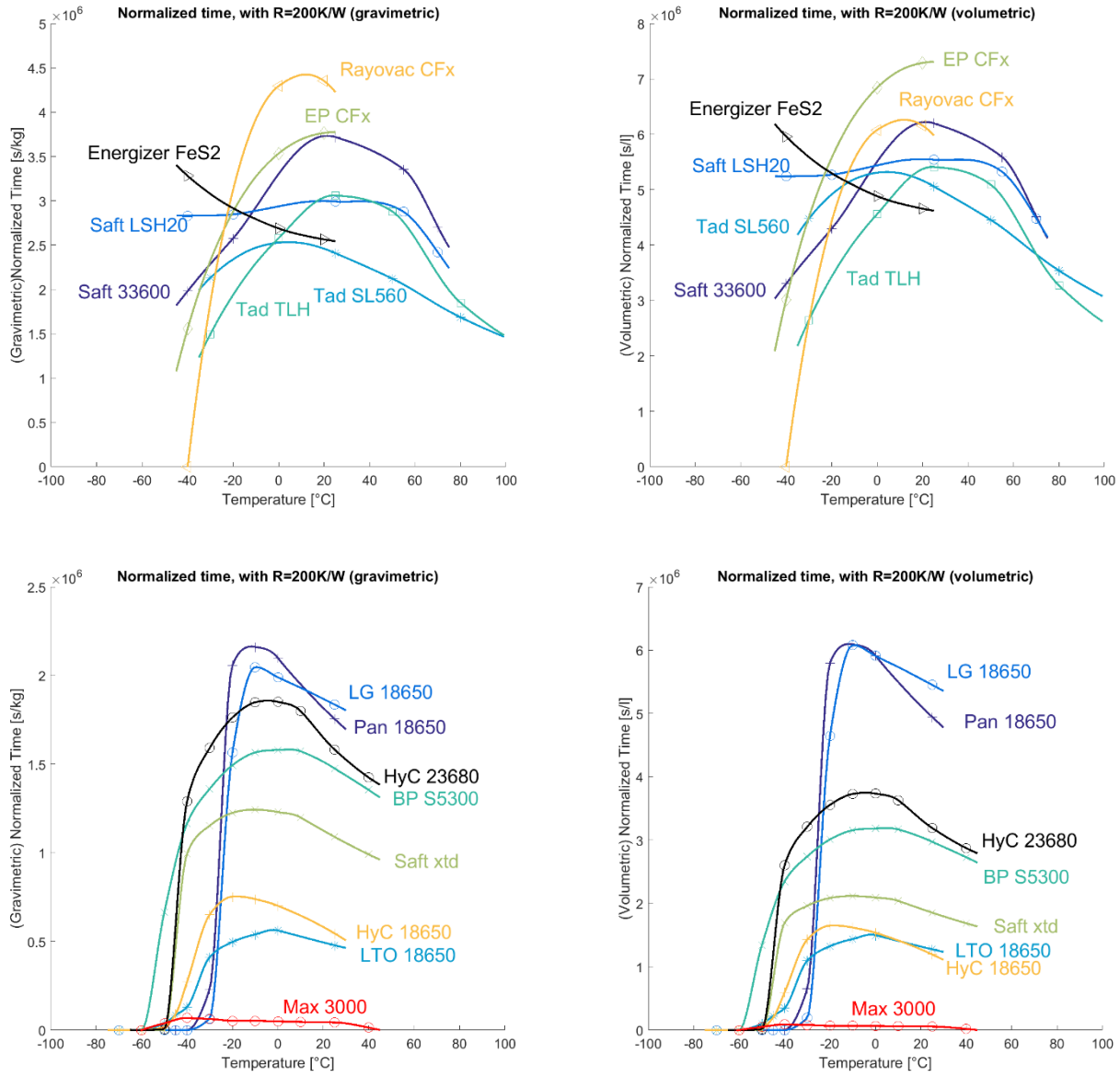

Figure 4-7: Gravimetric (left) and volumetric (right) normalized times of investigated primary batteries (top) and rechargeable energy storage devices (bottom) for a system with an internal thermal resistance of R=200K/W.

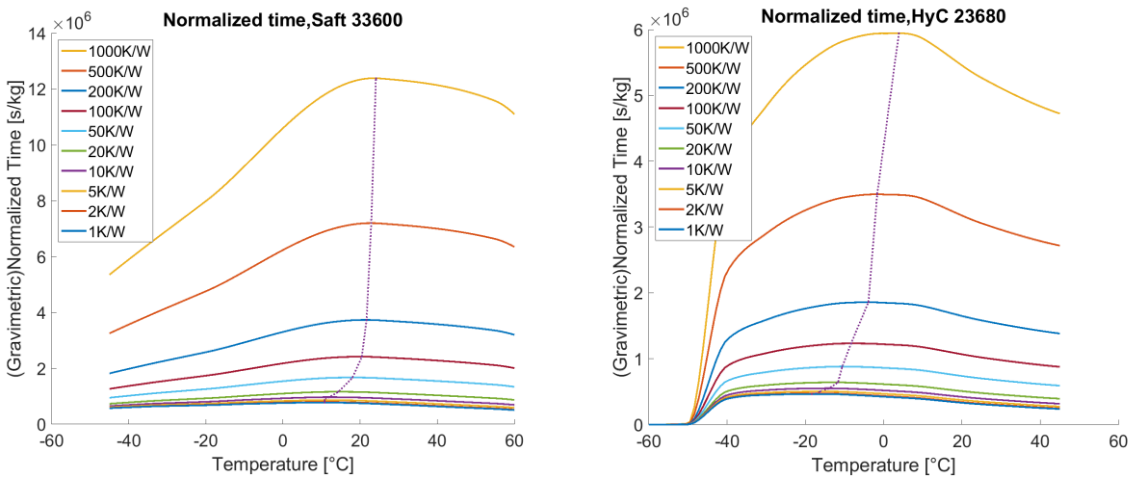

Figure 4-8: Normalized times for different thermal resistances of the Saft 33600 and HyC 23680 devices. The dotted line connects the optimum operational points.

4.3.3 Survival of Cryogenic Temperatures

Figure 4-9 shows the temperature profile of the liquid nitrogen cooling test as well as the measured discharge energy of the cells after each cycle. Only the Pan 18650, LG 18650, HyC 18650, LTO 18650, Saft xtd and BP S5300 cells were tested. The Max 3000 already failed at much higher temperatures and the HyC 23680 could not be tested as only a single cell was available, which was damaged after the temperature testing due to long-term storage at an inappropriate charge state during a COVID-19 related shutdown of the testing activities. The cells were cooled to -180°C in about 30 min (see Figure 4-9), which corresponds to a temperature drop of about 6.7 K/min, which is significantly faster than what is expected on the lunar surface. The second cooling only achieved about -150°C because insufficient LN2 was poured into the cooler. The measured discharge energies showed slight variations between each cycle, but no significant change is apparent. The variations could be due to slight changes in room temperature, as this was not controlled. No visible damage or alteration to any of the cells was visible during visual inspection.

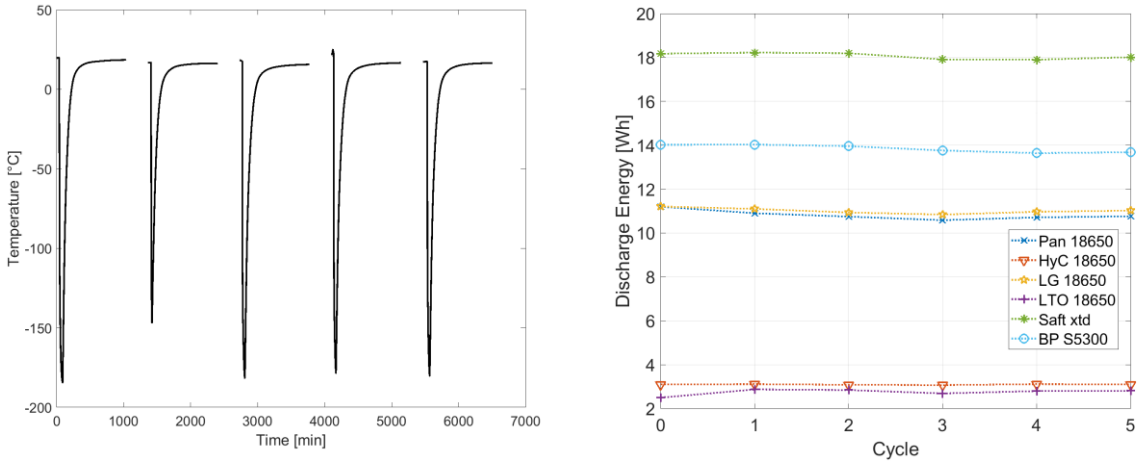

Figure 4-9: Temperature curve of the LN2 coolings (left) and discharge energy (right) after each of the five cooling cycles.

4.4 Discussion

This chapter addressed the second research objective of this thesis:

Objective 2:	**Identify ideal energy storage and its optimal operating point for lunar night survival.**

A selection of eight energy storage devices was tested for low temperature performance at low discharge currents and the presented results were compared to existing datasheet values of four primary battery types and three classes of PCMs. The temperature dependent energy densities were then used to calculate expected operation times during the lunar night based on a simple generic thermal model and for various amounts of insulation. It was shown that the choice of optimum energy storage depends on the insulation and therefore selection should be done for a specific system. Primary batteries outperform rechargeable lithium ion batteries in terms of gravimetric energy density for single use applications, but in volume restricted applications rechargeable lithium cells achieve similar operation times. Hence, primary batteries can be useful in mass restricted applications, if survival for a single shadow period is necessary.

The presented data indicates that **specialty low temperature batteries do not provide an advantage over common high energy density cells, because the reduced heat loss does not make up for lower energy density of these batteries**. The study did not include some of the most interesting available low temperature batteries due to procurement reasons, such as the Saft MP176065 int xc or the ester-based Mars Insight batteries from Eagle-Picher/Yardney. The former has a nominal energy density of only 174 Wh/kg (Saft 2014), with about 110 Wh/kg remaining at -40°C, the latter has a demonstrated energy density of 122 Wh/kg at -40°C (Smart et al. 2017) and are therefore comparable to the presented results of the HyC 23680 and BP S5300, with 111 Wh/kg and 98 Wh/kg at -40°C (Although it should be noted that the Saft MP176065 int xc and Eagle-Picher/Yardney models were tested at higher discharge currents). Furthermore, it was shown that the use of PCMs in this context is of limited use, as the energy densities of available compounds is much lower for PCMs than it is for common battery types. However, **PCMs could become viable at very low temperatures (<40°C), where batteries lose their capacity to ensure passive survival at a certain temperature level**.

A limitation of the presented research is the limited sample size of just one tested cell per datapoint, therefore the presented data should be considered with caution. Slight manufacturing differences can yield differences in cell capacities, therefore a larger sample size would be preferable. However, low discharge current testing inherently takes a long time and it was not possible to test more cells with the available resources. In addition, the data points for the primary batteries were taken visually from datasheets and are therefore not the most precise. In addition, only four data points were available over the temperature range per cell. More datapoints would be needed to verify the exact shape of the energy density curves and for the temperature range below -40°C. Nonetheless, the presented study provides a good indication of the strengths and weaknesses of each technology for lunar night operation.

With the exception of the supercapacitor, all of the investigated cells withstood the thermal cycling or repeated cryogenic freezing, with no apparent damage or change to capacity. During testing, the thermal gradients exceeded expected values on the lunar surface, which is likely to be the most important factor. The cryogenic temperatures were not maintained over extended periods and certainly less than the full length of a lunar night. Cells were only exposed at a low charge state, as it is expected that lunar surface applications will likely drain their batteries during night-time operation before hibernation. However, charge states affect the chemistry of electrodes and electrolytes and therefore the results may not be applicable to charged cells. Nonetheless the results are consistent with other studies that also included longer exposure (Grandjean et al. 2019; Nandini et al. 2018) and with the experience of the Rosetta Philae lander. After an unfortunate landing (Ulamec et al. 2016), Philae received insufficient power. After depleting its primary (32 Saft LSH20) and secondary (28 Sony 18650 HC) batteries, it experienced temperatures down to -100°C (Boehnhardt et al. 2017). Despite this, the lander was able to reboot once sufficient illumination was available. Contact was established in July 2015 and the batteries appeared to be in good shape. **It can therefore be concluded that controlled exposure to cryogenic temperatures is likely tolerable to the majority of lithium ion batteries and hybrid capacitors**, at least for a limited amount of cycles.

Nonetheless, this does not replace individual qualification testing. Also it is unclear if repeated cycling to cryogenic temperatures will accelerate aging, but this is not relevant to the presented application where the survival of even a small number of cycles can be considered a success.

5 Case Studies

The results from chapter 3 have shown that a majority of components can be operated at temperatures as low as -120°C, even though they are only rated at automotive/industrial (-40°C) or military (-55°C) standards. However, the results of chapter 4 have shown that no suitable energy storage technologies exist that can provide a meaningful amount of energy at temperatures below -60°C and that overall better performances are achieved, when batteries are operated at higher temperatures. This poses a significant problem to lunar surface system designs aiming to utilize low temperature rerating to improve lunar night survival. If batteries need to be maintained at temperatures between -20°C to +20°C, then what use are electrical components that can withstand much lower temperatures.

This chapter aims to answer this question on the basis of three case studies: Case A is the LUVMI-X DPP that needs to remain operational in shadow for as much time as is possible to survive partial lunar nights (<14 days) at the lunar south pole with limited available battery volume. Similarly, case B represents a small lunar rover that also attempts to survive (partial) lunar nights at the polar areas. Finally, case C investigates a lunar lander throughout the lunar day. For each case, a thermal simulation model of a functional baseline thermal design is developed. These baseline designs are then varied with different grades of component rerating. The performances of the resulting design variations are then compared to determine the utility of each and thus to investigate whether or not component rerating can meaningfully improve system performance in these three cases.

The aim of this study is to investigate low temperature rerating as an efficient means to improve the night survival and operation capability for lunar surface systems. This relies on the assumption that rerated subsystems can more or less be used in the same way as originally intended, thus the overall system architecture will not have to be completely revised. Therefore, this study will only investigate minor changes to existing architectures, such as changes in surface emissivity, changes of thermal conductivity between components (e.g. achieved by the introduction or removal of thermal spacers or heat straps) or minor geometric changes like the rearrangement of the stacking order of a PCB stack. In addition, the effect of battery temperature on the night survival time shall also be investigated to verify the results obtained in section 4.3.2.

5.1 Case A: Deployable Payload Platform

This section extends the work of Bauer (2021), a master thesis supervised by the author of the present thesis. His thesis built on an earlier work of Biswas et al. (2021a) that presented the original baseline thermal design for the DPP.

The DPP baseline thermal design maintains the temperatures of its components within their rated limits. The subsystem limits are shown in Table 5-1. The most crucial element is the battery, which is rated from -20°C to +60°C. If appropriate margins are applied (+/- 15 K for a Phase A design), this leaves a -5°C to +45°C temperature window. The other subsystem electronics are rated at -55°C or -40°C to +70°C or +85°C. In terms of heat dissipation, the S-Band transceiver is the most crucial element, as it can have a heat dissipation of up to 14 W.

Table 5-1: Nominal temperature limits of DPP components (reproduced from Bauer 2021)

Component	Operational temperature limits (nominal)	Operational temperature limits (with ± 15 K margin)
ISIS S-Band Transceiver	-40 °C…+70 °C	-25°C…+55 °C
CDH Module	-55 °C…+85 °C	-40 °C…+70 °C
MOVE/OroraTech EMPS	-55 °C…+85 °C	-40 °C…+70 °C
Panasonic NCR18650 BF	-20 °C…+60 °C	-5 °C…+45 °C
VCAS Payload	-40 °C…+60 °C	-25 °C…+45 °C
External panels (with solar cells)	-150 °C…+250 °C	-135 °C…+235 °C

Figure 5-1 shows a schematic of the thermal architecture of the DPP. It employs a combination of the island and layered architecture. The support module and VCAS payload are mostly separated thermal systems (islands), while the individual subsystems of these modules are arranged in a layered configuration. Each module is insulated from the environment by low emissivity coatings on the inside of the structure and PEEK spacers separate the PCB stack from the structure. A thin plate heat switch (Sierra Nevada Cooperation 2018) manages heat flow from the PCB stack to a dedicated radiator panel. In the support module, the heat switch is directly connected to the S-Band transceiver, thus ensuring optimal heat flow from the greatest source of heat dissipation. The stack then includes the power system, data handling system and finally the most critical system, the battery. This way, the battery is farthest removed from the radiator and heat lost from the battery is used to heat the other subsystems, which corresponds to a layered architecture. The different subsystems on the stack are thermally connected by spacers, the material of which can be chosen based on the desired thermal resistance. The outer structure, including the panels, solar cells and antenna are allowed to cool down / heat up significantly. A major limitation for the thermal design are the electrical connections between the subsystems, as the thermal bridges created by each wire becomes a hard limit for the maximum insulation between subsystems, especially for high current connections. A schematic of the wiring is presented in Figure 8-18, Table 8-5 shows the cable dimensions and resulting thermal resistances.

In its baseline configuration, the DPP is able withstand 52.6 h of lunar night exposure until its 96 Wh battery is fully depleted. At the same time, it withstands the worst case solar illumination during the day and can maintain its battery temperature below 45°C during battery charging.

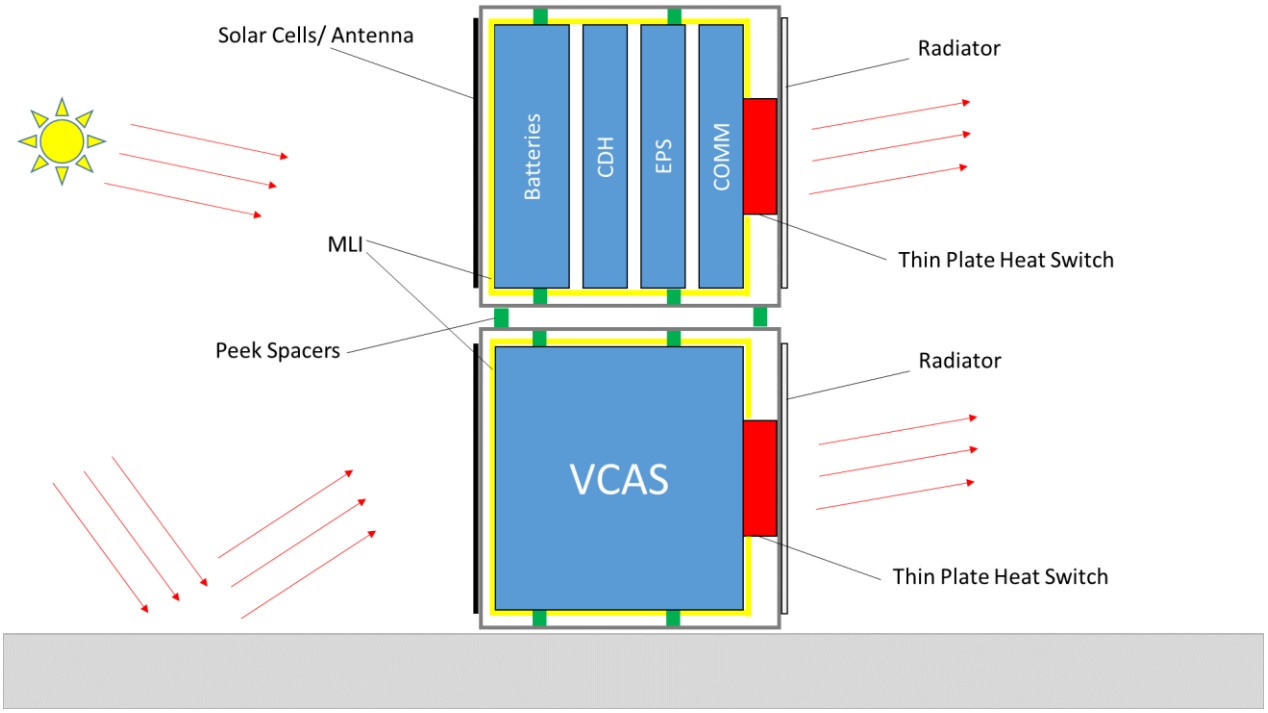

Figure 5-1: Baseline thermal architecture of the DPP

5.1.1 Model Description

A lumped parameter model was implemented for the DPP on the lunar surface in Simulink/Simscape. The three dimensional system was reduced to a total of 17 nodes, which is appropriate for a relatively small and simple system at an early phase. Simulink/Simscape was chosen as it allows the coupled simulation of internal logic, electronics, energy budget and data budget alongside thermal simulations, which was useful in the context of DPP development. The model was implemented in a highly parameterized way that allowed the investigation of many thermal design variation by simple inputs to a parameter input file. The model was integrated with a set of MATLAB scripts that further facilitated this process by automatically calling and evaluating the simulations of the different design variations.

Table 8-6 shows the node masses and heat capacities. The model is based on the following notable assumptions / simplifications:

- All subsystems / major components were modelled as a single node with uniform temperature. The model therefore does not capture the heat distribution inside these subsystems, such as the thermal gradient on an individual PCB. This needs to be accounted for by additional margins of +/- 15 K, which is appropriate for early phase design work. Furthermore, the thermal architecture of the DPP was designed in way to facilitate this. Thermal resistances were chosen such that resistances between subsystems are significantly higher than on individual components. For example, the structure was chosen to made from aluminium, which ensures an even temperature distribution on the structure elements due to its high thermal conductivity.
- Radiative heat exchange is calculated based on analytic view factors determined for simplified geometric models of the subsystems. For example, PCBs were considered either as flat 2-dimensional surfaces or as rectangular boxes. Individual surface properties of different parts of a PCB were not taken into account, instead a single value was used for each node. Reflections and transparent surfaces were neglected. A schematic of the geometric model used for the calculation of the view factors is shown in Figure 5-2.
- Minor components, like cables, screws, etc. are not taken into account. Masses for these components were accounted for by the application of margins to the system masses. Cables were

taken into account as thermal bridges between subsystems, but not as thermal nodes. This is a common assumption for all early phase thermal models.

- Ideal conductive couplings were assumed for the contact resistances in this model. They are hard to predict and usually experiments are necessary to generate valid values. The thermal model of the DPP is evaluated against some experimental data in chapter 6, but the results shown in this chapter were not correlated against these experimental results. Contact resistances are a major problem where good thermal contacts are required, but in this case, the design mostly tries to provide good insulation, therefore the impact of additional contact conductance will not have a large impact and even work in favour.
- External heat fluxes are highly simplified. A very simple model for the lunar surface is implemented. The surface has a given temperature and only radiative heat exchange is taken into account. Thermal conductivity of lunar regolith is extremely low, especially at low temperatures and the thermal design of the DPP allows the structure to cool down significantly with high temperatures maintained only on the PCB stack, thus this is justified. For the hot case, solar heat flux is equal to 1420 W/m^2 and zero for the cold case. A conservative albedo factor of 0.2 is assumed for lunar surface for the hotcase.
- Physical properties are assumed to remain constant over temperature to reduce complexity.

The simulation model is used in two scenarios: the hot case and the cold case. This is important, as the thermal design of the system needs to work throughout the lunar day and during the night. Each case represents the worst case conditions. For the hot case, this means that the solar elevation is at its maximum of 10° and illumination reaches the DPP diagonally and therefore illuminates the maximum surface area. The surface temperature is set to 250 K, corresponding to maximum temperatures in polar latitudes. In this scenario, the DPP will operate its S-Band receiver, CDH and electrical power system (EPS) and must further charge its battery, while maintaining the battery temperature within acceptable levels. In the coldcase, the surface temperature is set to 50 K and no solar illumination is available. In this scenario, only the EPS is active and will activate heaters to maintain system temperatures at required levels.

The hot and cold case scenarios represent steady state conditions, however the model in fact performs a transient simulation. For the hot case, the system starts at an initial temperature of 300 K and with an empty battery. The simulation is run for 350 h, equivalent to a full lunar day. During the initial hours, the structure and subsystems heat up and the battery is charged. Once the battery is full, charging stops and steady state temperatures are achieved. For the cold case, the system is also initialized at 300 K, but with a fully charged battery. The temperatures then drop during the initial hours until heater set temperatures are reached and the temperatures are maintained at a constant level. After the battery is drained, the heaters cease to function and temperatures fall to ambient temperatures. A more detailed description of the model and a sensitivity analysis for model verification can be found in (Bauer 2021).

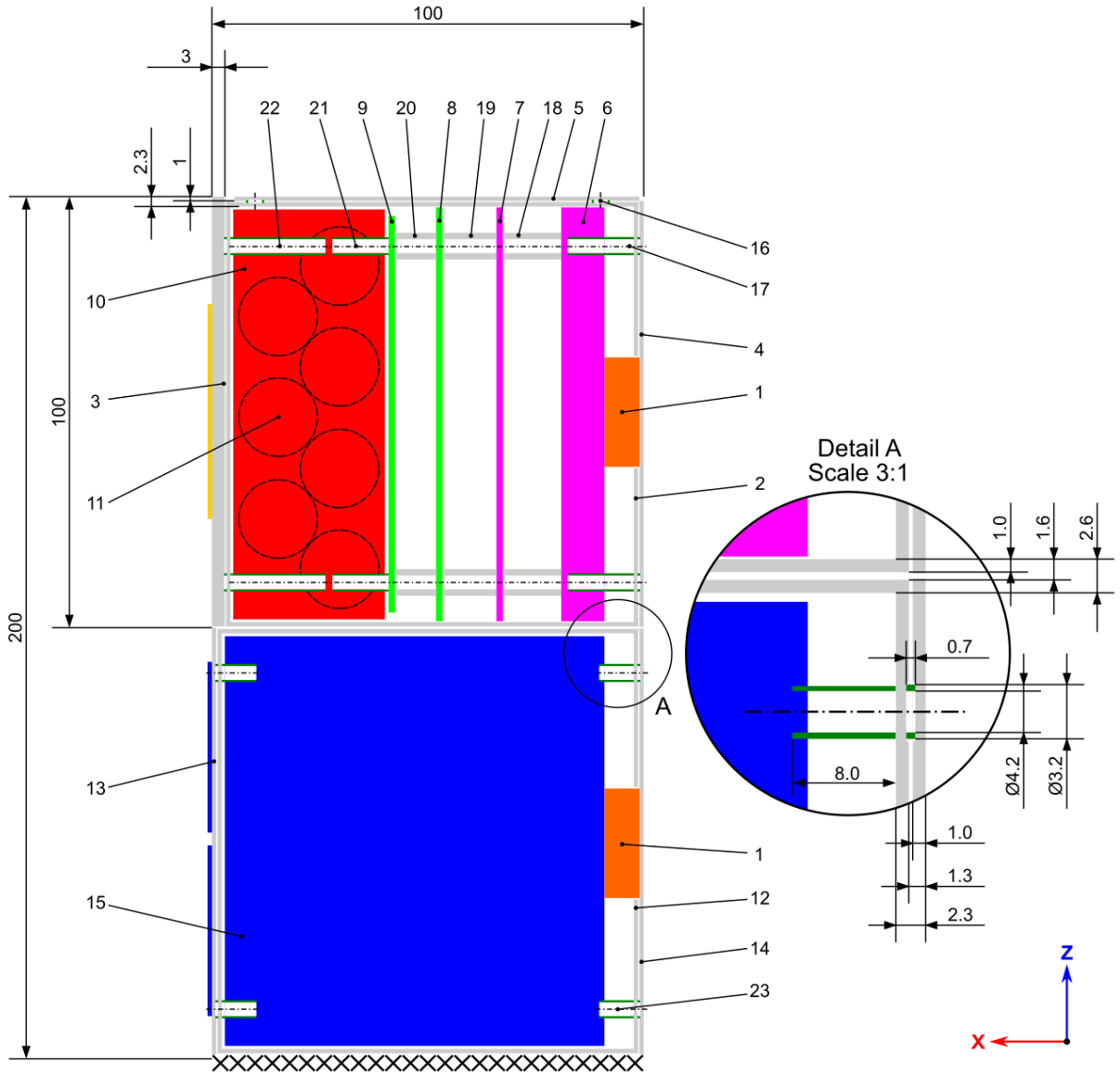

Figure 5-2: Schematic of the DPP geometric model used as basis for the thermal model (from Bauer 2021). Annotations: (1) Heat Switch; (2) SM structure; (3) SM front panel / antenna; (4) SM back panel; (5) SM top panel; (6) S-Band Transmitter; (7) S-Band receiver; (8) CDH module; (9) EPS module; (10) Battery module; (11) Battery cell; (12) PM structure; (13) PM front panel; (14) PM back panel; (15) VCAS payload; (16-23) spacers;

5.1.2 Design Variations of the thermal model

A range of model variants were created, both conventional thermal design variants and variants that include different low temperature rerating were generated. Table 5-2 lists the investigated model variants with a brief description. A more detailed description of the conventional variants is provided in (Bauer 2021). The inclusion of conventional design variations will allow the comparison of the impact of rerating to conventional design optimisation.

Note that the rerating variants that include additional thermal insulations will see fairly high battery temperatures during charging in the hot case. In this scenario, only a 6 K margin can be maintained (instead of 15 K). Thus, these variants will need charge current limitations during the hot case scenario.

Table 5-2: Investigated model variants for the DPP

Name	Designator	Description
Baseline	Baseline	The original baseline design. Heater set temperatures in accordance with datasheet temperature limits (see Table 5-1).
Alternative Battery Concept: Primary Batteries	ABP	This group includes 7 variants that utilize primary batteries instead of rechargeable ones. A selection of primary batteries discussed in chapter 4 is used.
Alternative Battery Concept: Secondary Batteries	ABS	This group includes 6 variants that utilize alternative rechargeable battery models. The baseline Panasonic NCR18650 is replaced by a selection of models discussed in chapter 4.
Alternative external surfaces	AES	This group includes 11 variants, all of which use different surface finishes on external surfaces that are not covered by solar cells or the antenna, with a focus on different radiator surface finishes. Investigated radiator finishes are Dow Coming Thermatrol DC-92-007 white paint, Magnesium Oxide white paint, Barium sulphate white coating and Sheldal SSM tape.
Additional Internal Insulation	AIN	This group includes 4 variants that increase the internal insulation of the DPP. Variants include other wire materials to increase thermal resistances of cables, low emissivity coatings on internal subsystems.
Alternative Spacer Concepts	ASC	This group includes 5 variants with different spacers used between the individual subsystems. Variations include different wall strengths and material choices.
Rerated, no VCAS	Rerated (1)	In this variant, the SM subsystems are assumed to be rerated, such that the heater set temperature is set to 10 K increments between -200°C and -40°C. The VCAS is assumed to passively hibernate, requiring it to passively survive temperatures below -200°C. The battery is maintained at -5°C.
Rerated, all systems	Rerated (2)	In this variant, all subsystems of the SM and the VCAS are assumed to be rerated, such that the heater set temperature is set to 10 K increments between -200°C and -40°C. The battery is maintained at -5°C.
Rerated, VCAS normal	Rerated (3)	In this variant, the SM subsystems are assumed to be rerated, such that the heater set temperature is set to 10 K increments between -200°C and -40°C. The VCAS is not rerated, and thus maintained at -25°C. The battery is maintained at -5°C.
Rerated, VCAS only	Rerated (4)	In this variant, only the VCAS is rerated, such that the heater set temperature is set to 10 K increments between -200°C and -40°C. SM subsystems are maintained at -25°C. The battery is maintained at -5°C.
Rerated, no VCAS + Additional Internal Insulation	Rerated (1), AIN	Like variant Rerated (1), but with low emissivity coating on the battery module and high thermal resistance spacers between battery module and the rest of the stack.
Rerated, all systems + Additional Internal Insulation	Rerated (2) , AIN	Like variant Rerated (2), but with low emissivity coating on the battery module and high thermal resistance spacers between battery module and the rest of the stack.
Rerated, VCAS normal + Additional Internal Insulation	Rerated (3) , AIN	Like variant Rerated (3), but with low emissivity coating on the battery module and high thermal resistance spacers between battery module and the rest of the stack.
Rerated, VCAS only + Additional Internal Insulation	Rerated (4) , AIN	Like variant Rerated (4), but with low emissivity coating on the battery module and high thermal resistance spacers between battery module and the rest of the stack.

5.1.3 Results

Baseline

Figure 5-3 shows the temperature and battery charge curves for the hot case. As expected, the temperatures increase steeply at the beginning. Once the battery temperature approaches the upper battery temperature limit, the charging current is reduced to prevent overheating. Charging then continues steadily until the battery is fully charged, at which point the temperatures of the battery and power systems drop slightly and then remain constant. In total, battery charging in this configuration takes 51.07 h, equivalent to an average charging current of 0.5 A. All temperatures remain within their specified limits.

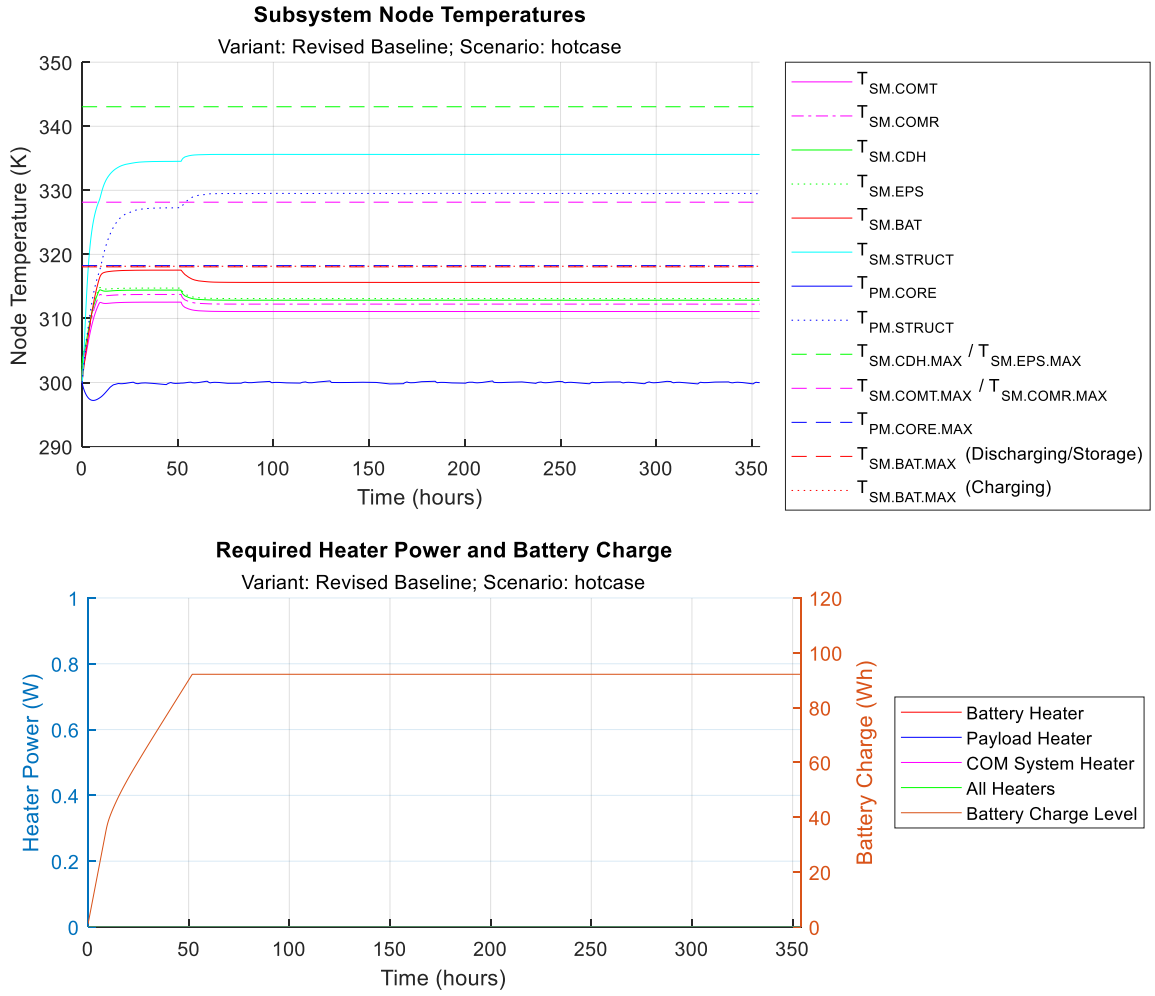

Figure 5-3: Subsystem temperatures for the DPP baseline design coldcase (top); Heater Power consumption and battery charge (bottom).

Figure 5-4 shows the corresponding results for the cold case simulation. Temperatures start to fall at the beginning of the simulation until the battery heater becomes active after 7.8 h. Temperatures are then kept constant at their heater set points for the duration of the battery lifetime. After 52.9 h, the battery is completely empty and the subsystem temperatures start to fall towards ambient temperatures. Therefore the lifetime of the baseline variant is 52.9 h. Note that this does not account for depth of discharge margins that would be appropriate for an actual mission.

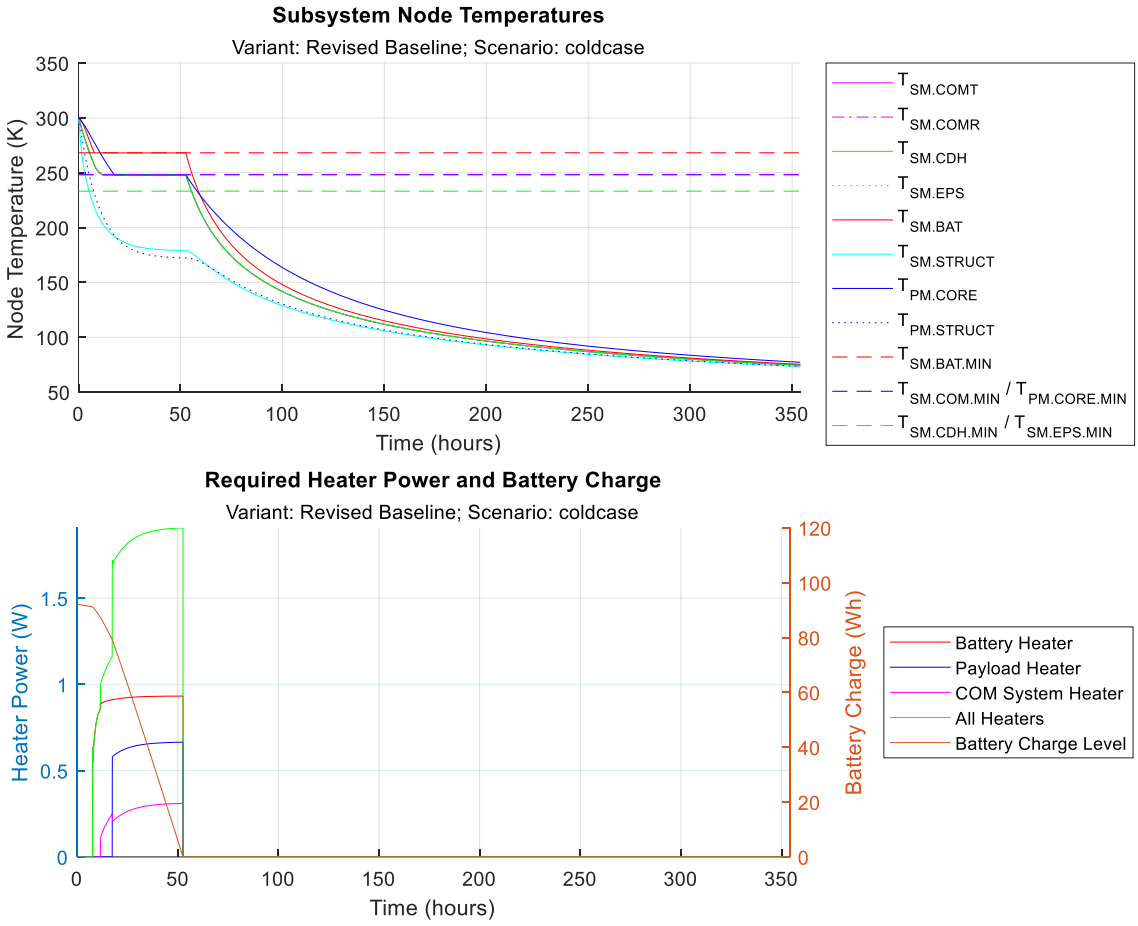

Figure 5-4: Subsystem temperatures for the DPP baseline design hotcase (top); Heater Power consumption and battery charge (bottom).

Design Variations

Figure 5-5 shows the results for the different variations (presented in section 5.1.2). The graph shows the average battery charging power over the expected night survival time. The baseline results are depicted in black, the conventional design variations are plotted in grey and the variants that rely on temperature rerating are shown in blue and red. The average charging power is also shown, as it provides a good indication on the hot case performance, while the night survival time indicates the cold case performance. Each rerating variant has been plotted for in 10 K increments from -200°C to -40°C. It can be seen that of the conventional variations, only AIN (Additional Internal Insulation) and ABP (Primary Batteries) and AES (Alternative External Surfaces) variants provide a meaningful cold case performance improvement. The best AES version enables 58 h of night survival, or a 10% increase against the baseline design by reducing the radiator emissivity. This however comes at the expense of achievable charging power, which needs to be reduced by 86% to avoid overheating. The best AIN variant allows 57.9 h of survival by increasing the internal insulation, but this reduces the average battery charging power by 93%. The highest increase in survival time for the conventional variants is achieved by the use of a primary battery with a survival time of 69.6 h, equivalent to a 32% increase against the baseline performance. However, primary batteries are non-rechargeable and therefore the effective charging power is reduced to zero. Some variants have slightly improved the survival time and the average charging power, but these improvements are only in the range of 1-2%. This shows that the baseline design is sound overall and it provides a reference for the performance of rerated variants to compare against. Meaningful cold case improvements by conventional variants are only possible when hot case performance is sacrificed.

On the other hand, rerating increases survival times without impacting the hotcase performance. The blue variants, essentially the baseline version with different heater set points, enable increases in night survival by up to 31%. The red variants, a combination of rerating and additional internal insulation (AIN), are even more effective. A maximum survival time of 98 h can be achieved. Compared to the conventional AIN variant that the variants are based on, this is a 70% increase in cold case performance.

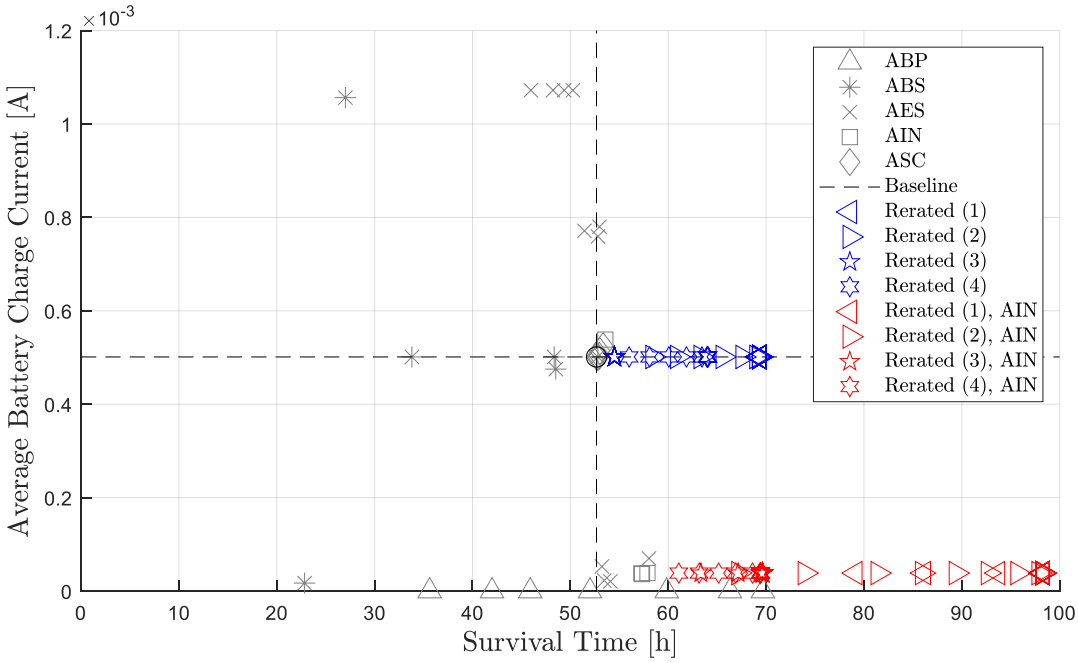

Figure 5-5: Average battery charge current over survival time for various configurations.

Figure 5-6 shows the survival times over the heater set temperatures used. The set temperatures only refer to the rerated parts, for example the battery temperatures is maintained at -5°C in all cases. The plot gives an indication to which temperatures rerating is useful in this context. It can be seen, that in all cases, a limit temperature is reached below which no further temperature reduction is useful. At this point, only the battery needs to be heated and the heat loss from the battery is sufficient to maintain the necessary temperatures of all other subsystems. The blue curves show the first set, which is the baseline variant with temperature rerating for the subsystems, the red curves show the rerating variants that use additional internal insulation. It can be seen, that rerating variants, in which all subsystems are rerated (Rerated (2) and Rerated (2), AIN) show the best performance and benefit from the lowest rerating temperatures. The variants in which the VCAS is passively hibernating (and thus does not require heating) show similar performance, but the remaining systems do not require equally low rerating temperatures. Expectedly, those variants that only use rerating for some subsystems (Rerating (3) and Rerating (4) do not perform as well. Across all cases, the lowest heater set temperature that still provides a benefit is -120°C. It is also shown that the relative increase in performance is more pronounces for the variants that include additional internal insulation. This is also expected, as the additional insulation prevents heat loss from the battery and therefore allows the surrounding subsystems to drop to lower temperatures.

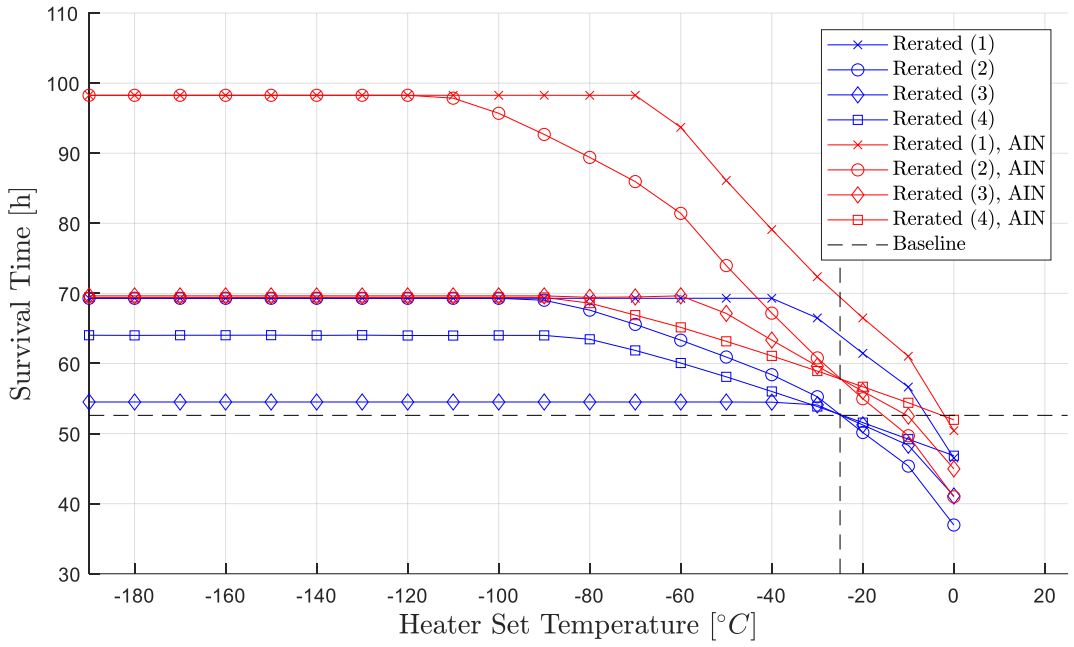

Figure 5-6: Survival time over heater set temperatures for various rerating configurations. Set temperatures in this graph only refer to the rerated components.

Battery Temperature

Figure 5-7 shows the survival time over the heater set temperature of the battery heater for the baseline and two rerating variants. In this case the heater set temperature for the rerated components was set to -100°C and only the battery temperature was varied. The purpose of this simulation was to verify the results of chapter 4 on an actual system. For the baseline variant, the highest performance is achieved at a battery temperature of -5°C, which is also the baseline battery temperature. In case of the rerated baseline configuration (blue curve), the optimal temperature is at -15°C, which provides a 4.5% improvement over the reference temperature of -5°C. For the rerated variant with addition internal insulation (red), the optimum is also at -15°C, though this represents only a 1% increase in performance.

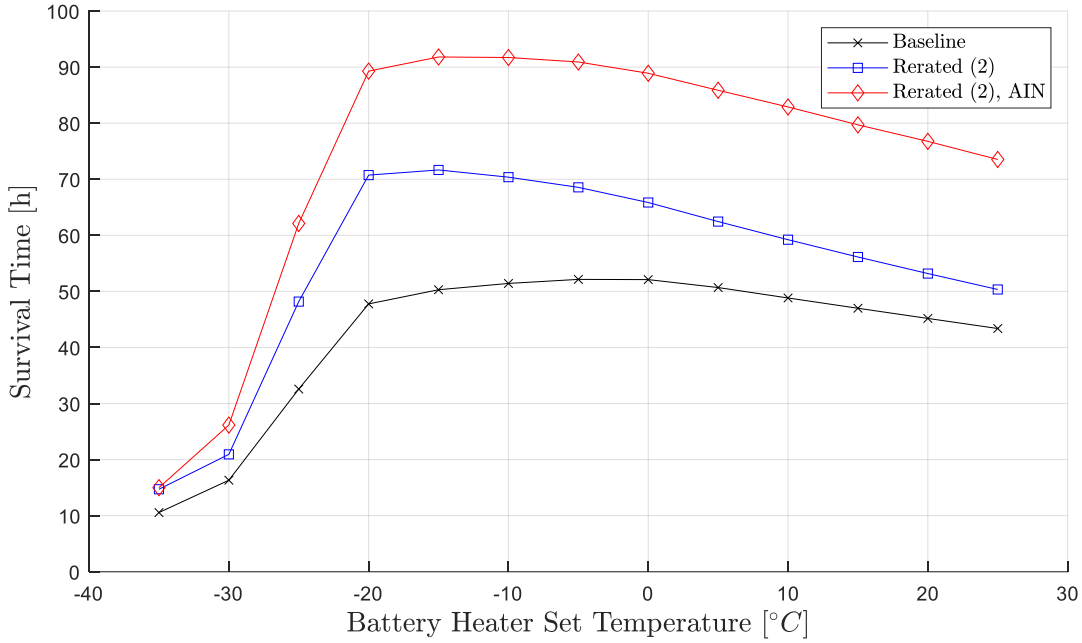

Figure 5-7: Survival times over battery temperature for different DPP configurations.

5.2 Case B: Polar Rover

The second case study is a small lunar polar rover based on the Polar Ice Explorer mission concept (Gscheidle et al. 2022). The rover is designed to carry the LVS soil sampling instrument and its main objective is to investigate lunar volatiles at the lunar polar areas. Its reference landing site is the close to the Amundsen crater (82.0° S, 66.4° E) and was selected, because it provides an ideal combination of sufficient illumination, indication of elevated volatile abundances from remote sensing, benign topography for landing operation and close proximity to potentially accessible permanently shadowed areas. The four wheeled rover has an approximate mass of 20 kg, a height of 37 cm, a length of 53 cm and a length of 60 cm. Its 70 Wh battery allows for up to 6 h of operation in shadow. An image of the rover concept is shown in Figure 5-8 (rover avionics and side panels not shown).

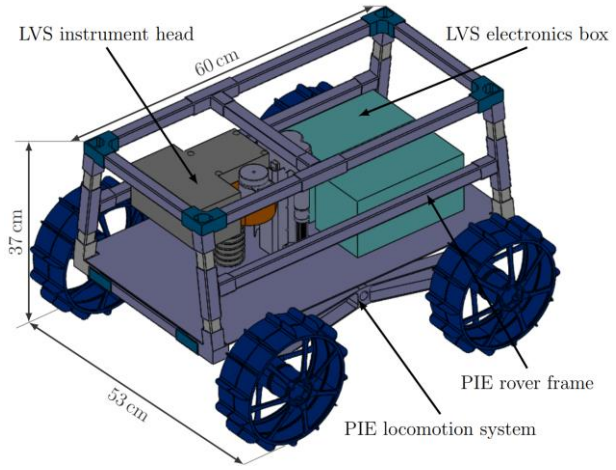

Figure 5-8: Render image of the Polar Ice Explorer rover concept (Gscheidle et al. 2022).

No detailed thermal design has been published, thus the following assumptions have been made: The overall thermal architecture was assumed to be similar to the Hakuto rover (Tanaka 2018), which was

designed by the same company as PIE. As such, its internal electronics are attached to the top plate of chassis, which acts as a radiator. This plate is indented, meaning it is lowered slightly below the rim of the side panels to reduce the amount of solar light reaching the radiator. Heat flow to and from other parts of the rover are minimized by thermal spacers between panels, MLI and low emissivity / absorptivity coatings on external surfaces. It is further assumed that the radiator is covered by a louver that will cover the radiator in cold temperatures to better deal with the extreme temperature environment encountered during the mission. The temperature limits of its core components have been estimated and are shown in Table 5-3.

Table 5-3: Nominal temperature limits for the components of the Polar Rover

Component	Operational temperature limits (nominal)	Operational temperature limits (with ± 15 K margin)
COMM	-40 °C…+70 °C	-25°C…+55 °C
CDH / EPS	-55 °C…+85 °C	-40 °C…+70 °C
Motor Controllers	-55 °C…+85 °C	-40 °C…+70 °C
Battery	-20 °C…+60 °C	-5 °C…+45 °C
Payload Electronics	-40 °C…+60 °C	-25 °C…+45 °C
Payload	-40 °C…+60 °C	-25 °C…+45 °C
Motors	-55 °C… +125°C	-40°C… +110°C

5.2.1 Model Description

A simplified representation of the polar rover was recreated in Thermal Desktop to simulate its behaviour under lunar conditions. The chassis of the rover was modelled as a rectangular box of 50 cm length, 35 cm width and 30 cm height. The chassis is divided into two parts, the payload compartment and the avionics compartment. The payload compartment is open at the bottom, as the LVS drill is required to make contact with the surface. The avionics compartment is fully enclosed. The core electronics of the rover have been modelled as boxes attached to the radiator, the payload electronics is mounted below but attached to the radiator by a thermal strap. The four wheels of the rover and their motor housings were modelled, however the rover legs have been neglected, as these elements are passive structures. Thermal conductivities of the most important electrical connections were taken into account. Figure 8-19 shows a schematic of the electrical connections, Table 8-7 shows the wires and respective thermal resistances of the connections. Below the rover, a 10 m x 10 m patch of lunar regolith was modelled with a depth of 1 m to provide accurate boundary conditions. The regolith was modelled to have an emissivity of 0.90, an absorptivity of 0.93 and thermal conductivity based on Cremers (1975). The sides and bottom of the regolith block are assumed adiabatic. The surface is modelled at a 75° latitude, to account for potential sun facing slopes and the solar heat flux is set to 1354 W/m^2 for the hotcase.

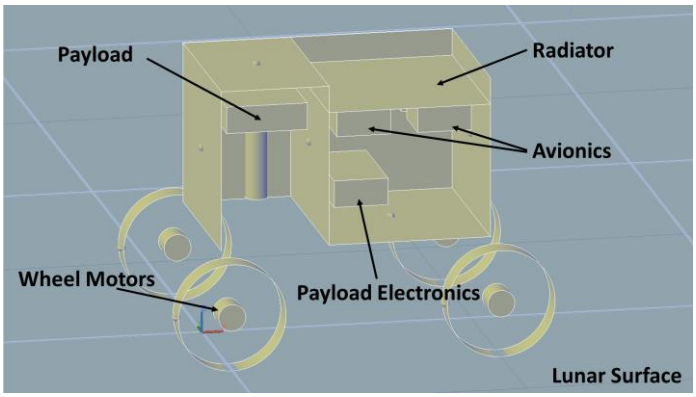

Figure 5-9: Image of the Geometrical Mathematical Model of the Polar rover.

5.2.2 Design Variants

Table 5-4 shows the investigated design variants. The baseline design was investigated under a hotcase and a coldcase. In the hotcase, the rover is illuminated by the sun, moving at full power and actively communicating. In the coldcase, the rover is assumed to be hibernating in shadow, thus no solar illumination was available and internal heat dissipation was necessary to maintain appropriate temperatures.

In addition to the baseline design, two thermal designs were investigated with three variants of thermal rerating. First the baseline thermal design was investigated under the assumption of reduced heater set temperatures due to low temperature rerating, either for all components except the battery, for only the wheel motors or for only the payload and payload electronics. Then a different thermal architecture was investigated, in which the louver was removed by a common radiator panel and thin plate heat switches were introduced between each electronic component and the radiator. This creates an insular thermal architecture, in which there is little heat exchanged between components.

Finally, each case is additionally investigated for a moving rover. In this case, regular heat dissipation cycles occur, as shown in Figure 5-10. It is assumed, that the rover movement will occur in 5 min cycles. First, the COMM system is active for 10 s when the rover receives its command. Then the rover will start moving for 60 s, after which an additional 10 s communication occurs in which the rover transmits its new status. The rover will then rest for 220 s, as the ground control group assess the new situation and determines a new path.

Table 5-4: Investigated model variants for the polar rover

Name	Description
Baseline	The baseline design. Heater set temperatures in accordance with component temperature limits (see Table 5-3).
Baseline Rerated – All	The baseline design, but heater set temperatures for all components except the battery are set to temperatures between -180°C and -40°C. Battery is maintained at -5°C.
Baseline Rerated – Motors	The baseline design, but heater set temperatures for the wheel motors are set to temperatures between -180°C and -40°C.
Baseline Rerated - Payload	The baseline design, but heater set temperatures for the payload and payload electronics are set to temperatures between -180°C and -40°C.
Insular Rerated - All	Louver replaced with heat switches between component and radiator. Heater set temperatures for all components except the battery are set to temperatures between -180°C and -40°C. Battery is maintained at -5°C.
Insular Rerated – Motors	Louver replaced with heat switches between component and radiator. Heater for the wheel motors are set to temperatures between -180°C and -40°C.
Insular Rerated - Payload	Louver replaced with heat switches between component and radiator. Heater for the payload and payload electronics are set to temperatures between -180°C and -40°C.
Baseline Rerated – All - Moving	Identical to Baseline Rerated – All but with additional heat dissipation due to rover movement (see Figure 5-10)
Baseline Rerated – Motors - Moving	Identical to Baseline Rerated – Motors but with additional heat dissipation due to rover movement (see Figure 5-10)
Baseline Rerated – Payload - Moving	Identical to Baseline Rerated – Payload but with additional heat dissipation due to rover movement (see Figure 5-10)
Insular Rerated – All - Moving	Identical to Insular Rerated – All but with additional heat dissipation due to rover movement (see Figure 5-10)
Insular Rerated – Motors - Moving	Identical to Insular Rerated – Motors but with additional heat dissipation due to rover movement (see Figure 5-10)
Insular Rerated – Payload - Moving	Identical to Insular Rerated – Payload but with additional heat dissipation due to rover movement (see Figure 5-10)

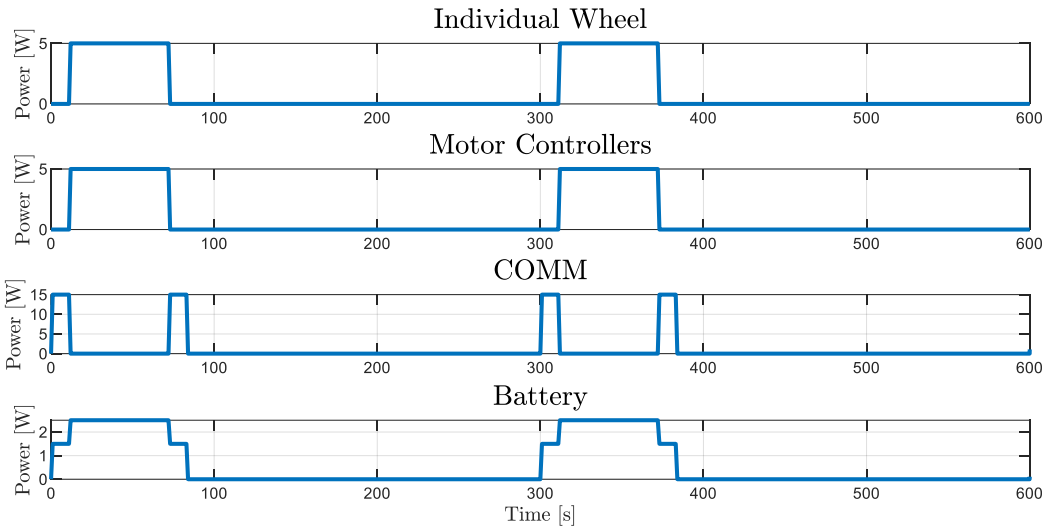

Figure 5-10: Heat dissipation over time for two cycles for the moving rover case.

5.2.3 Results

Baseline

Figure 5-11 shows the steady state temperatures for the hot and cold cases for the baseline variant. The temperature values of the most important elements are also listed in Table 5-5. In both cases, all components can be maintained within their temperature limits. In the hotcase, the temperatures of the electronic elements within the rover vary significantly, with the COMM system reaching almost its limit temperature of 328 K, but the battery remaining at 308 K. For the coldcase, the electronics temperatures are almost equal, with only a 4 K difference between the hottest and coldest of the electronic components.

For the hotcase, the lunar surface temperature at the edge of the simulated area is 287 K, while for the coldcase it is only 10 K. The hotcase value is realistic and within range of expected surface temperatures at the simulated latitudes (Williams et al. 2017). For the coldcase, the simulated surface temperatures of 10 K are in fact much too cold. This is a limitation of a steady state simulation, which does not fully capture the lunar day/night cycle. In addition, no heat flux from the Moon's interior was taken into account.

In terms of operation in shadow, the heat dissipation for the cold case is the most important quantity. Survival heaters maintain components at their respective heater set temperatures. For the baseline design, 9.3 W are required, equivalent to 3.3 h in battery lifetime if a maximum depth of discharge of 40 % is allowed, but not accounting for the thermal inertia of the rover. If the rover enters shadow from an initial temperature of 293.15 K, it takes about 1 h until the wheel motor heaters become necessary and 3.6 h for the battery heater. Thus overall survival time for this case is 4.3 – 6.9 h, with 6 h as the given value by Gscheidle et al. (2022).

Table 5-5: Steady state temperatures for the baseline design

	Temperatures [K]								Heat Dissipation [W]
	Battery	CDH / EPS	COMM	Motor Controllers	Payload	Payload Electronics	Wheels (average)	Lunar Surface	
Hotcase	308.80	316.55	327.89	309.27	296.56	315.53	347.69	287	55
Coldcase	268.90	262.24	262.7	262.32	249.72	262.09	234.77	10	9.3

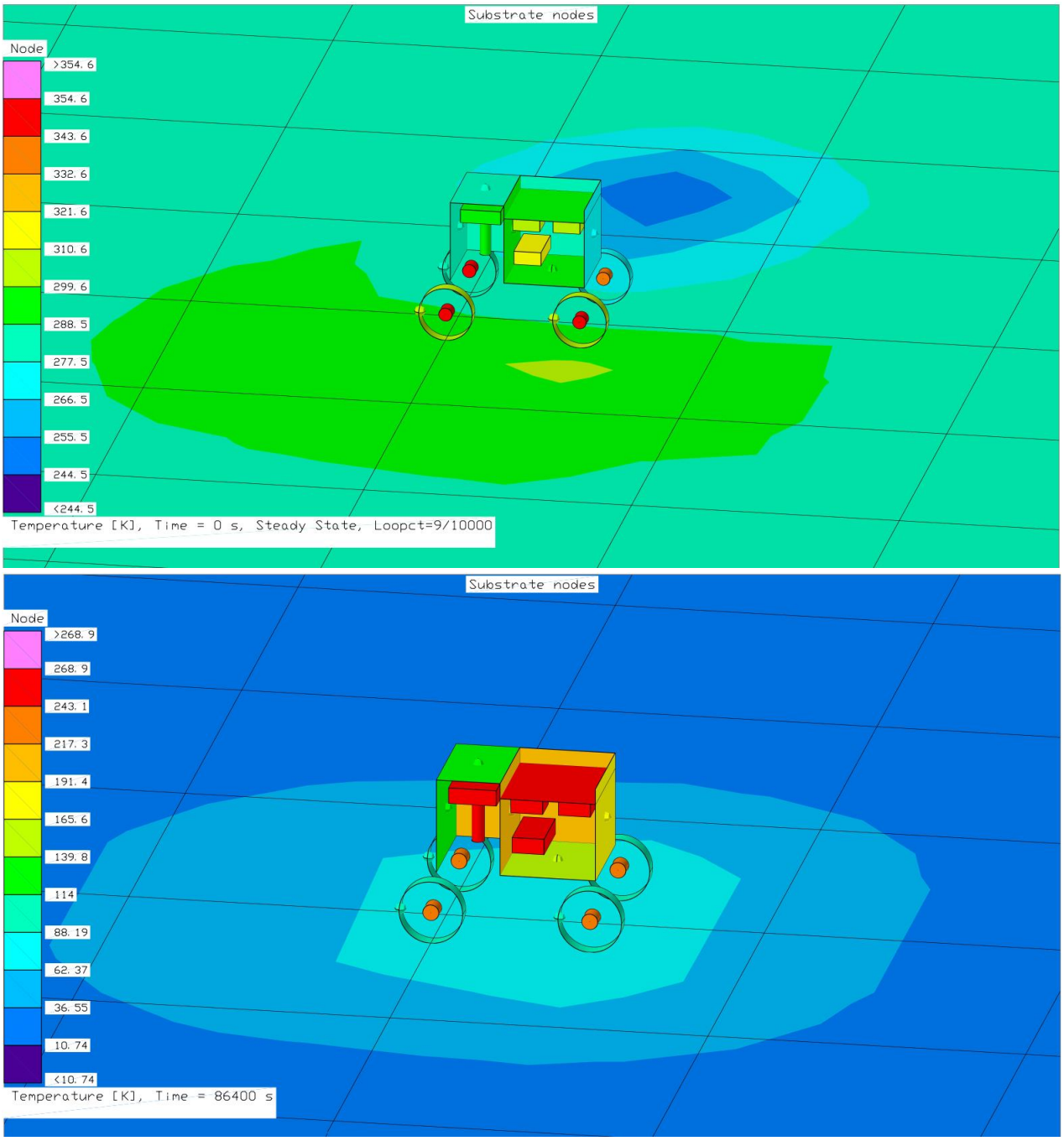

Figure 5-11: 3d visualisations of node temperatures for the baseline hotcase (top) and coldcase (bottom).

Baseline Architecture with Rerated Components

Figure 5-12 shows average heat loss of the rover as a function of the heater set temperatures for the rerated components (other components remain within their rated limits). For the ‘Rerated All’ and ‘Rerated Motors’ configurations, heat loss decreases significantly from 9.3 W to 3.7 W and 3. 9 W. If only the payload components are rerated, no visible reduction in heat loss occurs for lower heater set temperatures. In both cases, the lowest heat loss is reached at a heater se temperature of -140°C, no further reduction occurs at smaller temperatures. The small difference between these configurations indicates, that very little heat loss reduction is achieved from the rerating of the core electronic components and the majority is gained from the rerating of the wheel motors. This is to be expected, as the battery is maintained at -5°C and the other electronics are connected to the same radiator. Thus, the battery heater is maintaining all electronics at similar temperatures.

Slight random variations are visible in the ‘Rerated Payload’ case. These are numeric errors. The steady state is calculated as an average over a transient computation. This allows heaters to be modelled realistically, that is as constant power heat sources that switch on and off at pre-set limit temperatures. This causes temperatures to oscillate between these limit temperatures. The average heat loss is then calculated as the average over a period of 24 h.

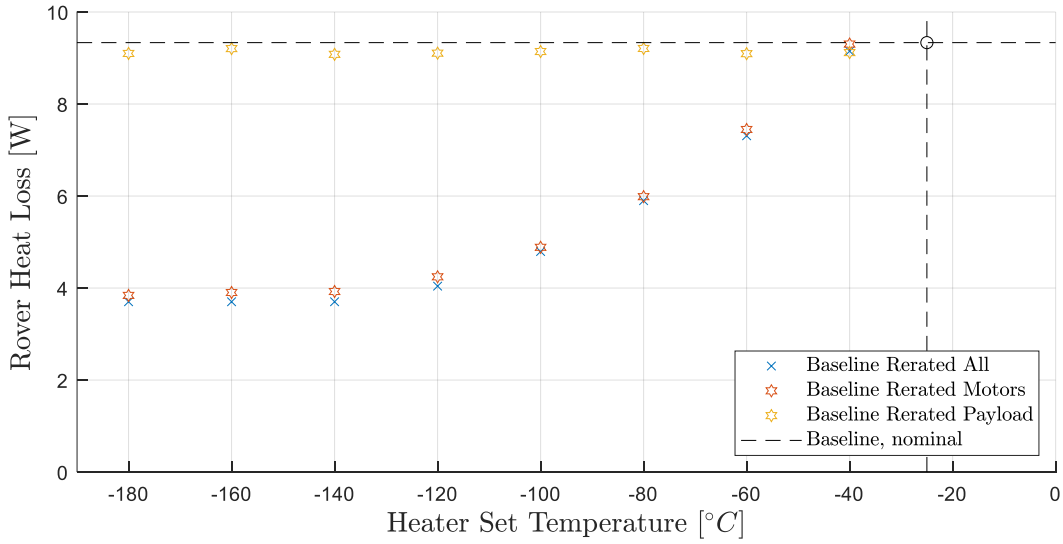

Figure 5-12: Average rover heat loss over heater set temperatures for rerated components for the baseline architecture.

Insular Architecture with Rerated Components

Figure 5-13 shows average heat loss of the rover as a function of the heater set temperatures for the rerated components in the insular architecture. In this case, the heat loss at nominal temperatures is at about 11 W, thus slightly higher than for the baseline design. However, all rerating configurations show significant reduction in heat loss for lower heater set temperatures. If only the payload elements are rerated, heat loss can be reduced to 9.2 W. The configuration ‘Rerated, Motors’ enables a reduction to 5.1 W and a rerating of all components allows a reduction to just 1.4 W. In all cases, the benefit of lower heater set temperature diminishes significantly towards lower temperatures, the biggest benefits are achieved between -40°C and -100°C. For example, in the ‘Rerated, All’ configuration, a heat loss reduction of 69% is achieved by lowering the heater set temperature to -100°C. Lowering the temperatures further to -180°C only provides an additional 18% reduction to 87%.

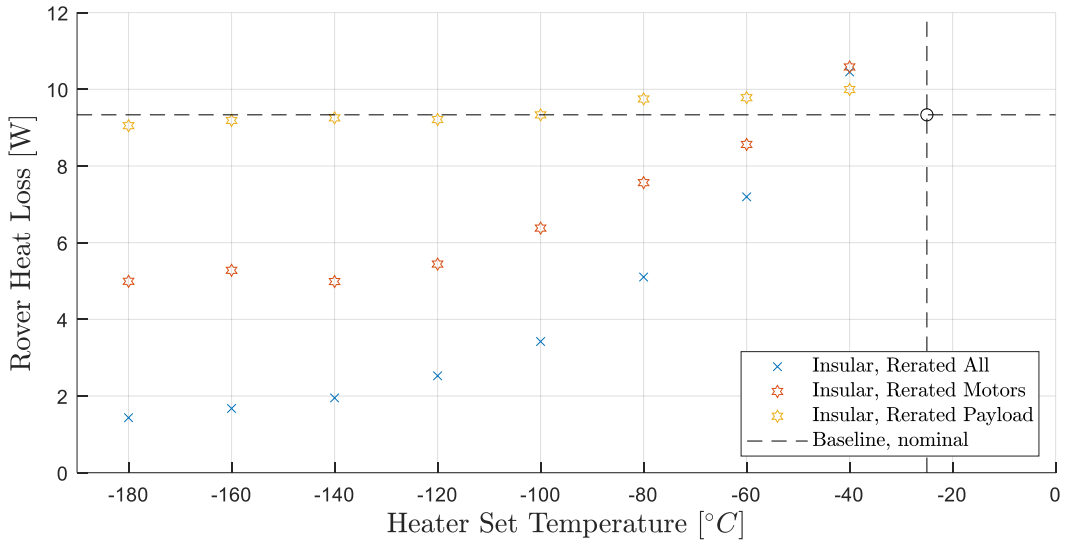

Figure 5-13: Average rover heat loss over heater set temperatures for rerated components for the insular architecture.

Moving Rover

Figure 5-14 and Figure 5-15 show the resulting heat losses for the moving rover with baseline and insular architecture. In the moving scenario, part of the required heating power is supplied by the heat dissipation occurring during the movement, which on average is about 6 W. This maintains the rover at elevated temperatures regardless of the heater set temperatures for the individual rover subsystems. For this reason, a significant reduction in heat loss only occurs down to a temperature of -60°C for the baseline design (- 20 %) and -80°C for the insular design (- 30 %). As with the stationary rover, the heat loss reduction for the baseline design is almost exclusively achieved by a reduction in temperature at the rover wheels. For the insular design, further reduction is achieved through lower temperatures at other components. In the Insular Rerated – All case, heating power is almost exclusively supplied by the heat dissipation from the rover movement and very little additional heat is required.

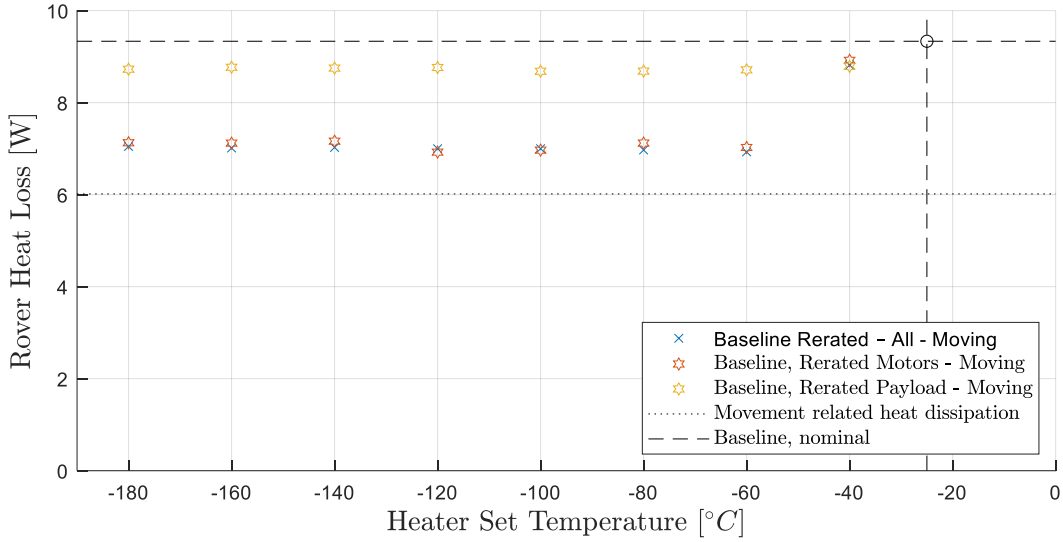

Figure 5-14: Average rover heat loss over heater set temperatures for rerated components for the baseline architecture for the moving case.

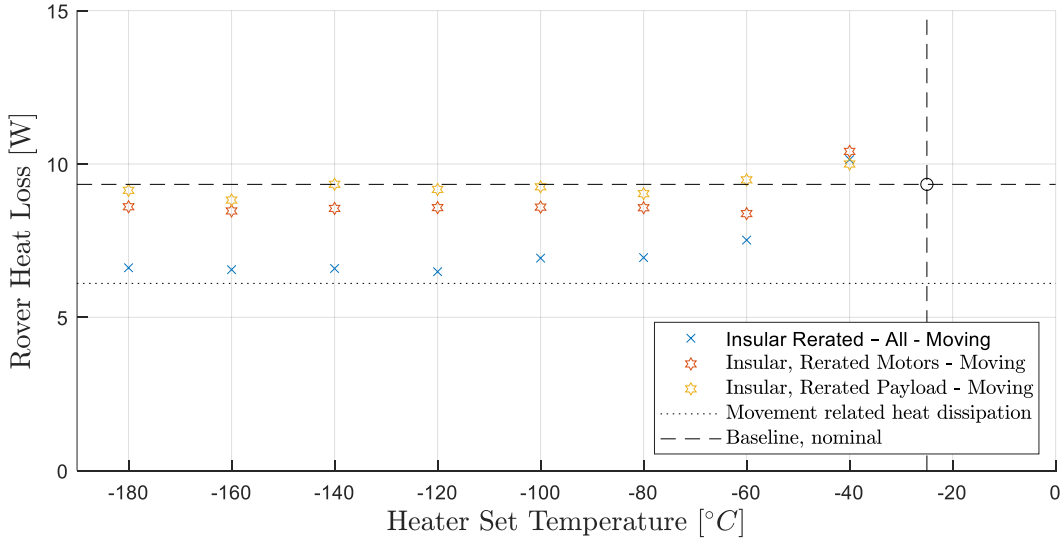

Figure 5-15: Average rover heat loss over heater set temperatures for rerated components for the insular architecture for the moving case.

5.3 Case C: Payloads on a Lunar Lander

The final case is a lunar lander that is modelled loosely after the Astrobotic Peregrine lander (Astrobotic 2020b). Peregrine has a payload capacity of 100 kg and is designed to operate for 192 h on the lunar surface, with no night survival provisions. Each payload may draw 1 W / kg of power and can send up to 10 kbps of data. It should be noted that only limited information is available on the Peregrine lander and that its thermal design will be mission specific. Thus, it is not the goal of this study to create an accurate model of Peregrine. However, the model can be used to investigate the general problems faced by payload thermal designs for static lunar landers.

A thermal model was created in Thermal Desktop that reflects the mid-latitude configuration of the lander. An image of both the Peregrine lander and the thermal GMM are shown in Figure 5-16. The approximate size of the lander model is 2000 mm x 2000 mm x 1200 mm and its most important features are the lander

bus, fuel tanks, payload deck and solar panel. Two payloads of 10 kg each with dimensions of 150mm x 450mm x 200mm are attached to the payload deck: Payload 1 at the illuminated front and Payload 2 at the back in shadow.

For this case, the lander is placed at an arbitrary location of 45° latitude and is investigated at different local times. The main purpose is to determine whether low temperature rerating can provide benefits for individual payloads on lunar landers and not just at night, but also during the daytimes, when parts of the lander are shadowed by the rest of the structure. For this purpose, a steady state thermal simulation is performed to determine if the necessary amount of heating power for the two payloads. The investigation is performed for local times of 12 pm (noon), 3 pm, 4 pm, 5 pm and 12 am (midnight).

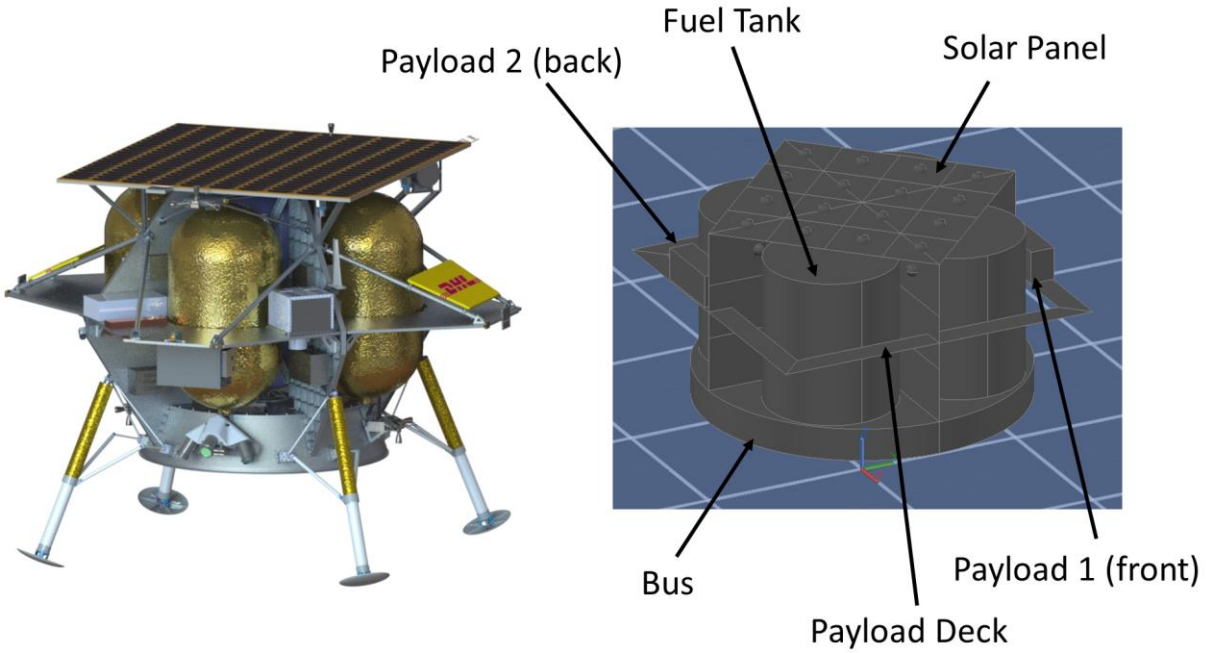

Figure 5-16: Left: Image of the Peregrine lander configuration for the M1 mission (Astrobotic 2020b); Right: GMM of the lunar lander in Thermal Desktop.

5.3.1 Model Description

The model consists of a cylindrical element at the bottom above which two crossed structural plates are placed. The four fuel tanks are mounted in the four corners between the structural plates and the payload deck surrounds the fuel tanks. Finally, the solar panel covers the lander. For the purposes of this study, it was assumed that the cylindrical element will house the core elements of the lander systems to provide power, data handling and communication (the system bus) and the payloads are mounted on the payload deck. The model relies on a passive thermal design, in which the structural plates are used as radiators. The structural plates and payload decks are assumed to have a thermal conductivity equivalent of 5 mm Aluminium plates and the bus and payloads are attached to the structure by thin plate heat switches. The bus, payloads and underside of the solar panels are covered by MLI, 254 µm second surface mirror tape is used on the tanks and bottom of the bus and the structure is covered in Magnesium Oxide White Paint (see Table 2-2 for details). Table 5-6 provides the baseline temperature envelopes for the payloads and bus. The model sits above a 10 m x 10 m x 1 m lunar regolith block, the sides and bottom of which are considered adiabatic. The sky is open to deep space, solar flux of 1367 W/m^2 is assumed and sun position are calculated by Thermal Desktop. As with the previous case studies, the heater set temperatures for the two payloads are varied from -40°C down to -180°C and the necessary heating power to maintain the payload temperatures is monitored.

Table 5-6: Nominal temperature limits for the subsystems of the lander.

Component	Operational temperature limits (nominal)	Operational temperature limits (with ± 15 K margin)
Bus	-20 °C…+85 °C	-5°C…+70 °C
Payload 1 (front)	-55 °C…+85 °C	-40 °C…+70 °C
Payload 2 (back)	-55 °C…+85 °C	-40 °C…+70 °C

5.3.2 Results

Figure 5-7 shows the steady state temperatures for 12 pm, 3 pm and 4 pm local times. As expected, the shadow moves with daytime and becomes longer as sunset approaches. Payload 1 remains illuminated continuously, while Payload 2 remains shadowed in all cases. The 12 pm case represents the hot case scenario and for this reason, an additional 10 W heating power is applied to the payloads representing the heat dissipation from the active payloads. In this case, the surface has an average temperature of 92°C, which is slightly above the 80°C indicated by Astrobotic (2020b) and Williams et al. (2017). This is discrepancy is likely caused by the steady state simulation, which does not take into account the transient heating of the lunar regolith within finite time. Nonetheless, this serves well as a worst case scenario. The resulting system temperatures in this case are 52°C for the bus, 68°C for Payload 1 and 25°C for Payload 2, all within acceptable limits. The relevant temperatures for the other local times are all lower than for the 12 pm hotcase. Figure 5-18 shows the necessary power to maintain payload temperatures above heater set temperatures between -180°C and -40°C. No heating power is necessary for the 12 pm and 3 pm cases. For the 4 pm case, about 0.3 W of heating power become necessary to maintain Payload 2 at -40°C and at 5 pm this rises to 0.7 W for -40°C and 0.05 W for -60°C. In the 12 am case, the lander and its surroundings lie in shadow. In this case, the total necessary heating power both payloads is 7 W at -40°C and steadily drops to zero at -180°C.

As with the simulations for Case B, slight random variations are visible in simulated heating powers. This causes the heating power for -120°C to be slightly higher than for -100°C, which is unexpected. These are numeric errors, likely caused by unideal values for the heater control parameters.

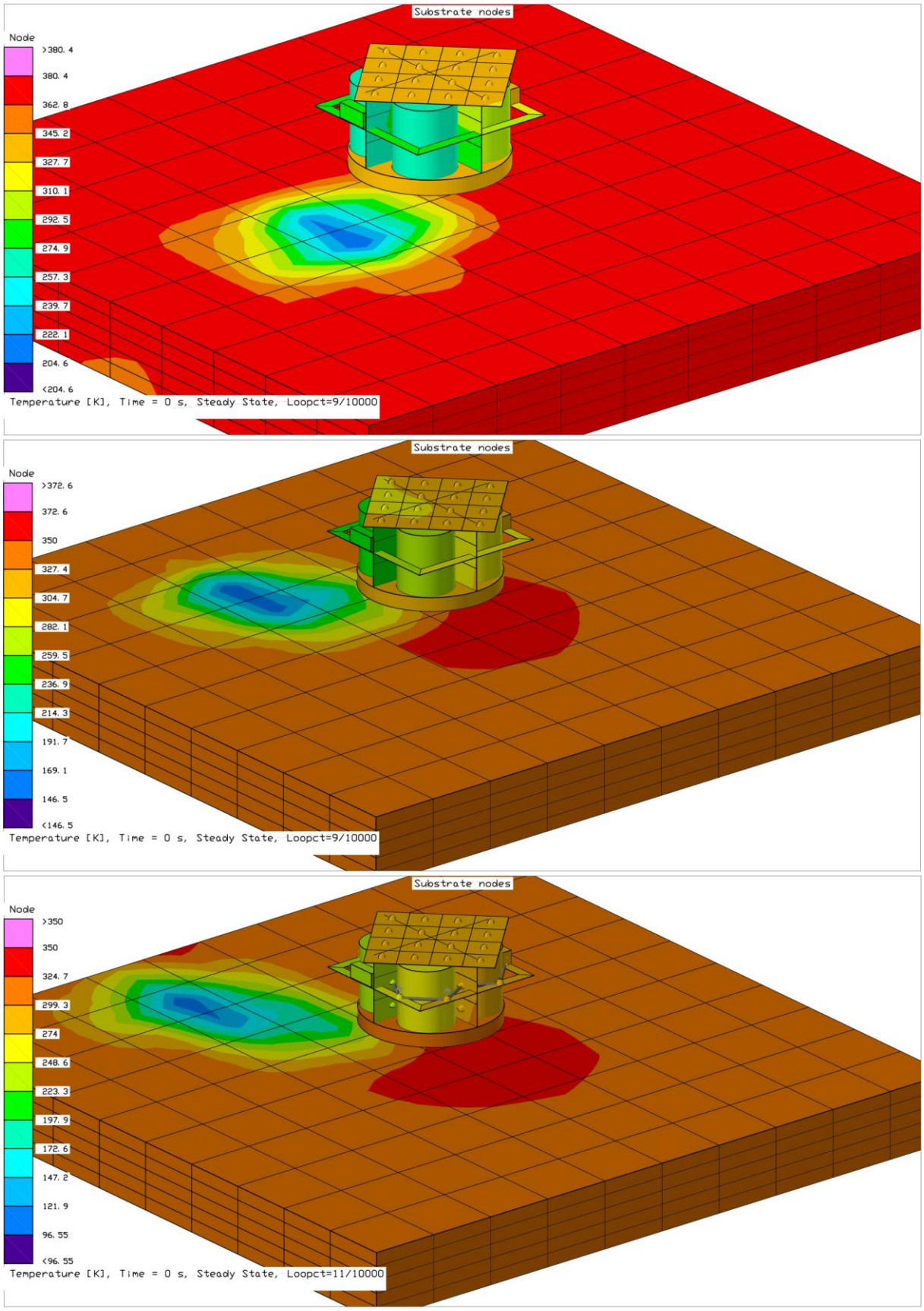

Figure 5-17: Resulting steady-state temperatures for local daytime of 12 pm (top), 3 pm (center) and 4 pm (bottom).

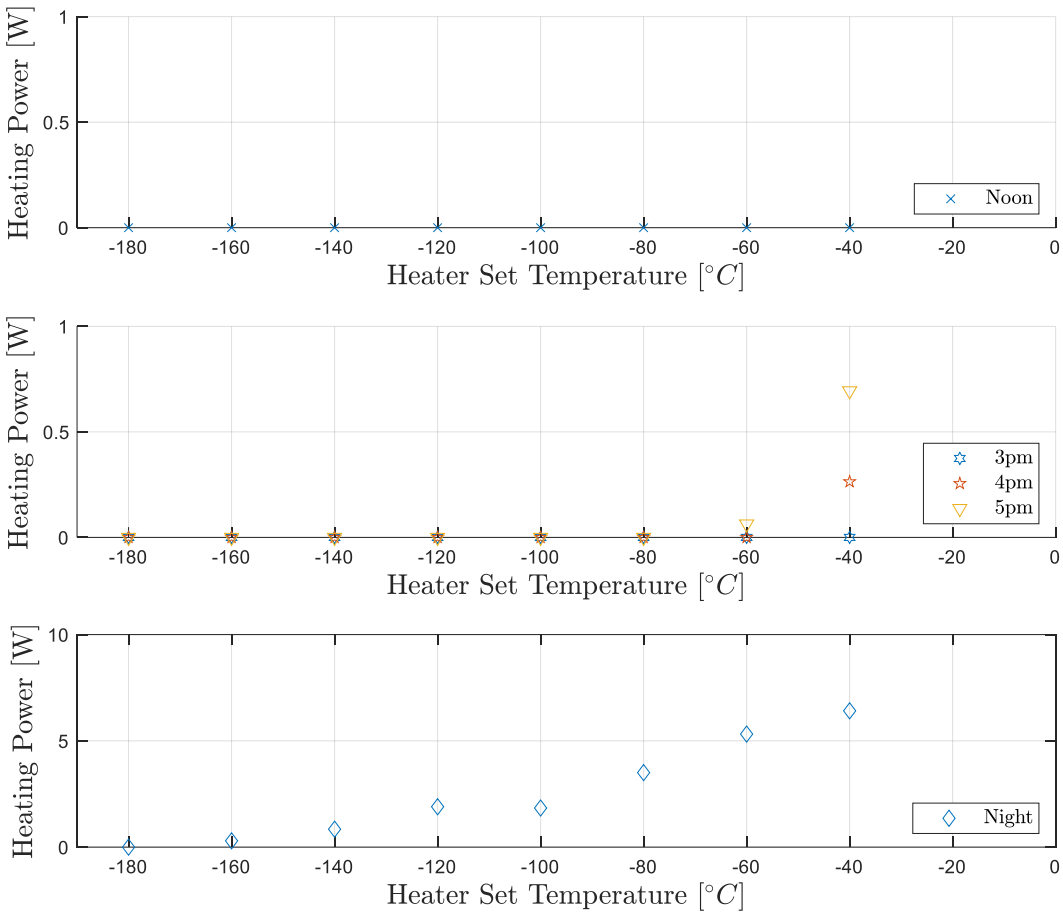

Figure 5-18: Required total heating power to maintain operational temperatures for both payloads in the lunar lander case.

5.4 Discussion

This chapter addresses the third research objective of this thesis:

Objective 3:	**Investigate how extended temperature ranges of subsystems can be translated into valid thermal systems and determine their benefit compared to standard temperature ranges.**

Three case studies were presented to investigate the potential benefit of low temperature rerated components in the context of lunar missions: The LUVMI-X DPP, a lunar polar rover inspired by the Polar Ice Explorer concept and a mid-latitude lander.

For the DPP, a set of conventional thermal design variation were compared to the baseline design with rerated components and an advanced design with more internal insulation and rerated components. It was shown that **low temperature rerating significantly outperformed possible improvements by conventional thermal design improvements**. Lower operational temperatures significantly improve survival times for the unchanged baseline design down to temperatures of -90°C. Improved internal insulation can further synergize with rerated components, but no further benefit is achieved below -110°C. No further improvements were possible beyond this temperature due to heat loss from the battery to other components through electrical connections and physical limitations in insulation. However, this lowest temperature was only reached by the VCAS payload, which was farthest, removed from the battery. For the

other components, the lowest beneficial temperatures were -40°C for the baseline and -70°C with additional internal insulation.

The polar rover was closely modelled after the Polar Ice Explorer mission concept (Gscheidle et al. 2022). The published concept did not yet include a detailed thermal design, but the presented thermal model does approximate the known rover parameters (size, mass, battery capacity). The resulting heat losses of the baseline model in the cold case were within range of the published numbers (see section 5.2.1). In the stationary case, it was shown for the baseline model that heat losses at night could be significantly reduced due to decreased temperatures. However, this only applies to the wheel motors that are removed from the central chassis. No significant benefit can be achieved by rerating of the core components for the baseline design, due to the low thermal resistance between the warm battery and the rest of the electronics. The results show, that **an insular architecture is necessary to increase thermal resistances between components and thus to increase the benefit of lower temperature limits**. With the insular architecture and for the stationary rover case, temperatures of core components can be reduced and overall heat loss can be reduced for heater set temperatures down to -140°C.

For the moving rover case, the benefit of lower temperature limits decreases significantly. Due to the increased heat dissipation, component temperatures remain higher regardless of heater set temperatures. For the baseline architecture, only the heater set temperature for the wheel motors provides a reduction in heat loss and only down to a temperature of -60°C. In this case, once again the insular architecture allows component temperatures and thus heat loss to drop further. But also in this case, no further improvement is achieved below -80°C. It should be noted, that the moving rover case depends heavily on the actual used movement pattern. The assumed heat dissipation used in this scenario included significant pauses between rover actual movements. More continuous rover movement would further increase heat dissipation and thus elevate component temperatures. In that case, lower heater set temperatures would have very little to no effect.

The lunar lander case was loosely modelled after the Astrobotic Peregrine lander. However, only limited information was available on the exact design and especially the thermal design, which is also mission specific. Nonetheless, a simple and functional thermal design for a lander was presented and the necessary heating power for two payloads on the lander was investigated. It was shown that even **during the lunar day, temperatures at the shadowed part of the rover can drop sufficiently low to require some heating**. Low temperature rerating could be a possible solution, but a more elaborate thermal design that transfers heat from the hot illuminated parts of the lander to the cold shadowed parts would likely yield better results during daytime. During the night, a significant amount of heating is necessary to maintain payload temperatures and reducing heater set temperatures can minimize the required heating power. A temperature reduction from -40°C to -80°C already reduces heating power by 50%. However, this will first require a lander with core systems that are able to survive during the night, which Peregrine does not have at this point.

In summary, the presented use cases show that **night time heat loss can be significantly decreased and thus operational lifetime can be meaningfully increased by lowering the operational temperature limits of utilized components.** The benefit is greatest for small, compact systems. **It was also shown, that optimal use of such lower operational limits requires an insular thermal architecture**. However, it was also shown that due to the necessity to keep the battery warm and the resulting heat loss from the battery to other components, there is little benefit for lowering operational temperature limits below certain thresholds. This threshold depends on the thermal design and operational scenario of the system, but for the presented cases, there was very little benefit for temperatures below -120°C.

6 Experimental Validation

The previous chapters have shown that most electronic components can be operated at temperatures significantly lower than their manufacturer ratings indicate and the operation of subsystems of lunar surface systems at decreased temperatures can significantly increase operational lifetimes despite the need to keep batteries at elevated temperatures. These results shall be further verified by an experimental demonstration with a simplified prototype of the LUVMI-X DPP system. The prototype includes a fully operational battery, power system and operational thermal control and is tested in thermal vacuum conditions. The experiment has two purposes: demonstrate the actual low temperature operation of the DPP and to validate the thermal model for the DPP and derived conclusions. Two prototype variants are investigated: the baseline prototype, representing the DPP baseline design (see section 5.1) and an advanced prototype that employs low temperature rerating.

6.1 Baseline Prototype

The baseline prototype was designed to approximate the baseline design of the DPP (see section 5.1). It contains an operational battery and EPS, but its CDH, COMM and VCAS systems were approximated by Aluminium plates covered with resistive Capton heaters to mimic their heat dissipation. It also contains a battery heater to maintain battery temperature. The subsystems and heaters are connected to output channels of the EPS (see Figure 8-18) and activated / deactivated periodically to maintain a specific temperature or heat dissipation. Heater set temperatures were chosen in accordance with the baseline design specifications as shown in Table 6-1. Subsystems are mounted inside the cube structures on stacks, connected by four threaded PLA rods. Aluminium spacers are placed between the subsystems PCBs to ensure a good thermal connection. The COMM dummy is further connected to the radiator panel by a heat switch dummy that was 3d printed from PEEK and designed to mimic the thermal resistance of an open thin plate heat switch. The stacks are enclosed by an aluminium structure covered with aluminium panels. The inside surfaces of the panels were covered with low emissivity Mylar foil to simulate the low emissivity surface coatings used in the actual baseline design. Unlike the actual baseline design, the prototype does not feature solar cells or a patch antenna on its outside surfaces. To still allow a meaningful comparison between experiment and simulation, the simulation model was adjusted to reflect these changes. Figure 6-1 shows a set of images of the baseline prototype. Thermocouple sensors were applied to all subsystems and to the radiator surfaces of both support module and payload module. Additionally, an electrical connection from the outside to the EPS was required to provide UART communication to retrieve telemetry and to allow battery recharging between tests.

Table 6-1: Heat dissipation of dummy subsystems and heaters

Component	Voltage [V]	Resistance [Ω]	Power (active) [W]	Output Channel	Heater set temperature [°C]
CDH	3.3	30.8	0.35	Chan 5	-40
COMM	7.2 / 3.3	4.0 / 15.0	13.7	Chan 1 + Chan 4	-25
VCAS	5	4.1	6.2	Chan 2	-25
Battery Heater	5	8.1	3.1	Chan 3	-5

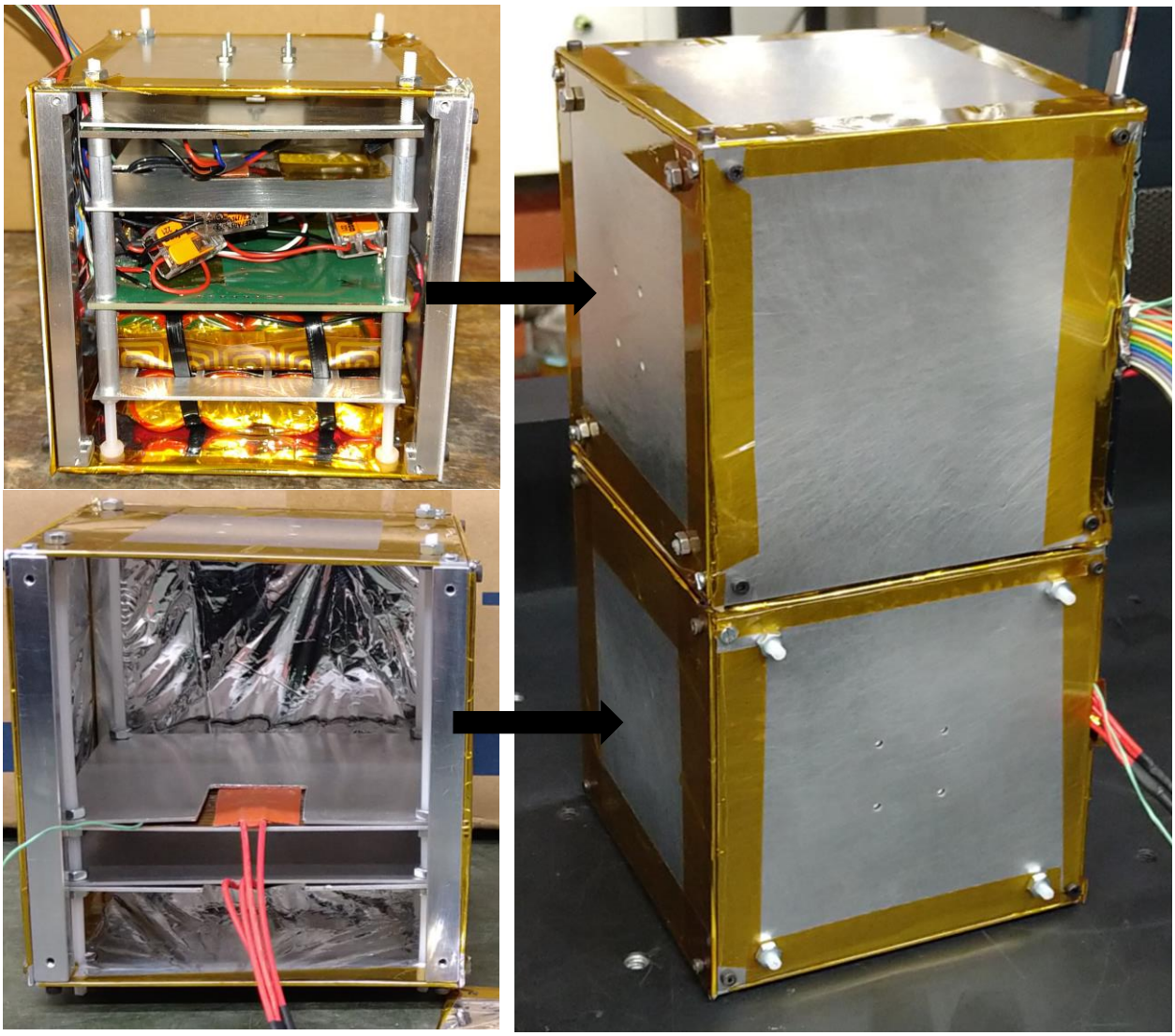

Figure 6-1: Images of support module prototype (top left), the VCAS payload prototype (bottom left) and the assembled baseline prototype (right).

6.2 Advanced Prototype

The advanced prototype was designed to most accurately reflect the ‘Rerated (2), AlN’ variant of the DPP (see section 5.1.2). This mean it utilizes decreased operational temperatures for all subsystems except the battery and it includes additional internal insulation between the battery and the remaining subsystems. For the experiments, a heater set temperature of -85°C was chosen for the electronic subsystems, as shown in Table 6-2. The test results in chapter 3.5 determined that the original design for the EPS was fully operational to -84°C and partially operational to -123°C (not accounting for margins). Design adjustments were discussed to decrease the lower temperature limit for full operational capability down to -120°C. However, due to the global supply chain issues occurring at the time, it was not possible to produce a prototype that

implemented these design changes. For this reason, a prototype of the original EPS design was used. To provide the necessary safety margins, only functions of the EPS were used that were operational to -120°C. For this reason, the 5 V output channels could not be used during the experiments and the electrical connections for the prototype had to be adjusted. Low emissivity Mylar foil was added around the battery module and the diameter of the electrical connections between battery and EPS were reduced. Additionally, the aluminium spacers between battery and EPS were replaced by PEEK spacers to further reduce the thermal connection. An image of the advanced version of the prototype is shown in Figure 6-2.

Table 6-2: Heat dissipation of dummy subsystems and heaters

Component	Voltage [V]	Resistance [Ω]	Power (active) [W]	Output Channel	Heater set temperature [°C]
COMM / CDH	3.3	3.3	1.0	Chan 4	-85
VCAS	3.3	4.0	2.7	Chan 5	-85
Battery Heater	7.2	8.1	6.4	Chan 1	-5

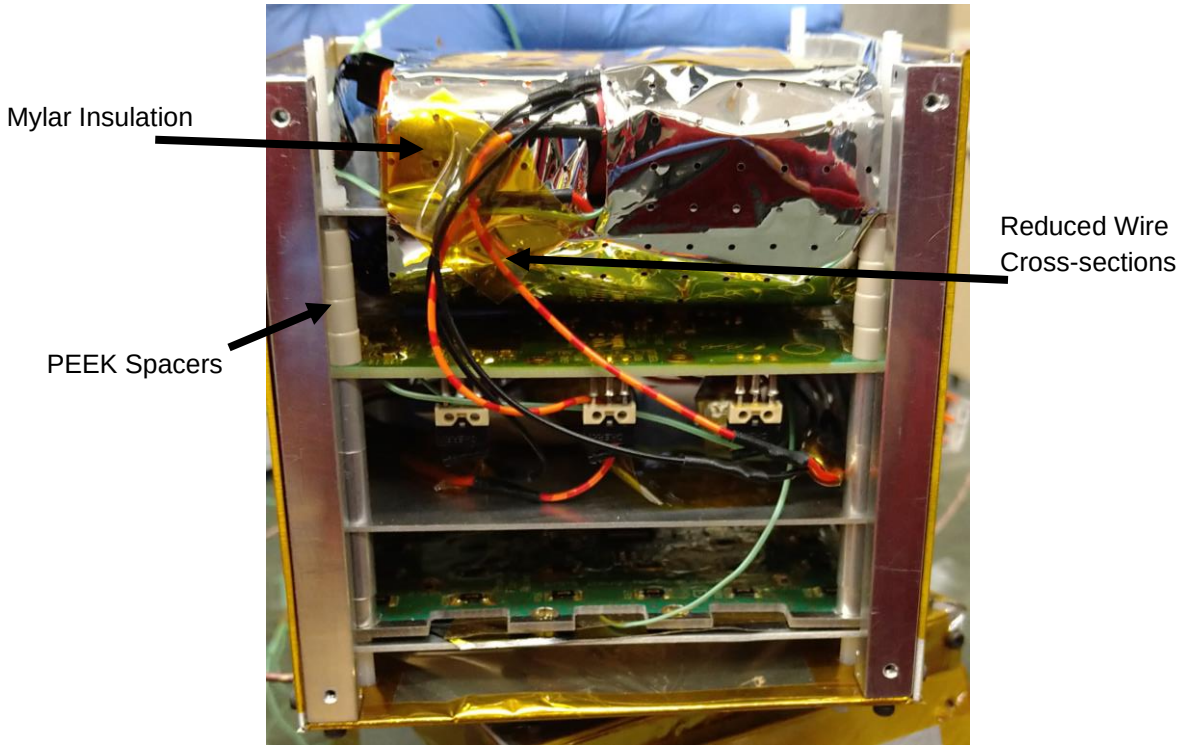

Figure 6-2: Image of the support module of the advanced prototype.

6.3 Experimental Setup and Procedure

The target of the experimental setup is to emulate the cold case conditions for the DPP. To this end, a thermal vacuum test setup was designed. The DPP prototype was placed in a liquid nitrogen cooled cold shroud inside a vacuum chamber at TUM Chair of Astronautics. Figure 6-3 shows an image of the full test setup and of the cold shroud. The cold shroud is a cube shaped enclosure made from 5 mm thick brass sheets of 230 mm x 230 mm x 230 mm dimensions. Attached to the cold shroud is a stainless steel tube that is connected to a 200 l self-pressurized Dewar vessel for liquid nitrogen cooling. On the outside, the shroud is covered by low emissivity Mylar foil for insulation. This allows the shroud to be cooled to about -170°C. On the inside, it is painted black to increase emissivity to facilitate thermal heat exchange to the test specimen. The test specimen are placed in the cold shroud on ceramic tiles to minimize heat loss through conduction.

Before each test, the battery of the prototype was fully charged. Once charged, the test prototype was switched on and temperature monitoring was activated. The test chamber was then evacuated to a pressure below $10^{-4}\ mbar$. Once evacuated, a full liquid nitrogen Dewar was connected to the test setup and self-pressurization of the Dewar was started. This started the liquid nitrogen flow through the cooling loops of the cold shroud to cool down the experiment. One full Dewar allows the cold shroud to cool down to operational temperature, but then the Dewar needs to be refilled to maintain temperatures for the experiment to reach a stationary condition. Figure 8-20 shows the resulting temperatures of the full baseline test.

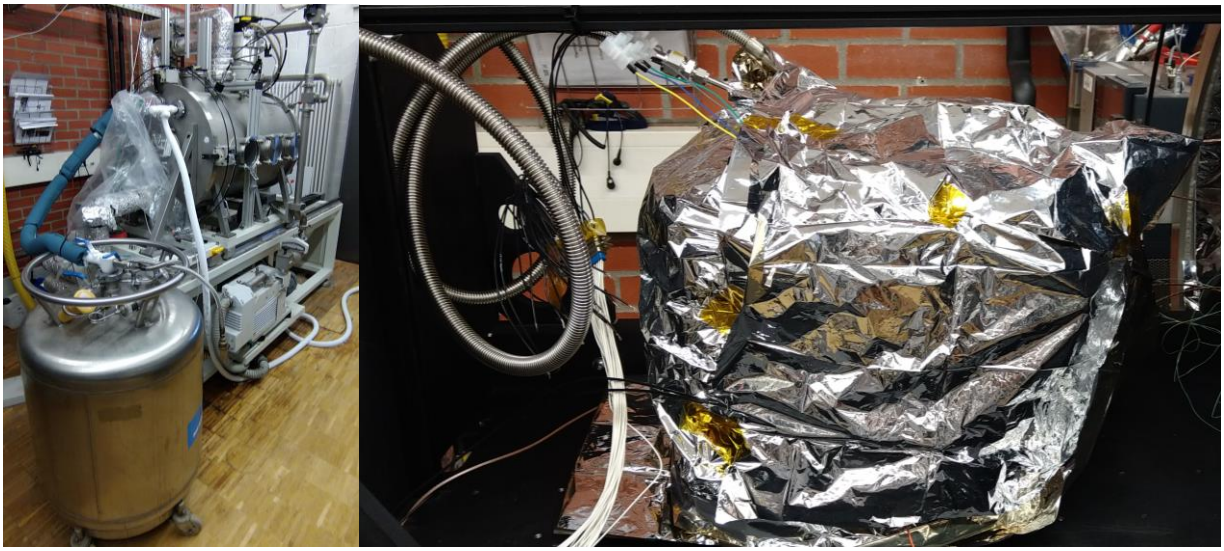

Figure 6-3: Images of the experimental setup. Left: Thermal-vacuum chamber with liquid nitrogen supply; Right: Liquid nitrogen cold shroud inside the vacuum chamber.

6.4 Results

Figure 6-4 shows the results the baseline prototype. The figure shows temperatures and heating power for a quasi-stationary one hour window. In this case, the shroud reached a temperature of -160°C, while the core systems of the DPP were maintained within their operational temperatures. Temperature control was based on an on/off control, causing temperatures of heated systems to oscillate between their switch on and switch off temperatures. Due to the design of the DPP, only battery and VCAS payload heating was necessary, other DPP subsystems were kept sufficiently warm due to heat loss from the battery. The battery temperatures oscillated between -5.1 °C and 2.5 °C and VCAS payload temperatures between -25 °C and -16 °C. EPS, CDH and COMM were maintained at -15 °C, -21 °C and 25°C. On average, 0.71 W of heating power was necessary for the battery heater and 0.47 W for the VCAS heater, resulting in a total heater power consumption of 1.18 W in total. Note that this in addition to 0.11 W of heat dissipation of the EPS.

The results for the advanced prototype are shown in Figure 6-5. Like in the baseline case, only the battery and the VCAS heater were active. In this case the battery oscillates between -5 °C and 7 °C even though the heater set temperature for the battery was not changed. This is due to the change in heater power caused by the switching of the output channels and results in fewer but more intense heating intervals but is of no further relevance here. Due to the added internal insulation, EPS, CDH and COMM were maintained at -60 °C, -61 °C and -73°C. The VCAS payload oscillated between -85 °C and -80 °C. The reduced temperatures resulted in a lower average power consumption of 0.48 W for the battery heater and 0.17 W for the VCAS heater. Thus the total heater consumption for the advanced prototype was reduced to 0.65 W, a 45 % reduction in heater power and a 42 % in total power consumption.

Figure 6-6 and Figure 6-7 show a comparison between simulated temperatures and measured temperatures for both baseline and advanced prototypes. Note that the simulations have been adapted to account for the specific conditions of the prototypes and experiments. One of the biggest distinctions between experiment and simulation comes from the heater control logic. In the experiment, an on/off logic was used, causing

temperature oscillations between the on/off set temperatures. In the simulation, a proportional-integral-derivative power control was used, which resulted in stationary temperatures. In the graphs, this is accounted for by showing the time averaged values for each temperature in addition to the minimum and maximum values. The simulations also appear to underestimate the temperatures of the core elements, because in the experiment, the heater set temperatures of the simulation were used as the lower temperature boundary. Despite this, there is a good agreement between simulation and experiment for both baseline and advanced prototypes. All measured temperatures are within +/- 10 K of the predicted temperature, which is good for a highly simplified model. Note that a +/- 15 K uncertainty margin was used for all component safety limits.

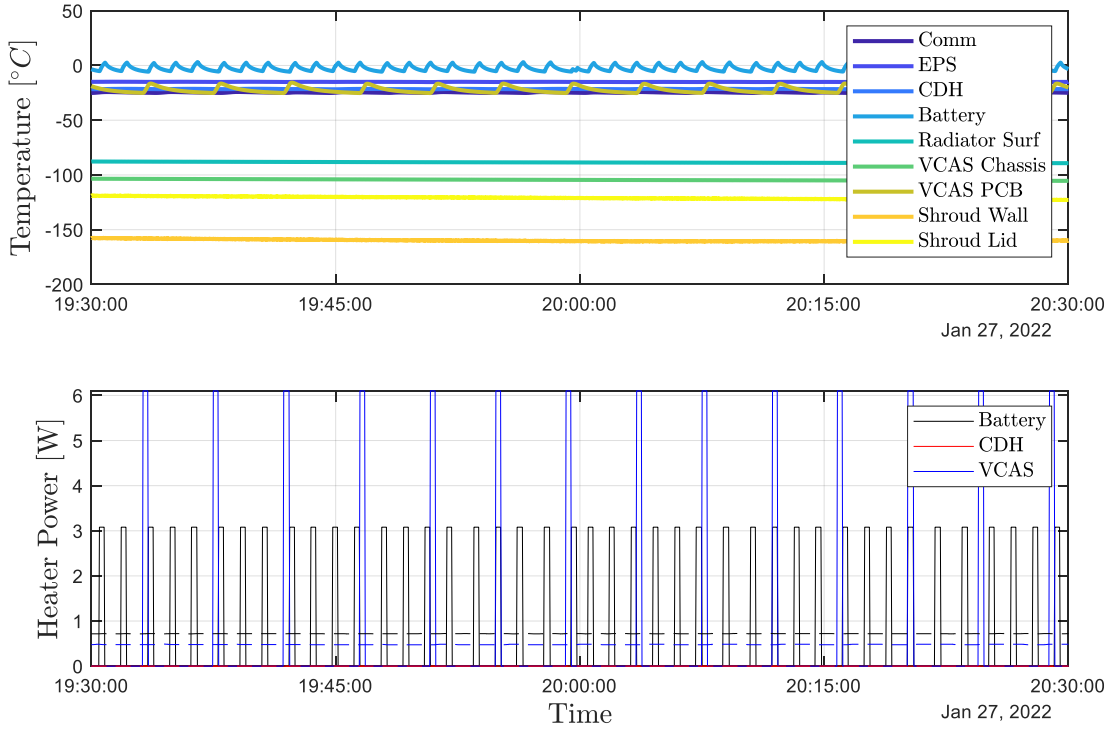

Figure 6-4: Quasi-stationary cold case results for the baseline prototype. Top: Temperatures; Bottom: Heating power for different subsystems (dotted lines indicate time averaged values).

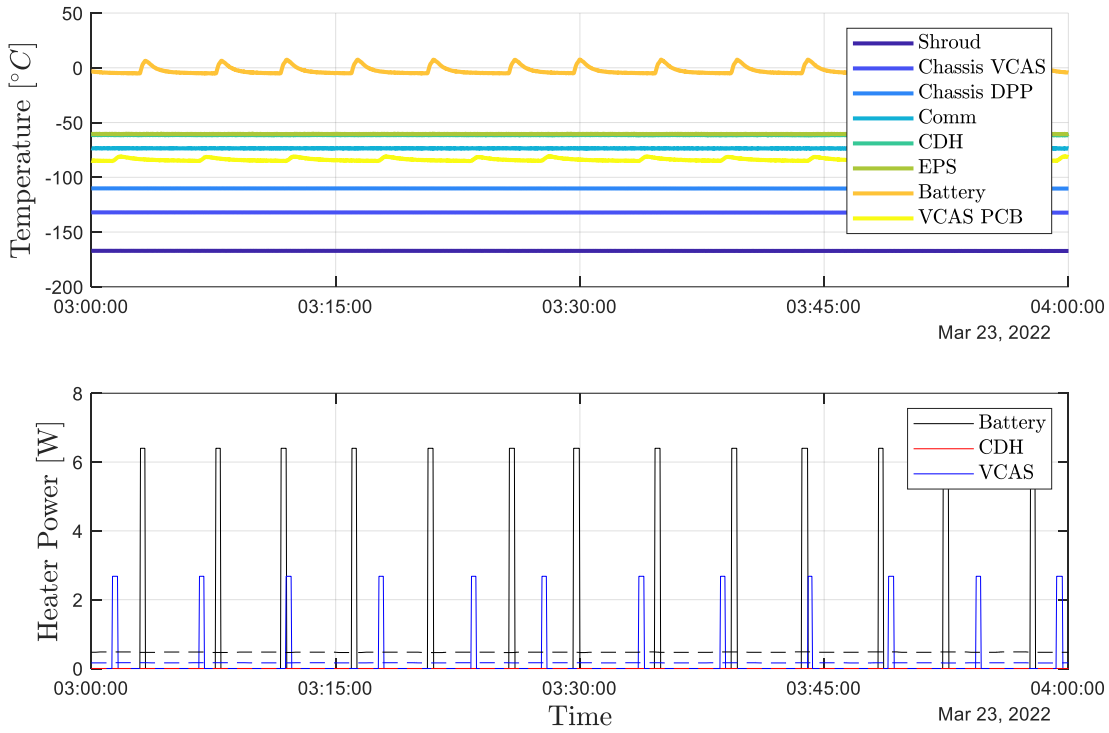

Figure 6-5: Quasi-stationary cold case results for the advanced prototype. Top: Temperatures; Bottom: Heating power for different subsystems (dotted lines indicate time averaged values).

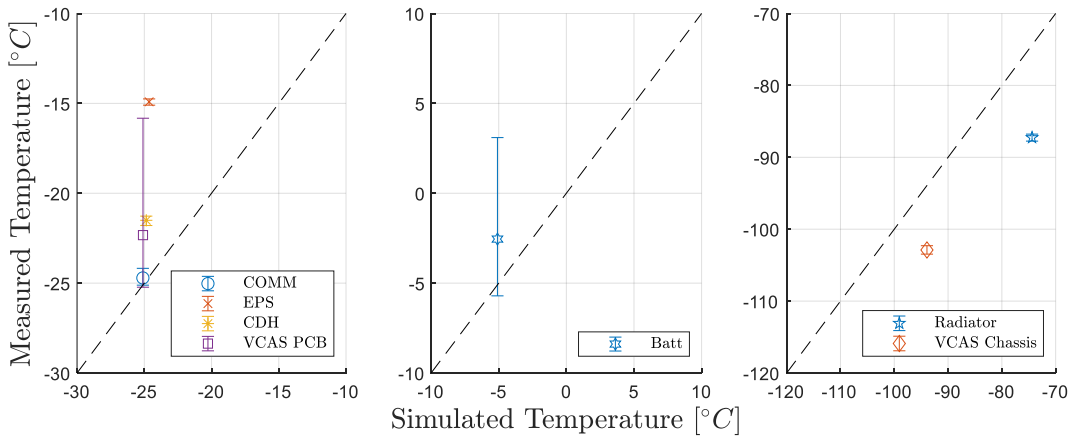

Figure 6-6: Measured temperature during the experiment over simulated temperature from the SIMULINK / SIMSCAPE model for the baseline prototype.

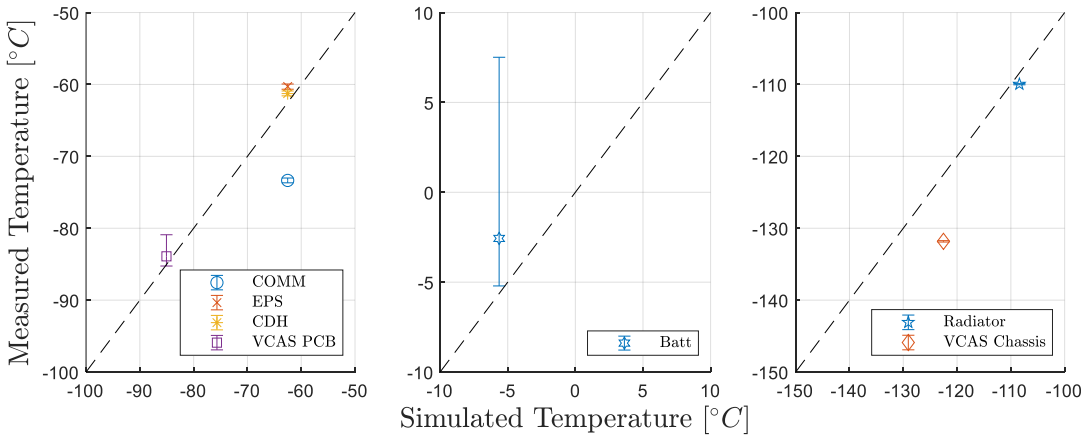

Figure 6-7: Measured temperature during the experiment over simulated temperature from the SIMULINK / SIMSCAPE model for the advanced prototype.

6.5 Discussion

This chapter has two purposes: demonstrate the actual low temperature operation of the power system and to validate the thermal model for the DPP and derived conclusions. To this end, two prototypes of the DPP were designed, built and tested under representative cold case conditions and the results were compared with simulations.

The electronics of the advanced prototype were adapted to operate at -85 °C. The temperature was chosen, because the results of chapter 3 showed that with some adjustments, the EPS can remain operational down to -120° C. Accounting for appropriate margins (see 2.4), this results in heater set temperatures of -85 °C. The operation of the advanced prototype was successful, however stationary cold case temperatures for the operational EPS only reached -60 °C due to internal heat dissipation and residual heat loss from the battery. Nonetheless, even in this case, the necessary heating power could be reduced by 45%, thus **this demonstration can be considered as a successful proof-of-concept for the use of low temperature rerating to increase lunar night time survival**.

It must be noted, that neither the prototypes nor the experimental setup are fully comparable to the conditions of the DPP on the lunar surface. Thus the measured reduction in heating power cannot be translated directly to power savings on the lunar surface. However, they can be used to validate the simulation model used in section 5.1. Thus, the experimental results were compared with adjusted simulations that took the conditions of the test setup into account. The comparison shows good agreement. A maximum deviation of +/- 10 K is very good for a simulation model with only 17 nodes and the deviation is within the +/-15 K margin that was taken into account for temperature uncertainty.

7 Summary & Conclusion

This thesis investigated the potential of low temperature rerating of EEE components and its utility for improved night survival of lunar surface systems. The thesis was structured along three research objectives that were addressed in the previous chapters.

Chapter 3 investigated the rerating potential of EEE components. Six different types of microcontroller were investigated, determining functional temperature limits between -65 °C and -126 °C and 5 out of 6 device types fully functional below -98°C. For the LUVMI-X DPP, the support module subsystems were investigated. The command & data handling module remains fully functional down to -109 °C, a simplified version of the communication system remains operational down to -94 °C. The electrical power system is fully functional to -84 °C and partially operational to -123 °C. Minor design modification have been identified that will allow full functionality of the power system down to -120°C. For the investigated DPP system, **the results confirm the first part of the research hypothesis, that components can be utilized at temperatures significantly below their temperature ratings**. Extrapolation of these results to EEE components in general must be done cautiously, due to the small sample size. However, the especially the results on microcontrollers indicate, that functional lower temperature limits between -100 °C and -120 °C are achievable through rerating and minor system modification / exchange of susceptible parts. Modification of subsystems beyond these values will likely require the use of custom built microcontrollers, which will require a modification effort close to a complete redesign. As discussed in section 2.5, appropriate safety margins need to be applied to these values, so taking into account a total 35 K safety margin, design temperatures for these systems can be between -65 °C and -85 °C.

Chapter 4 investigated energy storage options with regard to lunar night survival. A literature review was presented and alternative options to battery storage were discussed. It was shown that ideal energy storage selection needed to balance low temperature performance and high energy density. The presented data indicated that **specialty low temperature batteries do not provide an advantage over common high energy density cells**, because the reduced heat loss does not make up for lower energy density of these batteries. The energy storage of choice for current generation lunar surface systems are therefore common high energy density lithium ion batteries, like the Panasonic NCR18650BF or LG Chem INR18650MJ1 cells. The ideal operational temperature for these cells depends on the amount of thermal insulation, but is between -20 °C and 0 °C. Promising energy storage options for future lunar surface exploration are regenerative fuel cells with pressurized gas storage and next generation lithium metal batteries, but currently these technologies are not mature enough yet.

Chapter 5 investigated the potential benefit of low temperature rerating. Three lunar surface systems were modelled with thermal simulation software: The LUVMI-X DPP, a small polar rover and a lunar lander. Variations of each system were generated and heater set temperatures were varied to investigate if heat loss could be reduced and battery lifetime during lunar nights could be increased. The core problem in this regard is the discrepancy between the temperature limits of the battery module and the remainder of the system. This leads to heat loss from the battery towards the other systems that limit the temperatures for the other systems. This can be improved by the adoption of insular thermal architectures that thermally insulate individual subsystems, though this is limited by the thermal conductivity of the electrical wiring. **For the DPP it was shown that the use of low temperature rerating can improve survival time by up to 70%. The maximum lifetime can be achieved with a heater set temperature of -110 °C, no further improvements are possible below this threshold**. Similar results were obtained for the polar rover. If an insular thermal design is realised, heat loss at night can be reduced by up to 87%. A reduction of 69% can already be achieved if heater set temperatures are set to -100 °C. In the case of the moving rover, savings are generally smaller and maximum benefits can be achieved already at -80°C. For the lunar lander it was shown that even during daytime, shadowed parts of the lander can require some heating, which could be alleviated by low temperature rerating though other solutions will likely yield better results for landers that only operate

during daytime. For night-time operation, it was shown that the necessary heating power to maintain payload temperatures could be reduced by 50% if heater set temperatures are reduced from -40°C to -80°C.

The results confirm the second part of the research hypothesis, that **low temperature rerating has significant potential to decrease night time heat loss and improve operational lifetime at night**. However, it was also highlighted that it is not necessary to withstand the full envelope of environmental temperatures. The majority of heat loss savings can be realised with a moderate reduction in temperatures down to -80 °C. Incidentally, this is consistent with the result of chapter 3, which showed that minor modifications and requalification are likely sufficient for many parts to achieve operational temperatures in this range. Thus, the core conclusion of this study is **that low temperature rerating for EEE components can deliver a majority of the benefits of a low temperature system architecture without the need of dedicated development of low temperature components**.

It is likely that not all subsystems of a given surface system will be able to be rerated to the same temperature levels. Multiple options exist to deal with this problem. Ideally, an insular thermal design will enable each subsystem to be operated to its limit. If that is not possible, e.g. due to tight volume restrictions like in the case of the DPP, a subsystem stack must either be operated at the highest necessary temperature or subsystems need to be selectively switched off. For example, in case of the DPP, the simplified communications module had a stricter temperature limit than the other components. In this case, the device could be switched off for the majority of the time and only switched on if temperatures are raised. Another method would be a rearrangement of the stack, to move it closer to the battery and thus raising its temperature. However, this would lead to problems during the daytime, due to the high heat dissipation of this component. In this study, particular attention was given to the power management system, as it is the most fundamental subsystem that controls the activity of all other systems.

In chapter 6 an experimental demonstration for the DPP is described. Two prototype variants of the DPP were built: a baseline variant representing the original design and an advanced prototype that utilizes lower operational temperatures. The prototypes feature a fully operational power system including battery module and power distribution system and include dummy systems that mimic the heat dissipation for the other subsystems. The results demonstrate successful operation of the advanced prototype at temperatures below the rated limits of its components and validate the simulation results from section 5.1.

8 References

8.1 Literature

AI-Tinker (2017): ESP32-CAM Product Specification. Available online at https://www.seeedstudio.com/ESP32-CAM-Development-Board-with-camer-p-3153.html, checked on 3/24/2022.

Akturk, A. et al. (2012): CoolSPICE: Spice for Extreme Temperature Range Integrated Circuit Design and Modeling. In *SISPAD, Denver, CO,*, Article ISBN 978-0-615-71756-2.

Altreonic NV (2019): Hybrid Carbon-based Supercapacitor Cell Specifications. Available online at https://docplayer.net/139158780-Hybrid-carbon-based-supercapacitor-cell-specifications.html, checked on 9/8/2022.

Amann, R. (2019): Controllable Battery Charge Regulator for CubeSat Applications. Master Thesis. TUM, Munich, Germany. Department of Electrical Engineering and Computer Engineering.

Anderson, W. G. et al. (2009): Variable Conductance Heat Pipe Radiators for Lunar and Martian Environments. In : AIP Conference Proceedings. *SPACE, PROPULSION & ENERGY SCIENCES INTERNATIONAL FORUM: SPESIF-2009.* Huntsville (Alabama), 24–26 February 2009: AIP, pp. 57–66.

Andrea, D. (2020): Lithium-Ion Batteries and Applications. A Practical and Comprehensive Guide to Lithium-Ion Batteries and Arrays, from Toys to Towns: Volume 1: Batteries. *Norwood*: Artech House.

Astrobotic (2020a): CubeRover Payload User's Guide v1.4. Available online at https://space.skyrocket.de/doc_sdat/change-3.htm, checked on 8/7/2020.

Astrobotic (2020b): PEREGRINE LUNAR LANDER. PAYLOAD USER'S GUIDE. Available online at https://www.astrobotic.com/wp-content/uploads/2021/01/Peregrine-Payload-Users-Guide.pdf, checked on 7/21/2022.

Atmel Corporation (2005): Atmel ATmega640/V-1280/V-1281/V-2560/V-2561/V. 8-bit Atmel Microcontroller with 16/32/64KB In-System Programmable Flash. *San Jose, CA, United States*. Available online at http://ww1.microchip.com/downloads/en/DeviceDoc/Atmel-2549-8-bit-AVR-Microcontroller-ATmega640-1280-1281-2560-2561_datasheet.pdf, updated on Feb. 2014, checked on 9/16/2019.

Avery, K. et al. (2011): Total Dose Test Results for CubeSat Electronics. In : 2011 IEEE Radiation Effects Data Workshop. *2011 IEEE Radiation Effects Data Workshop.* Las Vegas, NV, 25.07.2011 - 29.07.2011: IEEE, pp. 1–8. Available online at https://ieeexplore.ieee.org/abstract/document/6062504, checked on 11/26/2019.

Barco, A. et al. (2019): Design and Development of the ESA Am-Fueled Radioisotope Power Systems. In : 2019 IEEE Aerospace Conference. *2019 IEEE Aerospace Conference.* Big Sky, MT, USA, 02.03.2019 - 09.03.2019: IEEE, pp. 1–11.

Bauer, B. (2020): Evaluation of COTS Electronic Components for Use on the Lunar Surface. Semester thesis. TUM.

Bauer, B. (2021): Coupled Power-/Thermal System Optimization for a Small Lunar Surface System. Master Thesis. Technische Universität München. Chair of Astrnoautics.

Benna, M. et al. (2019): SEAL: SURFACE AND EXOSPHERE ALTERATIONS BY LANDERS. In *Lunar and Planetary Science Conference*. Available online at https://www.hou.usra.edu/meetings/lpsc2019/pdf/2364.pdf, checked on 10/23/2021.

Bewick, R.; Sanchez Cuartielles, J.-P.; McInnes, C. (2011): Use of orbiting reflectors to decrease the technological challenges of surviving the lunar night. In *62nd International Astronautical Congress 2011*. Available online at https://strathprints.strath.ac.uk/33360/.

Biswas, J. et al. (2020): Searching for potential ice-rich mining sites on the Moon with the Lunar Volatiles Scout. In *Planetary and Space Science* 181, p. 104826. DOI: 10.1016/j.pss.2019.104826.

Biswas, J.; Kullak, K.; Gancet, J. (2021a): LUVMI-X: Platforms Detailed Design Report. Part 2: Payload Platform Detailed Design (LUVMI-X-SPACEAPPS-WP7-D7.2-v1.0).

Biswas, J.; Malzone, P. Q.; Rößler, F. (2021b): Energy storage selection and operation for night-time survival of small lunar surface systems. In *Acta Astronautica* 185, pp. 308–318. DOI: 10.1016/j.actaastro.2021.04.042.

Boehnhardt, H. et al. (2017): The Philae lander mission and science overview. In *Philosophical transactions. Series A, Mathematical, physical, and engineering sciences* 375 (2097). DOI: 10.1098/rsta.2016.0248.

BostonPower (2011): Swing 5300 Rechargeable Lithium-Ion Cell - Datasheet. With assistance of Stephen Christo (BPI.DS.SWG5300_0312), checked on 4/22/2020.

Bourne, J. et al. (2008): Ultra-Wide Temperature (-230°C to 130°C) DC-Motor Drive with SiGe Asynchronous Controller. In : 2008 IEEE Aerospace Conference. *2008 IEEE Aerospace Conference.* Big Sky, MT, 01.03.2008 - 08.03.2008: IEEE, pp. 1–15.

Buchanan, E. D. et al. (2012): Cryogenic applications of commercial electronic components. In *Cryogenics* 52 (10), pp. 550–556. DOI: 10.1016/j.cryogenics.2012.06.017.

Buchmann, I. (2016): Batteries in a portable world, 4th edition. A Handbook on Rechargeable Batteries for Non-Engineers. *Richmond*: Cadex Electronics.

Cai, G. et al. (2020): An ester electrolyte for lithium–sulfur batteries capable of ultra-low temperature cycling. In *Chem. Commun.* 56 (64), pp. 9114–9117. DOI: 10.1039/D0CC03798B.

Calzada-Diaz, A.; Acierno, K.; Lamamy, J. (2018): Ispace's Polar Ice Explorer: A commercial ISRU exploration mission to the south pole of the Moon. In *International Astronautical Congress*, Article IAC-18,A3,2B,4,x43069.

Cardarelli, F. (2018): Materials Handbook. *Cham*: Springer International Publishing. Available online at https://link.springer.com/book/10.1007/978-3-319-38925-7, checked on 2/7/2021.

Carpenter, J. (2019): ESA Strategy for Science at the Moon. Available online at https://exploration.esa.int/web/moon/-/61371-esa-strategy-for-science-at-the-moon, checked on 6/29/2021.

Carrasco, J. A. et al. (2018): Review of Design Strategies and Benefits for Electronic Assemblies Operating at Low Temperatures in Space Applications. In *Journal of Space Exploration* (7).

Cénac-Morthé, C. et al. (2016): ROSETTA LANDER BATTERIES EXPERIENCE DURING ALL OPERATION PHASES. In *European Space Power Conference*.

Chen, R. et al. (2018): Core Characterization and Inductor Design Investigation at Low Temperature. In : 2018 IEEE Energy Conversion Congress and Exposition (ECCE), pp. 4218–4225.

Chen Deng-yi et al. (2016): Design and Experimental Verification of Chang'E-3 Moon-night Survival Device for APXS. In *Chinese Astronomy and Astrophysics* 40 (3), pp. 414–424. DOI: 10.1016/j.chinastron.2016.07.001.

Chin, K. B. et al. (2014a): Li-ion battery and super-capacitor Hybrid energy system for low temperature SmallSat applications. In *28th Conference on Small Satellites*. Available online at https://www.researchgate.net/publication/265087633_Li-ion_battery_and_supercapacitor_Hybrid_energy_system_for_low_temperature_Smallsat_applications.

Chin, K. B. et al. (2014b): Li-ion battery and super-capacitor Hybrid energy system for low temperature SmallSat applications. In *28th Annual Conference on Small Satellites* 2014. Available online at https://www.researchgate.net/publication/265087633, checked on 1/28/2020.

Colaprete, A. et al. (2018): Multi-Lunar Day Polar Missions with a Solar-Only Rover. Survive and operate through the lunar night workshop, 2018, checked on 1/23/2019.

Colaprete, A. et al. (2020a): The Volatiles Investigating Polar Exploration Rover (VIPER) Mission: Measurement Goals and Traverse planning. In *Lunar and Planetary Science Conference*, Article 2241.

Colaprete, A. et al. (2020b): THE VOLATILES INVESTIGATING POLAR EXPLORATION ROVER PAYLOAD. In *51st Lunar Planetary Science Conference*.

COMCHIP (2002): Datasheet - SMD Zener Diode CZRU52C2. Available online at https://media.digikey.com/pdf/Data%20Sheets/Comchip%20PDFs/CZRU52C2-CZRU52C39_DS.pdf, checked on 1/27/2022.

Conel, J. E.; Nash, D. B. (1970): Spectral reflectance and albedo of Apollo 11 lunar samples: Effects of irradiation and vitrification and comparison with telescopic observations. In *Geochimica et Cosmochimica Acta Supplement* 1, p. 2013.

Creel, R. (2018): Lessons Learned from Missions that Have Survived Lunar Night (Surveyor, ALSEP, Lunokhod). In *Survive and operate through the Lunar Night Workshop*.

Cremers, C. J. (1975): Thermophysical properties of Apollo 14 fines. In *J. Geophys. Res.* 80 (32), pp. 4466–4470. Available online at https://www.scopus.com/inward/record.uri?eid=2-s2.0-77957335872&partnerID=40&md5=ba57a1c48fe36dcdfa4fc21ab2784384.

Currie, D. G. et al. (2020): THE NEXT GENERATION LUNAR RETROREFLECTOR (NGLR) FOR 2021 DEPLOYMENT. In *Lunar and Planetary Science Conference*. Available online at https://www.hou.usra.edu/meetings/lpsc2020/pdf/3003.pdf, checked on 10/22/2021.

Darcy, E. (2012): COTS Li-ion Cells; How rugged are new designs. In *Nasa Aerospace Battery Workshop, Huntsville, AL*.

De-Leon, S. (2017): Space Batteries Market Review 2017. In *Nasa Aerospace Battery Workshop,* checked on 12/20/2019.

Department of Defence (2016): TEST METHOD STANDARD. Microcircuits. Department of Defence, United States of America. *Washington D.C. (*MIL-STD-883K). Available online at http://everyspec.com/MIL-STD/MIL-STD-0800-0899/MIL-STD-883K_54326/, checked on 2/16/2020.

Donabedian, M. et al. (2002): Insulation. In David G. Gilmore (Ed.): Spacecraft thermal control handbook. 2. ed. El Segundo, California: Aerospace Press, pp. 161–205.

Donini, L. et al. (2016): Move-II Command and Data Handling. Critical Design Review - Documentation. Institute of Astronautics, Technical University of Munich.

DOOSAN (2021): DP30 Powerpack - Specification. Available online at https://www.doosanmobility.com/en/products/powerpack/, checked on 3/19/2021.

Dutczak, J. (2013): Compressed hydrogen storage in contemporary fuel cell propulsion systems of small drones. In *IOP Conf. Ser.: Mater. Sci. Eng.* 421, p. 42013. DOI: 10.1088/1757-899X/421/4/042013.

ECSS Executive Secretariat (2016): Thermal Analysis Handbook. Space Engineering (ECSS-E-HB-31-03A).

ECSS Executive Secretariat (2021): Space product assurance. Electrical, electronic and electromechanical (EEE) components (ECSS-Q-ST-60C Rev.2). Available online at https://ecss.nl/standard/ecss-q-st-30-11c-rev-2-derating-eee-components-23-june-2021/, checked on 4/25/2022.

Emerson J. Speyerer; Mark S. Robinson (2013): Persistently illuminated regions at the lunar poles: Ideal sites for future exploration. In *Icarus* 222 (1), pp. 122–136. DOI: 10.1016/j.icarus.2012.10.010.

Energizer: Product Datasheet - Energizer L91. With assistance of Corey Crell (L91GL1218). Available online at https://data.energizer.com/pdfs/l91.pdf, checked on 3/18/2021.

England, T. et al. (2014): Cold-capable, radiation-hardened SiGe BiCMOS wireline transceivers. In *IEEE Aerosp. Electron. Syst. Mag.* 29 (3), pp. 32–41. DOI: 10.1109/MAES.2014.6805364.

eoPortal Directory (2019): Beresheet (Hebrew for "Genesis") Lunar Lander of SpaceIL, Israel. ESA. Available online at https://directory.eoportal.org/web/eoportal/satellite-missions/b/beresheet, checked on 11/10/2021.

eoPortal Directory (2021): CLPS (Commercial Lunar Payload Services) Program. ESA. Available online at https://directory.eoportal.org/web/eoportal/satellite-missions/c-missions/clps, checked on 10/22/2021.

ESA (2020): An overview of missions to the Moon. Available online at https://www.esa.int/ESA_Multimedia/Images/2019/07/Lunar_missions_overview, updated on 6/18/2020, checked on 4/29/2021.

Evans, A. (2019): Design and Testing of the CubeSat Form Factor Thermal Control Louvers. In *33rd Annual AIAAIUSU Conference on Small Satellites*, Article SSC19-P4-23.

Fairchild, M. R. et al. (2002): Emerging Substrate Technologies for Harsh-Environment Automotive Electronics Applications. In *SAE Technical Paper Series* (2002-01-1052).

Fairchild Semiconductor (2007): Datasheet - FDS8870 N-Channel Power Trench MOSFET. Available online at https://rocelec.widen.net/view/pdf/azxt79yuql/FAIRS24715-1.pdf?t.download=true&u=5oefqw, checked on 1/27/2022.

Fairchild Semiconductor (2013): Datasheet - FPF2700 / FPF2701 / FPF2702 — AccuPower™ 0.4~2A Adjustable Over-Current Protection Load Switches (Rev. 1.0.3). Available online at https://rocelec.widen.net/view/pdf/mhyxqjr8f0/FAIRS46409-1.pdf?t.download=true&u=5oefqw, checked on 1/27/2022.

Fau, G. et al. (2019): LUVMI Payload Design Report. H2020 Project Report. Space Applications Services (LUVMI-D6.1).

Fisch, P. R. M.; Bitanga, J. M.; Whittaker, W. L. (2020): THERMAL MODELING AND DESIGN OF A MICRO-ROVER FOR LUNAR POLAR EXPLORATION. In *i-Sairas* (5058). Available online at https://www.hou.usra.edu/meetings/isairas2020fullpapers/pdf/5058.pdf.

G. H. Heiken; D. T. Vaniman; B. M. French (Eds.) (1991): Lunar Sourcebook : a user's guide to the Moon. Lunar and Planetary Insitute: Cambridge University Press.

Garceau, N. M. et al. (2015): Performance test of a 6 L liquid hydrogen fuel tank for unmanned aerial vehicles. In *IOP Conf. Ser.: Mater. Sci. Eng.* 101, p. 12130. DOI: 10.1088/1757-899X/101/1/012130.

Garrett, J. et al. (2007 - 2007): Development of a DC Motor Drive for Extreme Cold Environments. In : 2007 IEEE Aerospace Conference. *2007 IEEE Aerospace Conference.* Big Sky, MT, USA, 03.03.2007 - 10.03.2007: IEEE, pp. 1–12.

Geeroms, D. et al. (2019): ARDUSAT, AN ARDUINO-BASED CUBESAT PROVIDING STUDENTS WITH THE OPPORTUNITYTO CREATE THEIR OWN SATELLITE EXPERIMENTAND COLLECT REAL-WORLD SPACE DATA. Hasselt University. *Diepenbeek, Belgium*. Available online at https://pdfs.semanticscholar.org/5ab3/ad770bf2a97d944bc064f6fbcc8dac11756e.pdf, checked on 9/16/2019.

George, A. D.; Wilson, C. M. (2018): Onboard Processing With Hybrid and Reconfigurable Computing on Small Satellites. In *Proc. IEEE* 106 (3), pp. 458–470. DOI: 10.1109/JPROC.2018.2802438.

Gerber, S. S. et al. (2004): Performance of high-frequency high-flux magnetic cores at cryogenic temperatures. In : IECEC '02. 2002 37th Intersociety Energy Conversion Engineering Conference, 2002. *2002 37th Intersociety Energy Conversion Engineering Conference (IECEC).* Washington, WA, USA, 29-31 July 2004: IEEE, pp. 249–254.

German Orbital Systems GmbH (2016): CUBESAT ONBOARD COMPUTER. *Berlin, Germany*. Available online at http://www.orbitalsystems.de/produkte/gos-cubesat-obc/?lang=en, checked on 7/6/2019.

Gilmore, D. G. (2002a): Appendix A: Surface Optical Property Data. In David G. Gilmore (Ed.): Spacecraft thermal control handbook. 2. ed. El Segundo, California: Aerospace Press, pp. 791–801.

Gilmore, D. G. (2002b): Spacecraft Thermal Control Handbook. Volume 1 - Fundamental Technologies. (2nd edition). 2.th ed.: Aerospace Press. Available online at https://app.knovel.com/hotlink/pdf/id:kt007RIOL2/spacecraft-thermal-control/insulation-introduction, checked on 4/3/2020.

Gilmore, D. G.; Stuckey, W. K.; Fong, M. (2002): Thermal Surface Finishes. In David G. Gilmore (Ed.): Spacecraft thermal control handbook. 2. ed. El Segundo, California: Aerospace Press, pp. 139–160.

Gluck, D. F.; Baturkin, V. (2002): Mountings and Interfaces. In David G. Gilmore (Ed.): Spacecraft thermal control handbook. 2. ed. El Segundo, California: Aerospace Press, pp. 247–329.

Goode, A. (2021): Regolith Adherence Characterization (RAC) and the CLPS payload process. In *LSIC Dust Mitigation Focus Group*. Available online at https://lsic.jhuapl.edu/uploadedDocs/focus-files/983-DM%20Monthly%20Meeting%20-%202021%2009%20September_Presentation%20-%20Aegis%20Aerospace.pdf, checked on 10/22/2021.

Graf, J. (2017): Chlorate Oxygen Generator (Oxygen Candle). Review of the History of Candle Development. For eventual publication in NESC Report. NASA. *Houston, Texas*. Available online at https://ntrs.nasa.gov/archive/nasa/casi.ntrs.nasa.gov/20170002051.pdf, checked on 1/10/2020.

Grandjean, T. R.; Groenewald, J.; Marco, J. (2019): The experimental evaluation of lithium ion batteries after flash cryogenic freezing. In *Journal of Energy Storage* 21, pp. 202–215. DOI: 10.1016/j.est.2018.11.027.

Graphite24.com: Technical Data Sheet GraphiteECO. Available online at https://www.graphite24.de/media/pdf/56/c3/d5/G24_TDS-ECO.pdf, checked on 2/7/2021.

Greenhouse, M. A. et al. (2004): The James Webb Space Telescope integrated science instrument module. In John C. Mather (Ed.): Optical, Infrared, and Millimeter Space Telescopes. *SPIE Astronomical Telescopes + Instrumentation.* USA, Monday 21 June 2004: SPIE (SPIE Proceedings), p. 754.

Grimm, R. E. et al. (2020): A MAGNETOTELLURIC SOUNDER TO PROBE TERRESTRIAL PLANET AND SATELLITE INTERIORS. In *Lunar and Planetary Science Conference*. Available online at https://www.hou.usra.edu/meetings/lpsc2020/pdf/1568.pdf, checked on 10/22/2021.

Gscheidle, C. et al. (2022): Challenges of operating a drilling instrument on a small rover at the lunar poles - LVS-PIE phase A study results. In *Planetary and Space Science* 212, p. 105426. DOI: 10.1016/j.pss.2022.105426.

Guadalupi, A. (2019): MEGA2560_Rev3e. Arduino. Available online at https://content.arduino.cc/assets/MEGA2560_Rev3e_sch.pdf, updated on 1/23/2019, checked on 11/2/2019.

Gui, H. et al. (2020): Review of Power Electronics Components at Cryogenic Temperatures. In *IEEE transactions on power electronics* 35 (5), pp. 5144–5156. DOI: 10.1109/tpel.2019.2944781.

Gutiérrez-D, Edmundo A.; Deen, M. Jamal; Claeys, C. (Eds.) (2001): Low Temperature Electronics. *San Diego*: Academic Press.

Guzik, M. C. et al. (2018): Regenerative fuel cell-based energy storage systems for lunar surface exploration. In *Survive the Lunar Night Workshop*. Available online at https://www.hou.usra.edu/meetings/survivethenight2018/pdf/7024.pdf.

Hanamura, H. et al. (1986): Operation of bulk CMOS devices at very low temperatures. In *IEEE Journal of Solid-State Circuits* 21 (3), pp. 484–490. DOI: 10.1109/JSSC.1986.1052555.

Hardt, B. E.; Karam, R. D.; Eby, R. J. (2002): Louvers. In David G. Gilmore (Ed.): Spacecraft thermal control handbook. 2. ed. El Segundo, California: Aerospace Press, pp. 331–353.

Harris, R. S. (1972): Apollo Experience Report: Thermal Design of Apollo Lunar Surface Experiments Package. NASA (NASA TN D-6738). Available online at https://play.google.com/store/books/details?id=lrNxsR5w_34C&rdid=book-lrNxsR5w_34C&rdot=1, checked on 11/3/2021.

Hassan, A.; Savaria, Y.; Sawan, M. (2018): Electronics and Packaging Intended for Emerging Harsh Environment Applications: A Review. In *IEEE Trans. VLSI Syst.* 26 (10), pp. 2085–2098. DOI: 10.1109/TVLSI.2018.2834499.

He, H. et al. (2017): Imaging of plasmasphere by Chang'e 3. In : 2017 XXXIInd General Assembly and Scientific Symposium of the International Union of Radio Science (URSI GASS), pp. 1–3.

Hemingway, B. S.; Robie, R. A.; Wilson, W. H. (1973): Specific heats of lunar soils, basalt, and breccias from the Apollo 14, 15, and 16 landing sites, between 90 and 350\textdegreeK. In *Lunar and Planetary Science Conference Proceedings* 4, p. 2481.

Hollosi, B. et al. (2008): Delay-insensitive asynchronous ALU for cryogenic temperature environments. In : 2008 51st Midwest Symposium on Circuits and Systems, pp. 322–325.

Horizon (2013): Minipak - Product information. Horizon. Available online at https://www.horizonfuelcell.com/minipak, checked on 12/20/2019.

Howell, E. (2016): Lunokhod 1: 1st Successful Lunar Rover. Available online at https://www.space.com/35090-lunokhod-1.html, checked on 3/1/2019.

Huntress, W. t.; Marov, M. Y. (2011): Soviet Robots in the Solar System. Mission Technologies and Discoveries: Springer.

Ihmig, F. R.; Shirley, S. G.; Zimmermann, H. (2015): Batch screening of commercial serial flash-memory integrated circuits for low-temperature applications. In *Cryogenics* 71, pp. 39–46. DOI: 10.1016/j.cryogenics.2015.05.005.

IntelligentEnergy (2019): Cylinder Options for UAVs. Guide to cylinder options for UAV applications. Intelligent Energy. Available online at https://www.intelligent-energy.com/uploads/product_docs/Cylinder_Guide_August_2019_web_7wtWLeD.pdf, checked on 12/20/2019.

IntelligentEnergy (2020): IE-Soar 650 - 800 - 2400W - Product Datasheets. Available online at https://www.intelligent-energy.com/our-products/uavs/, checked on 3/19/2021.

Isabellenhütte Heusler GmbH & Co. KG (2014): Datenblatt // Manganin®. Available online at https://www.isabellenhuette.de/fileadmin/Daten/Praezisionslegierungen/Datenblaetter_Widerstand/MANGANIN.pdf, checked on 2/7/2021.

ISIS - Innovative Solutions In Space B.V. (2019): ISIS On board computer. Flight heritage since 2012. *Delft, The Netherlands*. Available online at https://www.isispace.nl/product/on-board-computer/, checked on 9/5/2019.

ISISpace (2020): S-Band Transceiver - Product information. Available online at https://www.isispace.nl/product/s-band-transceiver/, checked on 4/20/2020.

ispace (Ed.) (2020): Commercial Lunar Exploration Program "HAKUTO-R" Reveals Final Design and Plan for 'Mission 1' Lunar Lander. Available online at https://ispace-inc.com/news/?p=1636, checked on 9/25/2020.

Jin, L.-Z. et al. (2015): Development of a Low Oxygen Generation Rate Chemical Oxygen Generator for Emergency Refuge Spaces in Underground Mines. In *Combustion Science and Technology* 187 (8), pp. 1229–1239. DOI: 10.1080/00102202.2015.1031223.

Keymeulen, D. et al. (2007 - 2007): Extreme Temperature Electronics based on Self-Adaptive System using Field Programmable Gate Array. In : 2007 IEEE Aerospace Conference. *2007 IEEE Aerospace Conference.* Big Sky, MT, 03.03.2007 - 10.03.2007: IEEE, pp. 1–6.

Khan, M. S. et al. (2018): Hungarian Team Puli Towards Lunar Science and Exploration. In *Cospar, Pasadena*, Article MT-072.

Kim, T. (2014): NaBH4 (sodium borohydride) hydrogen generator with a volume-exchange fuel tank for small unmanned aerial vehicles powered by a PEM (proton exchange membrane) fuel cell. In *Energy* 69, pp. 721–727. DOI: 10.1016/j.energy.2014.03.066.

Kim, T. Y. (2020): Thermal shelter for survival of rover during cryogenic lunar night. In *Acta Astronautica* 171, pp. 151–155. DOI: 10.1016/j.actaastro.2020.02.048.

Kirschmann, R. K.; Sokolowski, W. M.; Kolawa, E. A. (1999): Die Attachment for -120C to 20C Thermal Cycling of Microelectronics for future Mars Rovers. An oveview. Available online at https://ntrs.nasa.gov/search.jsp?R=20000056903, checked on 2/28/2019.

Kolawa, E. A. (2007): Extreme environments technologies for futures space science missions. With assistance of T. Balint, G. Birur, G. S. Bolotin, E. J. Brandon, L. Del Castillo, H. Garret et al. (JPL D–32832).

Kolawa, E. A. et al. (2013): A motor drive electronics assembly for Mars Curiosity Rover: An example of assembly qualification for extreme environments. In : 2013 IEEE International Reliability Physics Symposium (IRPS). *2013 IEEE International Reliability Physics Symposium (IRPS).* Anaheim, CA, 14.04.2013 - 18.04.2013: IEEE, 2E.2.1-2E.2.9.

König GmbH Kunststoffprodukte (2016): PEEK - Polyetheretherketon. *Gilching, Germany*. Available online at https://www.koenig-kunststoffe.de/produkte/peek/technisches-datenblatt-peek.pdf, updated on June 2016, checked on 5/12/2021.

Korthauer, R. (2013): Handbuch Lithium-Ionen-Batterien. *Berlin, Heidelberg*: Springer.

Krause, F. C. et al. (2018): High Specific Energy Lithium Primary Batteries as Power Sources for Deep Space Exploration. In *J. Electrochem. Soc.* 165 (10), A2312-A2320. DOI: 10.1149/2.1061810jes.

Krebs, G. (2019): Chang'e 3, 4 (CE 3, 4) / Yutu 1, 2. Gunters Space Page. Available online at https://space.skyrocket.de/doc_sdat/change-3.htm, checked on 3/1/2019.

Kumar, V. et al. (2020): Formulation of micro-rover autonomy software for lunar exploration. In *i-Sairas*. Available online at https://www.hou.usra.edu/meetings/isairas2020fullpapers/pdf/5068.pdf.

Kundu, P. P.; Dutta, K. (2016): Hydrogen fuel cells for portable applications. In : Compendium of Hydrogen Energy: Elsevier, pp. 111–131.

Kurzweil, P.; Dietlmeier, O. K. (2015): Elektrochemische Speicher. *Wiesbaden*: Springer Fachmedien.

Kwon, S. et al. (2019): Development of a high-storage-density hydrogen generator using solid-state NaBH4 as a hydrogen source for unmanned aerial vehicles. In *Applied Energy* (vol 251). Available online at https://doi.org/10.1016/j.apenergy.2019.113331, checked on 1/10/2020.

Lawrence, S. (2016): The Lunar Exploration Roadmap:Exploring the Moon in the 21stCentury: Themes, Goals, Objectives, Investigations, and Priorities, 2016. A Community Endeavor Coordinated by theLunar Exploration Analysis Group (LEAG). With assistance of P. Abell, B. Bailey, D. Beaty, D. Beinhoff, M. S. Bell, M. Duke et al. ISECG. Available online at https://www.lpi.usra.edu/leag/roadmap/, checked on 6/29/2021.

LG Chem (2014): PRODUCT SPECIFICATION - Rechargable Lithium Ion Battery Model: INR18650MJ1 3500 mAh. With assistance of Kyung Su Oh (LRB-PS-CY3450_MJ1).

Li, C. et al. (2015): The Chang'e 3 Mission Overview. In *Space Sci Rev* 190 (1-4), pp. 85–101. DOI: 10.1007/s11214-014-0134-7.

Liang, Y.; Meng, Y. (2017 - 2017): The Analysis of Over-Temperature Using Avionics Device and Research of Uprating Method. In : 2017 International Conference on Sensing, Diagnostics, Prognostics, and Control (SDPC). *2017 International Conference on Sensing, Diagnostics, Prognostics and Control (SDPC).* Shanghai, 16.08.2017 - 18.08.2017: IEEE, pp. 699–703.

Lindner, M. et al. (2001): Cryogenics in Space - A review of the missions and technologies. In *ESA Bulletin* (107). Available online at https://www.esa.int/esapub/bulletin/bullet107/bul107_12.pdf, checked on 7/11/2021.

Linear Technology Corporation (1997): Datasheet - LTC1540 - Nanopower Comparator with Reference (LT 0817 REV). Available online at https://www.analog.com/media/en/technical-documentation/data-sheets/1540fb.pdf, checked on 1/27/2022.

Liu, J. et al. (2019): Pathways for practical high-energy long-cycling lithium metal batteries. In *Nat Energy* 4 (3), pp. 180–186. DOI: 10.1038/s41560-019-0338-x.

Losekamm, M. J. et al. (2021): LUVMI-X: A Versatile Platform for Resource Prospecting on the Moon. In *Earth & Space Conference*.

Losekamm, M. J. et al. (2022): Assessing the Distribution of Water Ice at the Lunar Poles with LUVMI-X: A Mission Concept. In *submitted to Planetary Science Journal (accepted 19.4.22)*.

LTO: TK18650 NT35 Datasheet.

Maddox, R. L. (1976): p-MOSFET parameters at cryogenic temperatures. In *IEEE Transactions on Electron Devices* 23 (1), pp. 16–21. DOI: 10.1109/T-ED.1976.18340.

Madzunkov, S. et al. (2020): Lunar Cube Sat Mass Spectrometer with Linear Energy Transfer Spectrometer Radiation Sensor. In *Lunar Surface Science Workshop*. Available online at https://www.hou.usra.edu/meetings/lunarsurface2020/pdf/5145.pdf.

Malzone, P. (2020): Extreme Temperature Evaluation of Commercial off-the-Shelf Components for Lunar Surface Application. Master Thesis. Technische Universität München. Chair of Astronautics.

Marquardt, J. et al. (2015): An overview of Ball Aerospace cryogen storage and delivery systems. In *IOP Conf. Ser.: Mater. Sci. Eng.* 101, p. 12086. DOI: 10.1088/1757-899X/101/1/012086.

Masten Space Systems (2019): Masten Lunar Delivery Service Payload Users Guide. Rev 1.0. Available online at https://explorers.larc.nasa.gov/2019APSMEX/MO/pdf_files/Masten%20Lunar%20Delivery%20Service%20Payload%20Users%20Guide%20Rev%201.0%202019.2.4.pdf, checked on 7/20/2022.

Matthes, C. S. R. et al. (2018): Next-generation radioisotope thermoelectric generator study. In : 2018 IEEE Aerospace Conference, pp. 1–9.

Mauracher, F. (2019): Scalable and Modular Architecture for Self-organizing Power Systems on Small Spacecrafts. Master Thesis. TUM, Munich, Germany. Department of Informatics.

Mauro, S. (2019): Challenges of Designing a Passive Thermal Control System for the Astrobotic Peregrine Lunar Lander. Thermal & Fluids Analysis Workshop 2019. *Nasa Langley Research Center, Hampton, VA*, 2019. Available online at https://tfaws.nasa.gov/wp-content/uploads/TFAWS19-PT-09.pdf, checked on 6/7/2021.

Maxwell (2013): K2 Series Ultracapacitors - Datasheet (1015370.4).

Mazarico, E. et al. (2011): Illumination conditions of the lunar polar regions using LOLA topography. In *Icarus* 211 (2), pp. 1066–1081. DOI: 10.1016/j.icarus.2010.10.030.

McDermott, S. A.; Jacobovits, A.; Yashiro, H. (2002): Automotive electronics in space: combining the advantages of high reliability components with high production volume. In : Proceedings, IEEE Aerospace Conference. *2002 IEEE Aerospace Conference.* Big Sky, MT, USA, 9-16 March 2002: IEEE, 4-1857-4-1869.

Microchip Technology Inc. (2019): Datasheet - MCP2515 Stand-Alone CAN Controller with SPI Interface Data Sheet (DS20001801J). Available online at https://www.digikey.com/en/products/detail/microchip-technology/MCP2515-E-ML/4739302, checked on 1/27/2022.

Molecular Products (2018): EO2-30-TDS-v10. Technical Data Sheet. Molecular Products. Available online at https://www.molecularproducts.com/wp-content/uploads/2018/03/EO2-30-TDS-v10.pdf, checked on 1/10/2020.

Mulder, G. et al.: Test methods for improved battery cell understanding. Draft White Paper. Available online at https://www.batterystandards.info/sites/batterystandards.info/files/draft_white_paper_test_methods_for_battery_understanding_v3_0.pdf, checked on 10/6/2020.

myFC (2013): myFC Powertrekk - Produktinformationen. myFC. Available online at https://www.beltrona.de/shop/datasheets/3055.pdf, checked on 12/20/2019.

Nandini, K. et al. (2018): Study on survivability of 18650 Lithium-ion cells at cryogenic temperatures. In *Journal of Energy Storage*. Available online at https://doi.org/10.1016/j.est.2018.03.018, checked on 10/2/2020.

NanoAvionics (2020): CubeSat On-Board Computer – Main Bus Unit SatBus 3C2. Available online at https://nanoavionics.com/cubesat-components/cubesat-on-board-computer-main-bus-unit-satbus-3c2/, checked on 2/6/2020.

NASA (2020): Multi-Mission Radioisotope Thermoelectric Generator (MMRTG). NASAfacts (NF-2020-05-619-HQ). Available online at https://mars.nasa.gov/internal_resources/788/, checked on 4/4/2022.

NASA (2022a): Power and Thermal Systems. General Purpose Heat Source. Available online at https://rps.nasa.gov/power-and-thermal-systems/thermal-systems/general-purpose-heat-source/, checked on 4/1/2022.

NASA (2022b): Power and Thermal Systems. Light-Weight Radioisotope Heater Unit. Available online at https://rps.nasa.gov/power-and-thermal-systems/thermal-systems/light-weight-radioisotope-heater-unit/, checked on 4/1/2022.

NASA Goddard (1996): INSTRUCTIONS FOR EEE PARTS SELECTION, SCREENING, AND QUALIFICATION. With assistance of G. P. Kramer (311-INST-001). Available online at https://nepp.nasa.gov/nepag/guidelines/GSFC-311-INST-001_rev_A.pdf, checked on 6/7/2022.

NASA JPL (Ed.) (1966): Surveyor-I-MissionReport. Part I - Mission Description and Performance.

NASA JPL (Ed.) (1967): Surveyor III - Mission Report. Part I Mission Description and Performance.

NASA JPL (Ed.) (1969): Surveyor - Program Results. With assistance of L. D. Jaffe, R. H. Steinbacher, C. O. Alley, S. A. Batterson, Se. E. Christensen. NASA JPL (SP-184).

Newell, M. A. et al. (2001): Extreme temperature (-170/spl deg/C to +125/spl deg/C) electronics for nanorover operation. In : 2001 IEEE Aerospace Conference Proceedings (Cat. No.01TH8542), vol. 5, 2443-2456 vol.5.

O'Brien, B. J. (2019): EASEP AND ALSEPs. Available online at https://www.brianjobrien.com/easep-and-alseps, checked on 3/6/2019.

Ogawa, K. et al. (2014): A thermal control system for long-term survival of scientific instruments on lunar surface. In *The Review of scientific instruments* 85 (3), p. 35108. DOI: 10.1063/1.4867906.

O'Hayre, R. P. et al. (2016): Fuel cell fundamentals. Third edition. *Hoboken New Jersey*: John Wiley & Sons Inc.

Oikawa, T. et al. (2018): Thermal Design and Analysis of conceptual flight model for a lunar exploration rover. In *International Astronautical Congress*, Article IAC-18,A3,2C,9,x48263. Available online at https://iafastro.directory/iac/paper/id/48263/summary/, checked on 5/23/2021.

Osterman, D. P. et al. (2019 - 2019): CIRiS, a CubeSat-compatible, imaging radiometer for earth science and planetary missions. In Charles D. Norton, Thomas S. Pagano, Sachidananda R. Babu (Eds.): CubeSats and SmallSats for Remote Sensing III. *CubeSats and SmallSats for Remote Sensing III.* San Diego, United States, 11.08.2019 - 15.08.2019: SPIE, p. 14. Available online at https://www.spiedigitallibrary.org/conference-proceedings-of-spie/11131/2531404/CIRiS-a-CubeSat-compatible-imaging-radiometer-for-earth-science-and/10.1117/12.2531404.full.

Ould Ely, T. et al. (2018): Lithium–Sulfur Batteries: State of the Art and Future Directions. In *ACS Appl. Energy Mater.* 1 (5), pp. 1783–1814. DOI: 10.1021/acsaem.7b00153.

Oxisenergy (2019): Ultra Light Lithium Sulfur Pouch Cell. Datasheet. Available online at https://45uevg34gwlltnbsf2plyua1-wpengine.netdna-ssl.com/wp-content/uploads/2019/07/OXIS-Li-S-Ultra-Light-Cell-spec-sheet-v4.2.pdf, checked on 10/6/2020.

Paige, D. A. et al. (2010): Diviner Lunar Radiometer observations of the LCROSS impact. In *Science (New York, N.Y.)* 330 (6003), pp. 477–479. DOI: 10.1126/science.1197135.

Panasonic: NCR18650BF_Spec_(4.10V)_171106. Available online at https://b2b-api.panasonic.eu/file_stream/pids/fileversion/3446, checked on 4/22/2020.

Panasonic (2021): Datasheet - Precision Thick Film Chip Resistors. Available online at https://industrial.panasonic.com/cdbs/www-data/pdf/RDA0000/AOA0000C304.pdf, checked on 1/27/2022.

Patterson, R. L. (2001): Development of electronics for low-temperature space missions. With assistance of A. Hammoud, J. E. Dickman, S. S. Gerber, E. Overton (NASA-TM-2001-210235).

Patterson, R. L. et al. (2002a): Electronics for Deep Space Cryogenic Applications (NASA/TM-2002-211695).

Patterson, R. L. (2003): Electrical Devices and Circuits for Low Temperature Space Applications. With assistance of A. Hammoud, J. E. Dickman, S. S. Gerber, E. Overton, M. E. Elbuluk (NASA/TM-2003-212600).

Patterson, R. L.; Hammoud, A. (2010a): Effects of Temperature on the Performance and Stability of Recent COTS Silicon Oscillators. In *NASA Electronic Parts and Packaging Program - Report*. Available online at https://ntrs.nasa.gov/citations/20100041300, checked on 1/19/2022.

Patterson, R. L.; Hammoud, A. (2010b): Test Results of Selected Commercial DC/DC Converters under Cryogenic Temperatures - A Digest. In *NASA Electronic Parts and Packaging Program - Report*. Available online at https://ntrs.nasa.gov/citations/20110012024, checked on 1/19/2022.

Patterson, R. L.; Hammoud, A.; Elbuluk, M. (2006): Assessment of electronics for cryogenic space exploration missions. In *Cryogenics* 46 (2-3), pp. 231–236. DOI: 10.1016/j.cryogenics.2005.12.002.

Patterson, R. L.; Hammoud, A.; Elbuluk, M. E. (2008): Evaluation of COTS Electronic Parts for Extreme Temperature Use in NASA Missions. In *International Energy Engineering Conference (IECEC)*. Available online at https://ntrs.nasa.gov/search.jsp?R=20090004581, checked on 7/30/2020.

Patterson, R. L.; Hammoud, A.; Panko, S. (2010): Evaluation of Fairchild's Gate Drive Optocoupler, Type FOD3150, under Wide Temperature Operation. In *NASA Electronic Parts and Packaging Program - Report*. Available online at https://ntrs.nasa.gov/citations/20100042191, checked on 1/19/2022.

Patterson, R. L.; Stone, R.; Hammoud, A. (2002b): Investigation of Stepper Motor Controllers For Ultra-Low Temperature Environments. In *NASA Electronic Parts and Packaging Program - Report*.

Patton, T. (2021): Thermal Control System Contract for VIPER Mission Awarded. Available online at https://exterrajsc.com/thermal-control-system-contract-for-viper-mission-awarded/2021/09/16/, checked on 11/8/2021.

PCM Products (2019a): PlusIce Eutectic (E) Range - Product Specification. With assistance of Adam Dicken. Available online at www.pcmproducts.net, checked on 12/11/2019.

PCM Products (2019b): PlusIce Hydrated Salt (S) Range - Product Specification. With assistance of Adam Dicken. Available online at www.pcmproducts.net, checked on 12/11/2019.

PCM Products (2019c): PlusIce Organic (A) Range - Product Specification. With assistance of Adam Dicken. Available online at www.pcmproducts.net, checked on 12/11/2019.

Petro, A. (2020): Surviving and Operating Through the Lunar Night. In *Proceedings of the IEEE Aerospace Conference*.

Plotog, I. et al. (2010 - 2010): PCBs thermophysical properties in lead-free assembling process assessment. In : 2010 IEEE 16th International Symposium for Design and Technology in Electronic Packaging (SIITME). *2010 IEEE 16th International Symposium for Design and Technology in Electronic Packaging (SIITME).* Pitesti, Romania, 23.09.2010 - 26.09.2010: IEEE, pp. 29–32. Available online at https://ieeexplore.ieee.org/document/5651792, checked on 3/10/2021.

PTS (2020): Audi Lunar Quattro. Description of the lunar rover of planetary transportation systems GmbH. Available online at https://www.pts.space/products/audi-lunar-quattro/, checked on 8/7/2020.

Pustovalov, A. A. (2007): Role and Prospects of Application of RTG on Base of Plutonium-238 for Planetary Exploration. In *Proceedings of the 5th European conference on thermoelectrics*. Available online at https://ieeexplore.ieee.org/stamp/stamp.jsp?tp=&arnumber=8741786, checked on 4/1/2022.

Rajashekara, K.; Akin, B. (2013 - 2013): A review of cryogenic power electronics - status and applications. In : 2013 International Electric Machines & Drives Conference. *2013 IEEE International Electric Machines & Drives Conference (IEMDC).* Chicago, IL, USA, 12.05.2013 - 15.05.2013: IEEE, pp. 899–904.

Ray, B. et al. (1995): 77 K operation of a multi-resonant power converter. In : Proceedings of PESC '95 - Power Electronics Specialist Conference. *PESC '95 - Power Electronics Specialist Conference.* Atlanta, GA, USA, 18-22 June 1995: IEEE, pp. 55–60.

Rayovac (2016): Marketing Data Sheet - Cell. DP-BR-20Al. With assistance of B. Bushong (123-BA02A).

Rochus, P. et al. (2011): Phase Change Material Device for Spacecraft Thermal Control. In *International Astronautical Congress*.

Rückerl, S. (2023): Specification of distributed computing for small satellites for boosting system performance. Dissertation (in progress). Technische Universität München. Chair of Astronautics.

Sacksteder, K.; Wegeng, R.; Suzuki, N. (2010): Lunar Prospecting Using Thermal Wadis and Compact Rovers Part A: Infrastructure for Surviving the Lunar Night. In : SPACE Conferences and Exposition. AIAA SPACE 2010 Conference & Exposition. *AIAA SPACE 2010 Conference & Exposition.* Anaheim, California. [Place of publication not identified]: [publisher not identified].

Saft (2006): LSH 20 Primary Lithium Battery - Datasheet.

Saft (2014): MP176065 Integration xc. Rechargeable lithium-ion cell (31108-2-1014). Available online at https://eshop.fulgurbattman.cz/priloha.php?ak=174080, checked on 10/9/2020.

Saft (2019a): Data.sheet.MP.174565.xtd. With assistance of Wayne PITT (31110-2-0819). Available online at https://www.saftbatteries.com/products-solutions/products/mp-small-vl, checked on 4/22/2020.

Saft (2019b): LS33600 Primary Lithium cell - Datasheet. With assistance of FOISSIER Méline (31007-2-0619).

Salisbury, J. W.; Hunt, G. R.; Logan, L. M. (1973a): Infrared spectra of Apollo 16 fines. In : Proceedings of the Fourth Lunar Science Conference (Supplement 4: Geochimica et Cosmochimica Acta), vol. 3, pp. 3191–3196. Available online at http://articles.adsabs.harvard.edu/cgi-bin/nph-iarticle_query?1973LPSC…4.3191S&defaultprint=YES&filetype=.pdf, checked on 1/9/2021.

Salisbury, J. W.; Hunt, G. R.; Logan, L. M. (1973b): Infrared spectra of Apollo 16 fines. In *Lunar and Planetary Science Conference Proceedings* 4, p. 3191.

Schoolcraft, J.; Klesh, A.; Werne, T. (2017): MarCO: Interplanetary Mission Development on a CubeSat Scale. In Craig Cruzen, Michael Schmidhuber, Young H. Lee, Bangyeop Kim (Eds.): Space Operations: Contributions from the Global Community. Cham: Springer International Publishing. Available online at https://trs.jpl.nasa.gov/bitstream/handle/2014/46089/CL%2316-1589.pdf?sequence=1&isAllowed=y, checked on 2/5/2020.

Schreiner, S. S. et al. (2016): Thermophysical property models for lunar regolith. In *Advances in Space Research* 57 (5), pp. 1209–1222. DOI: 10.1016/j.asr.2015.12.035.

Senyshyn, A. et al. (2015): Low-temperature performance of Li-ion batteries. The behavior of lithiated graphite. In *Journal of Power Sources* 282, pp. 235–240. DOI: 10.1016/j.jpowsour.2015.02.008.

Shamiul Alam et al. (2021): Cryogenic Memory Technologies.

Sheldal Corporation: The Red Book. *Northfield, Minnesot*a. Available online at http://www.sheldahl.com/sites/default/files/Documents/ShieldingMaterials/RedBook.pdf, checked on 1/20/2021.

Shepherd, P. et al. (2013 - 2013): A robust, wide-temperature data transmission system for space environments. In : 2013 IEEE Aerospace Conference. *2013 IEEE Aerospace Conference.* Big Sky, MT, 02.03.2013 - 09.03.2013: IEEE, pp. 1–13.

Shimizu, T.; Underwood, C. (2013): Super-capacitor energy storage for micro-satellites: Feasibility and potential mission applications. In *Acta Astronautica* 85, pp. 138–154. DOI: 10.1016/j.actaastro.2012.12.005.

SI, D. et al. (2014): Design and verification of thermal control system for Chang'E-3 probe (Translated to english by Google Translate). In *Sci. Sin.-Tech.* 44 (4), pp. 353–360. DOI: 10.1360/092014-40.

Siebes, G. et al. (2012): Thermal Margin Requirements Assessment & Recommendations. In *Thermal & Fluids Analysis Workshop*. Available online at https://tfaws.nasa.gov/TFAWS12/Proceedings/TFAWS2012-PT-010.pdf, checked on 6/7/2022.

Sierra Nevada Cooperation (2018): Space Technologies Product Catalogue.

Smart, M. C. et al. (1999a): Performance characteristics of lithium-ion cells for NASA's Mars 2001 Lander application. In *IEEE Aerospace and Electronic Systems Magazine* 14 (11), pp. 36–42. DOI: 10.1109/62.809207.

Smart, M. C. et al. (2004): Lithium-ion batteries for aerospace. In *IEEE Aerospace and Electronic Systems Magazine* 19 (1), pp. 18–25. DOI: 10.1109/MAES.2004.1263988.

Smart, M. C. et al. (2008): Li-Ion Electrolytes Containing Ester Co-Solvents for Wide Operating Temperature Range. In *ECS Transactions* 11 (29), pp. 99–108. DOI: 10.1149/1.2938912.

Smart, M. C. et al. (2010): Lithium-Ion Electrolytes Containing Ester Cosolvents for Improved Low Temperature Performance. In *J. Electrochem. Soc.* 157 (12), A1361. DOI: 10.1149/1.3501236.

Smart, M. C. et al. (2017): The Use of Ester Co-Solvent Based Low Temperature Electrolytes in Experimental and Large Capacity Prototype Graphite-LiNiCoAlO2 Lithium-Ion Cells. In *ECS Meeting Abstracts* (MA2017-01). Available online at https://doi.org/10.1149/MA2017-01/3/231.

Smart, M. C.; Ratnakumar, B. V.; Surampudi, R. (1999b): Electrolytes for Low-Temperature Lithium Batteries Based on Ternary Mixtures of Aliphatic Carbonates. In *J. Electrochem. Soc.* 146 (2), pp. 486–492. DOI: 10.1149/1.1391633.

SolidEnergy Systems (Ed.) (2019): HERMES 3Ah Data Sheet 8-25-17 rev5.docx. High Energy Rechargeable Metal Cells for Space. SolidEnergy Systems. Available online at http://assets.solidenergysystems.com/wp-content/uploads/2017/09/08171937/Hermes_Spec_Sheet1.pdf, checked on 12/20/2019.

Spruell, S. (2019): Chlorate-Candle-Technical-Data-Sheet-Revision-3. OC Lugo Co. Inc. (DM.130729.03.TDS1).

STMicroelectronics (2015): UM1956 User manual. STM32 Nucleo-32 boards (MB1180). Available online at https://www.st.com/resource/en/user_manual/dm00231744-stm32-nucleo32-boards-mb1180-stmicroelectronics.pdf, updated on 11/12/2018, checked on 10/26/2019.

STMicroelectronics (2017): UM2179 User manual. STM32 Nucleo-144 boards (MB1312). Available online at https://www.st.com/resource/en/user_manual/dm00368330-stm32-nucleo144-boards-mb1312-stmicroelectronics.pdf, updated on 11/26/2019, checked on 1/20/2020.

STMicroelectronics (2018): STM32L412xx. Ultra-low-power Arm® Cortex®-M4 32-bit MCU+FPU, 100DMIPS, up to 128KB Flash, 40KB SRAM, analog, ext. SMPS. Available online at https://www.st.com/resource/en/datasheet/stm32l412kb.pdf, updated on Sept. 2019, checked on 10/26/2019.

Summerer, L. (2006): Radioisotope Heater Units. Technical Aspects of Space Nuclear Power Sources (ESA-ACT-RPT-2327-RHU).

Summerer, L.; Stephenson, K. (2011): Nuclear Power Sources: A Key Enabling Technology for Planetary Exploration. In *Proceedings of the Institution of Mechanical Engineers, Part G: Journal of Aerospace Engineering* 225 (2), pp. 129–143. DOI: 10.1243/09544100JAERO766.

Sundararajan, V. (2018): Overview and Technical Architecture of India's Chandrayaan-2 Mission to the Moon. In : 2018 AIAA Aerospace Sciences Meeting. *2018 AIAA Aerospace Sciences Meeting.* Kissimmee, Florida. Reston, Virginia: American Institute of Aeronautics and Astronautics.

Swider-Lyons, K. et al. (01072013): Liquid Hydrogen Fuel System for Small Unmanned Air Vehicles. In : 51st AIAA Aerospace Sciences Meeting including the New Horizons Forum and Aerospace Exposition. *51st AIAA Aerospace Sciences Meeting including the New Horizons Forum and Aerospace Exposition.* Grapevine (Dallas/Ft. Worth Region), Texas. Reston, Virigina: American Institute of Aeronautics and Astronautics, p. 684.

Tadiran (2006): TLH-5930 Datasheet. With assistance of S. Danny.

Tadiran (2019): SL-560 - Datasheet.

Taica Corporation: λ-Gel® COH. Sheet-type Thermal Conductive GEL. Available online at https://docs.rs-online.com/3a78/0900766b81088d63.pdf, checked on 7/13/2021.

Tanaka, T. (2018): Design and Implementation of thermal control strategy for micro-size lunar exploration rover. In *International Astronautical Congress*, Article IAC-18,A3,2C,9,x48263. Available online at https://iafastro.directory/iac/paper/id/48263/summary/.

TDK Coorperation (2021): Datasheet - Multilayer ceramic chip capacitors. Automotive grade, general (Up to 75V). Available online at https://product.tdk.com/system/files/dam/doc/product/capacitor/ceramic/mlcc/catalog/mlcc_automotive_general_en.pdf, checked on 1/27/2022.

Team Indus (Ed.): Design Evolution of the TeamIndus rover ECA. Available online at https://medium.com/teamindus/design-evolution-of-the-teamindus-rover-eca-df4156e59a3d, checked on 9/25/2020.

Texas Instruments (2002a): Datasheet - Low-Power Rail-To-Rail Output 12-Bit Serial Input D/A Converter datasheet (Rev. B) (SBAS156B). Available online at https://www.ti.com/lit/ds/symlink/dac7512.pdf?HQS=dis-dk-null-digikeymode-dsf-pf-null-wwe&ts=1643298215020&ref_url=https%253A%252F%252Fwww.ti.com%252Fgeneral%252Fdocs%252Fsuppproductinfo.tsp%253FdistId%253D10%2526gotoUrl%253Dhttps%253A%252F%252Fwww.ti.com%252Flit%252Fgpn%252Fdac7512, checked on 1/27/2022.

Texas Instruments (2002b): Datasheet - SN65HVD23x 3.3-V CAN Bus Transceivers datasheet (Rev. H) (SLLS557H). Available online at https://www.ti.com/lit/ds/symlink/sn65hvd233.pdf?HQS=dis-dk-null-digikeymode-dsf-pf-null-wwe&ts=1643281084725&ref_url=https%253A%252F%252Fwww.ti.com%252Fgeneral%252Fdocs%252Fsuppproductinfo.tsp%253FdistId%253D10%2526gotoUrl%253Dhttps%253A%252F%252Fwww.ti.com%252Flit%252Fgpn%252Fsn65hvd233, checked on 1/27/2022.

Texas Instruments (2014): TS5A3166-Q1 0.9-Ω SPST Analog Switch datasheet (Rev. A) (SCDS357A). Available online at https://www.ti.com/lit/ds/symlink/ts5a3166-q1.pdf?HQS=dis-dk-null-digikeymode-dsf-pf-null-wwe&ts=1643297973302, checked on 1/27/2022.

Texas Instruments (2015): Datasheet - BQ29209-Q1 Voltage Protection with Automatic Cell Balance for 2-Series Cell Li-I datasheet (Rev. D). Texas Instruments (SLUSC62D). Available online at https://www.ti.com/lit/ds/symlink/bq29209-q1.pdf?HQS=dis-dk-null-digikeymode-dsf-pf-null-wwe&ts=1643292581804&ref_url=https%253A%252F%252Fwww.ti.com%252Fgeneral%252Fdocs%252Fsuppproductinfo.tsp%253FdistId%253D10%2526gotoUrl%253Dhttps%253A%252F%252Fwww.ti.com%252Flit%252Fgpn%252Fbq29209-q1, checked on 1/27/2022.

Texas Instruments (2017): SN74LVC126A Quadruple Bus Buffer Gate With 3-State Outputs datasheet (Rev. S) (SCAS339S). Available online at https://www.ti.com/lit/ds/symlink/sn74lvc126a.pdf?HQS=dis-dk-null-digikeymode-dsf-pf-null-wwe&ts=1643298442150&ref_url=https%253A%252F%252Fwww.ti.com%252Fgeneral%252Fdocs%252Fsuppproductinfo.tsp%253FdistId%253D10%2526gotoUrl%253Dhttps%253A%252F%252Fwww.ti.com%252Flit%252Fgpn%252Fsn74lvc126a, checked on 1/27/2022.

Texas Instruments (2018a): Datasheet - MSP430FR698x(1), MSP430FR598x(1) Mixed-Signal Microcontrollers datasheet (Rev. D) (SLAS789D). Available online at https://www.ti.com/lit/ds/symlink/msp430fr6989.pdf?HQS=dis-dk-null-digikeymode-dsf-pf-null-wwe&ts=1643299031601&ref_url=https%253A%252F%252Fwww.ti.com%252Fgeneral%252Fdocs%252Fsuppproductinfo.tsp%253FdistId%253D10%2526gotoUrl%253Dhttps%253A%252F%252Fwww.ti.com%252Flit%252Fgpn%252Fmsp430fr6989, checked on 1/27/2022.

Texas Instruments (2018b): Datasheet - LM7360x-Q1 3.5-V to 36-V, 5-A or 6-A Synchronous Step-Down Voltage Converter datasheet (Rev. A) (SNVSB12B). Available online at https://www.ti.com/lit/ds/symlink/lm73605-q1.pdf?HQS=dis-dk-null-digikeymode-dsf-pf-null-wwe&ts=1643296932720&ref_url=https%253A%252F%252Fwww.ti.com%252Fgeneral%252Fdocs%252Fsuppproductinfo.tsp%253FdistId%253D10%2526gotoUrl%253Dhttps%253A%252F%252Fwww.ti.com%252Flit%252Fgpn%252Flm73605-q1, checked on 1/27/2022.

Texas Instruments (2019): Datasheet - TPS63070 2-V to 16-V Buck-Boost Converter With 3.6-A Switch Current datasheet (Rev. B) (SLVSC58B). Available online at https://www.ti.com/lit/ds/symlink/tps63070.pdf?HQS=dis-dk-null-digikeymode-dsf-pf-null-wwe&ts=1643224617274, checked on 1/27/2022.

Texas Instruments (2020a): Datasheet - INA226-Q1 AEC-Q100, 36-V, 16-Bit, Ultra-Precise, I2C Output Current, Voltage, and Power Monitor With Alert datasheet (Rev. A) (SBOS743A). Available online at https://www.ti.com/lit/ds/symlink/ina226-q1.pdf?HQS=dis-dk-null-digikeymode-dsf-pf-null-wwe&ts=1643298883487&ref_url=https%253A%252F%252Fwww.ti.com%252Fgeneral%252Fdocs%252Fsuppproductinfo.tsp%253FdistId%253D10%2526gotoUrl%253Dhttps%253A%252F%252Fwww.ti.com%252Flit%252Fgpn%252Fina226-q1, checked on 1/27/2022.

Texas Instruments (2020b): Datasheet - TPS6213xA-Q1 3-V to 17-V 3-A Step-Down Converter With DCS Control datasheet (Rev. E) (SLVSCC2E). Available online at https://www.ti.com/general/docs/suppproductinfo.tsp?distId=10&gotoUrl=https%3A%2F%2Fwww.ti.com%2Flit%2Fgpn%2Ftps62130a-q1, checked on 1/27/2022.

Texas Instruments (2020c): Datasheet - TPS2553-Q1 Precision Adjustable Current-Limited Power-Distribution Switches datasheet (Rev. B) (SLVSBD0B). Available online at https://www.ti.com/lit/ds/symlink/tps2553-q1.pdf?HQS=dis-dk-null-digikeymode-dsf-pf-null-wwe&ts=1643282711575&ref_url=https%253A%252F%252Fwww.ti.com%252Fgeneral%252Fdocs%252Fsuppproductinfo.tsp%253FdistId%253D10%2526gotoUrl%253Dhttps%253A%252F%252Fwww.ti.com%252Flit%252Fgpn%252Ftps2553-q1, checked on 1/27/2022.

Texas Instruments (2021): Datasheet - TPS25940x-Q1 2.7-V to 18-V eFuse with Integrated Short-to-Battery Protection datasheet (Rev. D). Available online at https://www.ti.com/lit/ds/symlink/tps25940-q1.pdf?HQS=dis-dk-null-digikeymode-dsf-pf-null-wwe&ts=1643289995386&ref_url=https%253A%252F%252Fwww.ti.com%252Fgeneral%252Fdocs%252Fsuppproductinfo.tsp%253FdistId%253D10%2526gotoUrl%253Dhttps%253A%252F%252Fwww.ti.com%252Flit%252Fgpn%252Ftps25940-q1, checked on 1/27/2022.

Texas Instruments Inc. (2009): MSP430F552x,MSP430F551xMixed-SignalMicrocontrollers. *Dallas, Texas*. Available online at https://www.ti.com/lit/ds/symlink/msp430f5529.pdf, updated on 9/20/2018, checked on 10/28/2019.

Texas Instruments Inc. (2013): MSP430F5529LaunchPad™ DevelopmentKit(MSP--EXP430F5529LP). *Dallas, Texas*. Available online at http://www.ti.com/lit/ug/slau533d/slau533d.pdf, updated on 4/7/2017.

Torres, E. M. et al. (2017): Low Temperature Evaluation of EEE parts on Exomas ADE Rover. In *14h Symposium on Advanced Space Technologies in Robotics and Automation*. Available online at https://robotics.estec.esa.int/ASTRA/Astra2017/0.%20Tuesday%2020%20June/Poster%20Session/P14_Cueto.pdf, checked on 1/19/2022.

Torres Soto, L.; Summerer, L. (2008): Power to survive the lunar night - an SPS application? In *59th International Astronautical Congress* (IAC-08-C.3.1.2).

Tsakyridis, G. et al. (2019): Power system analysis and optimization of a modular experiment Carrier during an analog lunar demo mission on a volcanic environment. In *Acta Astronautica* 155, pp. 200–210. DOI: 10.1016/j.actaastro.2018.11.034.

Ulamec, S. et al. (2016): Rosetta Lander – Landing and operations on comet 67P/Churyumov–Gerasimenko. In *Acta Astronautica* 125, pp. 80–91. DOI: 10.1016/j.actaastro.2015.11.029.

Ulamec, S.; Biele, J.; Trollope, E. (2010): How to survive a Lunar night. In *Planetary and Space Science* 58 (14-15), pp. 1985–1995. DOI: 10.1016/j.pss.2010.09.024.

Urbina, D. et al. (2019): LOW TEMPERATURE TECHNOLOGIES AND ARCHITECTURE FOR EXTREME ENVIRONMENTS. In *International Astronautical Congress* (IAC-19.D1.3.6x52066).

Valiente-Blanco, I. et al. (2013): Characterization of commercial-off-the-shelf electronic components at cryogenic temperatures. In *Instrum Exp Tech* 56 (6), pp. 665–671. DOI: 10.1134/S0020441214010187.

Vaniman, D. et al. (1991): The Lunar Environment. In G. H. Heiken, D. T. Vaniman, B. M. French (Eds.): Lunar Sourcebook : a user's guide to the Moon: Cambridge University Press, pp. 27–60.

Vinaricky, Eduard (Ed.) (2016): Elektrische Kontakte, Werkstoffe und Anwendungen. *Berlin, Heidelberg*: Springer Berlin Heidelberg. Available online at https://link.springer.com/book/10.1007/978-3-642-45427-1, checked on 2/7/2021.

Vishay (2021): Datasheet - SFH6256 Optocoupler, Phototransistor Output, High Reliability, 5300 VRMS. Rev 2.9. Available online at https://www.vishay.com/docs/83671/sfh6156.pdf, checked on 1/27/2022.

VORAGO (2020): Vorago Development Kit datasheet. PEB1-VA41600, PEB1-VA41620, PEB1-VA41630. Available online at https://www.mouser.de/datasheet/2/805/Vorago_Development_Kit_datasheet1v2web-1815964.pdf, checked on 7/2/2020.

Wærnhus, I. et al. (2017): Regenerative Energy Storage System for Space Exploration Missions. In *E3S Web Conf.* 16, p. 10005. DOI: 10.1051/e3sconf/20171610005.

Walker, J. (2018): Flight System Architecture of the Sorato Lunar Rover. In *i-Sairas, Madrid,* checked on 9/25/2020.

Warner, C. (2020): First Commercial Moon Delivery Assignments to Advance Artemis. Available online at https://www.nasa.gov/feature/first-commercial-moon-delivery-assignments-to-advance-artemis, checked on 10/23/2021.

Williams, J.-P. et al. (2017): The global surface temperatures of the Moon as measured by the Diviner Lunar Radiometer Experiment. In *Icarus* 283, pp. 300–325. DOI: 10.1016/j.icarus.2016.08.012.

Wright, G. S. et al. (2015): The Mid-Infrared Instrument for the James Webb Space Telescope, II: Design and Build. In *Publications of the Astronomical Society of the Pacific* 127 (953), pp. 595–611. DOI: 10.1086/682253.

Würth (2020): Datasheet WE-MAPI SMT Power Inductor. Available online at https://www.we-online.com/katalog/datasheet/74438356022.pdf, checked on 1/27/2022.

Wyns, P.; Anderson, R. L. (1989): Low-temperature operation of silicon dynamic random-access memories. In *IEEE Transactions on Electron Devices* 36 (8), pp. 1423–1428. DOI: 10.1109/16.30954.

Yayathi, S. et al. (2016): Energy distributions exhibited during thermal runaway of commercial lithium ion batteries used for human spaceflight applications. In *Journal of Power Sources* 329, pp. 197–206. DOI: 10.1016/j.jpowsour.2016.08.078.

Ye, P. et al. (2017): An overview of the mission and technical characteristics of Change'4 Lunar Probe. In *Sci. China Technol. Sci.* 60 (5), pp. 658–667. DOI: 10.1007/s11431-016-9034-6.

Yingst, R. A. et al. (2020): THE HEIMDALL CAMERA SYSTEM: TURNING EYES ON THE MOON. In *Lunar and Planetary Science Conference*. Available online at https://www.hou.usra.edu/meetings/lpsc2020/pdf/1439.pdf, checked on 10/22/2021.

Yingzhuo Jia et al. (2018): The scientific objectives and payloads of Chang'E−4 mission. In *Planetary and Space Science* 162, pp. 207–215. DOI: 10.1016/j.pss.2018.02.011.

Zachny, K. et al. (2021): TRIDENT Drill for VIPER and PRIME1 Missions to the Moon. In *Lunar and Planetary Science Conference*. Available online at https://www.hou.usra.edu/meetings/lpsc2021/pdf/2400.pdf, checked on 10/23/2021.

Zak, A. (2018): The Day a Soviet Moon Rover Refused to Stop. A formerly secret report details the triumphs and setbacks of an early lunar mission. Available online at https://www.airspacemag.com/daily-planet/time-soviet-moon-rover-refused-stop-180967884/, checked on 3/1/2019.

8.2 List of Publications

First author publications

Biswas, J. et al: “Energy storage selection and operation for night-time survival of small lunar surface systems”, *Acta Astronautica*, 2021

Biswas, J. et al: “Exploring the Moon with the Lunar Volatiles Mobile Instrumentation – Extended (LUVMI-X) Platform”, *European Lunar Symposium*, Padua (virtual), 2020

Biswas, J. et al: "Searching for potential ice-rich mining sites on the Moon with the Lunar Volatiles Scout", *Planetary and Space Science*, vol 181, 2020

Biswas, J. et al: "Characterization of the Lunar Volatiles Scout for In-Situ Volatiles Extraction and Analysis", *European Lunar Symposium*, Manchester, 2019

Biswas, J. et al: "Mobile In-Situ Exploration of Lunar Volatiles with the LVS on LUVMI", *European Lunar Symposium*, Toulose, 2018

Biswas, J. et al: "Application of the LVS Subsurface Probe on the LUVMI Rover for a Lunar Volatiles Exploration Mission", *European Lunar Symposium*, Muenster, 2017

Co-author publications

Losekamm, M. J. et al: „Assessing the Distribution of Water Ice And Other Volatiles at the Lunar South Pole with LUVMI-X: A Mission Concept”, *Planetary Science Journal*, 2022

Gscheidle, C. et al: “Challenges of operating a drilling instrument on a small rover at the lunar poles - LVS-PIE phase A study results”, *Planetary and Space Science*, 2022

Tattusch, T. et al: “iDRILL – An Instrumented Drill for Lunar Volatile Prospecting”, ESMATS, held virtually, 2021

Gancet, J. et al: “LUVMI-X: An Innovative Instrument Suit and Versatile Mobility Solution for Lunar Exploration”, International Astronautical Congress, Dubai, 2021

Gscheidle, C. et al: “Searching for Lunar Water with the LVS on a Small Rover - Phase A Study Results”, *NASA Exploration Science Forum and European Lunar Symposium*, held virtually, 2021

Smolka, A. et al: "Investigating the Operational Setup for the Lunar Volatiles Scout“, *NASA Exploration Science Forum and European Lunar Symposium*, held virtually, 2021

Smolka, A. et al: “Extracting Volatile Water from Lunar Regolith with the Lunar Volatiles Scout”, *Workshop on Terrestrial Analogs for Planetary Exploration*, 2021

Losekamm, M. J. et al: „LUVMI-X: A Versatile Platform for Resource Prospecting on the Moon”, *Earth and Space*, 2021

Sheridan, S.: “The LUVMI Volatile Sampler and Volatile Analysis Package for In Situ ISRU Applications on the Moon and Other Airless Bodies”, *Earth and Space*, 2021

Losekamm, M. J et al: „ Searching for Water Ice with the LUVMI-X Lunar Rover”, *i-SAIRAS*, held virtually, 2020

Jouland, M. et al: “Candidate landing sites and possible traverses at the South Pole of the Moon for the LUVMI-X rover”, *14th Europlanet Science Congress*, held virtually, 2020

Gscheidle, C. et al.; „Determining Lunar Regolith Water Content Using Permittivity Measurements with the Lunar Volatiles Scout”, *European Lunar Symposium*, Padua (virtual), 2020

Gancet, J. et al: "Lunar Volatiles Mobile Instrumentation (LUVMI) Project Results", *70th International Astronautical Congress (IAC)*, Washington, 2019

Gancet, J. et al: "LUVMI AND LUVMI-X: LUNAR VOLATILES MOBILE INSTRUMENTATION: CONCEPT

AND EXTENSION", 15th Symposium on Advanced Space Technologies in Robotics and Automation, 2019

Urbina, D. et al: "LUVMI: an innovative payload for the sampling of volatiles at the Lunar poles", International Astronautical Congress, Adelaide, 2017

Richter, L. et al: “OHB INSTRUMENTS DEVELOPMENT FOR VOLATILE SCOUTING ON THE MOON, International Astronautical Congress, Adelaide, 2017

Reiss, P. et al: "In-Situ thermal Extraction and Analysis of Lunar Volatiles with the Lunar Volatiles Scouting Instrument", *European Lunar Symposium*, Amsterdam, 2016

8.3 List of Supervised Theses

Zheng, J.: “Pressure Response Characterization of the Lunar Volatiles Scout”, Semester Thesis, RT-SA 2022/04

Bauer, B.: “Coupled Power-/Thermal System Optimization for a Small Lunar Surface System”, Master Thesis, RT-MA 2020/21

Malzone, P.: “Extreme Temperature Evaluation of Commercial off-the Shelf Components for Lunar Surface Application”, Master Thesis, RT-MA 2020/10

Bauer, B.: “Development and Verification of a test setup for the evaluation of electronic COTS components under lunar conditions”, Semester Thesis, RT-SA 2019/16

Malzone, P. Q.: “Battery Evaluation for the Extreme Environmental Conditions on the Lunar Surface”, Semester Thesis, RT-SA 2019/14

Valero, T.: “Design of a Communication Architecture for a Lunar Surface System”, Semester Thesis, RT-SA 2019/15

Lösch, C.: “Investigation on Measurement Errors for Thermocouple Insertion in JSC-1A”, Semester Thesis, RT-SA 2018/08

Reganaz, M.: “Detailed Design, Assembly, Integration, Test and Contamination assessment for the LUVMI Instrument”, Master Thesis, RT-MA 2018/08

Miguel, B.: “Games in Science Communication: The LUVMI Iteractive Lunar Mission Simulator”, Interdisciplinary Project, IDP-2018/07

Junker, J. H.: “Thermal Design of the LUVMI Rover”, Semester Thesis, RT-SA 2017/20

Chatziioannou, G.: “Thermal Analysis and Optimization of the LUVMI Volatiles Sampler”, Semester Thesis, RT-SA 2017/12

Pluhár, G.: “Determination of Potential Traverse Paths for LUVMI Rover”, Semester Thesis, RT-SA 2017/05

Appendix A List of Figures and Tables

A.1 List of Figures

A.2 List of Tables

Appendix B Description of the DPP Elements

A render image showing the assembly of DPP is shown in Figure 1-5. Its major electronics subsystems are the Battery module, the Power Distribution System, the Command & Data Handling Module and the Communications module. Energy storage at low temperatures is a topic in itself and is discussed in detail in chapter 4. However, the other subsystems are described in the following.

8.3.1 Electrical Power System

The DPP uses an adapted version of the MOVE/Ororatec Extendable Modular Power Supply (EMPS) (Amann 2019; Mauracher 2019) as a power distribution system. No detailed design of these DPP adaptations were available at the time this study was performed, for this reason, this investigation will solely rely on the original EMPS design. It is implemented on a 80 mm x 88 mm single PCB and features an MSP430 microcontroller with CAN interface for communication with other subsystems, Maximum Power Point Tracker, battery charge regulators for two lithium-ion batteries in series and five switchable outputs at battery voltage, 5 V and 3.3 V, with current monitoring and overcurrent protection. A schematic showing the basic layout of the EMPS is shown in Figure 8-2, a render image of the assembled PCB is shown in Figure 8-1. The EMPS includes all necessary features that larger and more sophisticated power systems also include and is therefore a suitable system for this investigation. The power distribution system is also the most crucial of all systems, as control the power flow to all other systems. It is therefore the first to be switched on and the last to be switched off.

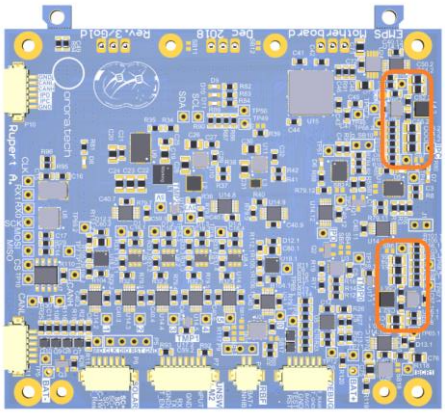

Figure 8-1: Rendering of the MOVE/Ororatec EMPS (Amann 2019)

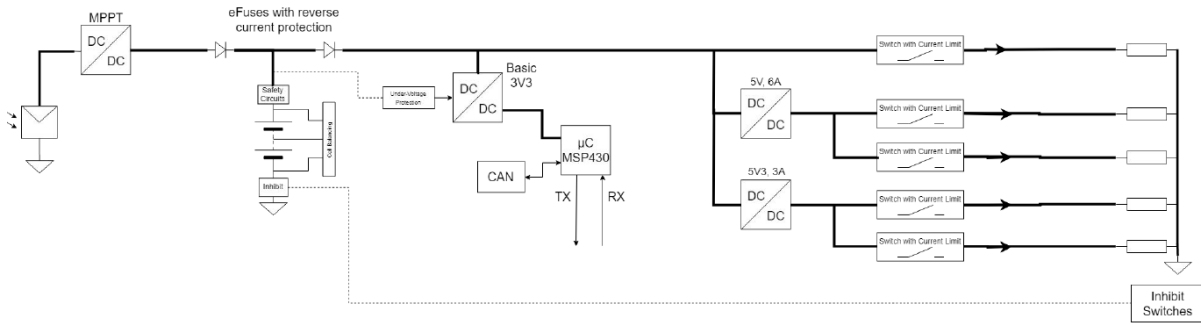

Figure 8-2: Schematic of the EMPS (Mauracher 2019)

8.3.2 Command & Data Handling Module

As the name suggests, this system is responsible for the handling and pre-processing of the payload and telemetry data, data storage and receiving and implementing commands. The DPP CDH is an evolution of the MOVE CDH (Donini et al. 2016) that relies on a Vorago VA41620 microcontroller for its core functionality. This element is a low-power, radiation hardened (up to 300 krad) implementation of the ARM Cortex-M4 architecture running on 100 MHz and is thus well suited for lunar application and powerful enough for simple data processing tasks. It features Error Detection and Correction (EDAC) and memory scrubbing capability that was already verified (Rückerl 2023) in radiation environment and it is rated at -55°C to 125°C. No advanced design of the DPP CDH is available yet, therefore the investigation relies on the PEB1-VA41620 development board, which includes all necessary peripheral components and is therefore a useful blueprint for a future DPP CDH. It includes an on-board crystal oscillator (20 MHz), clock generator, 256 kByte FRAM and necessary interfaces for UART, I2C, SPI, CAN, Spacewire connections (VORAGO 2020). Figure 8-3 shows an image of the development board.

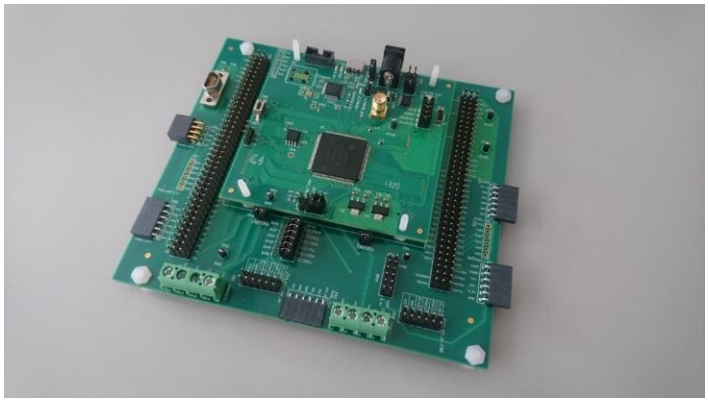

Figure 8-3: Image of the development board for the VA 41620 microcontroller.

8.3.3 Communication System

The DPP baseline design foresees the S-Band transceiver from ISISpace as its communication system. This module provides two-way S-Band communication at 2200 – 2290 MHz for transmission and 2025 – 2110 MHz for receiving. With 33 dBm transmission power it can achieve a maximum transmission rate of 5 Msym/s (ISISpace 2020). However, in combination with a 7.5 dBi patch antenna it will only transmit at 2 kbits/s. Unfortunately, insufficient funding was available for this study to experiment with this system, therefore only a simplified COTS transceiver was investigated (see section 3.6).

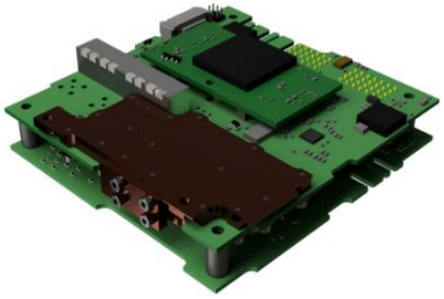

Figure 8-4: Render image of the ISISpace S-Band transceiver (ISISpace 2020)

Appendix C Supplementary Figures

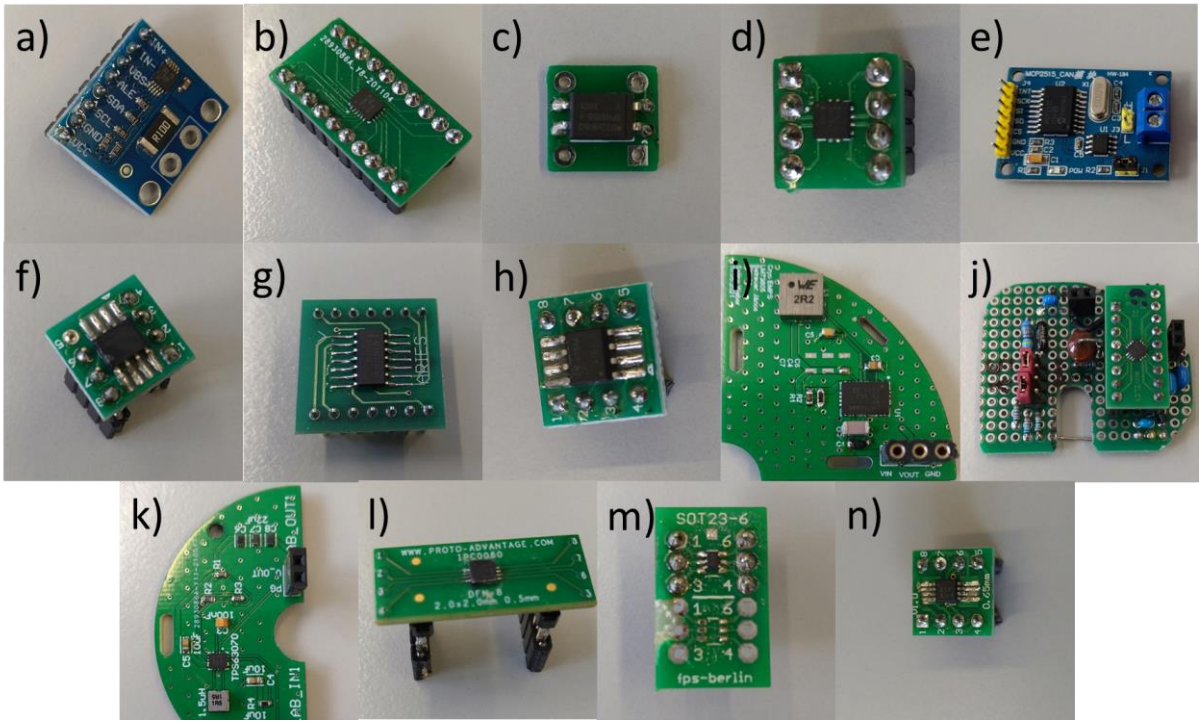

Figure 8-5: Images of the EMPS component test articles: a) Current Monitor INA226; b) eFuse TPS25940; c) Optocoupler SFH6156-4T; d) BCR BQ29209DRBT; e) CAN Controller MCP2515; f) CAN Transceiver SN65H; g) Buffer Gate SN74LVC126A; h) Power Switch FPF2701MX; i) Step-Down Converter LM73606; j) Voltage Regulator TPS62130; k) Buck-Boost Converter TPS63070; l) Comparator LTC1540; m) Analog Switch TS5A3166; n) DAC7512E/2K5;

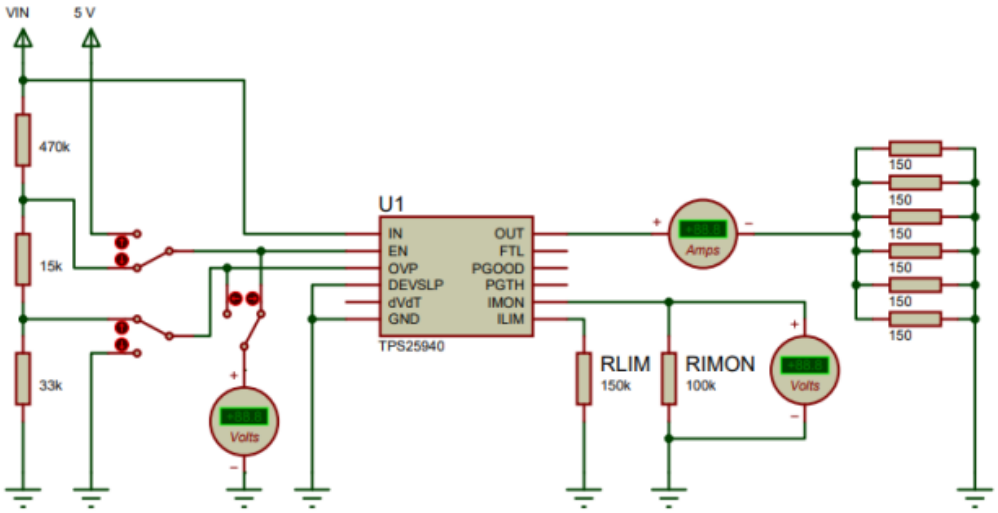

Figure 8-6: Test circuit used for the evaluation of the TPS25940 eFuse (Malzone 2020)

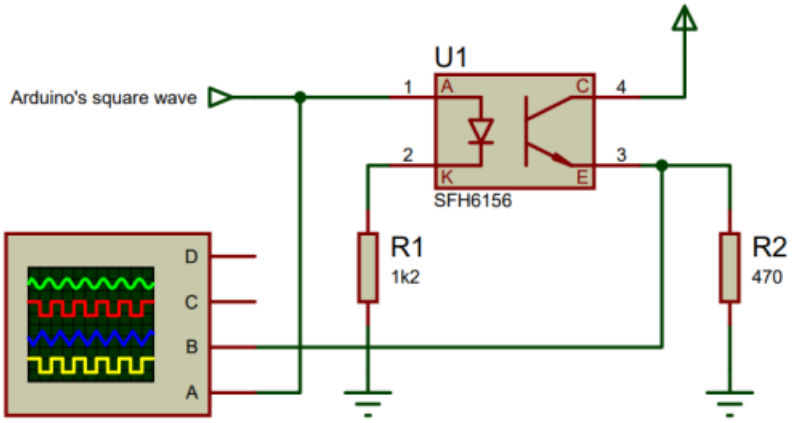

Figure 8-7: Test circuit for the evaluation of the SFH6156 optocoupler

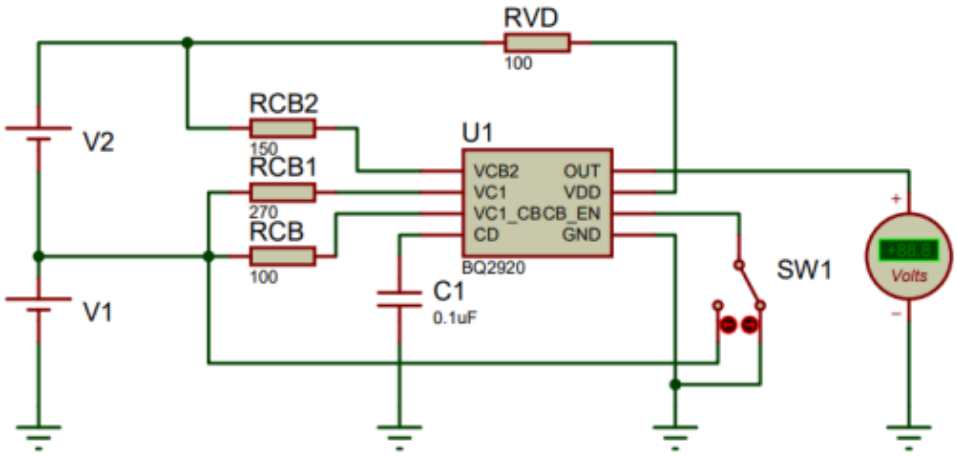

Figure 8-8: Test circuit for the evaluation of the BQ2920 battery charge regulator

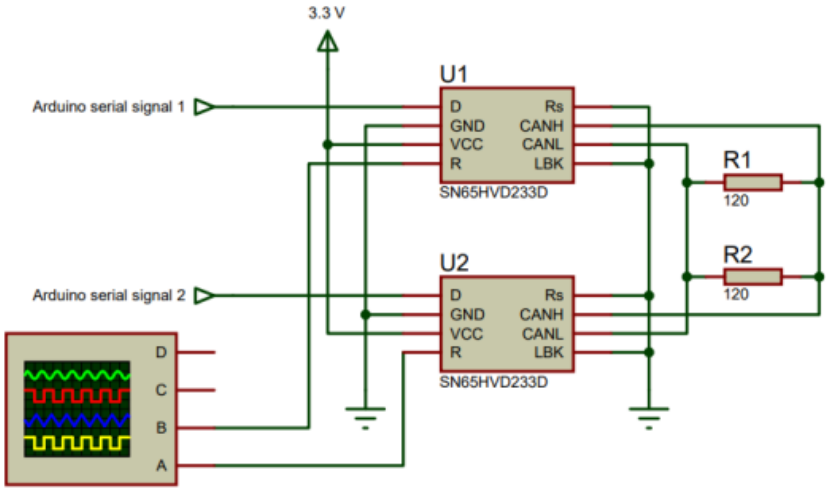

Figure 8-9: Test circuit for the SN65 CAN Transceiver

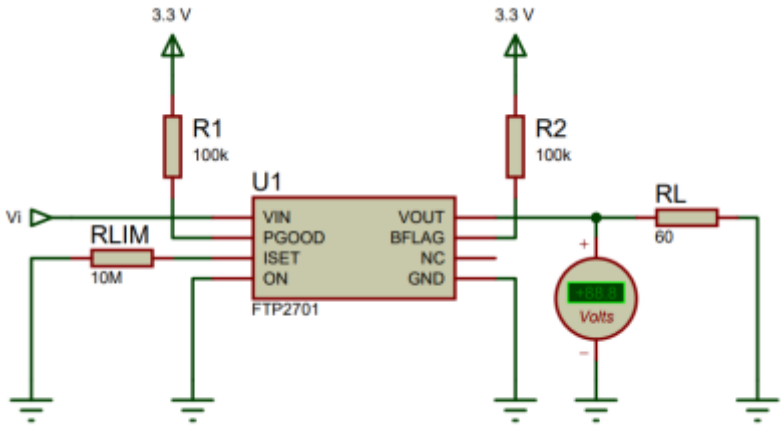

Figure 4-1: Load switch test circuit.

Figure 8-10: Test circuit for the FTP2701 load switch

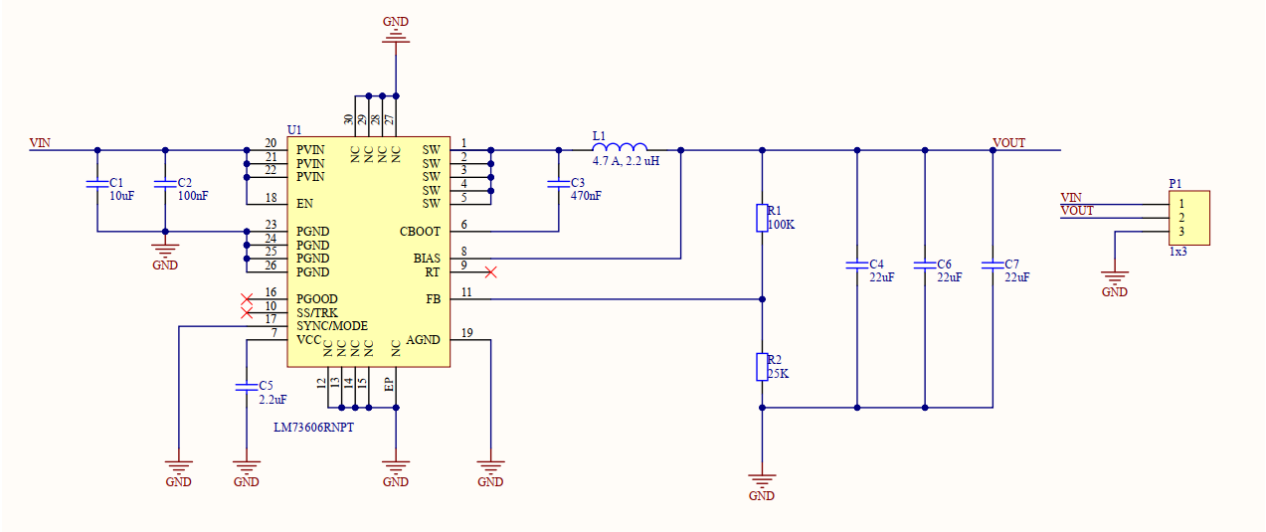

Figure 8-11: test circuit for the LM73605 Step-Down Converter

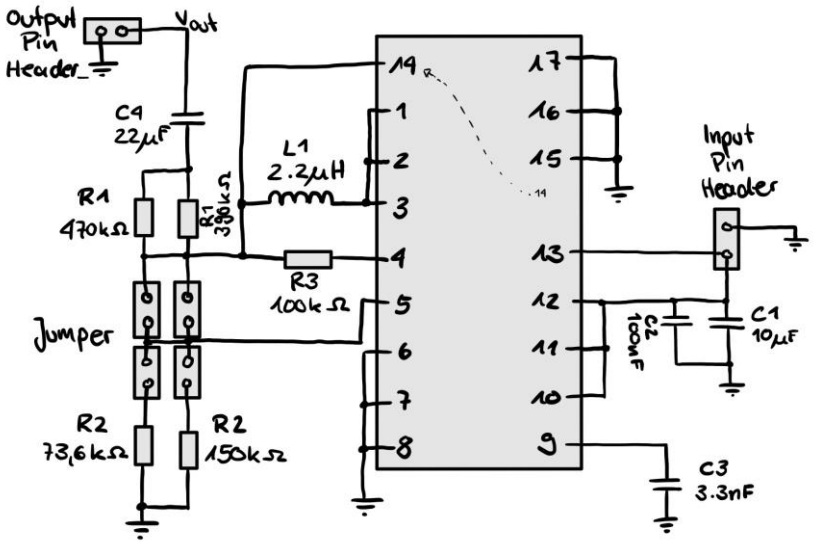

Figure 8-12: Test circuit for the TPS62130RGTT Step-Down Converter

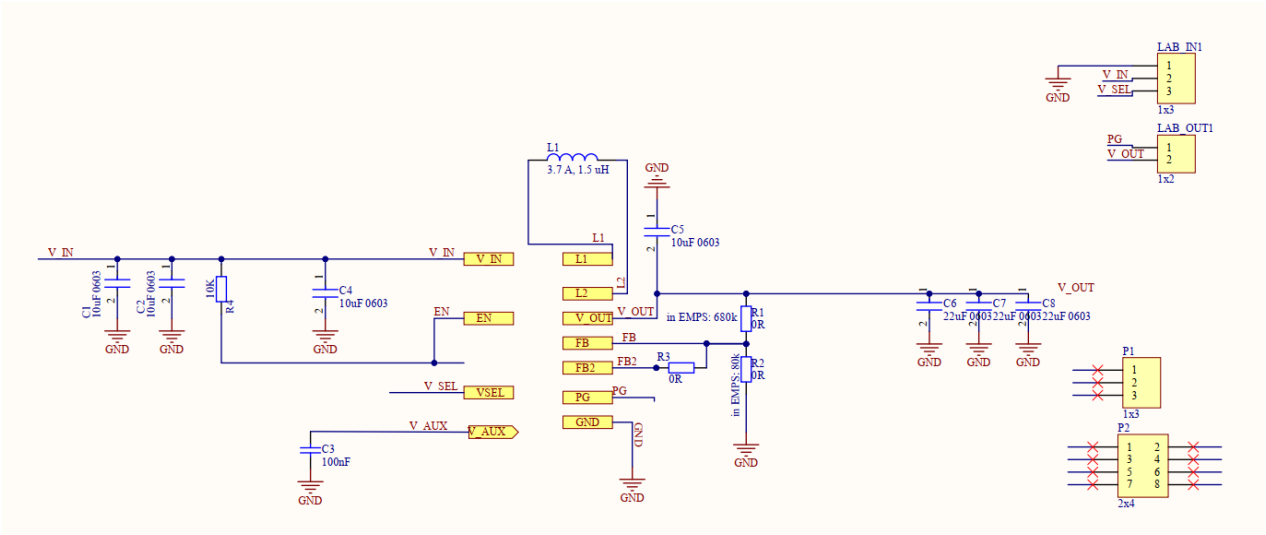

Figure 8-13: Test circuit for the TPS63070 buck-boost converter

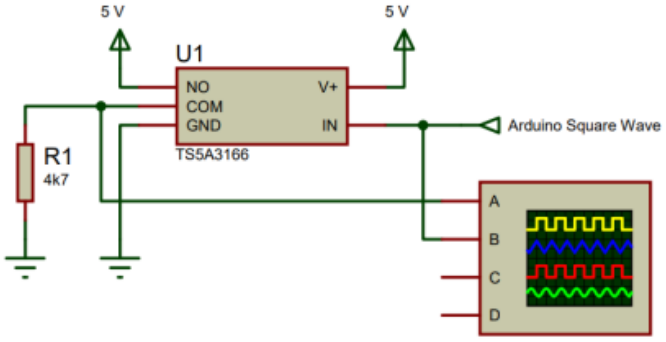

Figure 8-14: Test circuit for the TS5A3166 analogue switch

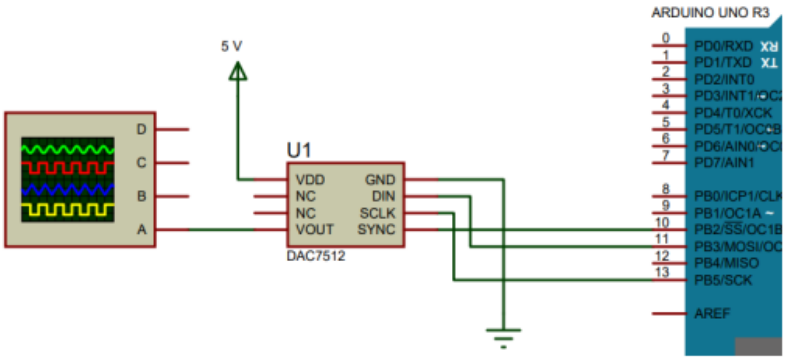

Figure 8-15: Test circuit for the DAC7512

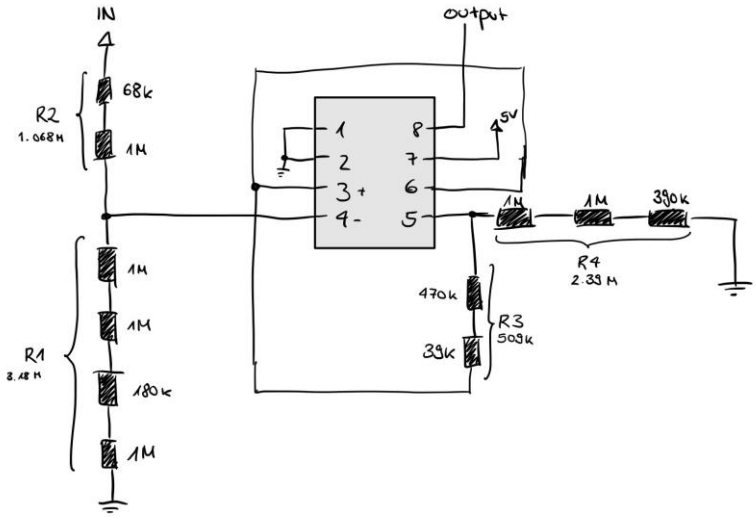

Figure 8-16: Test circuit for the LTC1540 Nano-comparator

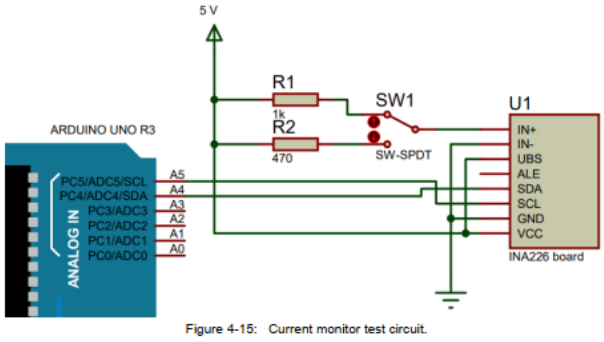

Figure 8-17: Test circuit for the INA226

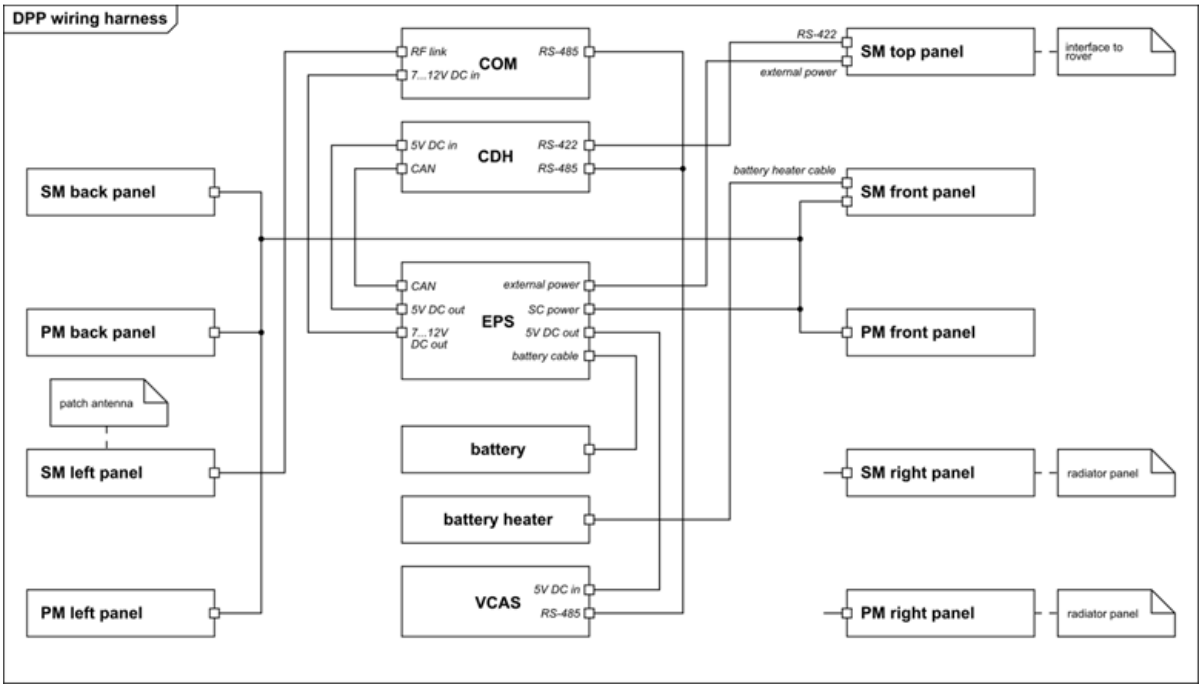

Figure 8-18: Schematic of the wiring connections inside the DPP (Bauer 2021).

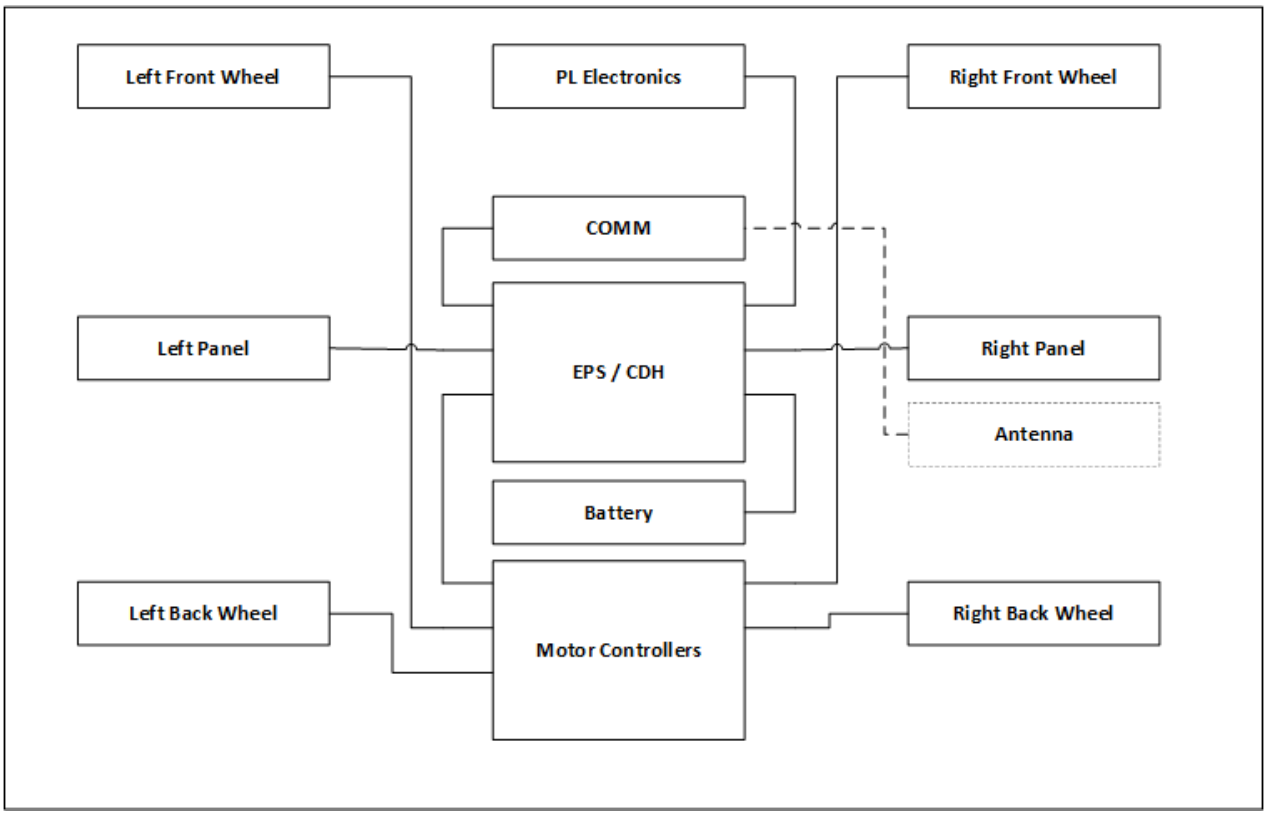

Figure 8-19: Schematic of the wiring connections inside the polar rover.

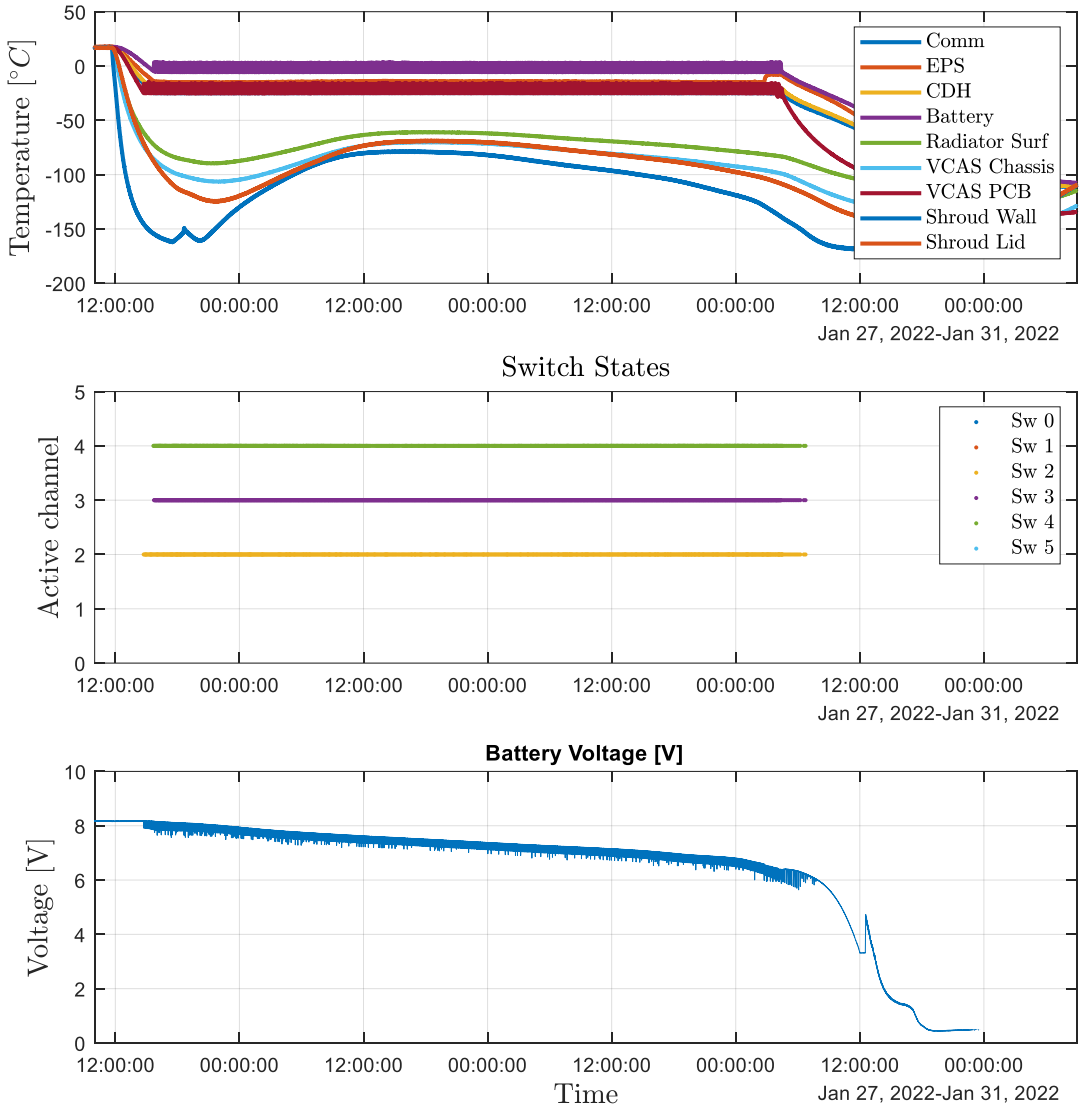

Figure 8-20: Results for the baseline prototype: Temperatures (top), Active channels (center) and battery charge (bottom).

Appendix D Supplementary Tables

Table 8-1: Overview over currently planned lunar surface missions or mission concepts

Name	Launch date	Expected Lifetime	Dry Mass [kg] (approx.)	Operation in shadow?	Reference
Peregrine Lander	2022	8 days	500		(Mauro 2019)
Nova C Lander	2022	n/a	600		Estimate
Masten XL-1 Lander	2022	12 days	675		(Masten Space Systems 2019)
Pulispace rover	2022	n/a	5		(Khan et al. 2018)
Hakuto lander (ispace)	2022	n/a	340		(ispace 2020)
Firefly Blue Ghost Lander	2023	14 days	500		(eoPortal Directory 2021)
Sorato Rover (ispace)	2023	10 days	4		(Walker 2018; Oikawa et al. 2018)
Polar Ice Explorer (ispace)	2023	10 days	12	✓	(Calzada-Diaz et al. 2018)
Viper	2023	90 days (using a solar oasis)	430	✓	(Colaprete et al. 2020b)
Audi Lunar Quattro (PTS)	2022	n/a	35		(PTS 2020)
Cuberover (Astrobotic)	2022	n/a	4		(Astrobotic 2020a)
LUVMI-X	2025	14 days	50	✓	(Losekamm et al. 2021)
LUVMI-X DPP Baseline	2025	14 days	3	✓	(Losekamm et al. 2021)
Remote Unit Small (Robex)	2026	n/a	3	✓	(Tsakyridis et al. 2019)
Remote Unit Large (Robex)	2026	n/a	10	✓	(Tsakyridis et al. 2019)
MoonRanger	2022	n/a	18	✓	(Kumar et al. 2020)
Orbit Beyond Z-01	-	n/a	210		
Axiom Space ECA rover	2022	n/a	10		(Team Indus)
Blue Moon (Blue Origin)	2024	n/a	7200		

Table 8-2: Overview of recently flown or planned lunar surface payloads

Payload	Mission	Purpose	Operation	Benefit from Night Survival	Reference
Lunar Compact Infrared Imaging System (L-CIRiS)	Masten XL-1	Infrared radiometer to explore regolith composition	Surface Scanner	No	(Osterman et al. 2019 - 2019)
Lunar CubeSat Mass Spectrometer (LCMS)	Masten XL-1	Exosphere Mass Spectrometery	Continuous / Event Based	Yes	(Madzunkov et al. 2020)
Heimdall Camera System	Masten XL-1	Mapping	Surface Scanner	No	(Yingst et al. 2020)
Neutron Spectrometer System	MoonRanger, Peregrine	Determination of subsurface hydrogen concentration	Surface Scanner	Yes, No	(eoPortal Directory 2021)
Mass Spectrometer Observing Lunar Operations (MSolo)	Masten XL-1, Peregrine	Exosphere Mass Spectrometery	Continuous / Event Based	Yes	(eoPortal Directory 2021)
Near-Infrared Volatile Spectrometer System (NIRVSS)	Masten XL-1, Peregrine, Viper	Infrared radiometer to explore regolith composition	Surface Scanner	No, No, Yes	(eoPortal Directory 2021)
Laser Retroreflector Array (LRA)	Masten XL-1, Nova-C, Peregrine	Passive Reflector	Passive	No	(eoPortal Directory 2021)
Sample Acquisition, Morphology Filtering, and Probing of Lunar Regolith (SAMPLR)	Masten XL-1	Robotic Sample Collection	Surface Scanner	No	(eoPortal Directory 2021)
Regolith Adherence Characterization (RAC)	Blue Ghost	Determine Regolith Properties	Continuous / Event Based	Yes	(Goode 2021)
Next Generation Lunar Retroreflectors (NGLR),	Blue Ghost	Passive Reflector	Passive	No	(Currie et al. 2020)
Lunar Environment Heliospheric X-ray Imager (LEXI)	Blue Ghost	X-Ray Imaging of Earths Magnetosphere	Continuous / Event Based	Yes	(eoPortal Directory 2021)
Reconfigurable, Radiation Tolerant Computer System (RadPC)	Blue Ghost	Demonstration of new Rad-tolerant electronics	Continuous / Event Based	Yes	(eoPortal Directory 2021)
Lunar Magnetotelluric Sounder (LMS)	Blue Ghost	Measure EM-Fields	Continuous / Event Based	Yes	(Grimm et al. 2020)
Lunar Instrumentation for Subsurface Thermal Exploration with Rapidity (LISTER)	Blue Ghost	Subsurface Heat Flow Probe	Continuous	Yes	(eoPortal Directory 2021)

Payload	Mission	Purpose	Operation	Benefit from Night Survival	Reference
Lunar PlanetVac (LPV)	Blue Ghost	Robotic Sample Collection	Surface Scanner		(eoPortal Directory 2021)
Stereo CAmeras for Lunar Plume Surface Studies (SCALPSS 1.1)	Blue Ghost	Monitor Interaction of landing exhaust with regolith	Single Event	No	(eoPortal Directory 2021)
Electrodynamic Dust Shield (EDS)	Blue Ghost	Electromagnetic dust handling experiment	Continuous	Yes	(eoPortal Directory 2021)
Lunar GNSS Receiver Experiment (LuGRE)	Blue Ghost	GPS Receiver	Continuous	Yes	(eoPortal Directory 2021)
Navigation Doppler Lidar for Precise Velocity and Range Sensing (NDL)	Nova-C IM-1, Peregrine	LIDAR for Navigation and Landing	Single Event	No	(Warner 2020)
Lunar Node 1 Navigation Demonstrator (LN-1)	Nova-C IM-1	Autonomous Navigation	Single Event	No	(Warner 2020)
Stereo Cameras for Lunar Plume-Surface Studies (SCALPSS)	Nova-C IM-1	Monitor Interaction of landing exhaust with regolith	Single Event	No	(Warner 2020)
Low-frequency Radio Observations for the Near Side Lunar Surface (ROLSES)	Nova-C IM-1	Low-Frequency Radio Experiment	Continuous	Yes	(Warner 2020)
Surface Exosphere Alterations by Landers (SEAL)	Peregrine	Mass Spectrometry to asses landing contamination and measure exosphere	Single Event / Continuous	Yes	(Benna et al. 2019)
Photovoltaic Investigation on Lunar Surface (PILS)	Peregrine	Solar Cell Qualification Experiment	Continuous	Yes	(Warner 2020)
Linear Energy Transfer Spectrometer (LETS)	Peregrine	Radiation Sensor	Continuous	Yes	(Warner 2020)
PROSPECT Ion-Trap Mass Spectrometer (PITMS) for Lunar Surface Volatiles	Peregrine	Lunar Exosphere Observation	Continuous	Yes	(Warner 2020)
Neutron Measurements at the Lunar Surface (NMLS)	Peregrine	Determination of subsurface hydrogen concentration	Surface Mapping	Yes	(Warner 2020)

Payload	Mission	Purpose	Operation	Benefit from Night Survival	Reference
Fluxgate Magnetometer (MAG)	Peregrine	Understand Charged Particle Movement	Continous / Surface Mapping	Yes	(Warner 2020)
The Regolith and Ice Drill for Exploration of New Terrains (TRIDENT)	Nova-C IM-2, VIPER	Subsurface Drill	Surface Mapping	No, Yes	(Zachny et al. 2021)
Radio Anatomy of Moon Bound Hypersensitive ionosphere and Atmosphere (RAMBHA)	Chanrayaan-2 Lander	Observe the lunar plasma environment	Continuous	Yes	(Sundararajan 2018)
Chandra's Surface Thermo Physical Experiment (CHaSTE)	Chanrayaan-2 Lander	Measure the temperature gradient in the lunar surface	Continuous	Yes	(Sundararajan 2018)
Instrument for Lunar Seismic Activity (ILSA)	Chanrayaan-2 Lander	Seismometer	Continuous	Yes	(Sundararajan 2018)
Alpha Particle X-ray Spectroscope (APXS)	Chandrayaan-2 Rover (Pragyaan), Chang'e 3 rover (Yutu)	X-Ray Spectrometer	Continuous	Yes	(Sundararajan 2018)
Laser Induced Breakdown Spectroscope (LIBS)	Chandrayaan-2 Rover (Pragyaan)	Measure elemental composition of regolith	Surface Scanner	Yes	(Sundararajan 2018)
Panoramic Cameras (PCAM)	Chang'e 3 rover (Yutu), Chang'e 4 rover (Yutu 2)	Mapping	Surface Scanner	Yes	(Li et al. 2015; Yingzhuo Jia et al. 2018)
Lunar Penetrating Radar (LPR)	Chang'e 3 rover (Yutu), Chang'e 4 rover (Yutu 2)	Subsurface radar measurements	Surface Scanner	Yes	(Li et al. 2015)
VIS-NIR Imaging Spectrometer (VNIS)	Chang'e 3 rover (Yutu), Chang'e 4 rover (Yutu 2)	Measure elemental composition of regolith	Surface Scanner	Yes	(Li et al. 2015)
Terrain Camera (TCAM)	Chang'e 3 lander, Chang'e 4 lander	Mapping	Surface Scanner	No	(Li et al. 2015; Yingzhuo Jia et al. 2018)
Landing Camera (LCAM)	Chang'e 3 lander, Chang'e 4 lander	Navigation	Single Event	No	(Li et al. 2015; Yingzhuo Jia et al. 2018)
Moon-based Ultraviolet Telescope (MUVT)	Chang'e 3 lander	UV Astronomy	Continuous	Yes	(Li et al. 2015)

Payload	Mission	Purpose	Operation	Benefit from Night Survival	Reference
Extreme Ultraviolet Camera (EUVC)	Chang'e 3 lander	Observation of the earth plasmasphere	Continuous	Yes	(He et al. 2017)
Low Frequency Spectrometer	Chang'e 4 lander	Low frequency radio astronomy	Continuous	Yes	(Yingzhuo Jia et al. 2018)
Lunar Lander Neutrons and Dosimetery (LND)	Chang'e 4 lander	Neutron dosimetry	Continuous	Yes	(Yingzhuo Jia et al. 2018)
Advanced Small Analyzer for Neutrals (ASAN)	Chang'e 4 rover (Yutu 2)	Measure flux of energetic neutral particles	Continuous	Yes	(Yingzhuo Jia et al. 2018)

Table 8-3: Summary table on low temperature data for various electronic components

Type	Typical Components	Results on low-temperature use	Tested down to:	References
Passive Components	Resistors	Various types useable to at least -180°C, Metal film types recommended, ceramic types should be avoided	-180°C	(Valiente-Blanco et al. 2013; Bourne et al. 2008)
	Capacitors	Electrolytic and ceramic capacitors should be avoided,	-180°C	(Valiente-Blanco et al. 2013)
	Inductors	Molypermalloy powder cores, high flux powder cores are recommended, ferrite cores discouraged	-190°C	(Gerber et al. 2004) (Chen et al. 2018)
Interfaces	Connectors	NanoD connectors were tested. Slight variations in contact resistance were measured, but no discontinuities.	-170°C	(Newell et al. 2001)
	Solders	Low temperature compatible soft solder available, could become an issue for high cycle numbers	-269°C	(Kirschmann et al. 1999)
Diodes	Diodes	Most types are useable. However reverse breakdown voltages decrease, Germanium based diodes should be avoided, GaAs show low reverse breakdown voltages at low temperature	-184	(Bourne et al. 2008)
	Zener Diodes	Changes in reference voltage (~10%)	-184°C	(Bourne et al. 2008)
	Bandgap reference diodes	Reference temperature changes, in this example from 2.487 at 25°C to 2.432 at -170°C.	-170°C	(Newell et al. 2001)
Transistors	Bi-polar transistors	Gain decreases with temperatures and reduces to zero at temperatures beneath -55°C To be avoided.		(Newell et al. 2001)
	MOSFETs	Various devices have been intensely tested down to 4.2 K. Operational parameters change and sufficient doping is required to ensure optimal functionality. However, gain actually improves at low temperatures.	-269°C; -170°C - 184°C	(Maddox 1976; Rajashekara and Akin 2013 - 2013; Newell et al. 2001; Bourne et al. 2008)

Type	Typical Components	Results on low-temperature use	Tested down to:	References
Integrated Circuits	CMOS	Low temperature leads to decreased propagation delays, increased gain and decreased channel resistance. Large temperature differences may cause hold time violations.	-170°C	(Newell et al. 2001)
	Analog to digital converters (ADCs)	Tested devices worked well, yet were only accurate to 12bit at low temperature instead of the 14bit at room temperature.	-170°C	(Newell et al. 2001)
	Operational Amplifiers	Operational at low temperatures.	-170°C	(Newell et al. 2001)
On-Board Computer	Microcontroller	Custom Moongoose V processor	-170°C	(Newell et al. 2001)
		Custom 8051 SiGe processor	-271°C	(Hollosi et al. 2008)
	Memory	Successful test of SRAM	-170°C	(Newell et al. 2001)
			-269°C	(Hanamura et al. 1986)
		Successful application of EEPROM	-170°C	(Newell et al. 2001)
		DRAM tested, fully operational at -98°C, partly operational at -84°C	-184°C	(Wyns and Anderson 1989)
		80% of investigated flash memories operational at -185°C.	-196°C	(Ihmig et al. 2015)
	Clocks	Multiple devices of various types investigated. Most devices show moderate deviation in frequency. MEMS types seem most stable.	-195°C	(Patterson et al. 2006) (Patterson and Hammoud 2010a)
	Digital interfaces	Custom RS-485 interface, operational at -175°C		(Shepherd et al. 2013 - 2013)
		Custom RS-485 interface, operational at -183°C		(England et al. 2014)
Power Distribution System	DC-DC converters	Successful operation of some COTS devices to -80°C or -120°C.	-195°C	(Patterson et al. 2006)
		Investigation of 9 COTS devices, failures at -40°C, -80°C, -120°C, -160°C, -180°C		(Patterson and Hammoud 2010b)
	SSRs / Optocoupler	Flawless operation down to -100°C, limited operation down to -190°C	-190°C	(Patterson et al. 2010)
Communication Module	Radio transceiver	Custom 9600 baud rate radio	-170°C	(Newell et al. 2001)
	FPGA	Successful operation of a COTS FPGA at -180°C.	-180°C	(Keymeulen et al. 2007 - 2007)
Motion Control	Motor Controllers	Brushless DC motor driver	-170	(Newell et al. 2001)

Table 8-4: Overview of the board condition at the time of last operation for each of the power channels. Temp MSP is the temperature of the MSP430 MCU, Temp Switch is the temperature of the power switch and Temp DCDC is the temperature of voltage converter.

Channel	Time of last operation	Temp MSP	Temp Switch	Temp DCDC
Chan 0	2752.8s	-123.5°C	-110.6°C	-118.1°C
Chan 1	2752.8s	-123.5°C	-110.6°C	-118.1°C
Chan 2	1796.3s	-99.6°C	-84.8°C	-91.6°C
Chan 3	1796.3s	-99.6°C	-84.8°C	-91.6°C
Chan 4	2752.8s	-123.5°C	-110.6°C	-118.1°C
Chan 5	2752.8s	-123.5°C	-110.6°C	-118.1°C

Table 8-5: Cross sections and thermal resistances of electrical connections within the DPP (Bauer 2021).

Electrical connection	Type	Power (W)	Voltage (V)	Nominal cross section (mm^2)	Selected cross section (mm^2)	Assumed length (mm)	Thermal resistance ($K\ W^{-1}$)
Antenna cable	RF	2.2	7.0	0.105	0.14	50	898
Battery cable	DC	14.8	3.6	1.373	1.50	100	84
CDH power	DC	0.37	5.0	0.024	0.41	150	464
COM data	RS-485	0.05	5.0	0.003	0.41	35	108
COM power	DC	14.3	5.0	0.955	0.41	35	108
EPS data	CAN	0.05	5.0	0.003	0.41	11	34
Rover data	RS-422	0.05	5.0	0.003	0.05	150	3797
Rover power	DC	14.8	5.0	0.988	1.00	150	190
Solar cell cables (PM)	DC	2.6	6.0	0.144	0.17	200	1489
Solar cell cables (PM)	DC	2.6	6.0	0.144	0.17	150	1117
PM data	RS-485	0.05	5.0	0.003	0.05	200	5063
PM power	RS-485	6	5.0	0.401	0.50	200	506
Battery heater	single wire	2.6	6.0	0.145	0.17	150	1117

Table 8-6: Thermal nodes with node masses, mass margins and specific heat (Bauer 2021).

Node name	Description	Node mass (g)	Mass margin (included in node mass)	Specific heat (J kg^{-1} K^{-1})
SM_COMT	Transmitter PCB	139	5 %	896
SM_COMR	Receiver PCB	89	5 %	896
SM_CDH	CDH PCB	54	20 %	896
SM_EPS	EPS PCB	147	10 %	896
SM_BAT	Battery volume	391	20 %	1000
SM_cubeStructure	SM structure	300	-	896
SM_cubeFront	SM front panel (solar panel)	20	-	1100
SM_cubeBack	SM back panel (solar panel)	20	-	1100
SM_cubeLeft	SM left panel (patch antenna)	70	10 %	1100
SM_cubeRight	SM right panel (radiator)	28	-	896
SM_cubeTop	SM top panel	20	-	1100
VCAS_cubeCore	VCAS payload stack	900	-	1100
VCAS_cubeStructure	PM structure	300	-	896
VCAS_cubeFront	PM front panel (solar panel)	20	-	1100
VCAS_cubeBack	PM back panel (solar panel)	20	-	1100
VCAS_cubeLeft	PM left panel (solar panel)	20	-	1100
VCAS_cubeRight	PM right panel (radiator)	28	-	896
	Total node mass:	**2566**	**Weighted avg. specific heat:**	**999**

Table 8-7: Cross sections and thermal resistances of electrical connections within the Polar Rover

Electrical connection	Type	Power (W)	Voltage (V)	Nominal cross section (mm^2)	Selected cross section (mm^2)	Assumed length (mm)	Number of wires	Thermal resistance (K W^{-1})
Motor Controllers / Wheel	DC / Data / TC	5	24	0.0037	0.205	500	4	1238
COMM Power	DC	15	28	0.0112	0.205	100	2	619
MC Power	DC	25	28	0.0186	0.205	200	2	1238
Battery / EPS	DC	50	28	0.0372	0.205	100	2	619
Solar Panel	DC	25	28	0.0186	0.205	500	2	3095
PL Power	DC	20	28	0.0149	0.205	300	2	1857